

DTIC FILE COPY

2

# NAVAL POSTGRADUATE SCHOOL Monterey, California

AD-A223 396



## THESIS

EFFECTS OF 1 HZ IMPOSED BULK FLOW  
UNSTEADINESS ON  
LAMINAR/TURBULENT TRANSITION IN A  
STRAIGHT CHANNEL

by

Thomas M. Coumes

December 1989

Thesis Advisor  
Co-Advisor

Phillip M. Ligrani  
Chelakara S. Subramanian

Approved for public release; distribution is unlimited.

90 07 2 015

Unclassified

security classification of this page

REPORT DOCUMENTATION PAGE					
1a Report Security Classification <b>Unclassified</b>			1b Restrictive Markings		
2a Security Classification Authority			3 Distribution/Availability of Report		
2b Declassification Downgrading Schedule			Approved for public release; distribution is unlimited.		
4 Performing Organization Report Number(s)			5 Monitoring Organization Report Number(s)		
6a Name of Performing Organization		6b Office Symbol	7a Name of Monitoring Organization		
Naval Postgraduate School		(if applicable) 34	Naval Postgraduate School		
6c Address (city, state, and ZIP code)			7b Address (city, state, and ZIP code)		
Monterey, CA 93943-5000			Monterey, CA 93943-5000		
8a Name of Funding Sponsoring Organization		8b Office Symbol	9 Procurement Instrument Identification Number		
NPS Direct Funding		(if applicable)	NPS Direct Funding (ONR Review)		
8c Address (city, state, and ZIP code)			10 Source of Funding Numbers		
Monterey, CA 93943-5000			Program Element No   Project No   Task No   Work Unit   Accession No		
11 Title (include security classification) <b>EFFECTS OF 1 HZ IMPOSED BULK FLOW UNSTEADINESS ON LAMINAR/TURBULENT TRANSITION IN A STRAIGHT CHANNEL</b>					
12 Personal Author(s) <b>Thomas M. Coumes</b>					
13a Type of Report		13b Time Covered		14 Date of Report (year, month, day)	
Master's Thesis		From To		December 1989	
15 Page Count 201					
16 Supplementary Notation The views expressed in this thesis are those of the author and do not reflect the official policy or position of the Department of Defense or the U.S. Government.					
17 Cosati Codes			18 Subject Terms (continue on reverse if necessary and identify by block number)		
Field	Group	Subgroup	Imposed Bulk Flow Unsteadiness, Laminar/Turbulent Transition, Tollmien-Schlichting Waves, Vortex, and Turbulent Spots, <i>Theses! jhd</i>		
19 Abstract (continue on reverse if necessary and identify by block number)					
<p>Laminar / turbulent transition is studied in a straight channel with 1 Hz imposed bulkflow unsteadiness for Reynolds numbers of 1103 to 2715 and Strouhal numbers of 0.06045 to 0.02455. Channel aspect ratio is 40 to 1 with 1.27 cm height, 50.8 cm width and 4.27 m length. Observations, videos, and photographs of smoke patterns show different subcritical transition events including Tollmien-Schlichting waves, vortex-array type motion evidenced by smoke swirls and ribbon like patterns, turbulent and fully turbulent flow. Fluctuating intensity magnitudes relative to velocities from imposed unsteadiness are determined from phase-averaged velocity traces. Of particular interest is whether the imposed unsteadiness advances or delays transition events. With the conditions that were investigated, transition events begin to occur at lower Reynolds numbers extend over a wider range of Reynolds numbers compared to flows with no imposed unsteadiness.</p> <p><i>Keywords:</i></p>					
20 Distribution Availability of Abstract			21 Abstract Security Classification		
<input checked="" type="checkbox"/> unclassified unlimited <input type="checkbox"/> same as report <input type="checkbox"/> DTIC users			Unclassified		
22a Name of Responsible Individual			22b Telephone (include Area code)		22c Office Symbol
Phillip M. Ligrani			(408) 646-3382		69Li

DD FORM 1473,84 MAR

83 APR edition may be used until exhausted  
All other editions are obsolete

security classification of this page

Unclassified

Approved for public release; distribution is unlimited.

Effects of 1 Hz Imposed Bulk Flow Unsteadiness on Laminar/Turbulent  
Transition in a Straight Channel

by

Thomas M. Coumes  
Lieutenant Commander, United States Navy  
B.S., Oregon State University, 1976

Submitted in partial fulfillment of the  
requirements for the degree of

MASTER OF SCIENCE IN MECHANICAL ENGINEERING

from the

NAVAL POSTGRADUATE SCHOOL

December, 1989

Author:

*Thomas M. Coumes*

Thomas M. Coumes

Approved by:

*Phillip M. Ligrani*

Phillip M. Ligrani, Thesis Advisor

*Chelakara S. Subramanian*

Chelakara S. Subramanian, Co-Advisor

*Anthony J. Healey*

Anthony J. Healey, Chairman  
Department of Mechanical Engineering

## ABSTRACT

Laminar/turbulent transition is studied in a straight channel with 1 Hz imposed bulk flow unsteadiness for Reynolds numbers of 1103 to 2715 and Strouhal numbers of 0.06045 to 0.02455. Channel aspect ratio is 40 to 1 with 1.27 cm height, 50.8 cm width and 4.27 m length. Observations, videos, and photographs of smoke patterns show different subcritical transition events including Tollmien-Schlichting waves, vortex-array type motion evidenced by smoke swirls and ribbon like patterns, turbulent spots and fully turbulent flow. Fluctuating intensity magnitudes relative to velocities from imposed unsteadiness are determined from phase-averaged velocity traces. Of particular interest, is whether the imposed unsteadiness advances or delays transition events. With the conditions that were investigated, transition events begin to occur at lower Reynolds numbers and extend over a wider range of Reynolds numbers compared to flows with no imposed unsteadiness.

Accession For	
NTIS GRA&I	<input checked="" type="checkbox"/>
DTIC TAB	<input type="checkbox"/>
Unannounced	<input type="checkbox"/>
Justification	
By	
Institution	
Accession Number	
Distribution	
A-1	



## TABLE OF CONTENTS

I. INTRODUCTION	1
A. BACKGROUND	1
B. OBJECTIVES	5
C. ORGANIZATION	6
II. EXPERIMENTAL FACILITIES	7
A. CHANNEL	7
B. UNSTEADY DEVICE	8
C. FLOW MEASUREMENTS	9
1. Bulk Velocity	10
2. Instantaneous Velocity	10
a. Hot-wire Probe and Probe Positioning	11
b. Hot-wire Bridge	11
c. Signal Conditioner	12
d. High Speed Data Acquisition System	12
e. Data Storage	13
f. Data Processing	13
D. FLOW VISUALIZATION	15
1. Smoke Wire System	15
2. Video Equipment	16
III. EXPERIMENTAL PROCEDURES	17
A. ORIFICE $\Delta P$ CALIBRATION	17
B. HOT-WIRE CALIBRATION	17

C. CHANNEL VALIDATION	18
1. Channel Flow Tests	18
2. Laminar Average Velocity Profile Calibration	18
D. FLOW MEASUREMENT	19
1. Reynolds Number Survey	19
2. Multi-run Averaging	19
3. Velocity Profiles	19
E. FLOW VISUALIZATION	20
IV. RESULTS AND DISCUSSION	21
A. CHANNEL FLOW QUALIFICATION	22
B. EFFECT OF REYNOLDS NUMBER ON LOCAL MEAN VELOCITY AT $y/d = 0.85$ DUE TO 1 Hz IMPOSED UNSTEADINESS	22
C. EFFECT OF REYNOLDS NUMBER ON RMS VELOCITY AT $y/d = 0.85$	23
D. EFFECT OF REYNOLDS NUMBER ON PHASE AVERAGED VELOCITY	23
E. MEAN VELOCITY PROFILES AND PHASE AVERAGED VELOCITIES	25
F. RMS VELOCITY PROFILES	26
G. FLOW VISUALIZATION	27
V. CONCLUSIONS	29
APPENDIX A. (SOFTWARE DIRECTORY)	31
APPENDIX B. (FIGURES)	33

LIST OF REFERENCES	192
INITIAL DISTRIBUTION LIST	194

## **I. INTRODUCTION**

### **A. BACKGROUND**

Many typical flows found in nature and in aerodynamic applications and almost all flows associated with turbomachinery involve freestream unsteadiness. Most of these flows, especially those of technological interest undergo transition from a laminar state to a turbulent condition. The accurate prediction of the location and extent of transition and the accompanying changes of important flow properties is vital to the design of aircraft and most energy transformation machines involving fluid flow.

Laminar-turbulent transition results in significant increases in local wall shear stress and convective heat transfer rates. This becomes evident by first considering laminar flows, where transport of heat and momentum normal to streamlines occurs only as a result of molecular diffusion. This is usually an advantage since tangential forces at solid surfaces (drag) and heat flux normal to surfaces are relatively low. Occasionally, laminar flows are undesirable since they tend to separate from surfaces more easily than turbulent flows. In most applications, laminar flows are unstable and transitional or fully turbulent flows exist. In the latter, higher rates of diffusion across mean streamlines due to turbulent transport cause significantly higher drag and heat flux at surfaces.

The parameter generally used to describe the onset of transition is the Reynolds number. In channel flows, linear stability theory predicts that the laminar flow becomes unstable to small amplitude disturbances at a critical Reynolds number of 5772. Here the Reynolds number is based on mean



centerline velocity and channel half-width. With large amplitude disturbances, however, the transitional Reynolds number for channel flow may be as low as 1000-1500. The value of Reynolds number at the onset of transition depends strongly on the disturbances existing in the flow and conditions which prevail in the entry region of the channel.

Also, the sequence of events which occur during transition are strongly dependent on upstream history, especially laminar boundary layer character and development. There is a growing collection of evidence which also suggests that turbulent shear layer development is more strongly dependent on its upstream history than previously believed. This would mean: (1) that transition affects turbulent boundary layer structure downstream, and (2) that turbulent boundary layer results obtained under equilibrium conditions (i.e. streamwise self-similarity) may not adequately represent flow behavior near surfaces of operating turbines and airfoils. Non-equilibrium shear layer development near turbine passage surfaces and near airfoils is due to varying surface curvature, varying pressure gradients, and freestream unsteadiness. Unsteadiness is particularly important in this regard since it affects shear properties at a given location in two ways: (1) by its local direct influence and (2) from its affect on shear layers upstream, whose history affects downstream development. The computational work of Singer, Ferziger and Reed [Ref. 1] indicates that moderately low frequency oscillations in the channel can initiate nonlinear effects which trigger transition on flow regimes where the steady flow remains laminar. These happen even though linear theory indicates that the flow is stable. Experimental clarification of these points is needed, along with the verification of the sequence of events occurring during the transition

process at different Strouhal numbers. The view of the overall transition process is especially valuable to the gas turbine research community.

Unsteadiness is additionally important since boundary layers which exist near turbulent blades are significantly different from equilibrium boundary studied in many laboratories. A number of recent studies indicate the inadequacy of results obtained from equilibrium boundary layers. Gillis and Johnston's [Ref. 2] measurements in boundary layers downstream of a convex curved surface and Ligrani's [Ref. 3] results in boundary layers downstream of artificial thickening devices showed that many structural changes persist long distances downstream of perturbations. This indicates that boundary layer behavior may depend on upstream history to a greater extent than previously believed. This is important regarding unsteadiness since it alters boundary layers locally as well as the history of boundary layers upstream.

Few experiments have been performed to study the stability or transition of oscillating flow in a plane channel. Most known information is from a handful of analytic studies and the full Navier-Stokes simulation undertaken at Stanford.

Regarding the latter, the work by Singer, Reed and Ferziger [Ref. 1] provides fascinating information as to the effects of unsteadiness on transition. For plane channel flow linear theory has been verified at a Reynolds number of 5000. With mean flow frequency in the range of the non-dimensional frequency of the least stable TS wave (Tollmien-Schlichting), they find that the mechanisms driving the transition are similar to those described by Herbert's secondary instability theory [Ref. 4 and 5] and observed experimentally by Nishioka et. al [Ref. 6 and 7], and Kozlov and Ramazanov

[Ref. 8]. In the plane channel flow these mechanisms have been studied extensively in previous computational investigations. The addition of mean flow modulation causes significant variations in the amplitude of the TS wave during the period, hence the dominant flow structures depend on the Strouhal number and the magnitude of the modulation.

In a straight channel without imposed unsteadiness the process of transition begins with TS waves experiencing mild growth at sufficiently high Reynolds numbers. When these waves grow to an amplitude of about 0.3 percent of the free stream velocity, three-dimensional waves become unstable. Transition often occurs at Reynolds numbers below that at which TS waves become unstable. These waves cause Lambda shaped vortices to lift from the near wall region and "burst" ejecting low speed fluid from close to the wall into the faster moving fluid away from the wall. These events then lead to a rapid breakdown of the laminar boundary layer into a turbulent one. The process can be modified by a number of different factors. Freestream turbulence can lead to non-sinusoidal oscillations in the nominally laminar boundary layer. Local disturbances, such as roughness elements, may lead to structures known as turbulent spots. These patches of turbulent-like flow form a characteristic arrowhead shape and spread in the downstream direction. Distributed roughness, acoustic disturbances, surface waviness and other factors all serve to complicate the basic process. There also exist equilibrium states where two dimensional waves (which are similar in form to TS waves) with a given amplitude will neither grow nor decay. The initial disturbances in the inlet of the channel can evolve into these or similar

structures, after which the strong secondary instability of three-dimensional waves can take place.

## **B. OBJECTIVES**

This research is a follow-on to the work undertaken by Longest [Ref. 9], and is believed to be the first experimental (quantitative) study, known to the author, on the effects of imposed mean flow unsteadiness on transition in straight channel flow. The objective is to investigate the effects of imposed, periodic, and deterministic unsteadiness on the transition process from laminar to turbulent flow. Answers to the following questions are sought:

- 1.) What parameters govern the unsteady flow?
- 2.) What events occur in the flow during the onset and development of transition?
- 3.) What is the interaction between the organized induced unsteadiness and transition (e.g., development of two-dimensional Tollmien-Schlichting waves into three-dimensional instabilities)?
- 4.) At what range of frequencies can one expect interactions between the organized imposed unsteadiness and transition phenomena?

Flow measurements (using hot-wire anemometry) and flow visualization are used to analyze the effect of oscillating the bulk flow in otherwise steady plane Poiseuille flow. An attempt is made to determine whether the type of unsteadiness studied (sinusoidal at one and two hertz) contributes to the early onset of transition, delay of transition, or has no effect. Sinusoidal oscillation was chosen to induce a deterministic periodic variation of velocity. The results are compared with the results of Singer's [Ref. 1] numerical simulation, which

which suggests that such oscillations provide a stabilizing effect at all but very low frequencies.

### **C. ORGANIZATION**

Section II follows this introduction and describes the experimental facilities. In section III experimental procedures are discussed, including calibrations, channel validation, flow measurements and flow visualization. The phase averaging technique is also detailed here. A discussion of the results follows in section IV. Conclusions are presented in section V.

## **II. EXPERIMENTAL FACILITIES**

### **A. CHANNEL**

The 40 to 1 aspect ratio straight channel, shown schematically in Figure 1, is located in the laboratories of the Department of Mechanical Engineering. The details of the design and construction are discussed by Ligrani and Subramanian [Ref 10]. Briefly, the channel is made of 6.35 mm thick plexiglass with a straight test section 4.27 m in length, with inside dimensions of 1.27 cm in height and 50.8 cm in width. The top and bottom walls of the channel are supported by ribs and cross beams along its length. The side walls are removable in order to gain access to the inside of the channel. The inlet section consists of a honeycomb assembly, 3 frames with screens and a 20:1 contraction ratio nozzle. Two layers of cheesecloth are placed at the inlet lip for filtering the air entering the channel. At the exit of the 4.27 m long test section are three 10.16 cm long frames with screens for housing the unsteady device ( the device used to create unsteadiness in the flow) and a second honeycomb. A two dimensional diffuser 45.72 cm long with a 3 degree total angle is located just upstream of the plenum chamber. The exit plenum chamber has inside dimensions of 60.96 cm by 60.96 cm. A 3.81 cm orifice plate assembly between the plenum chamber and the blower is provided to meter the flow through the channel. The exit of the plenum chamber is connected to the suction side of a 5 H.P. blower with a long 50.8 cm diameter pipe. A valve is provided between the plenum and the blower to regulate the flow. Bulk flow velocities up to 15 m/s are achieved in the

channel. In our experiments, bulk flow velocities in the range 1.0–4.5 m/s are used.

The channel is designed with a sufficient length such that transition occurs after the laminar velocity profile (parabolic) is fully developed (self similar). The initial flow development length is estimated [Ref. 11:p. 186] to be within about 25 per cent of the test section length for the range of speeds used in the present tests.

## **B. UNSTEADY DEVICE**

The most important aspect in the design of any unsteady device for a transition study is to ensure that the device produces a deterministic and periodic unsteadiness without adding other disturbances. To achieve this in an open circuit induction tunnel, the unsteady device is best located at the exit of the channel. This way, problems caused from the wakes and the flow disturbances resulting when the unsteady device is upstream of the test section are avoided.

The design is based on the design used by Miller and Fejer [Ref. 12] and is shown in Figure 2. Since the depth of the channel is only 12.7 mm, a single rotating vane driven through a spur gear train by a DC stepper motor is adequate to introduce the required unsteadiness in the flow. The rotating vane causes varying resistances to the flow in the test section. The frequency of the imposed unsteadiness is controlled by changing the vane rpm and the amplitude is controlled by using different vane widths. It is also important to match the flow speed with the vane speed. A vane 8.7 mm wide was used in this study.

The vane in Figure 2 is made of a 3.2 mm thick brass strip with rounded edges, and spans the entire width of the channel. The vane is supported at the ends by a 3.2 mm diameter shaft and bushings that are fitted to the side walls of the frame. Three additional intermediate spanwise struts are provided to increase the rigidity of the vane. One end of the shaft is extended to accommodate a 48 TPI (Threads Per Inch) spur gear. The driver spur gear has 12 TPI and is mounted on the Superior Electric, M092-FD310 Stepper Motor. To achieve a fine step control, a Modulynx MITAS PMS085-D050 Drive with Modulynx MITAS PMS085-C2AR Drive Controller is used. This combination facilitates motor shaft speeds up to 100 revolutions per second, with a constant 200 steps per motor shaft revolution. Note that, with a 1:4 gearing ratio and two cycles of imposed flow oscillations per vane rotation, one motor revolution corresponds to one half cycle of the imposed flow oscillation by the vane. The Drive Controller can be programmed for the required motor speed (rps). The Modulynx PMS085-D050 Drive was also used to provide a trigger signal to initiate data acquisition. This trigger also enabled the correlation of data taken with the position of the vane at the time that the data was recorded.

### **C. FLOW MEASUREMENTS**

The equipment used for flow measurement includes a digital manometer, hot-wire probe, hot-wire bridge, signal conditioner, digital multimeter, high speed data acquisition system, oscilloscope and a microcomputer. These are described in detail below.



## **1. Bulk Velocity**

The bulk flow velocity through the channel is determined from the pressure drop across the 3.81 cm orifice plate which is installed in the piping between the blower and the exit plenum chamber. This pressure drop is measured and displayed by a Validyne Model PS 309 digital manometer (inches of water).

## **2. Instantaneous Velocity**

A constant temperature hot-wire anemometer is used to measure instantaneous velocities of the flow. Briefly, the principles of hot-wire anemometry (constant temperature mode) are as follows.

The flow sensing element (hot-wire probe) consists of a short length of wire, connected to two supports, which forms the leg of a wheatstone bridge. This bridge maintains the wire at elevated temperature and is initially balanced prior to exposing the probe to the flow. This balancing resistance, referred to as "cold" resistance is multiplied by an "overheat ratio". Once the bridge is set to this value, and as the probe is exposed to the flow, the bridge is placed in operation and a small current (60 mA) passes through the circuit. Wire temperature increases because of resistive heating and the wire resistance increases until the bridge is rebalanced. The governing relationship is:

$$R = R_o(1 + \alpha(T - T_o))$$

where R is the resistance at temperature T,  $R_o$  is the resistance at the reference temperature  $T_o$ , and  $\alpha$  is the temperature coefficient of resistance.

Flow past the probe causes the wire to cool (by convection) and the bridge becomes unbalanced as the resistance decreases. The bridge is rebalanced by a feedback loop and amplifier. Response is rapid enough to maintain wire temperature and resistance nearly constant. As such, the variations in the bridge voltage are directly proportional to the current variations, and flow velocity can be calculated as a function of the bridge voltage.

Now the different components used to measure instantaneous velocity are described.

#### ***a. Hot-wire Probe and Probe Positioning***

A Dantec Electronics Inc. P51 probe, mounted such that the wire is horizontal and normal to the streamwise flow direction, is used. The wire sensor is 5.0 microns in diameter and approximately 1.25 mm long. The probe is mounted through the side wall of the channel and is held fixed by a rotatable lever arm which allows placing of the probe at various  $y/d$  positions ranging from 0.2 to 0.9. A scale graduated in terms of  $y/d$  is mounted adjacent to the lever arm for probe positioning to an accuracy of approximately 0.5 mm. Longitudinal and transverse position of the probe for this study were 46.12 cm and 15.64 cm, measured from the near flange at the end of the test section, and from the inside of the left channel wall (looking downstream), respectively. By rearranging the sidewalls the probe can be positioned at other streamwise locations for future studies.

#### ***b. Hot-wire Bridge***

The hot-wire is operated with a DISA 55 M10 constant temperature bridge. A five meter coaxial cable is used to connect the hot-wire to the

bridge. For the purposes of this study the cold resistance was multiplied by an overheat ratio of 1.8. The DC voltage from the bridge is measured with a Hewlett-Packard 3466A digital multimeter.

#### ***c. Signal Conditioner***

The hot-wire signal is filtered and amplified by a DISA 56W20 signal conditioner. The high-pass filter is set to 0.1 Hz in all cases to remove the DC signal. This however, did not alter the effects of 1 and 2 Hz imposed flow unsteadiness. The low-pass filter is set at 10 KHz to filter out noise existing above this frequency. The hot-wire signal is amplified using a gain of 10 to achieve an acceptable signal to noise ratio. Output from the signal conditioner is sent to the high speed data acquisition system and to a B & K Precision 10 MHz Oscilloscope used to signal monitor the signal.

#### ***d. High Speed Data Acquisition System***

A Hewlett-Packard 6944A Multiprogrammer is used in conjunction with a Hewlett-Packard series 9000, Model 310 microcomputer to acquire data. A buffered 69759A A/D card configuration is used with the Multiprogrammer to allow continuous data acquisition. The A/D card is externally triggered using 2-3 volt TTL type signals from the unsteady device motor drive. When the unsteady device is not in operation, triggering is provided by a Hewlett-Packard 3311A Function Generator set to the same frequency as that used with the unsteady device in operation. Sampling occurs as square wave voltage changes from high to low.

The storage capacity of the A/D buffer is 64,000 bytes. The number of imposed unsteadiness cycles which can be sampled depends on the desired number of data points per cycle. For example, if 100 points per cycle are

desired, then 640 cycles can be sampled. In this study, sampling was done at 100 points per cycle for all cases, where cycle refers to the cycle of flow blockage caused by the vane rotation of the unsteady device. 100 points per cycle were chosen so that there would be sufficient resolution to determine the effect of unsteadiness over the complete phase of each unsteadiness cycle.

### *c. Data Storage*

The Hewlett-Packard microcomputer is used to acquire the data from the A/D buffer, using a data acquisition program HOTWIREPAV, described in the software directory (APPENDIX A). Raw instantaneous voltage data is acquired and stored on standard 3.5 inch micro diskettes for further processing. Manual inputs to the program include bulk flow velocity, flow blockage frequency, and date and time.

### *f. Data Processing*

Processing of the data is done using a Hewlett-Packard microcomputer using the programs MAX\_MIN and AVG\_PLOT. This software is described in detail in the software directory (APPENDIX A). Many of the curves used to graphically display the results were generated using a Macintosh SE personal computer and the graphics program CRICKETGRAPH. The phase averaging technique employed by the program MAX\_MIN is described below.

In the case of an unsteady flow the instantaneous velocity can be split into three components.

$$U = \bar{U} + \tilde{U} + u'$$

where  $\bar{U}$  is the time averaged velocity,  $\tilde{U}$  is the imposed phase averaged velocity and  $u'$  is the instantaneous fluctuating component.  $\tilde{U}$  is the

component due to the unsteadiness, and is zero for steady bulk flow. In the present study  $\tilde{U}$  and  $\bar{U}$  are combined to represent the phase averaged velocity ( $\hat{U}$ ). Thus,

$$U = \hat{U} + U'$$

$\hat{U}$  is determined by phase averaging  $U$  over, say 640 cycles (ncycl), at different positions of the phase of each oscillation.

$$\hat{U}(n) \Big|_{n=1}^{100} = \frac{1}{ncycl} \sum_{m=1}^{ncycl} U(m, n) \Big|_{n=1}^{100}$$

When  $U'$  is a large percentage of  $\hat{U}$  then a larger number of cycles, sometimes up to 4640 cycles, are used to determine  $\hat{U}$ . For this, multi-run data acquisition is made, with the vane at the same starting position for each run. Only the last 580 data points (due to sampling procedure) of each run are used in the cumulative phase averaging. Once  $\hat{U}$  is determined,  $U'$  is calculated from  $U' = U - \hat{U}$ , and  $(U')^2 = (U - \hat{U})^2$ . Therefore, the phase averaged root mean squared velocity is,

$$\hat{U}'(n) \Big|_{n=1}^{100} = \sqrt{\frac{1}{ncycl} \sum_{m=1}^{ncycl} (U(m, n) - \hat{U}(n))^2} \Big|_{n=1}^{100}$$

Time averaged velocity,  $\bar{U}$ , and rms velocity  $\sqrt{(U')^2}$  are calculated by averaging over all the points (100 x ncycl) per run and in the case of multi-runs, 100 x ncycl x no. of multi-runs.

$$\bar{U} = \frac{1}{n_{cvc}} \sum_{m=1}^{n_{cvc}} \frac{1}{100} \sum_{n=1}^{100} U(m, n)$$

$$\sqrt{U'^2} = \sqrt{\frac{1}{n_{cvc}} \sum_{m=1}^{n_{cvc}} \frac{1}{100} \sum_{n=1}^{100} (U(m, n) - \bar{U})^2}$$

## D. FLOW VISUALIZATION

The equipment utilized for flow visualization studies includes a smoke wire for generating smoke in the channel and video equipment to photograph the flow in the channel. These are described in detail below.

### 1. Smoke Wire System

The smoke wire system is a modified Vertical Smoke Wire Instrument made by Flow Visualization Systems of Bolingbrook, IL. The system in its present configuration consists of a 0.127 mm diameter nichrome wire that is stretched across the width of the channel through access ports in the channel side walls. The wire is passed through these access ports through a thin stainless steel tube (hypodermic needle) which allows the wire to move freely. The smoke wire is connected to an A/C-D/C converter and this in turn has voltage supplied by a Calrad 45-740 (0-130 VAC) variac set at 45 VAC. The wire is energized by pulsing the "Momentary On" switch of the A/C-D/C converter. Since the wire acts as a resistor and heats up when a current is passed it becomes more elastic and has a tendency to sag in the channel. To prevent this from affecting the flow visualization, a tensioning device has been installed on one end of the wire to ensure that the wire is held taut in the channel when it is energized. This tension device consists of two pulleys

which support the wire and a third pulley with a weight attached between the two support pulleys. The wire is coated with a paraffin based oil which is applied by means of a thin rod with an absorbent piece of felt at the tip. When applied in this manner, the wire is coated evenly with small droplets of oil. Energizing the wire produces a thin even sheet of smoke until all the oil on the wire burns. The smoke from the wire lasts for about 4-8 seconds depending on the flow rate in the channel.

The wire is placed horizontally normal to the flow 76.8 cm upstream from the end of the test section. For the purposes of this study, the wire was located at a  $y/d$  value of 0.84 ( $d$  being the width of the channel and  $y$  the height from the bottom of the channel).

## **2 Video Equipment**

The video equipment used for flow visualization is the same as that described by Longest [Ref. 9]. Briefly, a high speed video camera is mounted on a tripod above the channel and focused on the area of interest. The focal plane from the camera lens to the channel is surrounded by an enclosure to exclude all extraneous light and thus decreasing the reflections which interfere with the flow visualization. The bottom of the channel was blacked out and lighting was provided by two 600 Watt floodlights placed 1 m from the sidewall on either side of the channel at the same height as the channel.

Still photographs were made by taking pictures of the aforementioned video when viewed on a monitor. A Nikon F-3 SLR and Kodak Tri-Xpan film were used to take the pictures. The shutter speed was one-eighth of a second and the focal aperture was set at  $f\ 5.6$ .

### **III. EXPERIMENTAL PROCEDURES**

#### **A. ORIFICE $\Delta P$ CALIBRATION**

The orifice differential pressure calibration for bulk velocity flow measurements was performed by Longest [Ref. 9]. Results of the calibration are shown in Figure 4.

#### **B. HOT-WIRE CALIBRATION**

The hot-wire was calibrated in the freestream of the wind tunnel, also located in the laboratories of the Mechanical Engineering Department of the Naval Postgraduate School.

The hot-wire probe is mounted normal to the flow in the center of the channel so that it is in the freestream. The hot-wire is connected to the same hot-wire bridge previously discussed. Output from the hot-wire bridge is read on a digital multimeter. Freestream velocity in the wind tunnel is measured utilizing a Kiel pressure probe, a wall static pressure tap, and a Validyne digital manometer. Voltage and differential pressure readings are taken for a range of pressure drops corresponding to velocities of 1.0 to 4.0 m/s. The computer program HWCAL is run on the Naval Postgraduate School's IBM main frame computer to calculate all calibration constants. Following the calibration, the hot-wire is installed in the straight channel.



## **C. CHANNEL VALIDATION**

### **1. Channel Flow Tests**

Assembly and installation of the straight channel in the Mechanical Engineering Laboratory of the Naval Postgraduate School, along with the initial flow visualization and measurement results are detailed by Longest [Ref. 9]. Prior to commencing flow measurements for this study a check of the channel flow quality is performed as follows. Smoke is generated using the smoke generator described by Longest [Ref. 9] and then drawn into the channel at a speed of approximately 2.0 m/s. The first few times this was performed, numerous leaks from the sidewalls of the channel were observed. These leaks are eliminated using removable spring clamps on both sides of the channel, along its entire length. The clamps are left in position while the channel is in operation.

### **2. Laminar Average Velocity Profile Verification**

Velocity profile verification is performed at a Reynolds number of 1103 (bulk velocity of 1.32 m/s) when the flow is laminar. Instantaneous velocity measurements were taken at eight  $y/d$  positions ranging from 0.2 to 0.9, at an  $x/d$  of 300.0. This data was taken using the HOTWIREPAV program, with no imposed unsteadiness. MAX\_MIN was used to process the data, and the time averaged local velocities were normalized with respect to the maximum value which occurred at the mid-channel location ( $y/d = 0.5$ ). A second order polynomial curve was fit to the data and is shown in Figure 5. The curve demonstrates that the flow is fully developed at this location and follows the expected parabolic behavior.

## **D. FLOW MEASUREMENT**

### **1. Reynolds Number Survey**

Velocity surveys are conducted for Reynolds numbers ranging from 1100 to 2700 with the hot-wire probe at a  $y/d$  position of 0.85, and a  $z/d$  of -7.7. This survey is done to determine how the imposed unsteadiness affects the transition process as Reynolds number varies. Data at each Reynolds number are taken by recording results with no imposed unsteadiness followed by results with imposed unsteadiness. Data sets of 64,000 points are taken using only the last 58,000 for data processing, as previously described. Average velocity and rms velocity values from such survey are used to generate Figures 6 and 7. These experiments were repeated at several Reynolds numbers to ensure consistent and repeatable data trends.

### **2. Multi-run Averaging**

Multi-run phase averaging using up to 4640 cycles of flow unsteadiness were conducted at several Reynolds numbers. The purpose of this multi-run averaging is to show that the survey data is statistically stable for higher Reynolds numbers where fluctuation levels are significant with respect to the local mean velocity. Results are presented in Figures 8-35.

### **3. Velocity Profiles**

Velocity profiles with and without imposed unsteadiness are taken at the same Reynolds numbers as used for the multi-run averaging. The purpose of these profiles is to record flow development as the Reynolds number is changed and to study the effect of imposed unsteadiness on average and rms velocities as a function of the Reynolds number and  $y/d$ . Data acquisition and

processing is performed as described in the Reynolds number survey. Results are provided in Figures 36-147.

#### **E. FLOW VISUALIZATION**

Smoke patterns were recorded on film using the video camera at Reynolds numbers ranging from 1140 to 2240 with 1 Hz imposed unsteadiness. Video sequences are taken at different Reynolds numbers spaced apart by approximately 50 units. The purpose of this flow visualization is to record transition events and denote any variations caused by the imposed unsteadiness. Still photographs are shown in Figures 148-158.

#### IV. RESULTS AND DISCUSSION

The coordinate system used in this study is a right handed coordinate system. The origin is at the spanwise centerline, at the bottom of the channel and at the beginning of the test section. The x-axis extends positively in the streamwise direction to the end of the test section. The y-axis extends vertically in the positive direction from the bottom of the channel to the top. The z-axis extends in the spanwise direction. Positive values of z are on the right hand side of the channel when looking downstream. Flow measurements were taken at  $x/d = 300$ ,  $z/d = -7.7$  and  $y/d$  values of 0.2 to 0.9, where d is the full channel height. Flow visualization was done with the smoke wire positioned at a  $y/d$  value of 0.85.

The Reynolds number,  $Re$ , is based on the bulk flow velocity,  $v_{bulk}$  and the channel height and is defined by the equation:

$$Re = v_{bulk} \cdot d/\nu$$

where  $\nu$  is the kinematic viscosity. The Strouhal number,  $Str$ , is defined by the equation:

$$Str = 2\pi \cdot f_{osc} \cdot d/v_{bulk}$$

where  $f_{osc}$  is the frequency of the imposed unsteadiness. This study was conducted at Reynolds numbers from 1103 to 2715. With 1 Hz imposed unsteadiness, Strouhal numbers range from 0.0605 to 0.0246.

### **A. CHANNEL FLOW QUALIFICATION**

For fully developed channel flow the theoretical velocity relationship is given by Schlichting [Ref 11:p. 280-281] as:

$$u/u_{max} = 4.0[y/d - (y/d)^2]$$

where  $u$  is the local velocity and  $u_{max}$  is the centerline ( $y/d = 0.5$ ) velocity.

Figure 5 shows the velocity profile taken at  $x/d = 300$  at a  $Re$  of 1103. The velocity profile (normalized with respect to  $u_{max}$ ) is parabolic in shape and is in good agreement with the theoretical relationship. With the bulk flow velocity of 1.32 m/s (measured from the orifice pressure drop) the maximum centerline velocity of 1.774 m/s is observed, giving a ratio of  $v_{bulk}/u_{max}$  of 0.774.

### **B. EFFECT OF REYNOLDS NUMBER ON LOCAL MEAN VELOCITY AT $y/d = 0.85$ DUE TO 1 HZ IMPOSED UNSTEADINESS**

Figure 6 shows the variation of the mean velocity with Reynolds number with and without imposed unsteadiness. Flow measurements are for  $y/d = 0.85$ . Bulk velocity is also shown in the plot. The mean velocity trace shows some non-linear behavior for Reynolds numbers from 1900 to 2200 and near a Reynolds number of 2700. This behavior is believed to be caused by the transitional behavior of the flow. The 1 Hz imposed unsteadiness has no effect on the mean velocity.

### C. EFFECT OF REYNOLDS NUMBER ON RMS VELOCITY AT $y/d = 0.85$

Figure 7 shows normalized longitudinal velocity fluctuations with and without imposed unsteadiness for Reynolds numbers from 1100 to 2700. The time averaged rms velocity,  $\sqrt{u'^2}$ , is normalized with respect to the time averaged velocity,  $\bar{U}$ , and is plotted versus the Reynolds number. For Reynolds numbers of 1100 to 1900, the imposed unsteadiness appears to have no effect on the rms velocity. For Reynolds numbers from 1900 to 2025, the 1 Hz imposed unsteadiness causes a significant increase in the rms velocity. This increase amounts to a maximum at a  $Re = 1980$  and is 7.06 %. At Reynolds numbers of 2025 to 2300 the effect of the imposed unsteadiness is reversed. In this range the imposed unsteadiness reduces the normalized rms velocity. The maximum amount of decrease occurs at  $Re = 2172$  and corresponds to a drop of 7.3 %. At higher Reynolds numbers, the imposed unsteadiness appears to have no effect on the rms velocity. The figure also seems to demonstrate that transition begins near  $Re = 1200$ , and that the flow becomes fully turbulent at  $Re = 2400$ .

### D. EFFECT OF REYNOLDS NUMBER ON PHASE AVERAGED VELOCITY

Figure 8 through Figure 35 show the phase averaged velocity traces at five Reynolds numbers (1153, 1826, 2005, 2085, and 2640). Figures 8-17 are the phase averaged plots with no imposed unsteadiness. Of these, figures ( 8, 10, 12, 14, and 16) plot phase averaged velocity  $\hat{U}$  (in this case  $\hat{U} = \bar{U}$  since  $\tilde{U} = 0$ ) versus phase angle. Figures 9, 11, 13, 15, and 17 plot the phase averaged rms velocity,  $\sqrt{u'^2}$ , normalized with respect to the temporal mean,  $\bar{U}$ , versus

phase angle. For these cases, phase averaging is done over 580 cycles of imposed unsteadiness with 100 data points per cycle.

Figures 18-35 present results of flow measurements with 1 Hz imposed unsteadiness. These figures show that the unsteady device produces deterministic and periodic unsteadiness, thereby validating its behavior. At  $Re = 1153$  the phase averaging is given for 580 cycles of imposed unsteadiness. For  $Re = 1826, 2005$  and  $2085$  eight runs of 580 cycles each (for a total of 4640 cycles) are averaged. For  $Re = 2640$  three runs of 580 cycles (total of 1740 cycles) are averaged. With 1 Hz imposed unsteadiness, statistically stable phase averaging is achieved using 580 cycles when the flow is laminar ( $Re = 1153$  for the plots presented). However, for the transitional Reynolds numbers,  $Re = 1826, 2005$  and  $2085$ , eight sets of 580 cycles are necessary to achieve statistically stable phase-averaged results. For the turbulent case,  $Re = 2640$ , statistically stable results are achieved after phase averaging three sets of 580 cycles of imposed unsteadiness. The effect of multi-run averaging is shown in Figures 20-35. Figure 20 shows  $\hat{u}$  after averaging using one set of 580 cycles. Figure 22 shows  $\hat{u}$  after averaging using eight sets of 580 cycles, and is clearly much smoother indicating its statistical stability. Figures 21 and 23 show the same effect on the rms velocity. Figures 24-27 show the same results of multi-run averaging for  $Re = 2005$ , Figures 28-31 for  $Re = 2085$  and Figures 32-35 for  $Re = 2640$ .

Normalized rms velocity values in these figures are fairly constant as the phase angle changes at all Reynolds numbers, with the exception of  $Re = 2085$ . These data are shown in Figure 31. Here, the rms velocity increases for the phase angles of 250-350. This increase occurs at the same phase

angles where  $\hat{u}$  is larger than surrounding values. The increase in rms velocity values may occur during decelerating portion of the  $\hat{u}$  cycle, followed by a phase shift relative to the  $\hat{u}$  trace. These rms velocity variations occur over the same Reynolds number range that imposed unsteadiness decreases the rms velocity relative to the flow without imposed unsteadiness.

#### **E. MEAN VELOCITY PROFILES AND PHASE AVERAGED VELOCITIES**

Figures 36-42 show mean velocity profiles at  $x/d = 300$  and  $z/d = -7.7$ .  $y/d$  positions vary from 0.2 to 0.9. Data is not given for  $y/d$  of 0.1 due to physical constraints imposed by the geometry of the hot-wire probe.

Figure 36 shows the profile development with Reynolds number with no imposed unsteadiness. Profiles are shown for  $Re = 1153, 1826, 2026, 2085$  and  $2640$ . With laminar flow, profiles are parabolic. Profiles are somewhat contorted at transitional Reynolds numbers ( $Re = 1826, 2026$  and  $2085$ ). At  $Re = 2640$ , the profile shows a flattened behavior expected for fully turbulent flow.

Figure 37 shows the profile development for the same Reynolds number with 1 Hz imposed unsteadiness. The imposed unsteadiness nominally has no effect on the mean velocity profiles. This is also shown in Figures 38-42 where mean velocity normalized with respect to the maximum observed mean velocity with and without unsteadiness are plotted for each Reynolds number, both with and without imposed unsteadiness.

Figure 43 shows the variation of the peak to peak magnitude of the phase averaged mean velocity as a function of  $y/d$ . On the plot, the peak to peak magnitude has been normalized with respect to  $\bar{u}$ . From the figure, the peak



to peak magnitude increases when the flow is near the wall. At the two transitional Reynolds numbers ( $Re = 2026$  and  $2085$ ), increases in magnitude near the wall are significantly higher than for other cases. These Reynolds numbers correspond to the situation in which the imposed unsteadiness decreases the rms velocity relative to flow with no imposed unsteadiness.

Figures 44-91 show phase averaged data corresponding to data just discussed. These data indicate that the unsteady device is successful in producing deterministic periodic unsteadiness at all positions where flow is measured, i.e. from  $y/d = 0.2$  to  $0.9$ .

#### **F. RMS VELOCITY PROFILES**

Figures 92-98 show the development of the rms velocity profiles as the Reynolds number. Again, the symmetry of the profiles is distorted due to the fact that no measurements are available at  $y/d = 0.1$ .

Figure 92 presents rms velocity profiles for the five Reynolds numbers with no imposed unsteadiness. Figure 93 shows the profile development with imposed unsteadiness at 1 Hz. Figures 94-98 are normalized rms velocity profile plots with and without imposed unsteadiness for each Reynolds number.

Figures 92 and 93 show that the imposed unsteadiness has no effect on the rms velocity profiles for the laminar and turbulent Reynolds numbers ( $Re = 1153, 1826$  and  $2640$ ). For the turbulent case, the rms velocities are much higher near the wall. For the two transitional Reynolds numbers, some different behavior is seen. With no imposed unsteadiness, the profiles show higher rms velocity magnitudes near the middle of the channel. With imposed

unsteadiness, the profiles at  $Re = 2026$  and  $Re = 2085$  differ sharply and resemble the turbulent profile.

Figures 99-146 present phase averaged data used to produce the plots described above. Rms values are constant as a function of phase angle both with and without imposed unsteadiness except for the case with imposed unsteadiness at  $Re = 2085$ . In Figures 116, 118, 120, 122, 124, 126, 128, and 130 rms velocities vary with phase angle. This was mentioned earlier for  $y/d = 0.85$ , however, here it is evident that this behavior occurs for  $0.2 < y/d < 0.9$ . Figure 147 shows the variation of rms peak to peak magnitude as a function of  $y/d$  for  $Re = 2085$ . At this Reynolds number, the peak to peak magnitude is largest near the wall with a secondary peak near the channel centerline.

## **G. FLOW VISUALIZATION**

Figures 148-158 show flow visualization results obtained with the smoke wire at  $y/d$  of 0.85. The camera was set up to take videos on the left side of the channel in the same area that the hot-wire was located ( $x/d = 300$ ). In the figures, flow is from the bottom of the picture to the top. The left side of the picture is near the left channel wall, and the right hand side is located near the center of the channel. The dark horizontal stripe emanating from the left sides of the pictures indicates the location of the hot-wire probe. There are also several dark shadows which extend diagonally upward from the left side of the channel. These are due to shadows cast by part of the support structure of the channel and should not be confused with effects of the flow on

the smoke patterns . The smoke generated by the wire appears as white lines or ribbons and the dark areas indicate absence of smoke.

Figure 148 shows flow at  $Re = 1136$  with 1 Hz imposed unsteadiness. In this picture, the flow is fully laminar as shown by the straight regular parallel smoke lines. Figure 149 is at  $Re = 1153$  also with imposed unsteadiness. Here flow is again laminar, but there are also TS (Tollmien-Schlichting) waves in addition to some small streamwise spirals due to secondary vortical flows. These are hereafter referred to as ribbons. Figure 150 at  $Re = 1278$  again shows laminar flow with TS waves. Figure 151 at  $Re = 1328$  also shows laminar flow with TS waves. Figures 152 and 153 are at  $Re = 1395$ , and show TS waves and ribbons which are larger than previously seen and which begin to spread out diagonally. Figures 154 and 155 are at  $Re = 1428$  again show the same ribbon structure, but here they have become larger and seem to develop into turbulent spots. These spots are defined by the large circular areas in the center of the ribbon break-up regions. Figures 156 and 157 are for  $Re = 1586$ . These pictures show the decay of ribbon structures as well as larger and more frequent turbulent spots. Figure 158 shows a time sequence of six pictures taken approximately one second apart for  $Re = 1428$ . In this sequence we see laminar flow with TS waves is present in addition to ribbons, ribbons developing into turbulent spots, followed by more ribbons and laminar flow with TS waves. The principal difference between the flows with and without imposed unsteadiness is the reappearance of such TS waves at higher Reynolds numbers with imposed unsteadiness. In this situation, the TS waves generally reappear just downstream of turbulent spots.

## V. CONCLUSIONS

The 1 Hz imposed bulk flow unsteadiness has no effect on the local mean velocity at all  $y/d$  values for the range of Reynolds numbers 1100 to 2700.

The imposed unsteadiness causes both destabilization and stabilization of the time averaged longitudinal velocity fluctuations. The flow is destabilized by the imposed unsteadiness for Reynolds numbers 1900 to 2025 and Strouhal numbers from 0.0351 to 0.0329. Stabilization of the flow by the unsteady device occurs for the Reynolds numbers 2025 to 2300 and for Strouhal numbers from 0.0329 to 0.0290.

Imposed unsteadiness affects the shape of the time averaged longitudinal velocity profile at the transitional Reynolds numbers,  $Re = 2026$  and  $Re = 2085$ .

The imposed unsteadiness also causes the time averaged longitudinal velocity fluctuations to vary as a function of phase angle at a Reynolds number of 2085 at  $y/d$  positions of 0.2 to 0.9. The maxima of the time averaged longitudinal velocity fluctuations and the maxima of the phase averaged velocity occur for the same phase angles.

Transitional flow structures which have been predicted by numerical simulations and observed in other experimental work are also observed in this study. As Reynolds number increases laminar flow, Tollmien-Schlichting waves, vortical ribbon-like structures and then turbulent spots are observed. These structures are observed to be present at many different Reynolds

numbers. Time sequence photography taken at particular Reynolds numbers during transition shows TS waves, vortical ribbons, turbulent spots, more vortical ribbons and TS waves. The growth and break-up of the ribbon-like vortical structures is followed by turbulent spots. As the Reynolds number is increased, the vortical structures grow in both the spanwise and streamwise direction. The frequency and size of the turbulent spots also increases as Reynolds number increases until the flow becomes fully turbulent. The principal difference between the flows with and without imposed unsteadiness is the reappearance of the TS waves at higher Reynolds numbers with imposed unsteadiness. In this situation, the TS waves generally reappear just downstream of turbulent spots.

## APPENDIX A

### SOFTWARE DIRECTORY

1. **HWCAL**: This program determines the constants for the King's Law calibration of the hot-wire. The program also provides a polynomial fit of the calibration data.
2. **HOTWIREPAV**: This program is used to read the data stored in the A/D buffer of the high speed data acquisition system and stores the information on micro diskettes. Manual inputs are: triggering frequency, hot-wire DC voltage (ungained), oscillation frequency (flow blockage), bulk velocity and date and time of run.
3. **MAX-MIN**: This program calculates instantaneous and phase averaged velocities. Initially a look up table is created. Here, effective velocities are calculated from the effective voltage values and stored for follow on calculations. The hot-wire calibration constants obtained from HWCAL, and the amplifier gain are incorporated into these calculations. The velocity calibration is given by the equation:

$$U_{eff} = k(E_{eff}^2 - E_0^2)^{1/N}$$

where  $k$  is the proportionality constant,  $E_{eff}$  is the effective voltage, and  $E_0$  is the reference voltage at no flow.  $N$  is a constant value of 0.45 for moderate Reynolds numbers. Once the look up table is created the program reads the instantaneous voltage values from the data file and converts them to

instantaneous velocities. At this point a plot of the instantaneous velocity versus time can be generated for any of 580 cycles (The first 60 cycles are discarded to allow for flow stabilization as the unsteady device is started.)

Next the program phase averages the 580 cycles, and velocity versus phase angle (of the flow blockage) plots are available. Two plots are available from the averaged values;  $\bar{u}$  versus phase angle and  $\sqrt{\bar{u}^2}$  divided by  $U$ , versus phase angle, where  $\bar{u}$  is the phase averaged velocity,  $\sqrt{\bar{u}^2}$  is the phase averaged root mean squared velocity, and  $U$  is the average velocity. In the case where there is no imposed unsteadiness, the phase averaged velocity,  $\bar{u}$ , is equal to the time averaged velocity,  $\bar{u}$ , since there is no superimposed phase average velocity component,  $\hat{u}$ .

The program can also be used to process a set of data when multi-run averaging is desired. In this case the averaged values are written to and stored in the computer hard disk memory. Once each of the desired data sets has been averaged and stored in the computer memory.

**4. AVGPLOT:** The program AVGPLOT is used to average any number of data sets. A maximum of eight sets of data (or 4,640 cycles) were averaged for this study. The program AVGPLOT provides the same graphs as those available from MAX\_MIN. Phase averaged data sets are copied to micro diskettes prior to purging them from the computers memory.

## **APPENDIX B**

### **FIGURES**



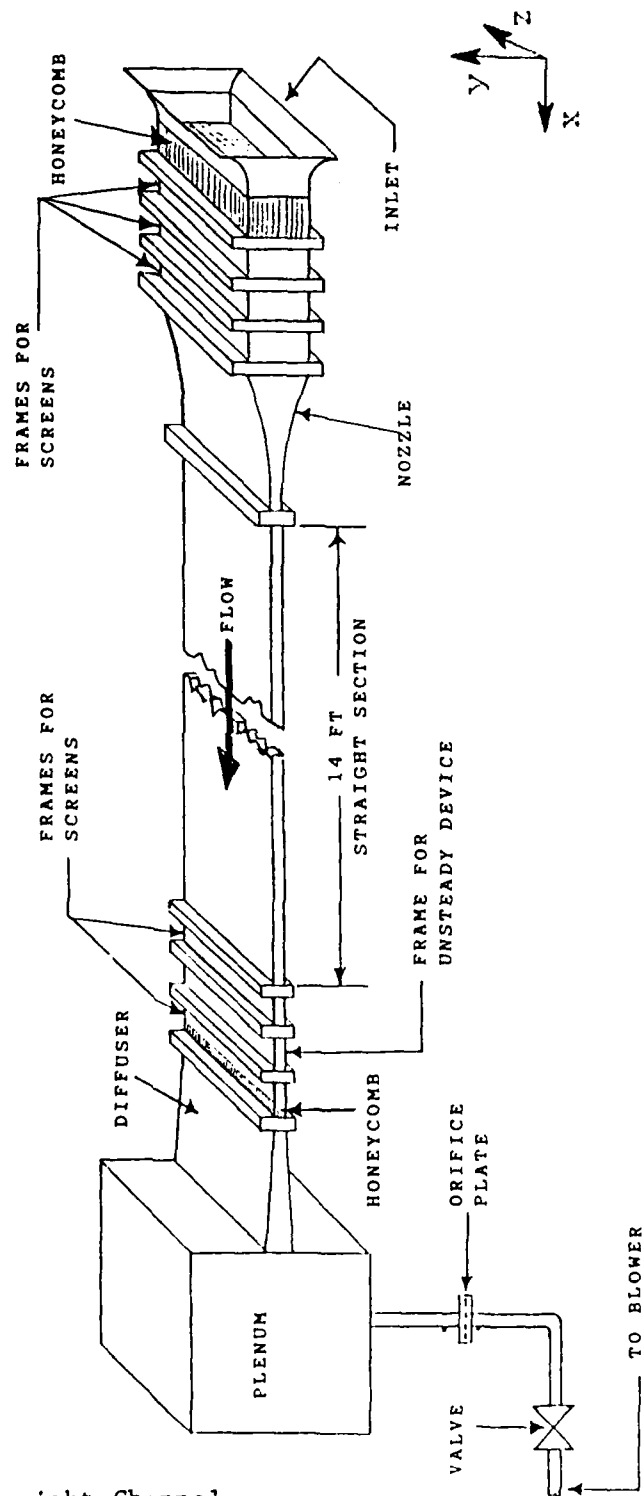


Figure 1. Straight Channel

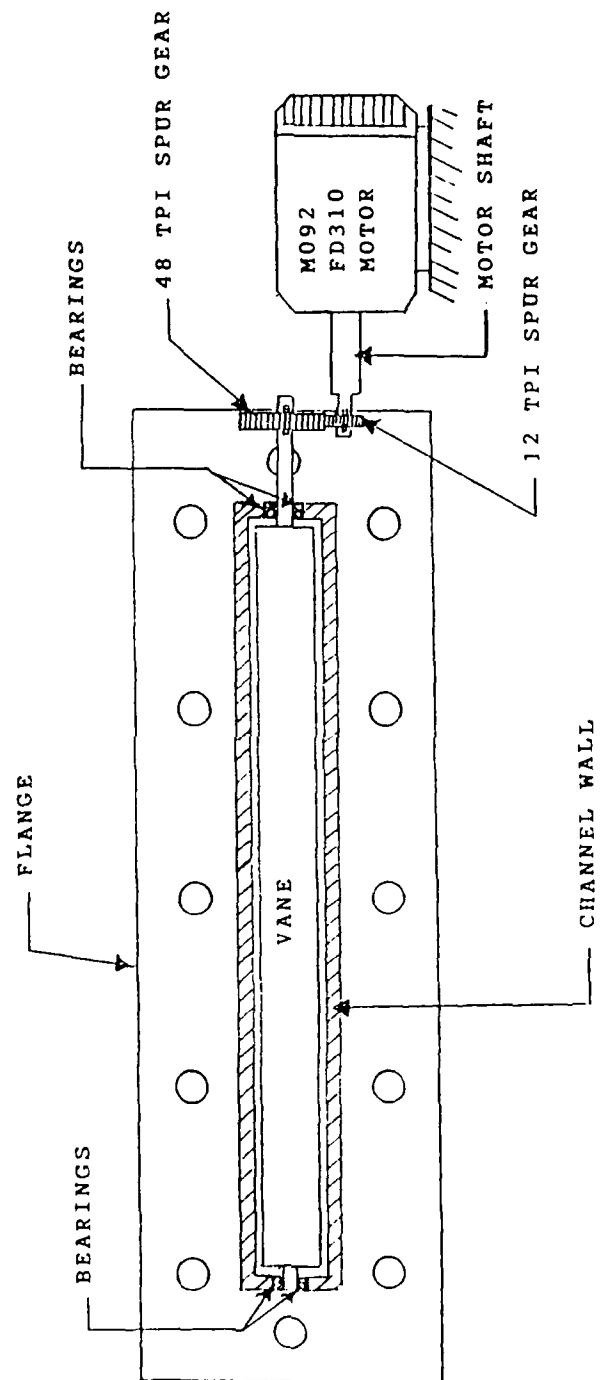


Figure 2. Unsteady Device

### SCHEMATIC OF FLOW MEASUREMENT EQUIPMENT

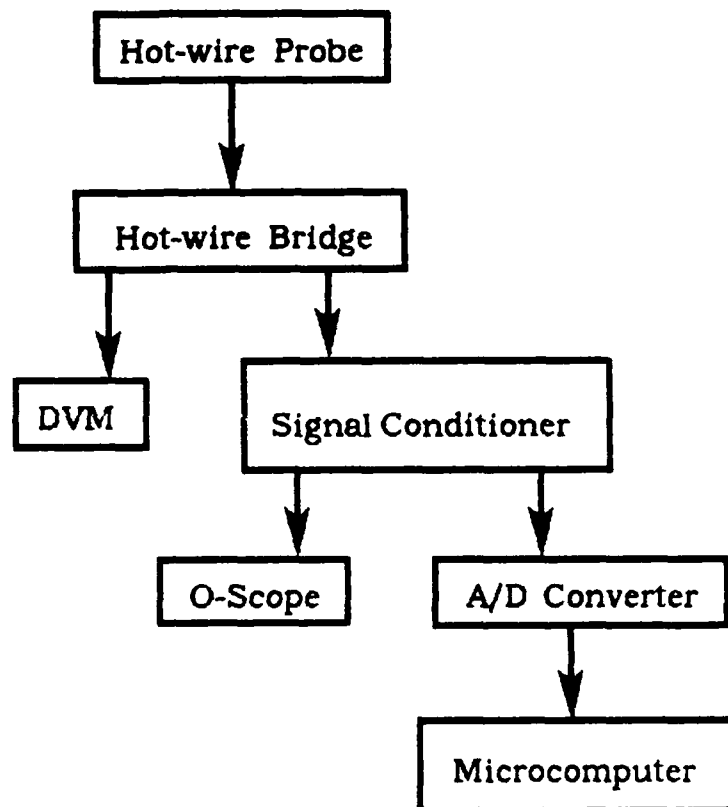


Figure 3.

# Orifice Differential Pressure Calibration

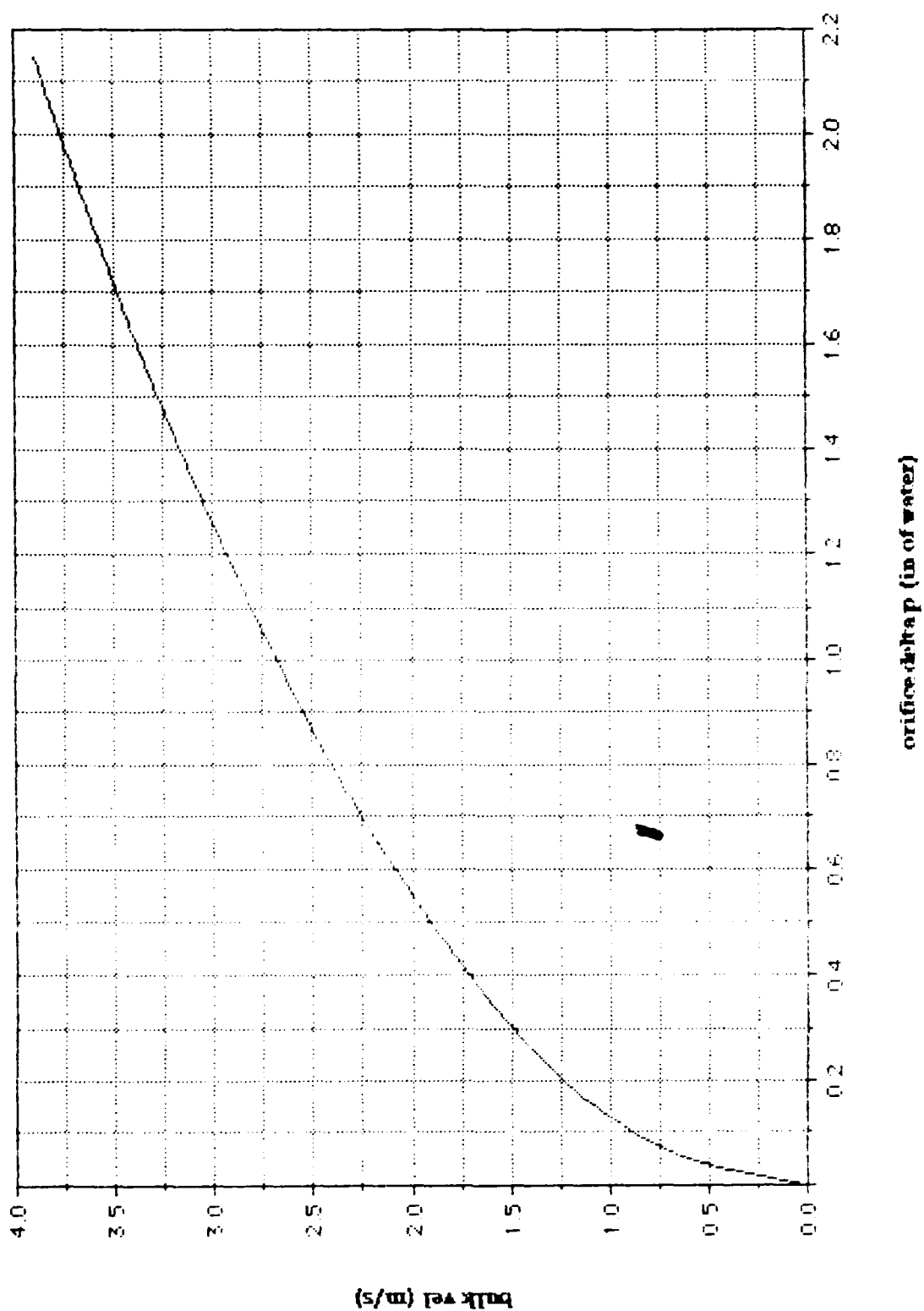


Figure 4.

**Fully Developed Flow Validation  
at Re No. = 1153**

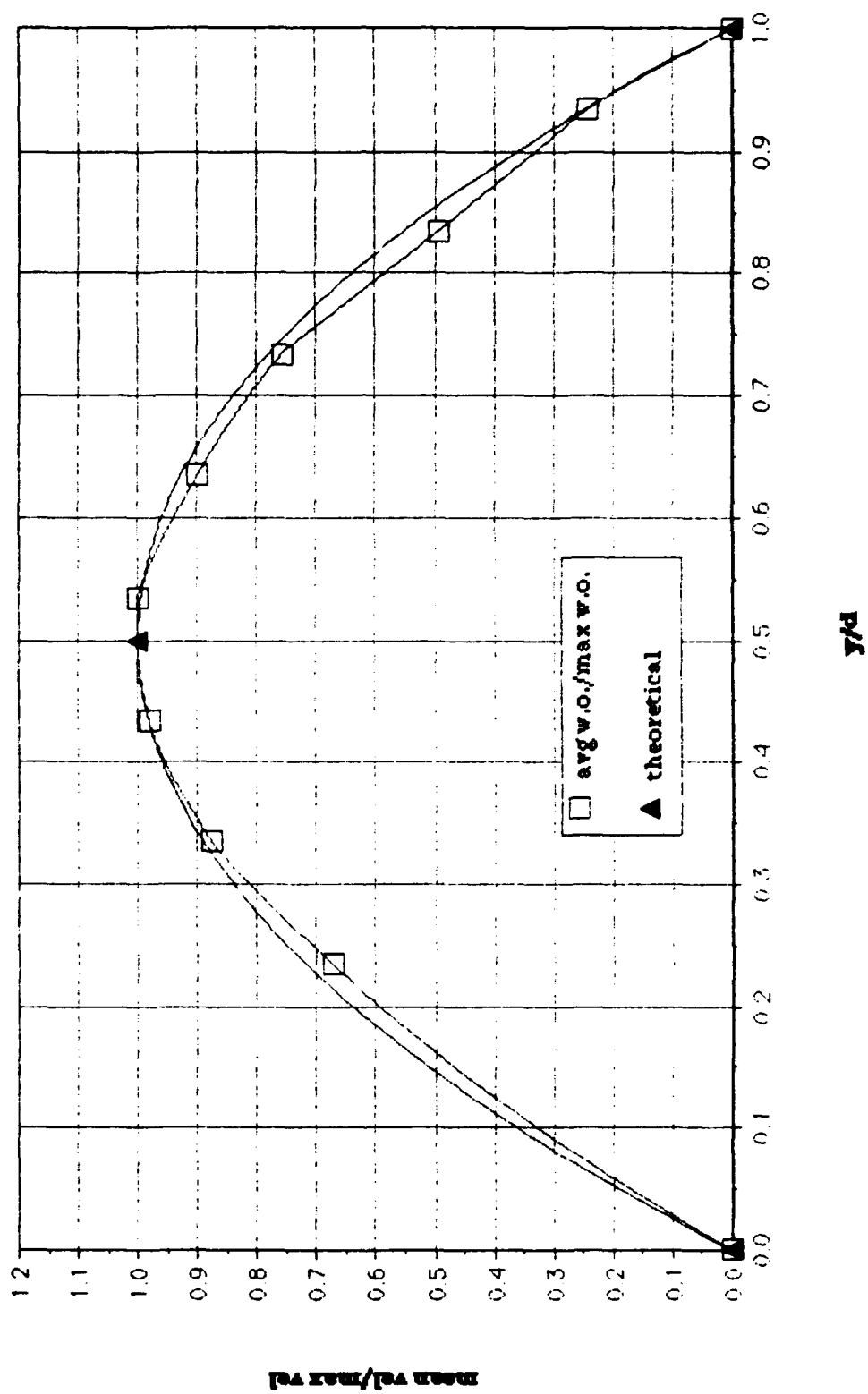


Figure 5.

Effect of Reynolds Number on Local Mean  
Velocity due to 1 Hz Imposed Unsteadiness

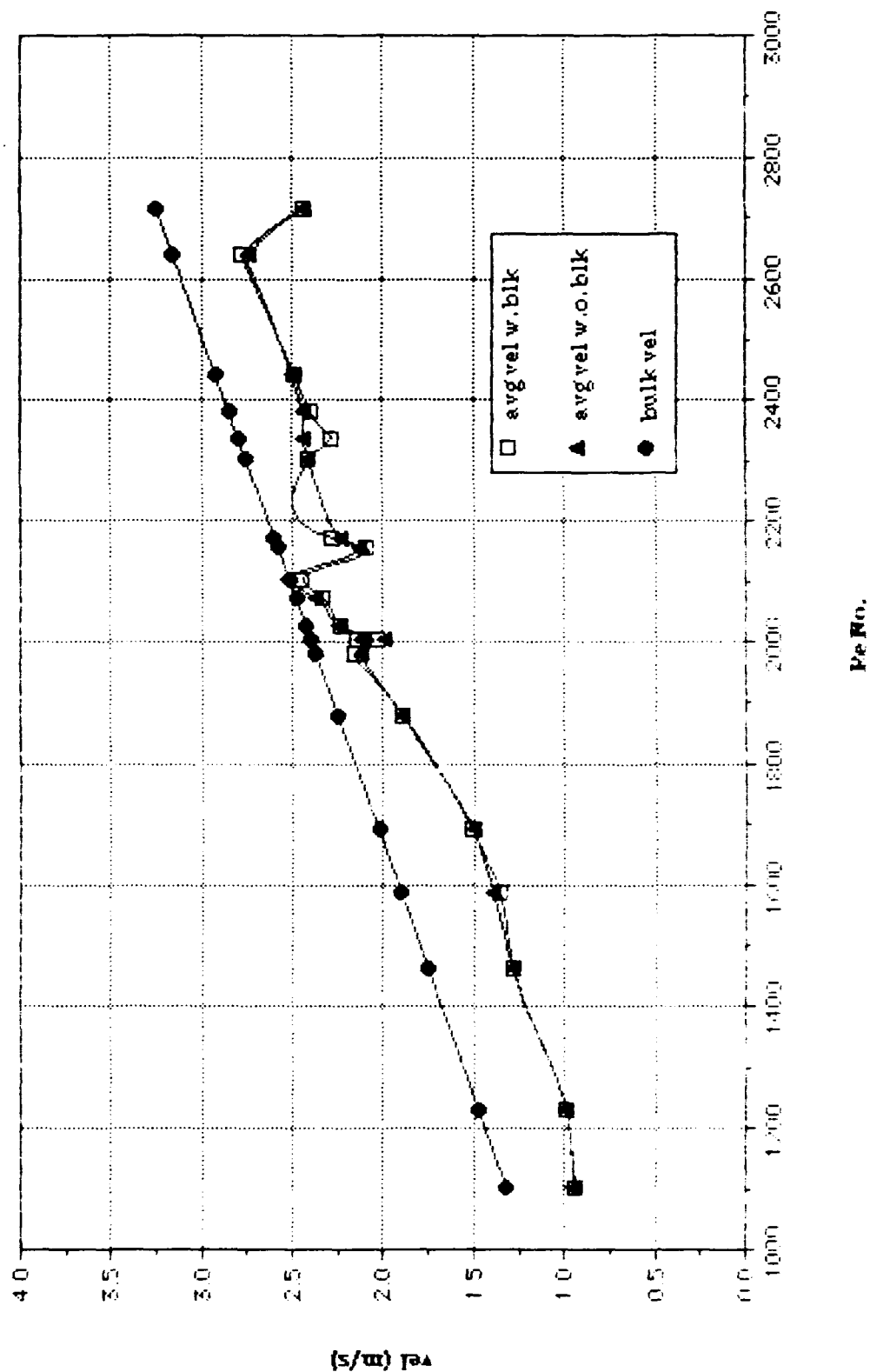


Figure 6.

# Reynolds Number Surveys With and Without 1 Hz Imposed Unsteadiness

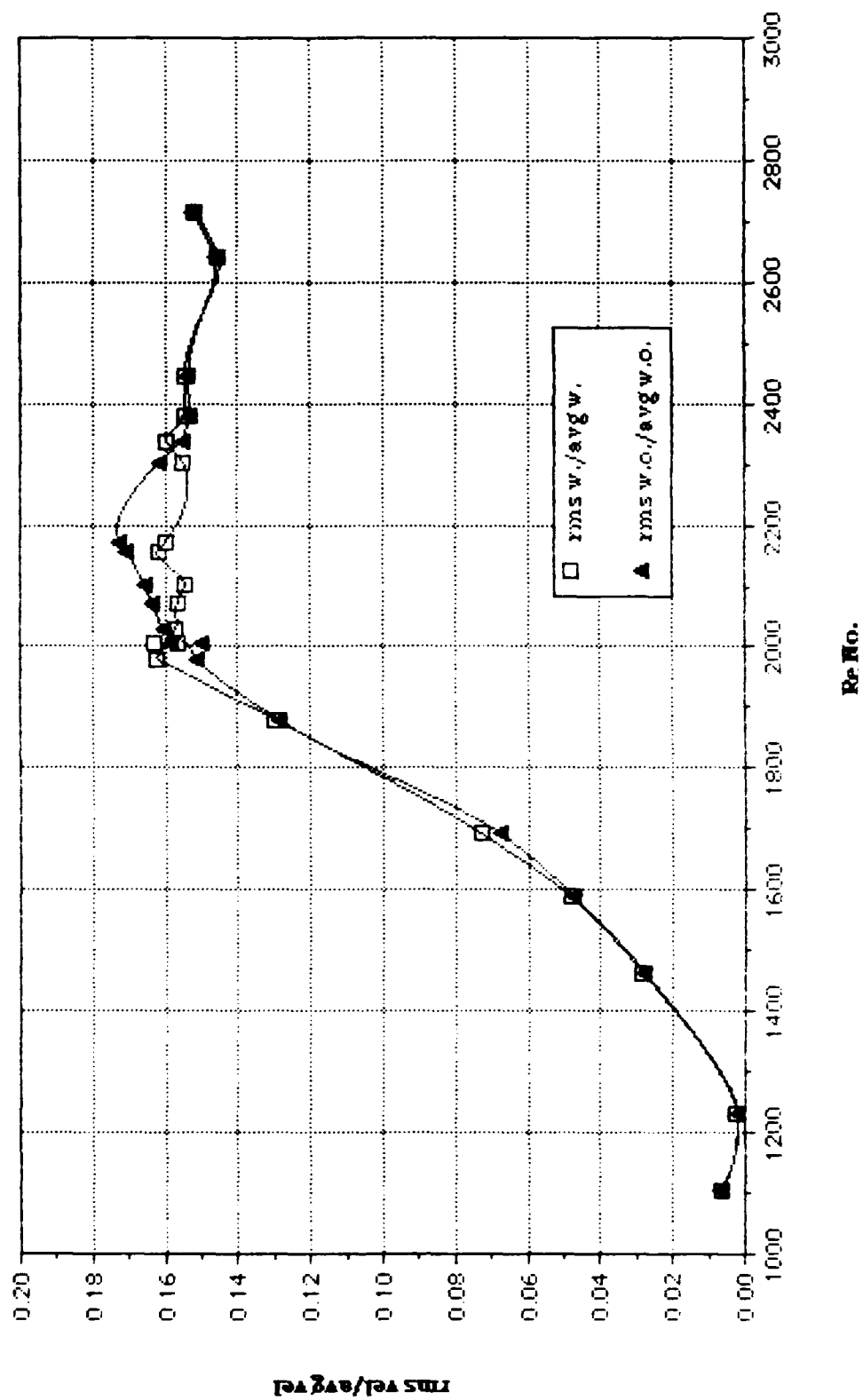


Figure 7.

RUN2J 130989.1938  
 AVG. VEL. .9151m/s RMS VEL. .001576m/s  
 OSC. FREQ. 0Hz STR. # 0  
 BULK VEL. 1.38m/s REY. # 1153

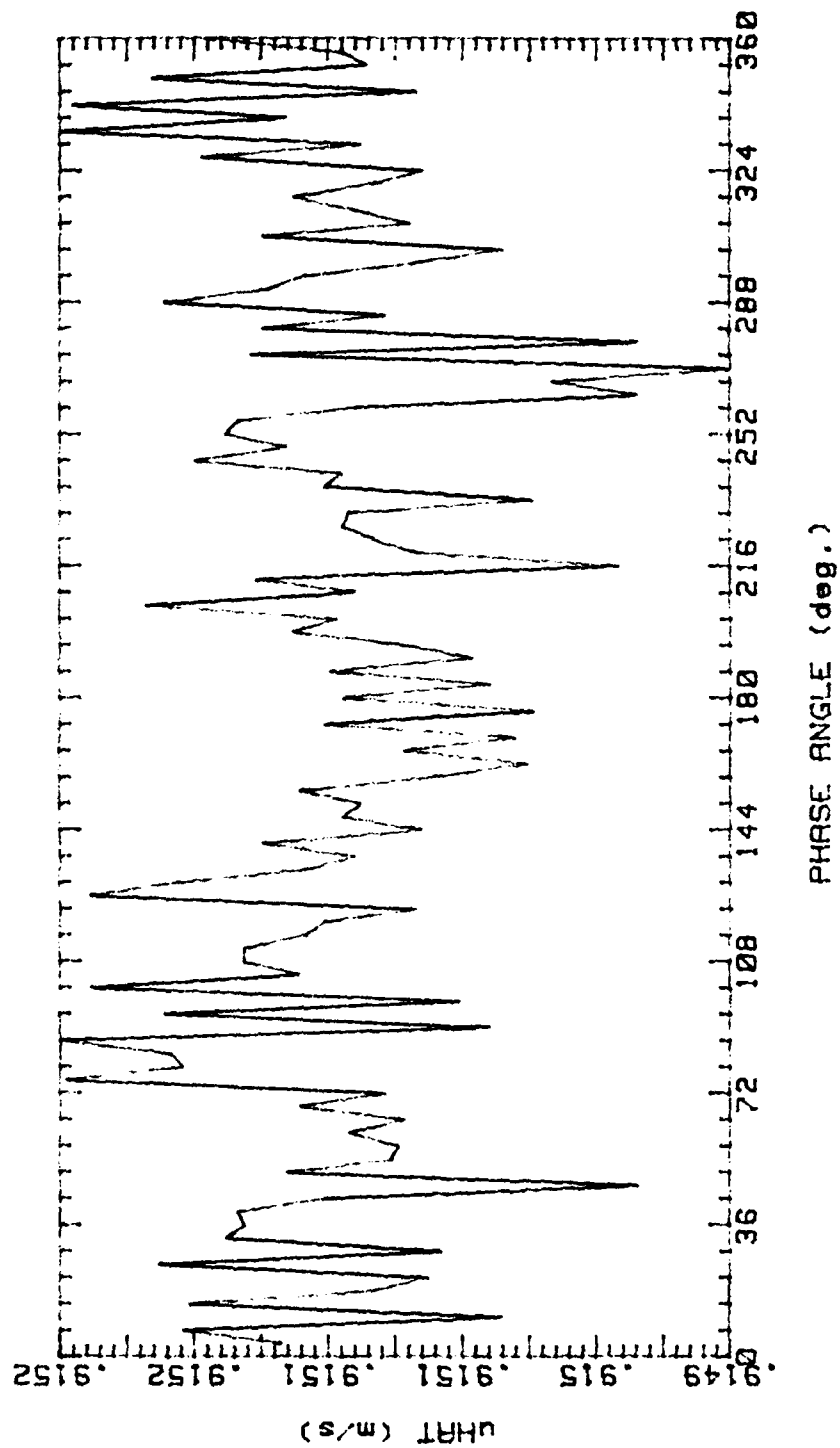


Figure 8.



RUN2J 130989.1938

AVG. VEL. .9151m/s RMS VEL. .001576m/s  
OSC. FREQ. 0Hz STR. # 0  
BULK VEL. 1.38m/s REY. # 1153

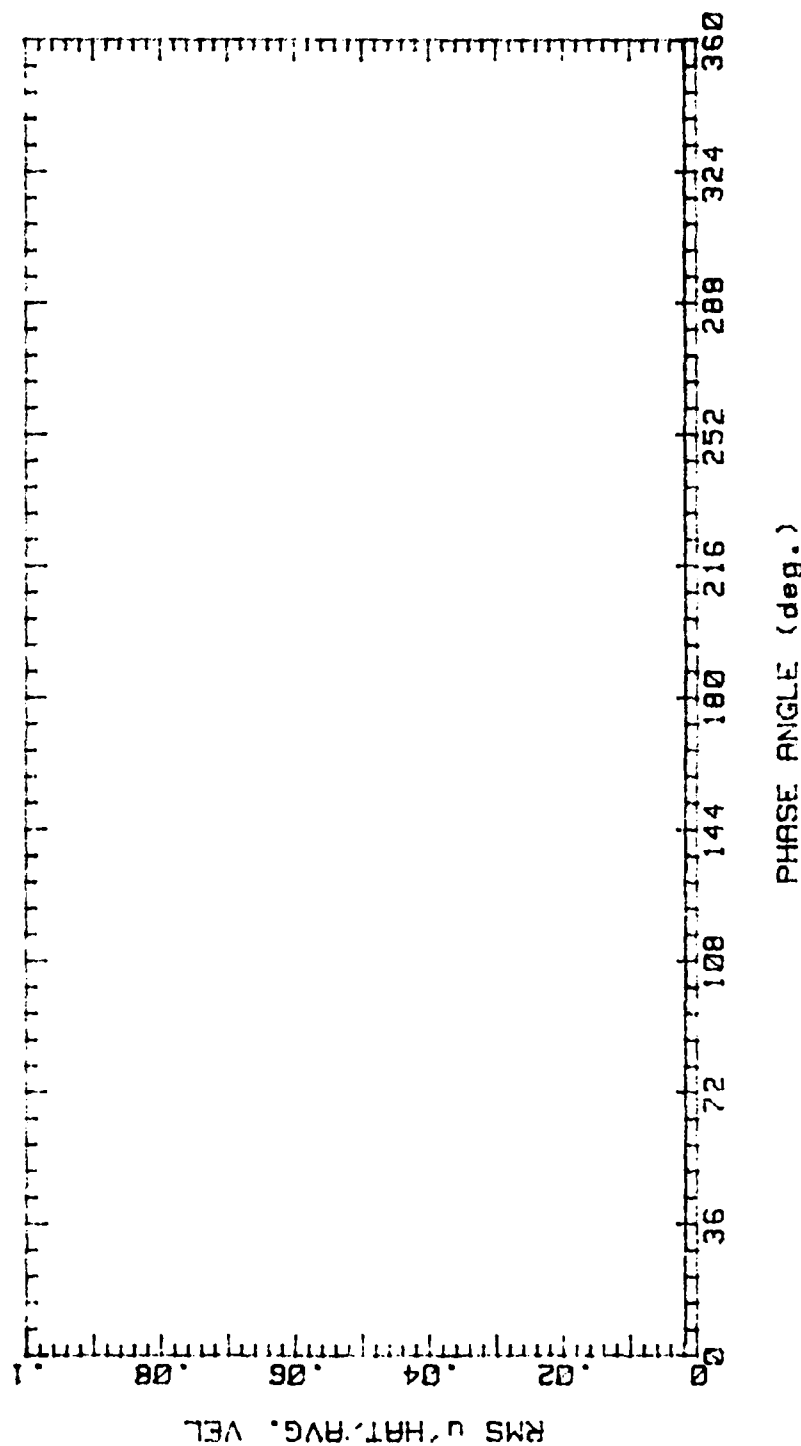


Figure 9.

RUN2N 170989.2047  
 AVG. VEL 1.607m/s RMS VEL .1653m/s  
 OSC. FREQ. 0Hz STR. # 0  
 BULK VEL. 2.185m/s REY. # 1826

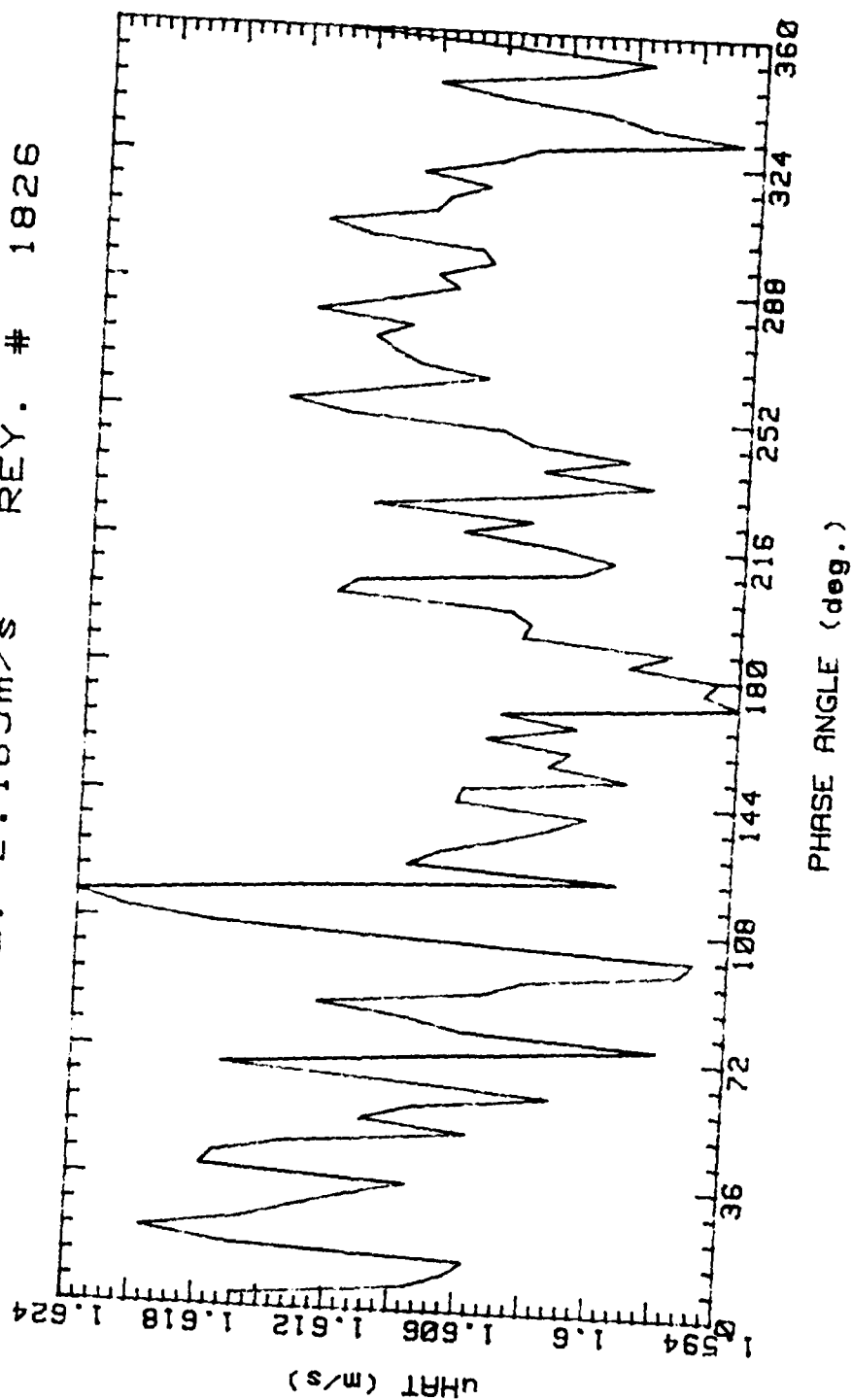


Figure 10.

RUN2N 170989.2047  
 AVG. VEL 1.607m/s RMS VEL .1653m/s  
 OSC. FREQ. 0Hz STR. # 0  
 BULK VEL. 2.185m/s REY. # 1826

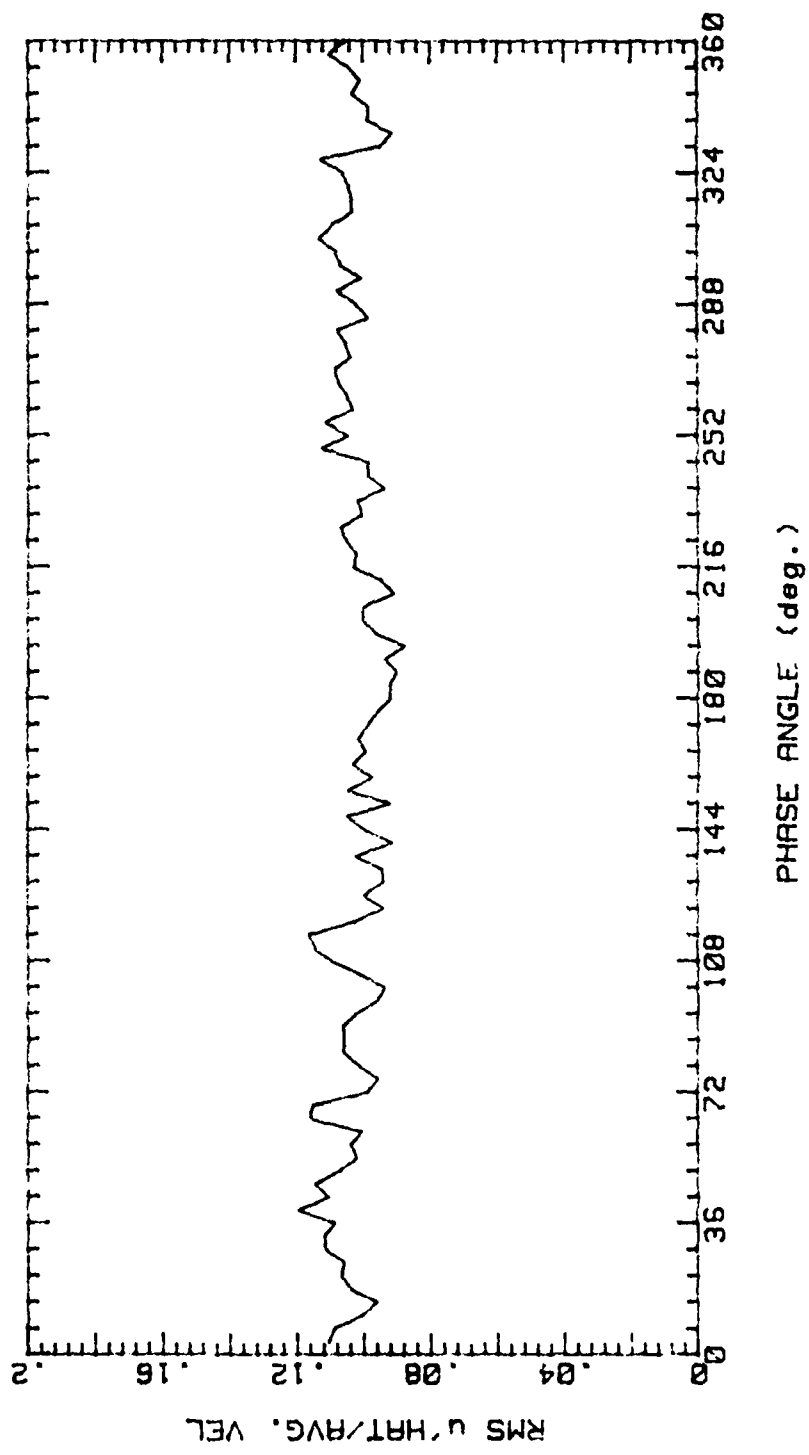


Figure 11.

RUN2L 150989.2201  
 AVG. VEL 2.082m/s RMS VEL .3061m/s  
 OSC. FREQ. 0Hz STR. # 0  
 BULK VEL. 2.4m/s REY. # 2005

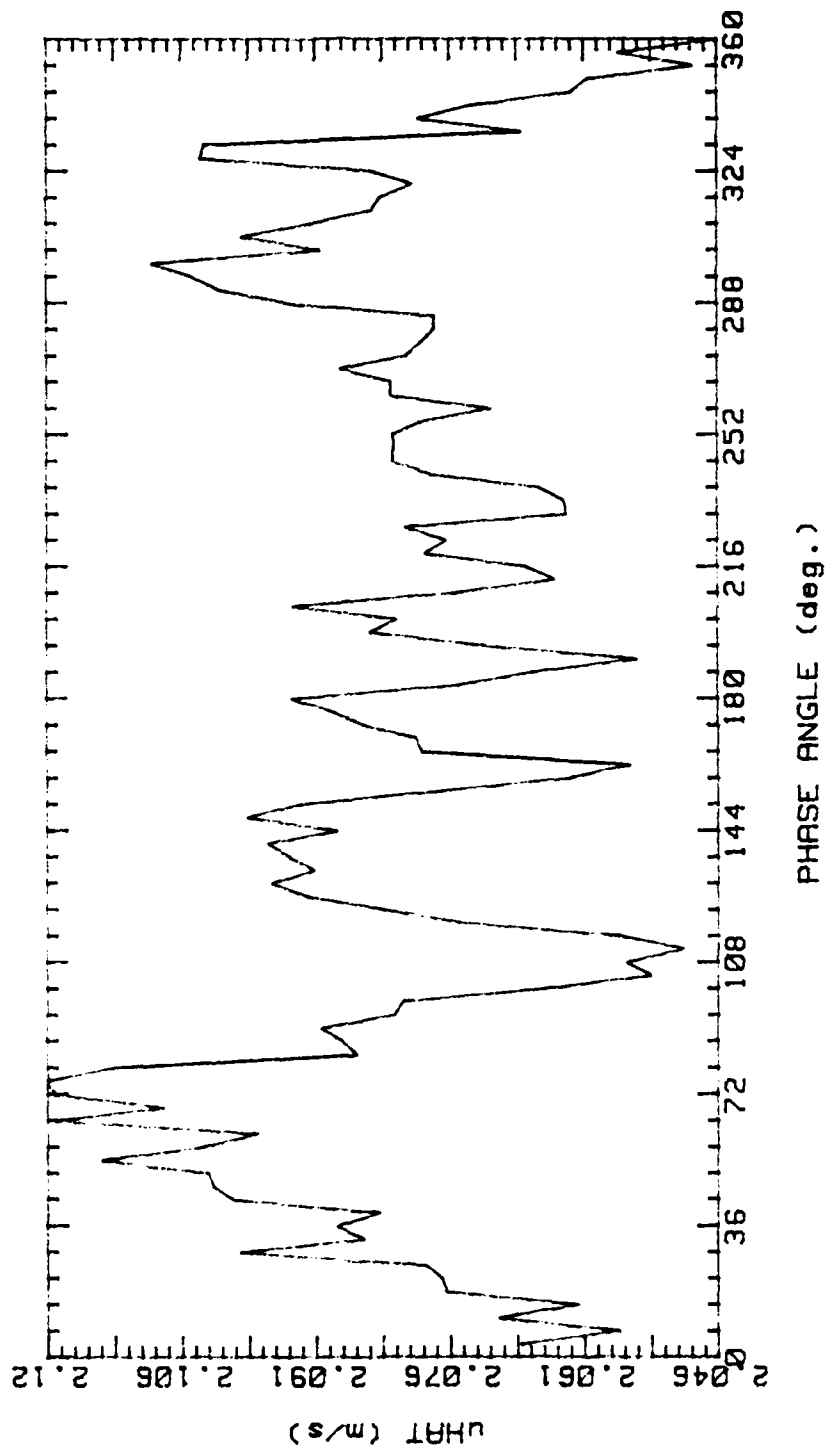


Figure 12.

RUN2L 150989.2201

AVG. VEL 2.082m/s RMS VEL .3061m/s  
OSC. FREQ. 0Hz STR. # 0  
BULK VEL. 2.4m/s REY. # 2005

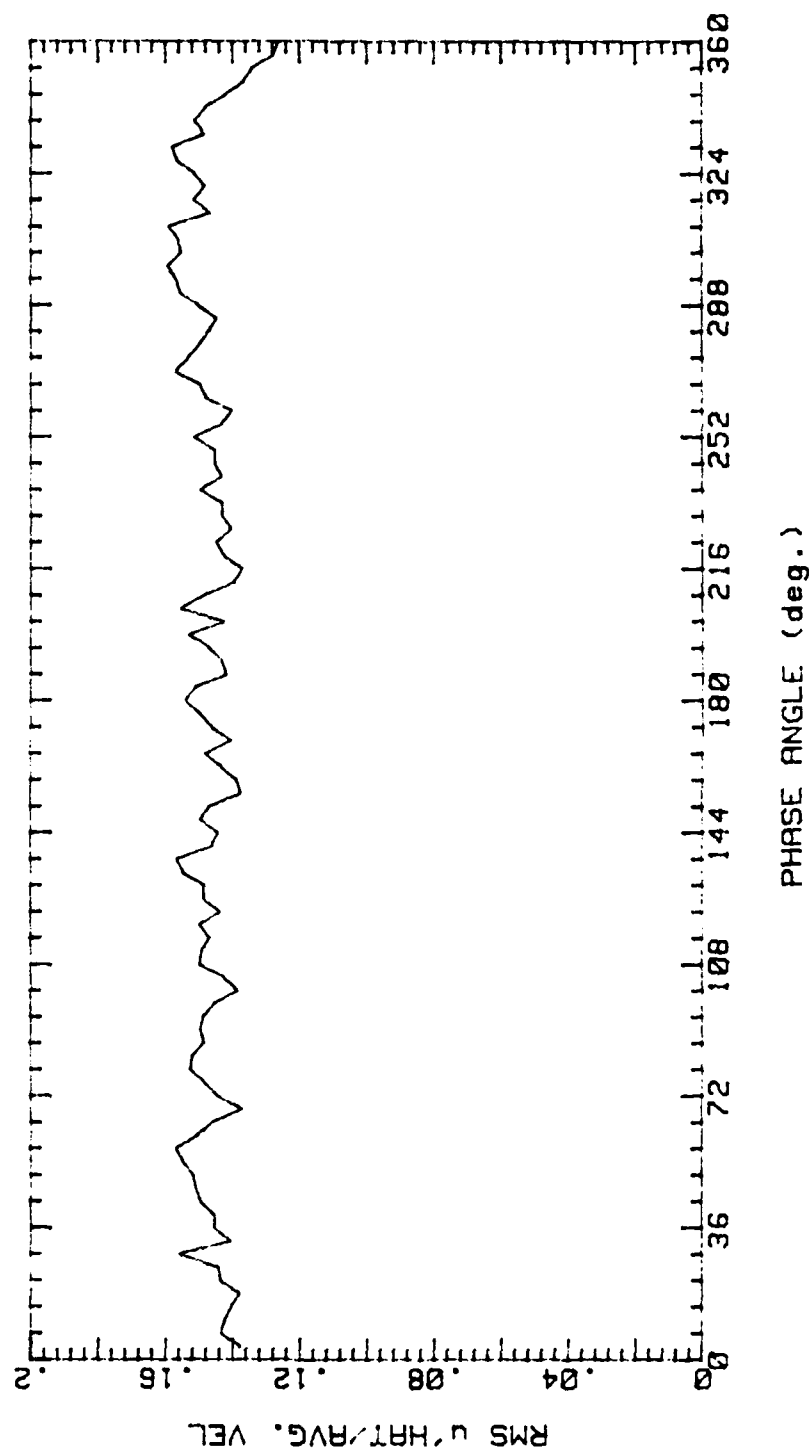


Figure 13.

RUN3L 150989.2354

AVG. VEL 2.202m/s RMS VEL .3558m/s

OSC. FREQ. 0Hz STR. # 0

BULK VEL. 2.495m/s REY. # 2085

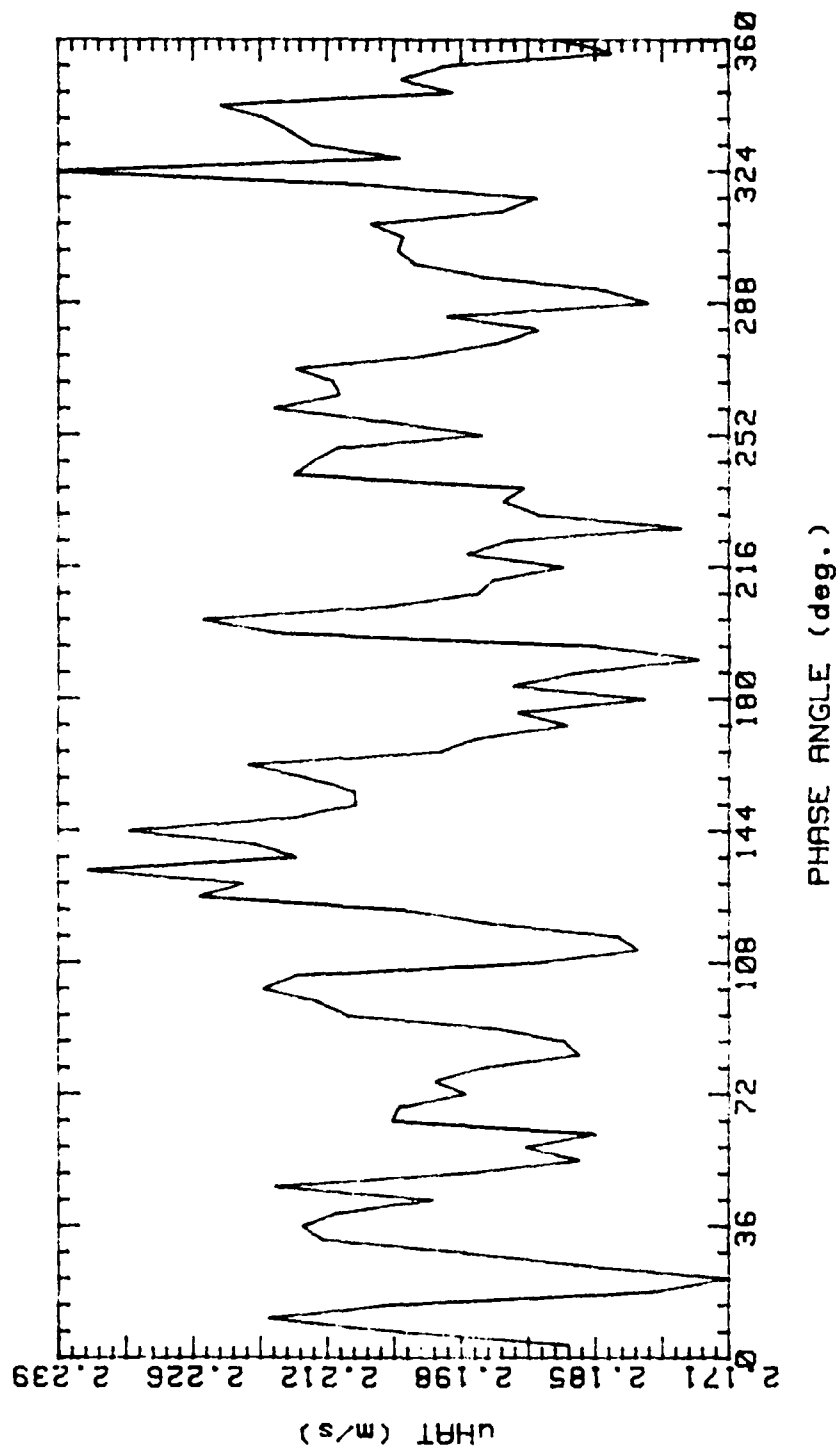


Figure 14.

RUN3L 150989.2354

AVG. VEL 2.202m/s RMS VEL .3558m/s

OSC. FREQ. 0Hz STR. # 0

BULK VEL. 2.495m/s REY. # 2085

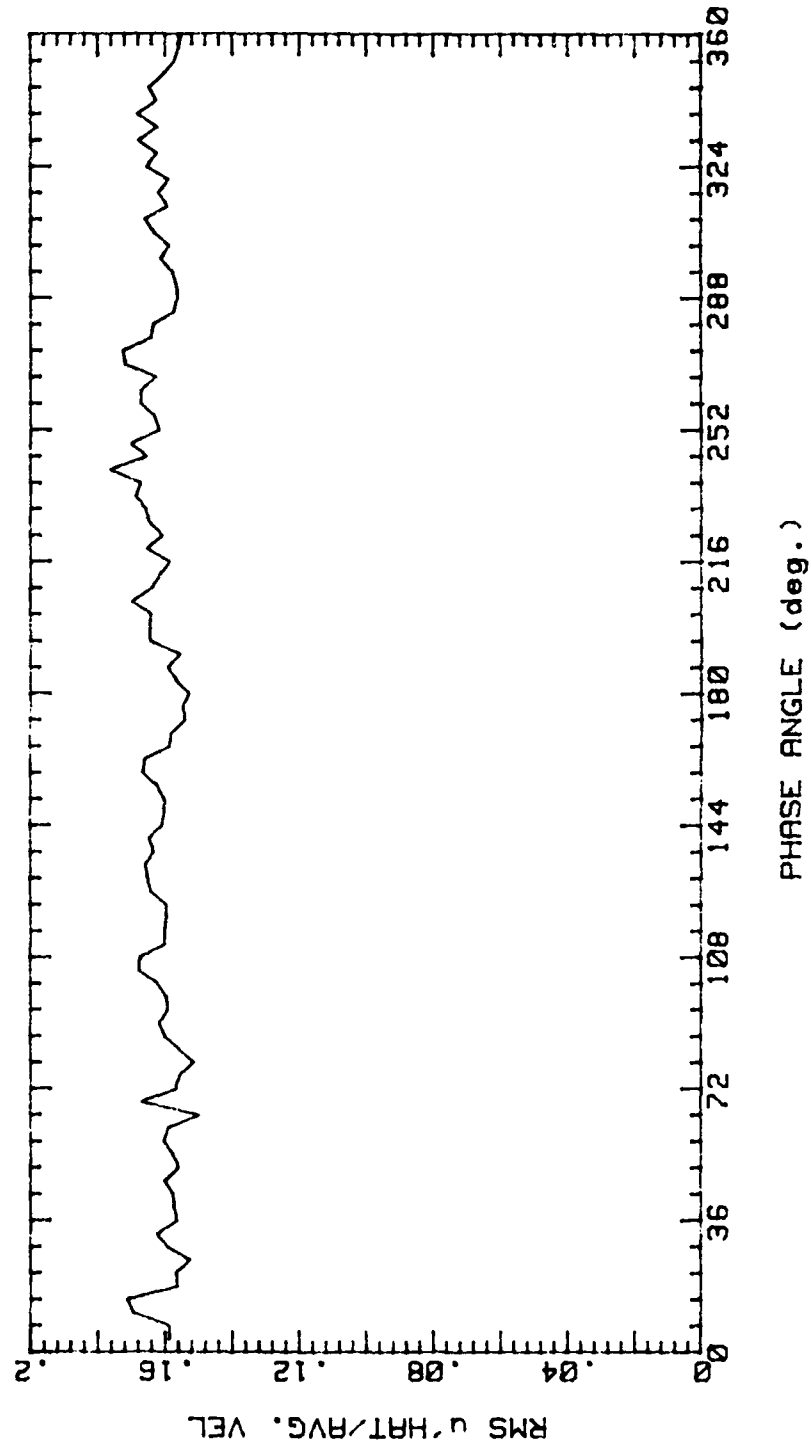


Figure 15.

RUN1S 200989.1846  
 AVG. VEL 2.744m/s RMS VEL .4014m/s  
 OSC. FREQ. 0Hz STR. # 0  
 BULK VEL. 3.16m/s REY. # 2640

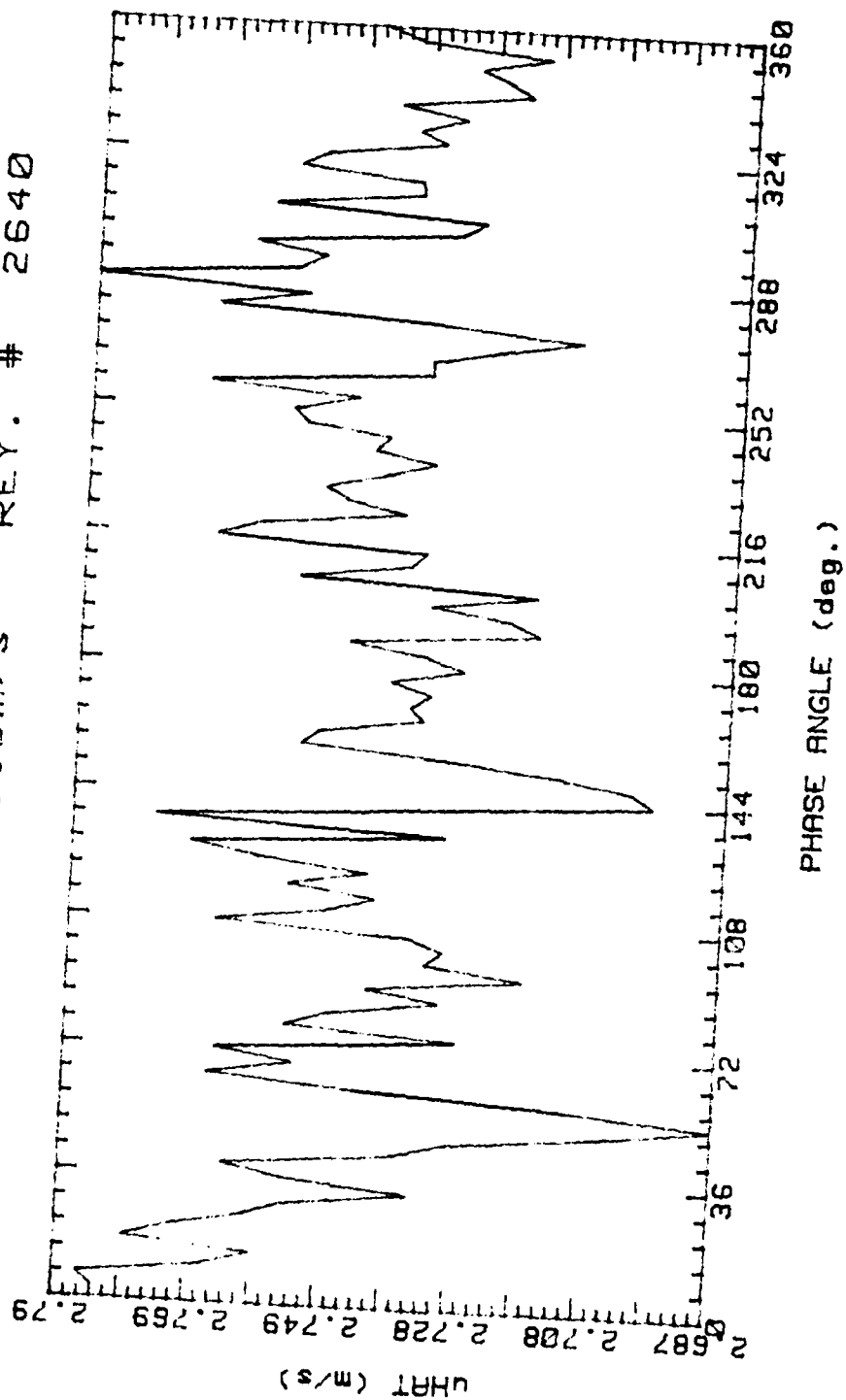


Figure 16.



RUN1S 200989.1846

AVG. VEL 2.744m/s RMS VEL .4014m/s

OSC. FREQ. 0Hz STR. # 0

BULK VEL. 3.16m/s REY. # 2640

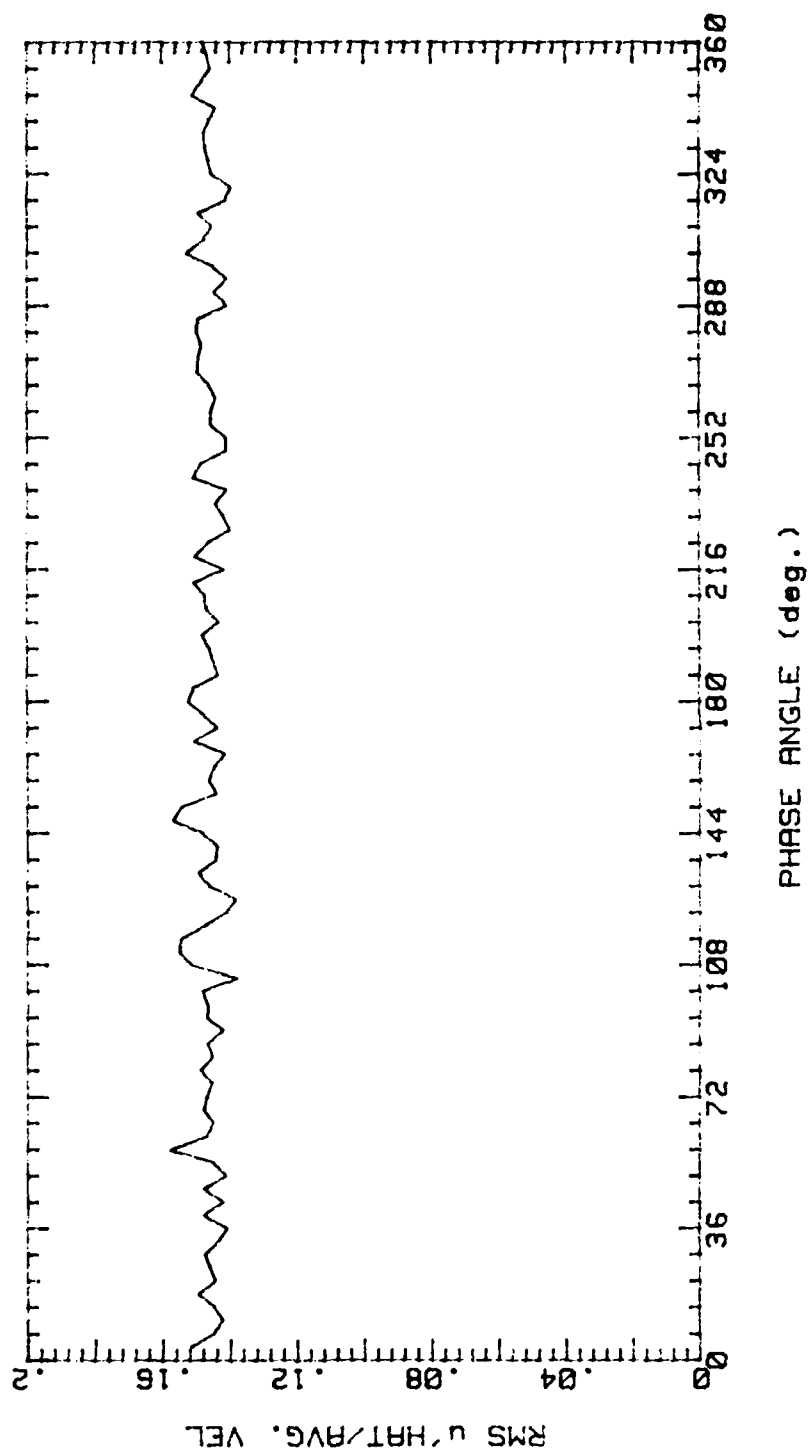


Figure 17.

RUN2I 130989.1926

AVG. VEL .9231m/s RMS VEL .00448m/s  
OSC. FREQ. 1Hz STR. # .05782  
BULK VEL. 1.38m/s REY. # 1153

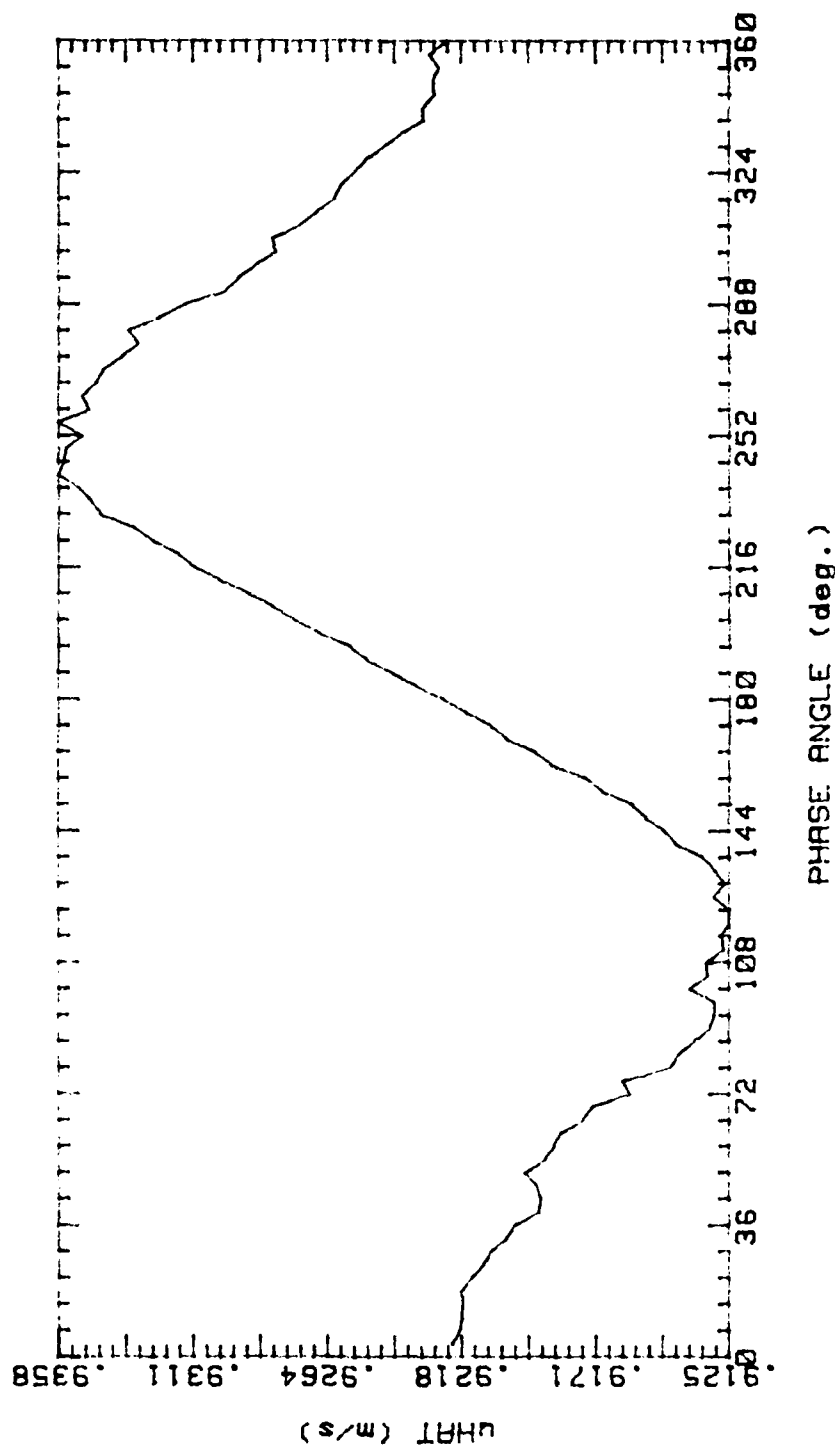


Figure 18.

RUN2I 130989.1926  
 AVG. VEL .9231m/s RMS VEL .00448m/s  
 OSC. FREQ. 1Hz STR. # .05782  
 BULK VEL. 1.38m/s REY. # 1153

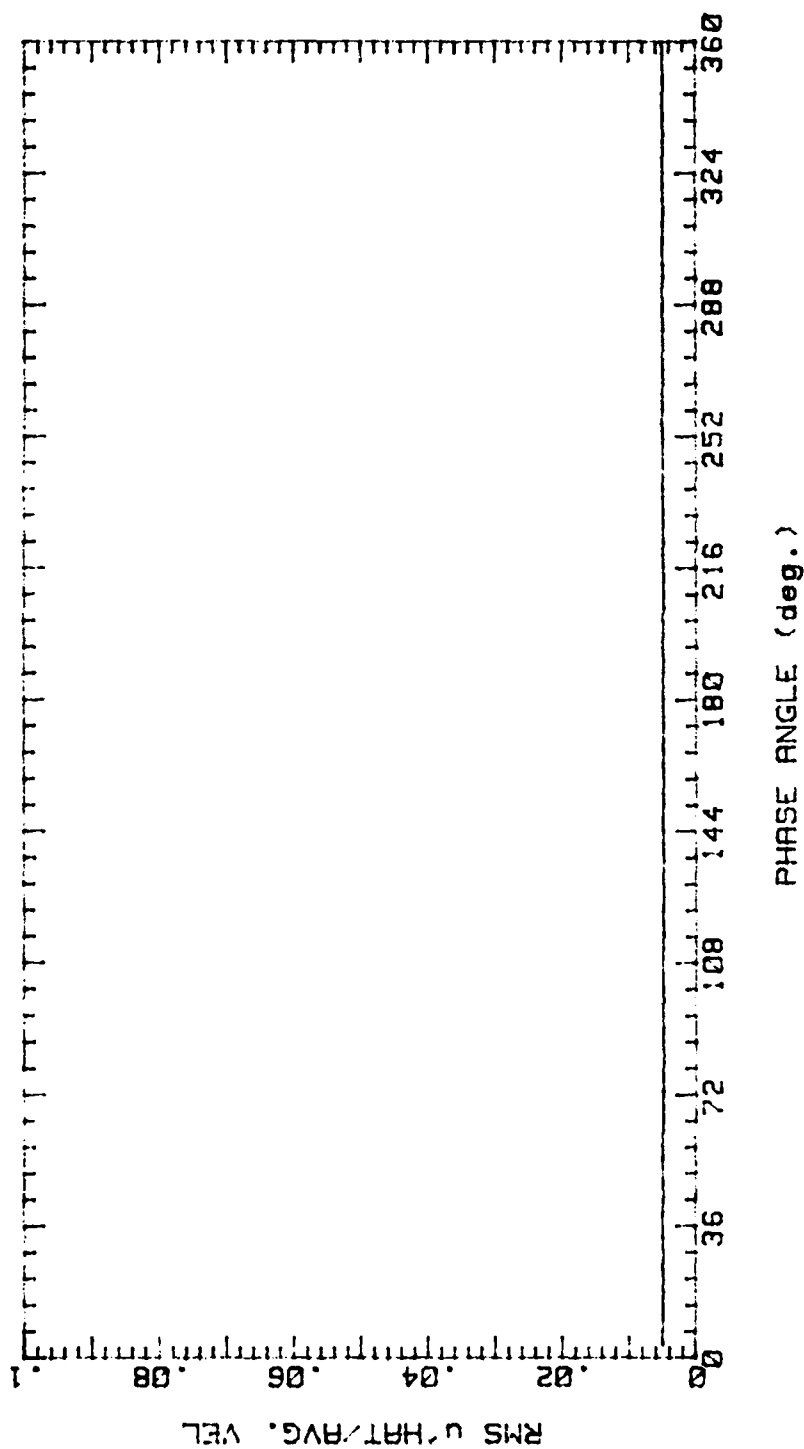


Figure 19.

MULTIRUN (2M, 1 RUNS) PH. AVE., 170989  
 AVG. VEL 1.61m/s RMS VEL .1585m/s  
 OSC. FREQ. 1Hz STR. # .03652  
 BULK VEL. 2.185m/s REY. # 1826

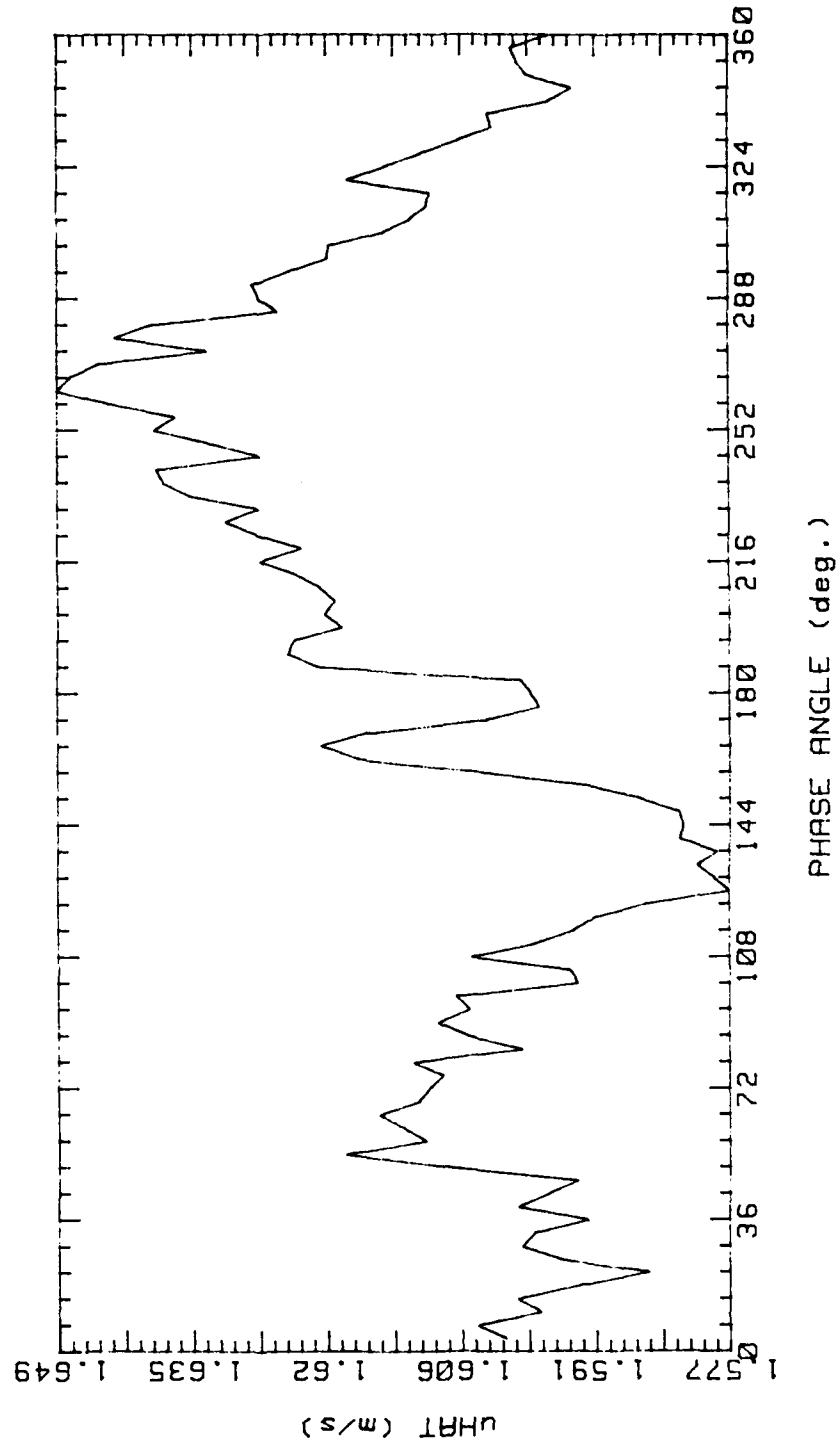


Figure 20.

MULTIRUN (2M, 1 RUNS) PH. AVE., 170989  
 AVG. VEL 1.61m/s RMS VEL .1585m/s  
 OSC. FREQ. 1Hz STR. # .03652  
 BULK VEL. 2.185m/s REY. # 1826

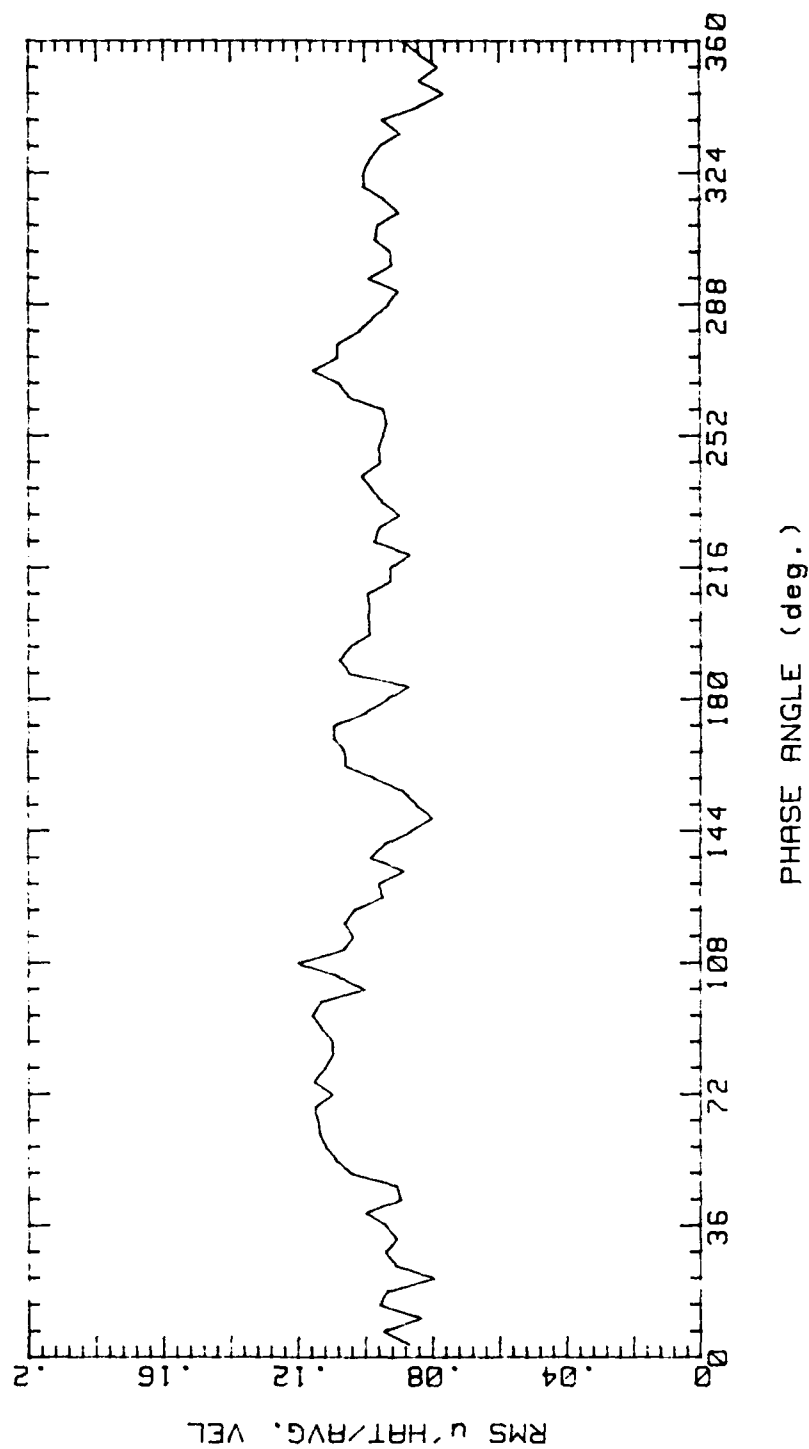


Figure 21.

MULTIRUN (2M, 8 RUNS) PH. AVE., 170989  
 AVG. VEL 1.609m/s RMS VEL .163m/s  
 OSC. FREQ. 1Hz STR. # .03652  
 BULK VEL. 2.185m/s REY. # 1826

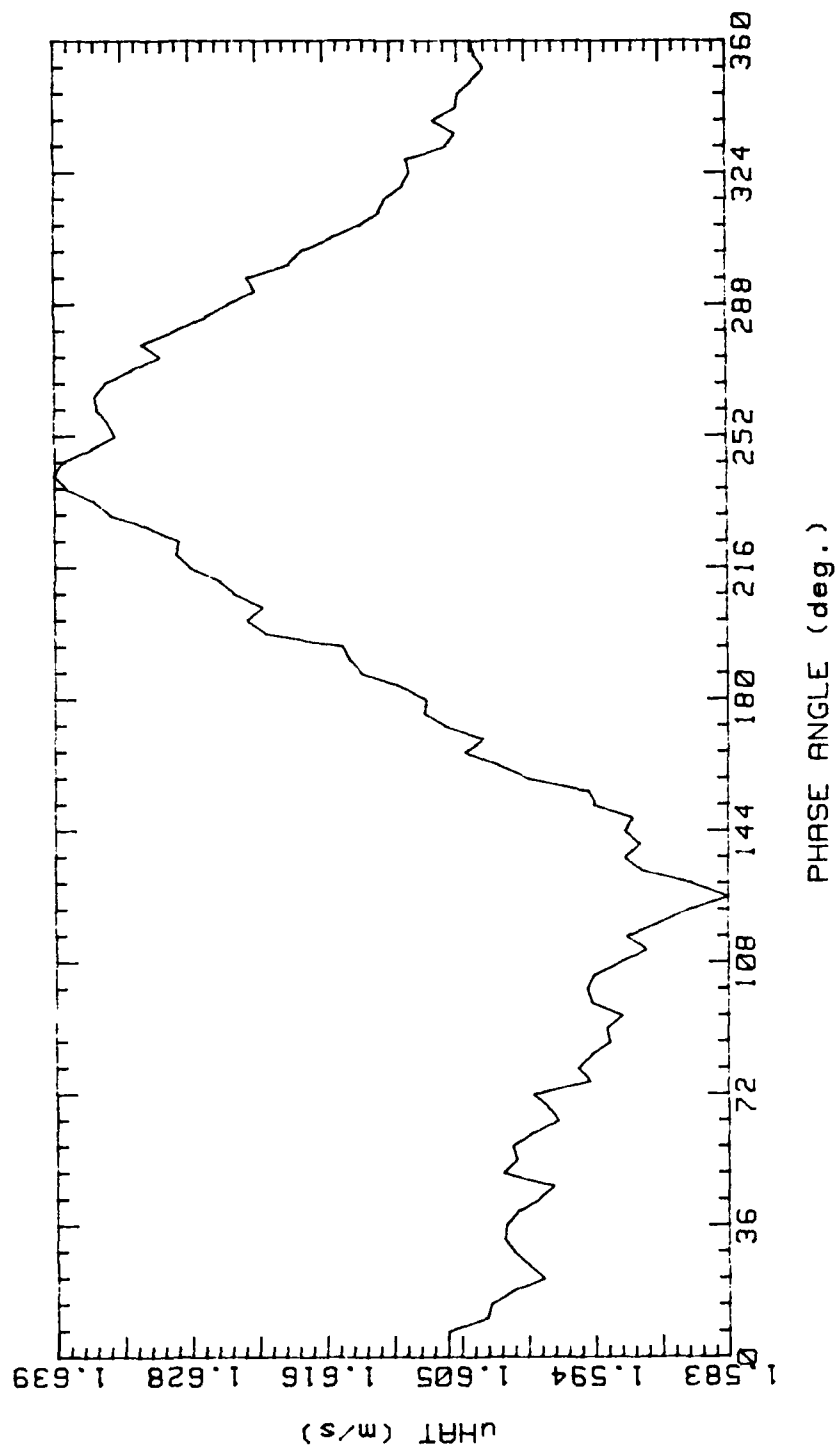


Figure 22.

MULTIRUN (2M, 8 RUNS) PH. AVE., 170989  
 AVG. VEL 1.609m/s RMS VEL .163m/s  
 OSC. FREQ. 1Hz STR. # .03652  
 BULK VEL. 2.185m/s REY. # 1826

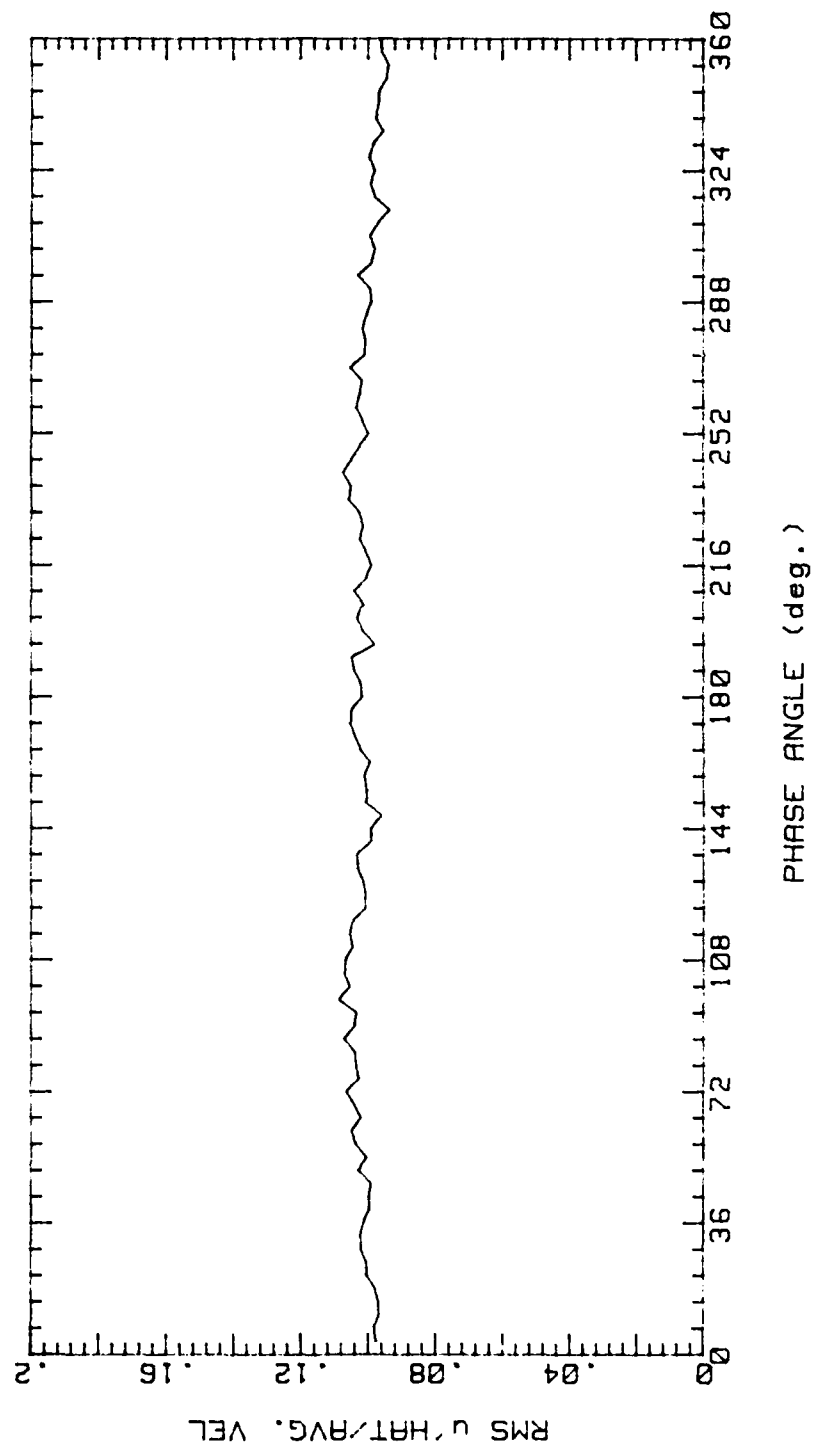


Figure 23.

MULTIRUN (2K, 1 RUNS) PH. AVE., 150989  
 AVG. VEL 2.12m/s RMS VEL .3202m/s  
 OSC. FREQ. 1Hz STR. # .03325  
 BULK VEL. 2.4m/s REY. # 2005

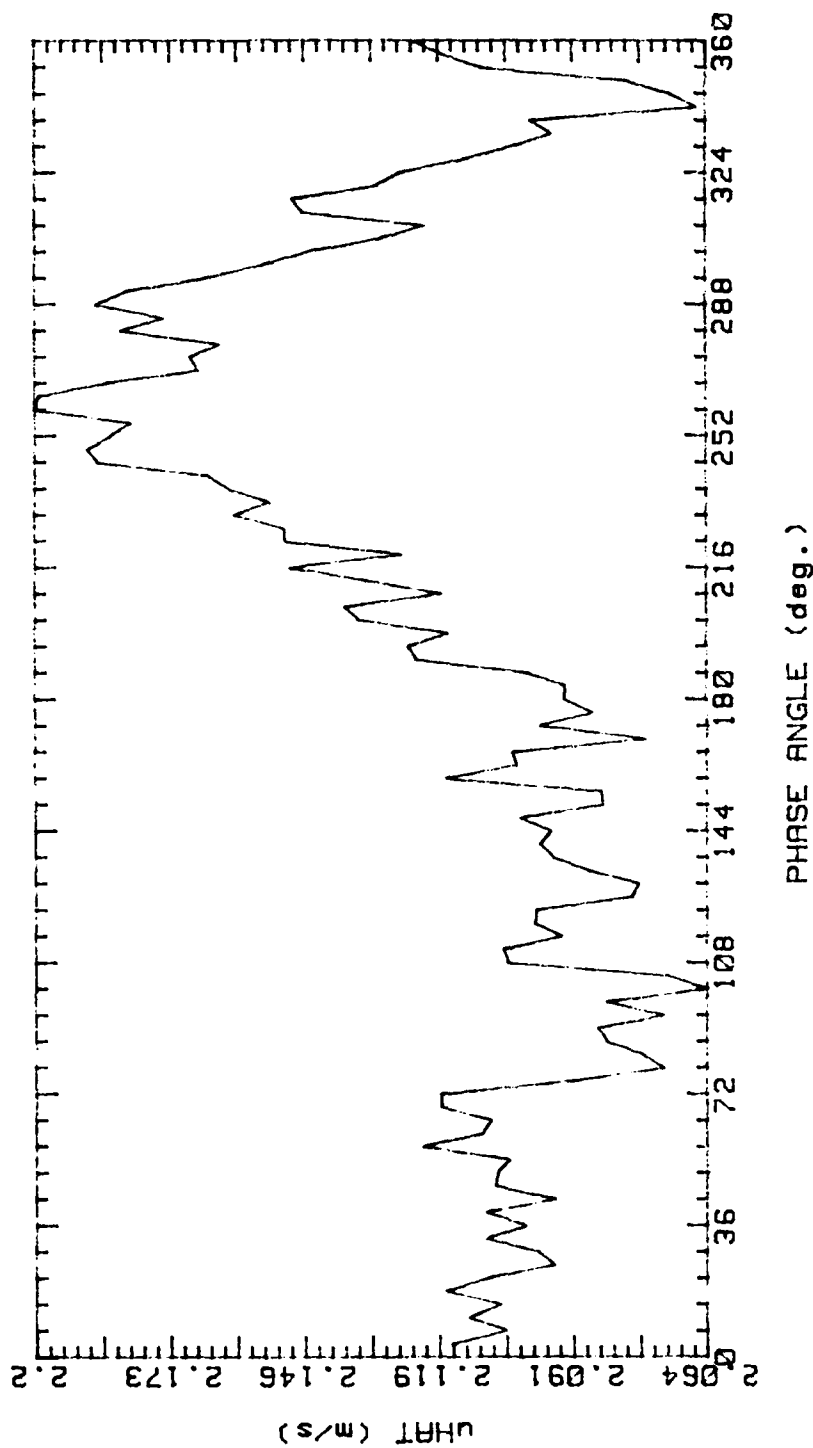


Figure 24.



MULTIRUN (2K, 1 RUNS) PH. AVE., 150989  
 AVG. VEL 2.12m/s RMS VEL .3202m/s  
 OSC. FREQ. 1Hz STR. # .03325  
 BULK VEL. 2.4m/s REY. # 2005

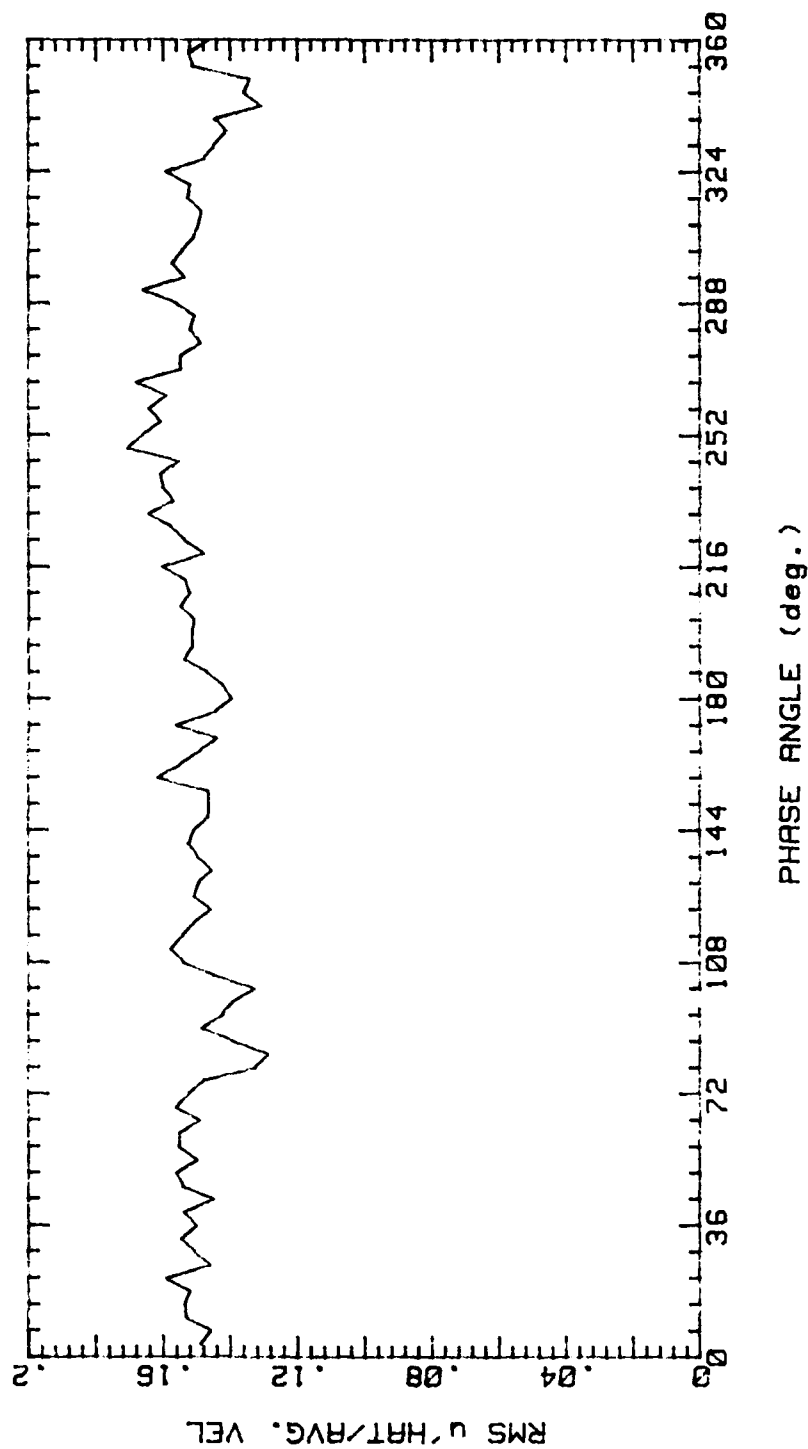


Figure 25.

MULTIRUN (2K, 8 RUNS) PH. AVE., 150989  
 AVG. VEL 2.09m/s RMS VEL .3087m/s  
 OSC. FREQ. 1Hz STR. # .03325  
 BULK VEL. 2.4m/s REY. # 2005

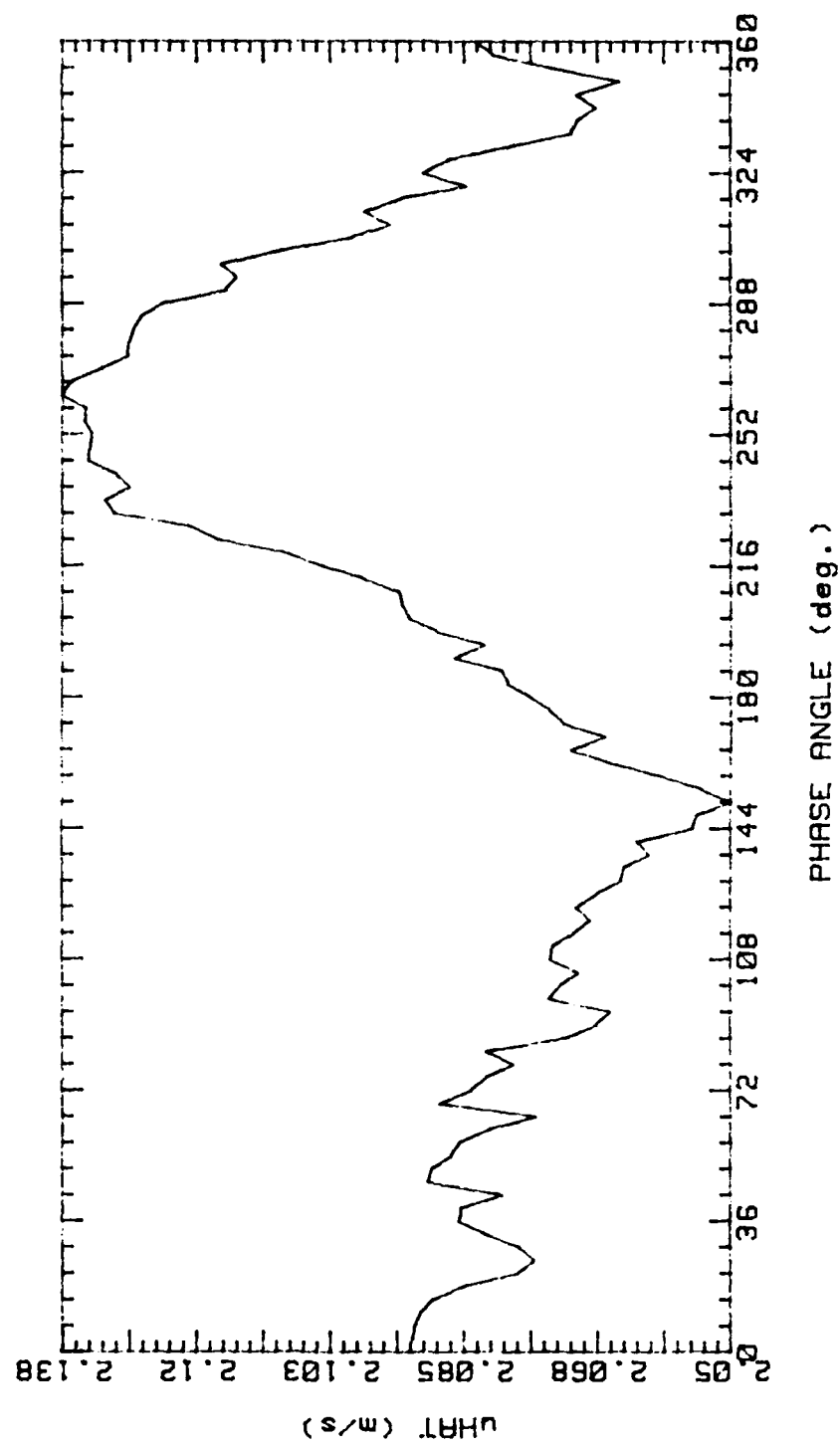


Figure 26.

MULTIRUN (2K, 8 RUNS) PH. AVE., 150989  
 AVG. VEL 2.09m/s RMS VEL .3087m/s  
 OSC. FREQ. 1Hz STR. # .03325  
 BULK VEL. 2.4m/s REY. # 2005

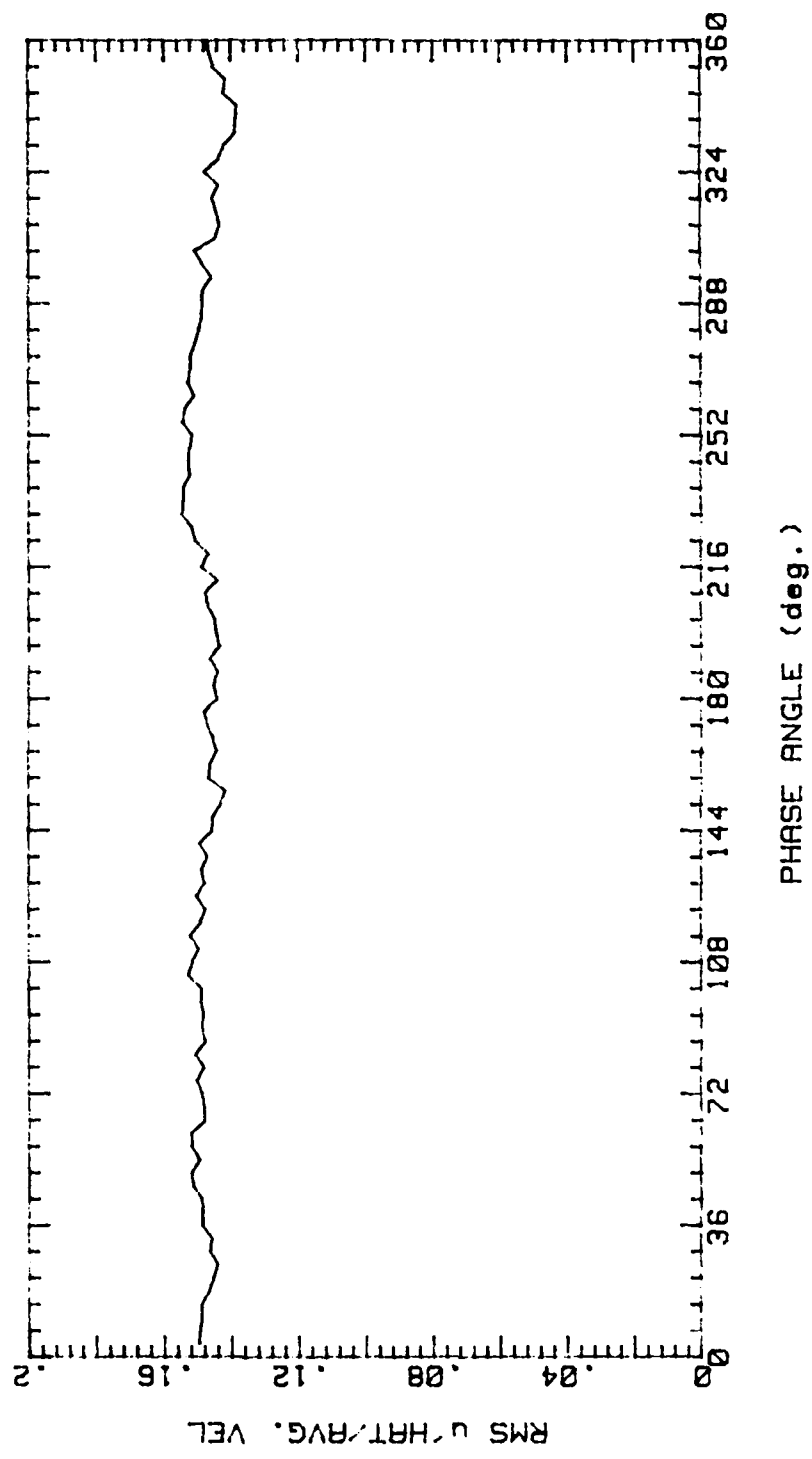


Figure 27.

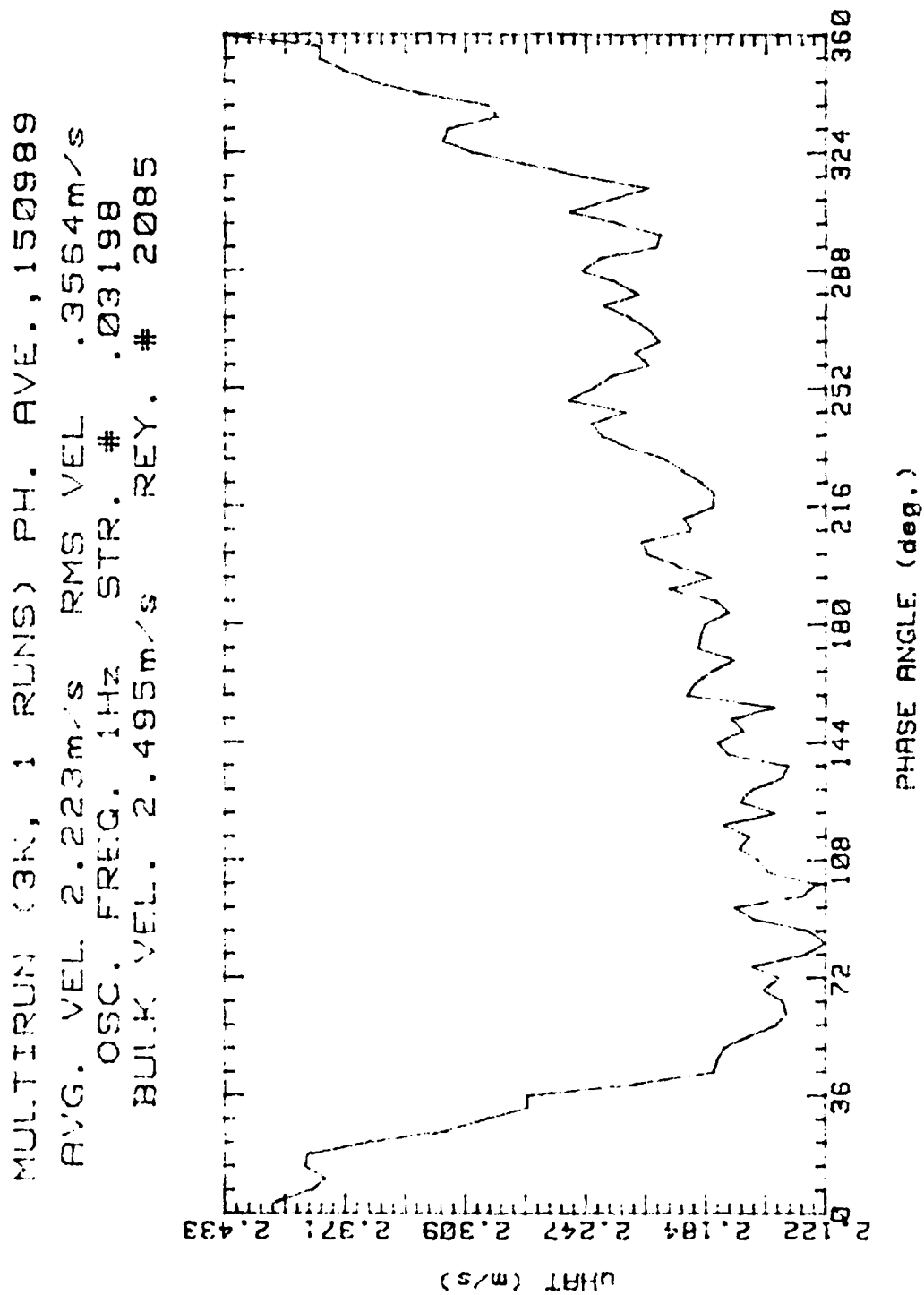


Figure 28.

MULTIRUN (3K, 1 RUNS) PH. AVE., 150989  
 AVG. VEL 2.223m/s RMS VEL .3564m/s  
 OSC. FREQ. 1Hz STR. # .03198  
 BULK VEL. 2.495m/s REY. # 2085

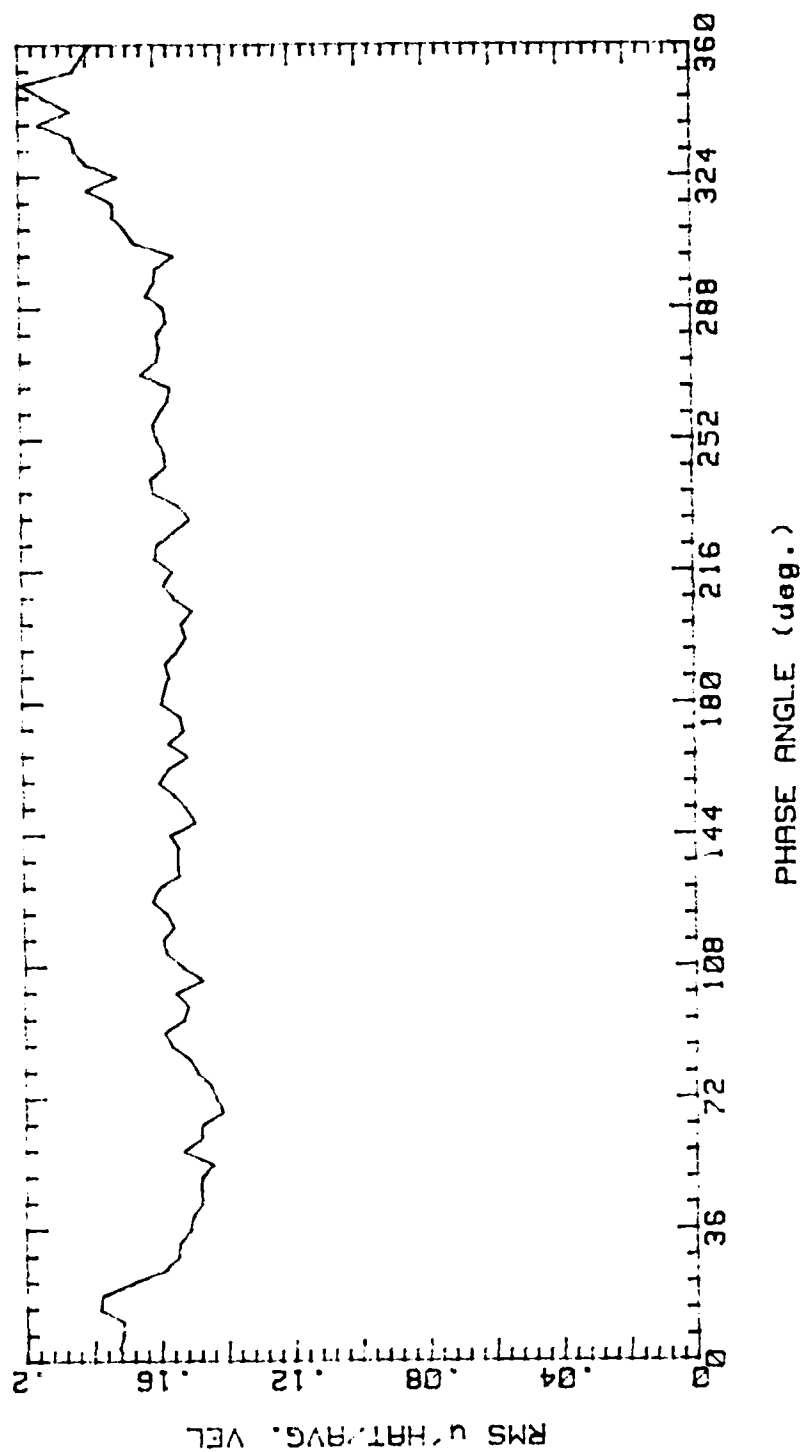


Figure 29.

MULTIRUN (3K, 8 RUNS) PH. AVE., 150989  
 AVG. VEL 2.217m/s RMS VEL .3564m/s  
 OSC. FREQ. 1Hz STR. # .03198  
 BULK VEL. 2.495m/s REY. # 2085

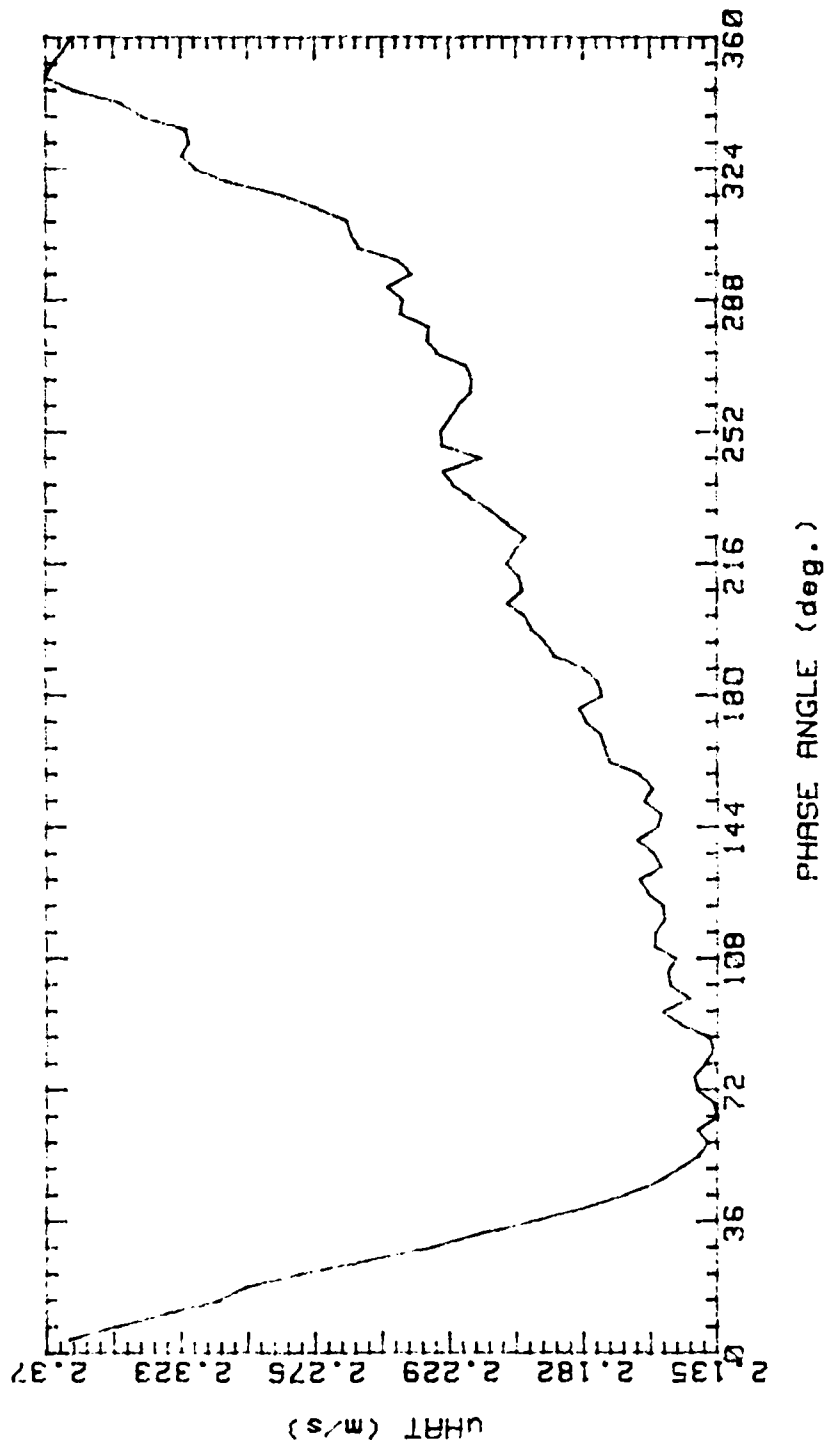


Figure 30.

MULTIRUN (3K, 8 RUNS) PH. AVE., 150989  
 AVG. VEL 2.217m/s RMS VEL .3564m/s  
 OSC. FREQ. 1Hz STR. # .03198  
 BULK VEL. 2.495m/s REY. # 2085

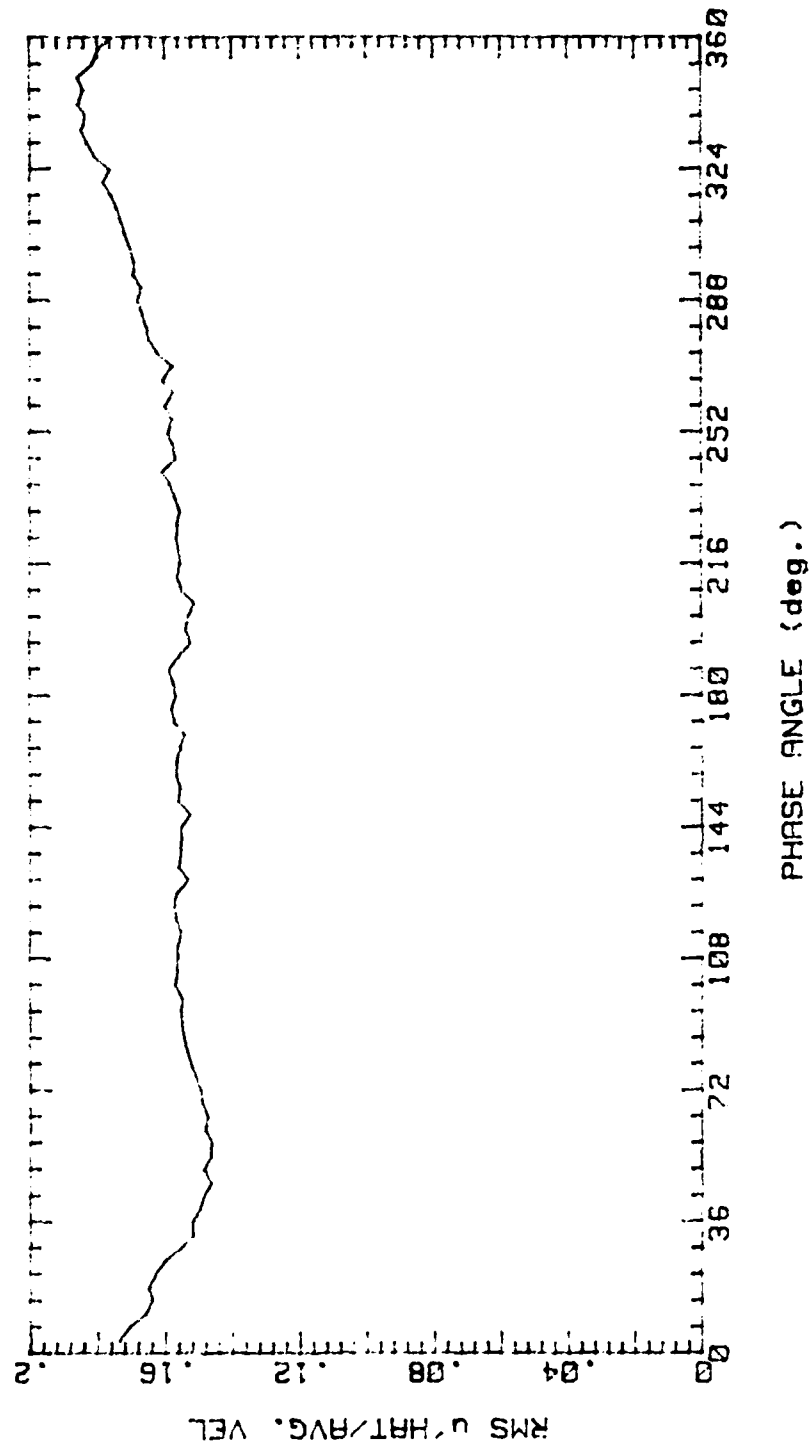


Figure 31.

MULTIRUN (1R, 1 RUNS) PH. AVE., 200989  
 AVG. VEL 2.788m/s RMS VEL .4037m/s  
 OSC. FREQ. 1Hz STR. # .02525  
 BULK VEL. 3.16m/s REY. # 2640

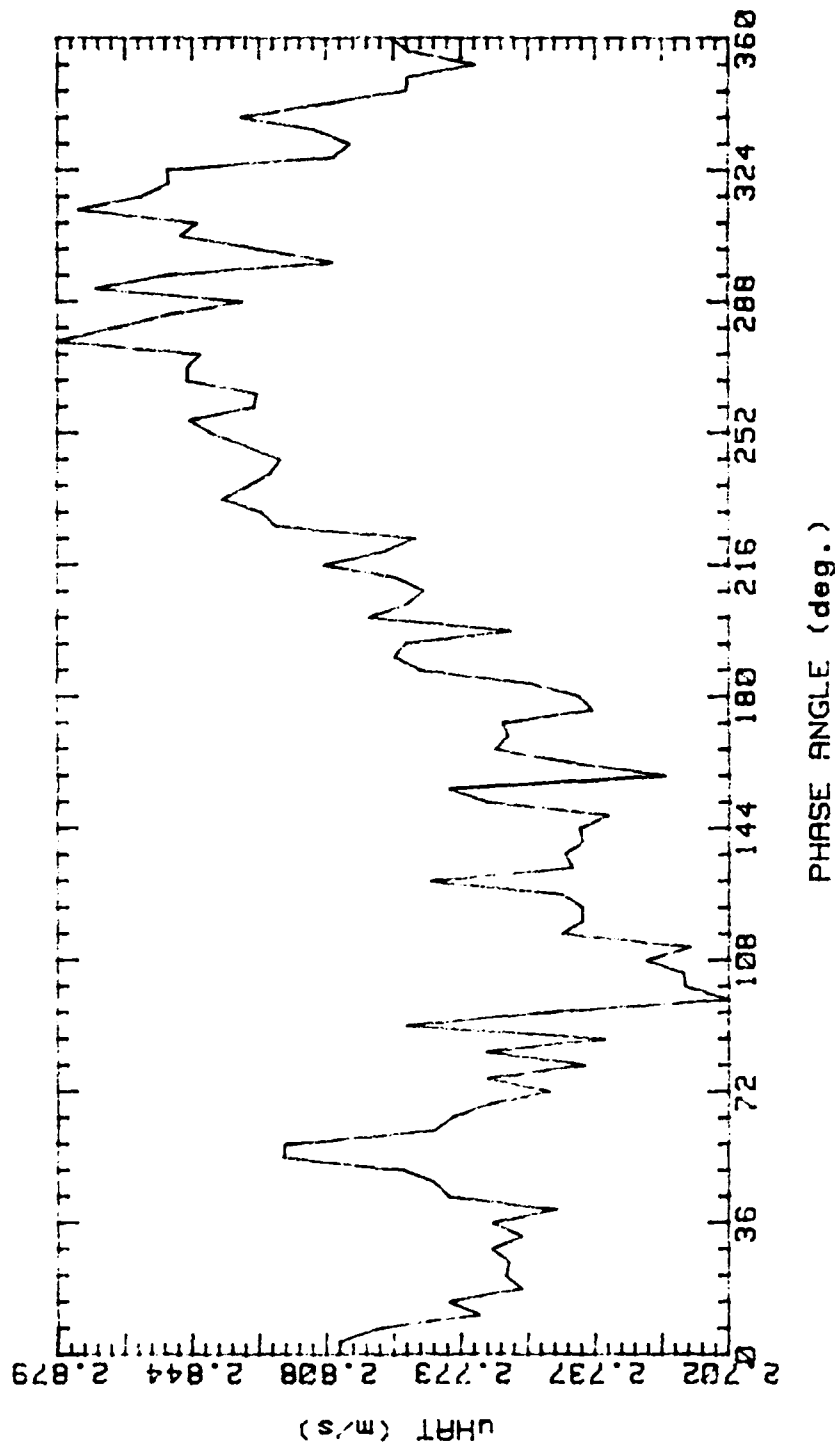


Figure 32.



MULTIRUN (1R, 1 RUNS) PH. AVE., 200989  
 AVG. VEL 2.788m/s RMS VEL .4037m/s  
 OSC. FREQ. 1Hz STR. # .02525  
 BULK VEL. 3.16m/s REY. # 2640

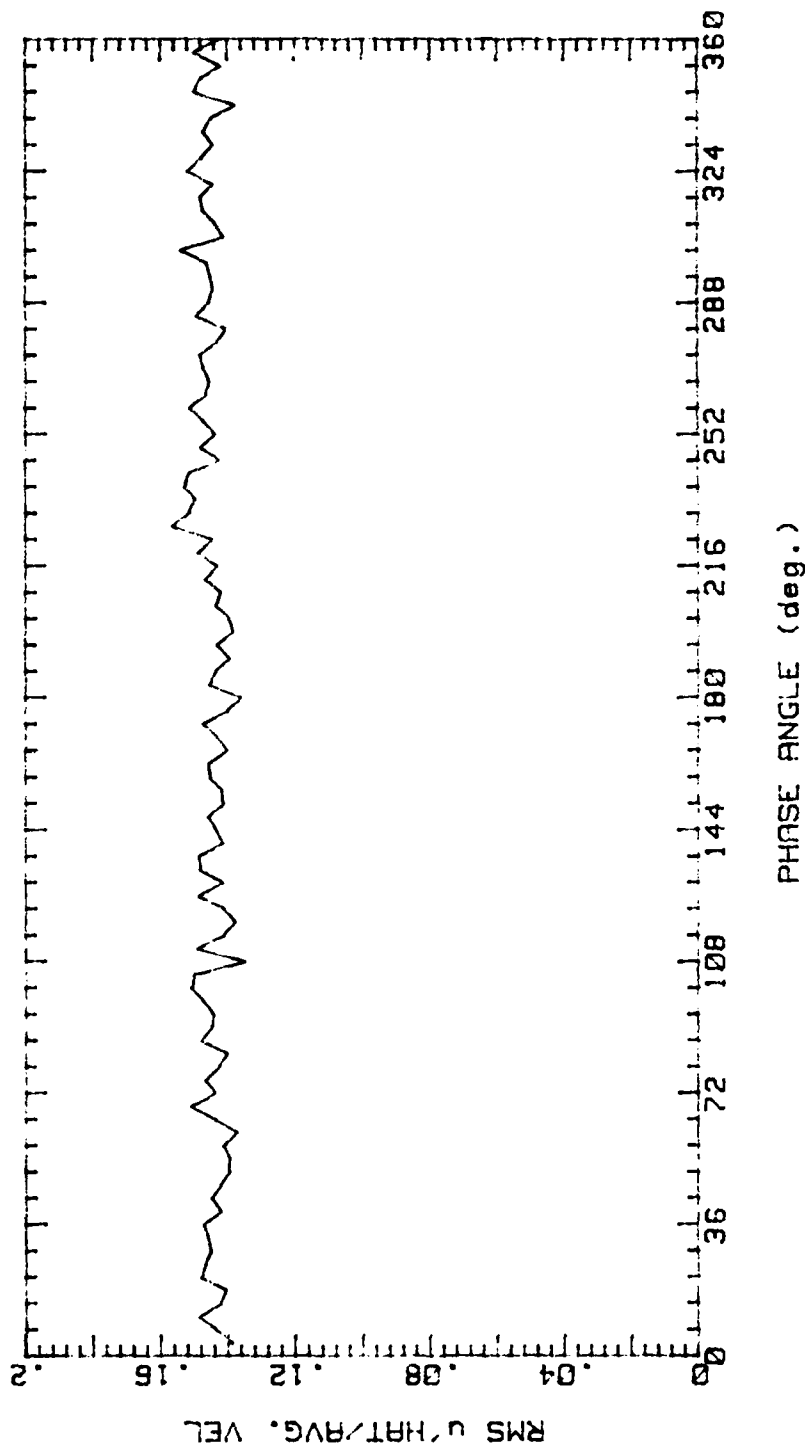


Figure 33.

MULTIRUN (1R, 3 RUNS) PH. AVE., 200989  
 AVG. VEL 2.762m/s RMS VEL .4024m/s  
 OSC. FREQ. 1Hz STR. # .02525  
 BULK VEL. 3.16m/s REY. # 2640

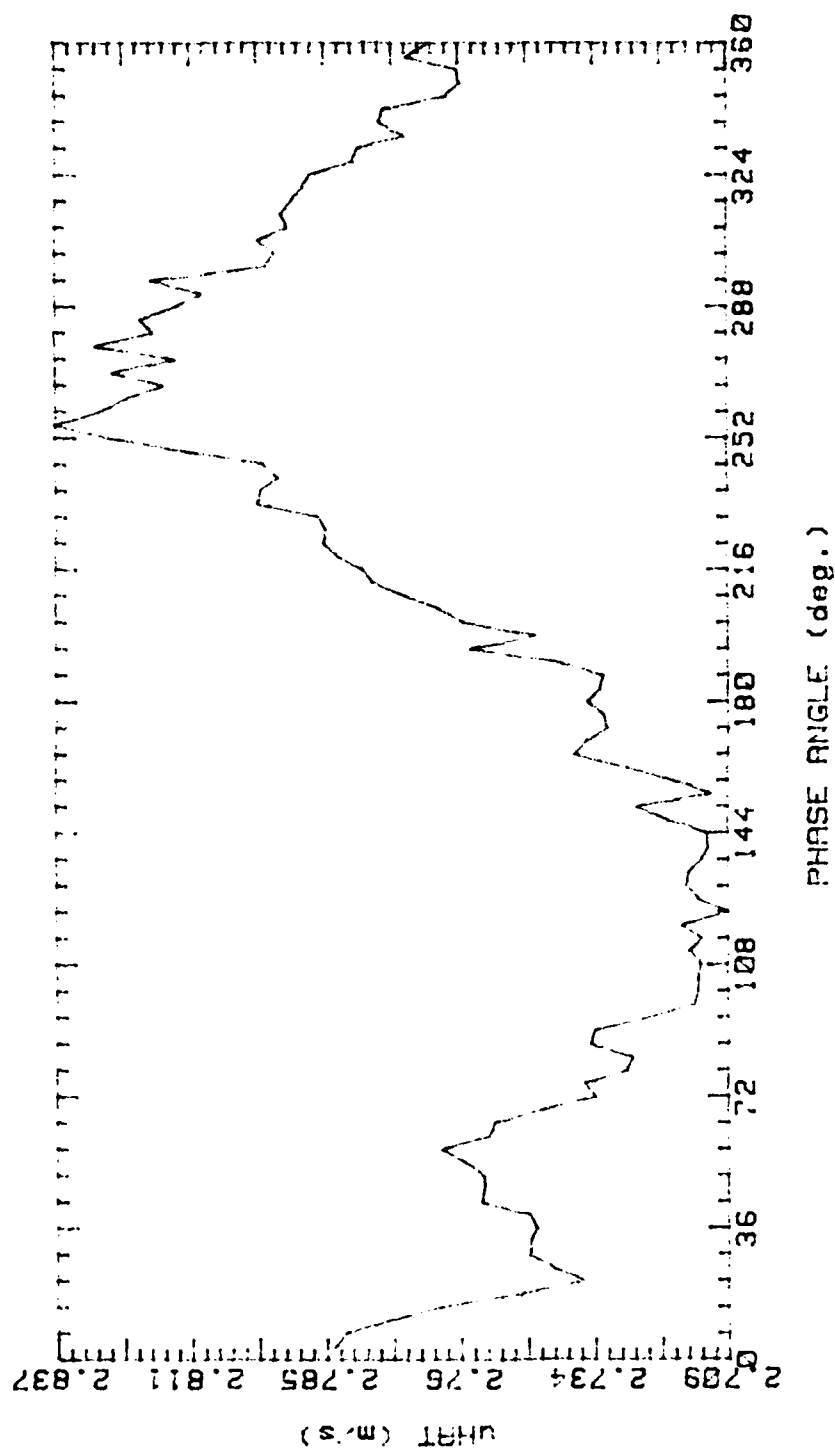


Figure 34.

MULTIRUN (1R, 3 RUNS) PH. AVE., 200989  
 AVG. VEL 2.762m/s RMS VEL .4024m/s  
 OSC. FREQ. 1Hz STR. # .02525  
 BULK VEL. 3.16m/s REY. # 2640

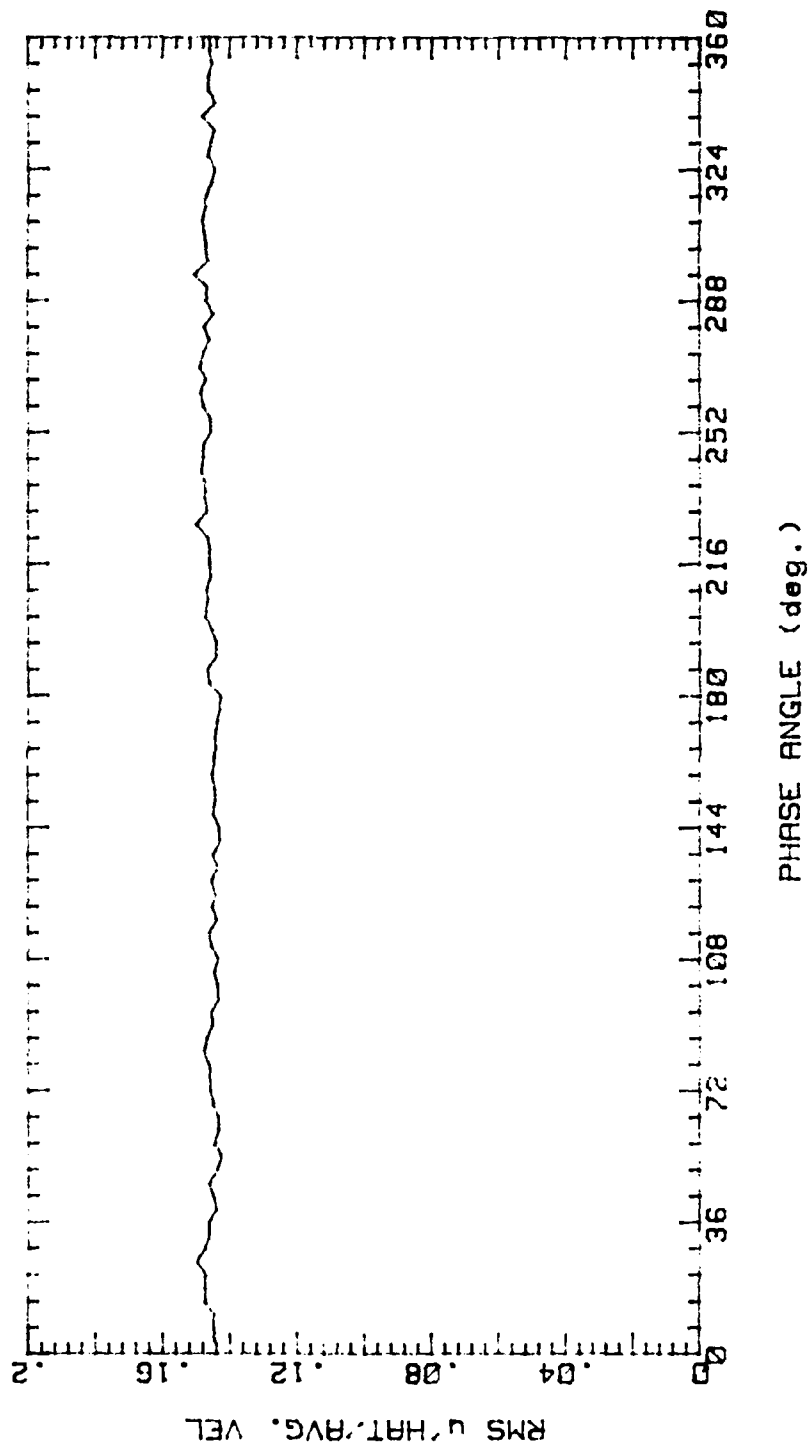


Figure 35.

Mean Velocity Profile Development  
with No Imposed Unsteadiness

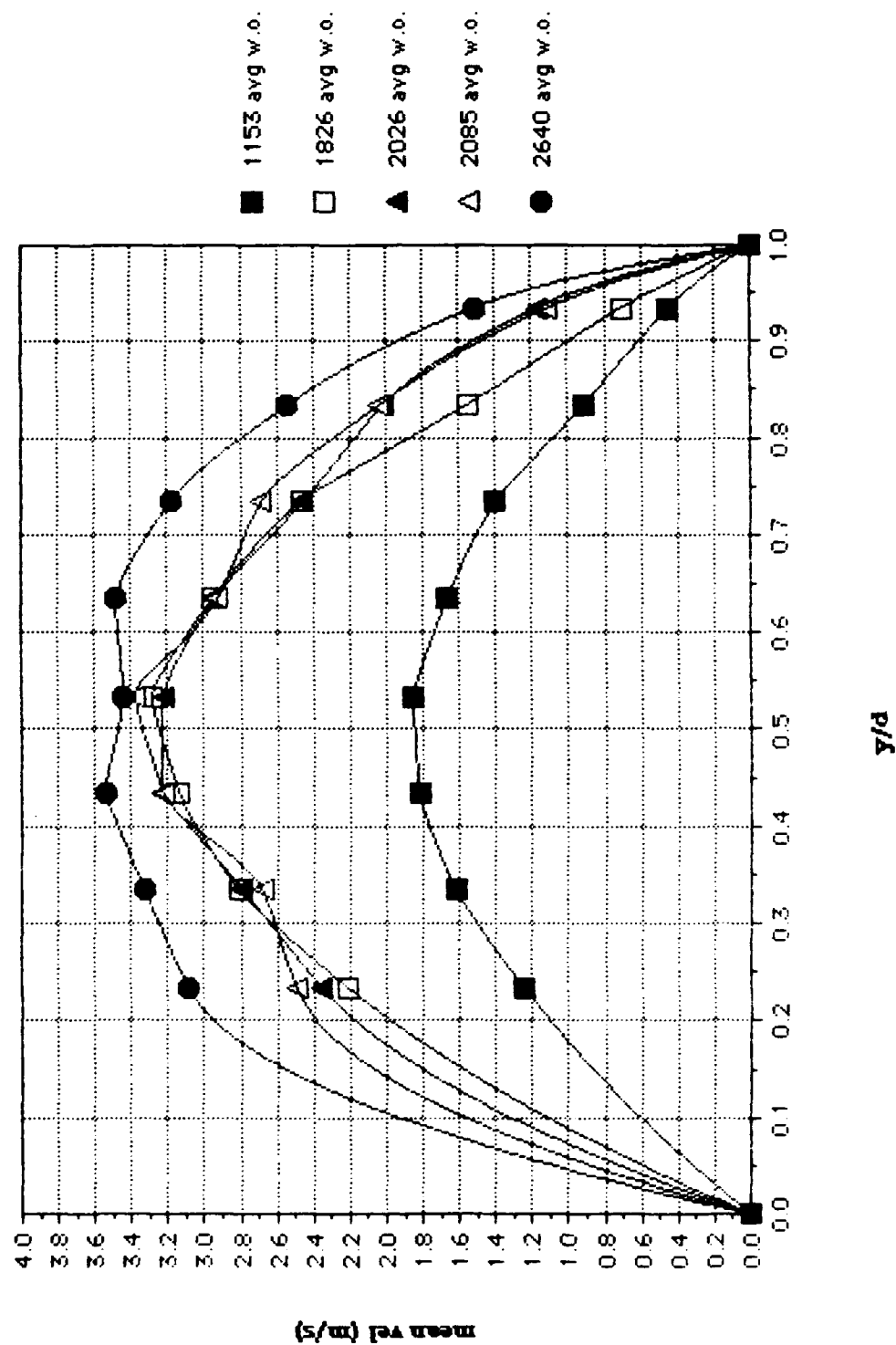


Figure 36.

Mean Velocity Profile Development  
with 1 Hz Imposed Unsteadiness

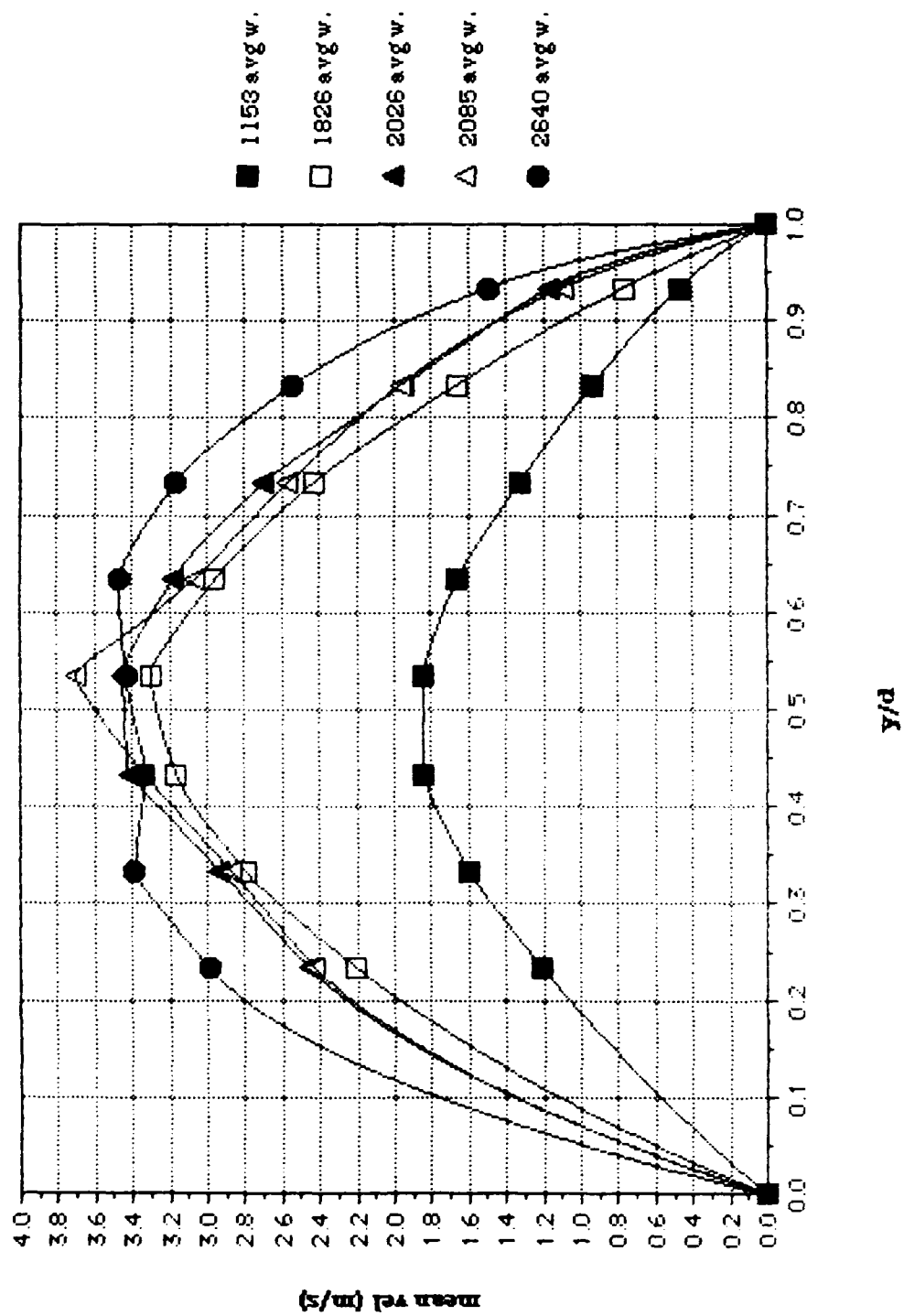


Figure 37.

Mean Velocity Profile at Re No. = 1153  
with 1 Hz Imposed Unsteadiness

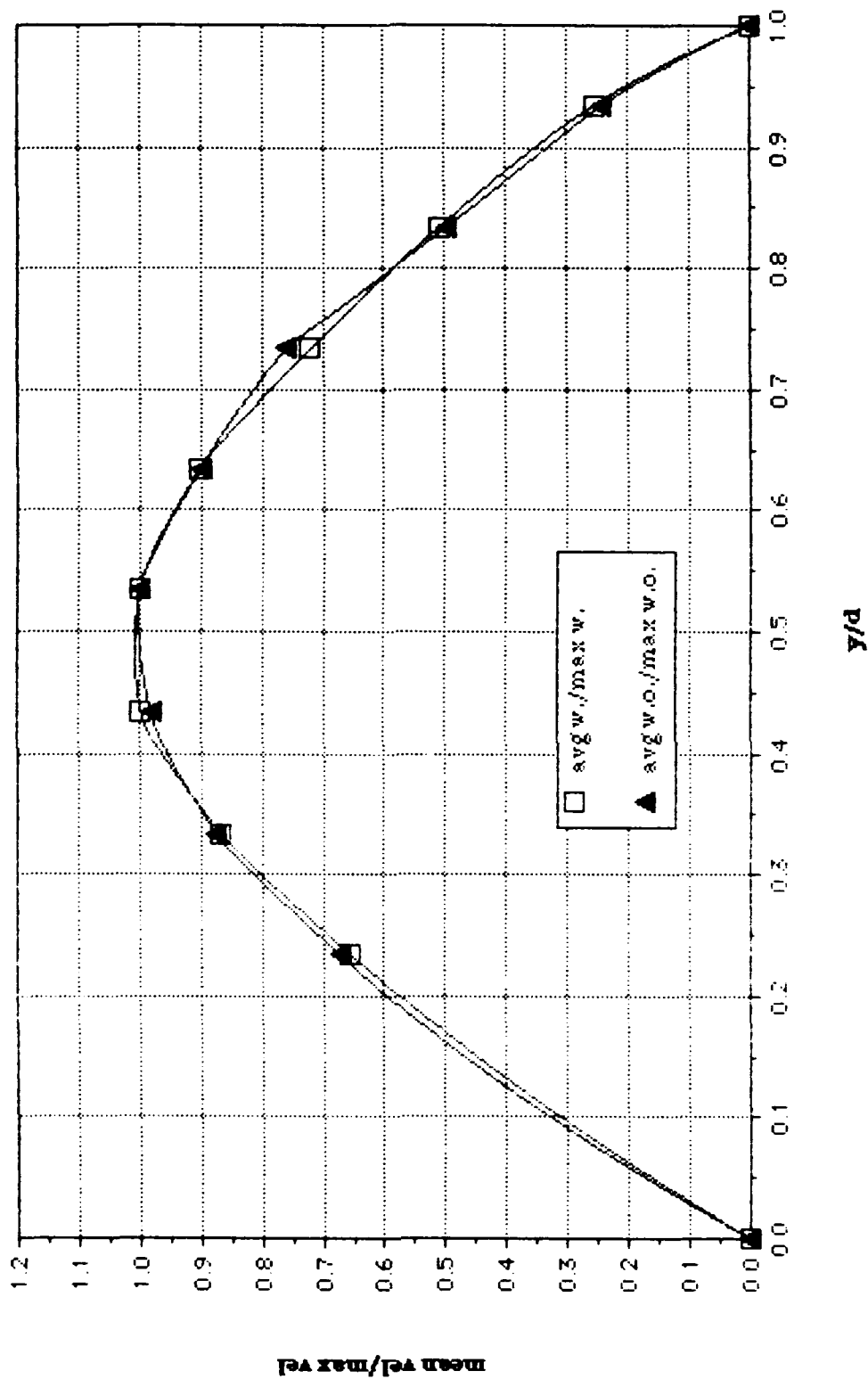


Figure 38.

Mean Velocity Profile at Re No. = 1826  
with 1 Hz Imposed Unsteadiness

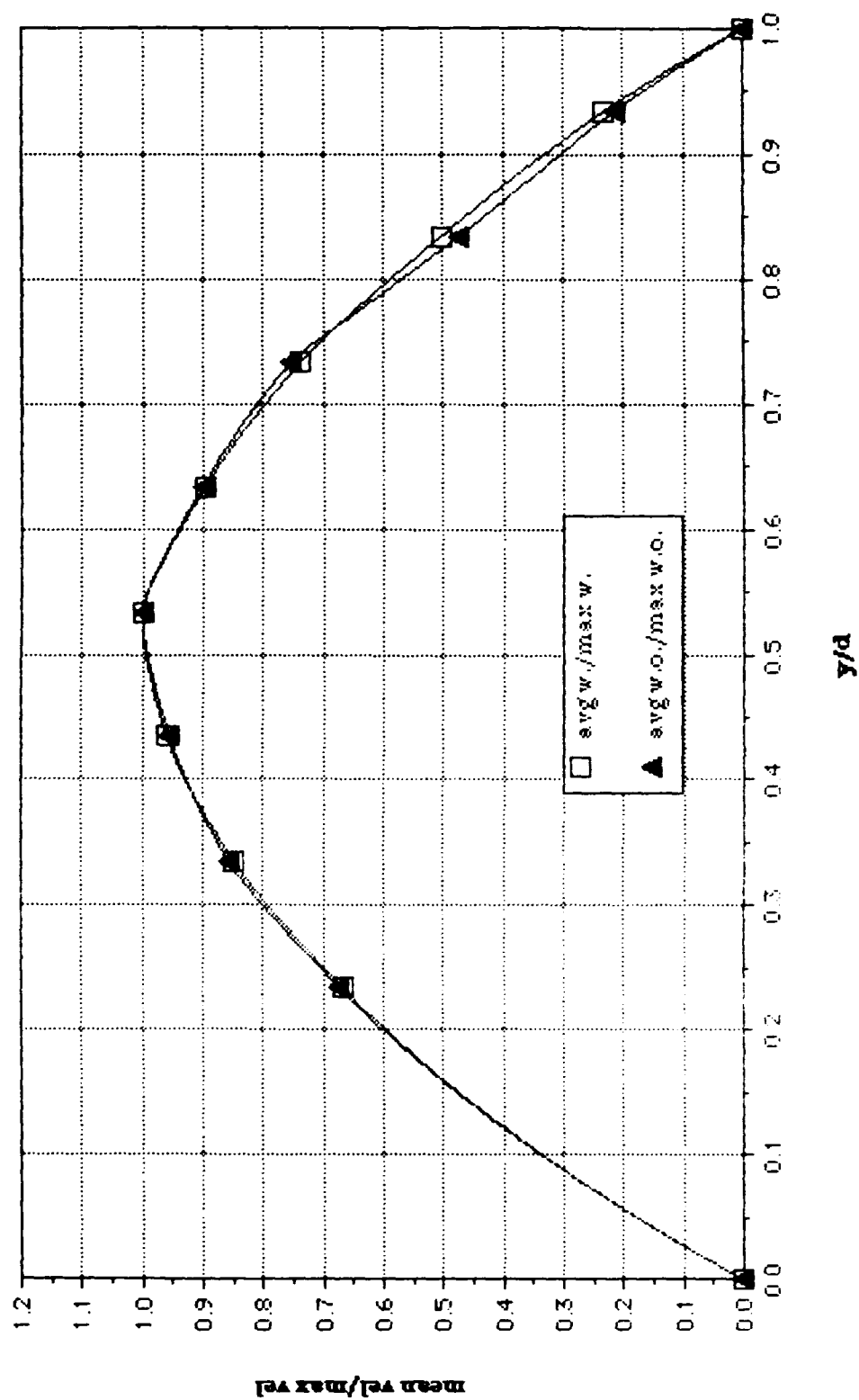


Figure 39.

Mean Velocity Profile at Re No. = 2026  
with 1 Hz Imposed Unsteadiness

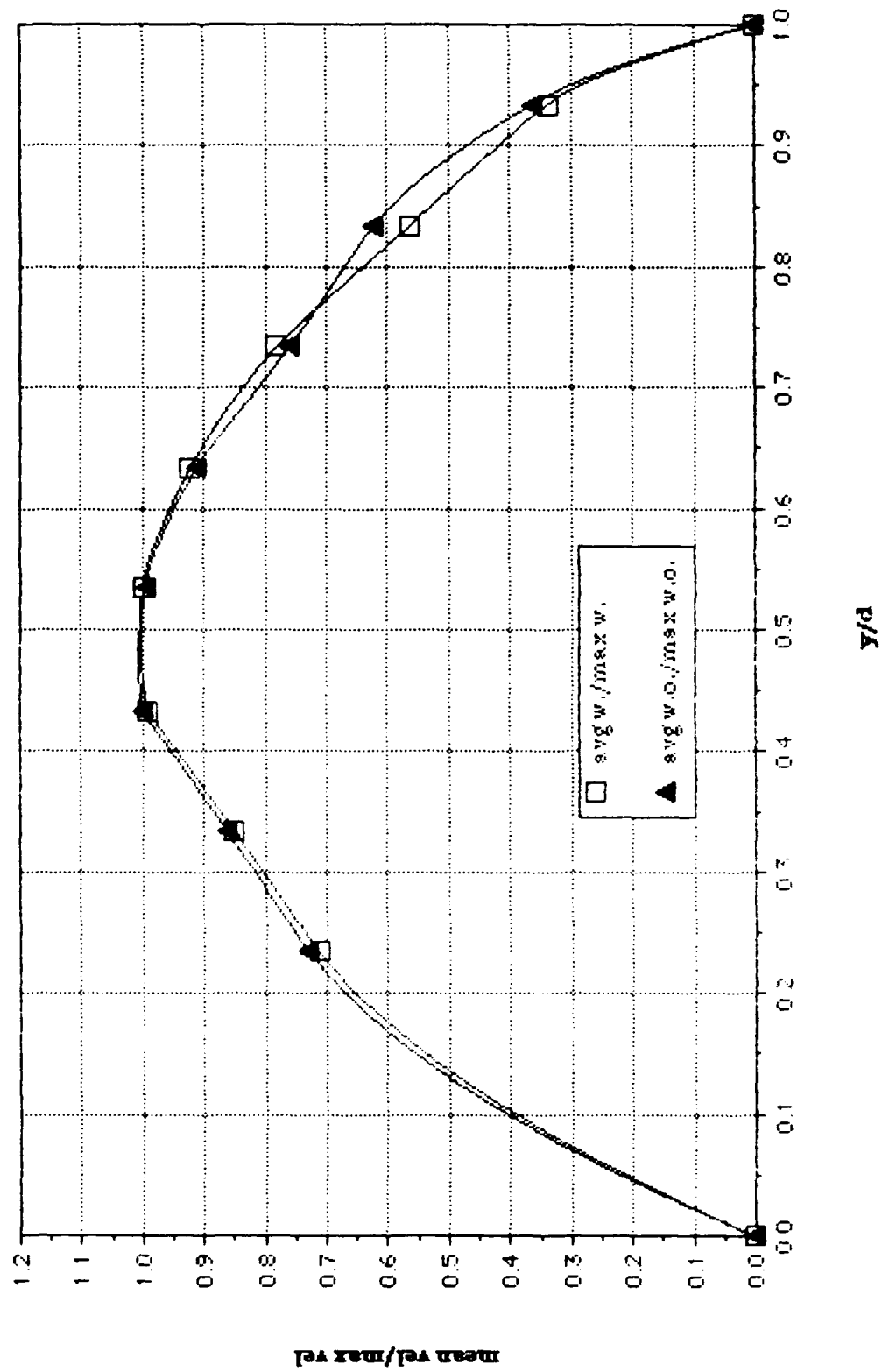


Figure 40.



Mean Velocity Profile at Re No. = 2085  
with 1 Hz Imposed Unsteadiness

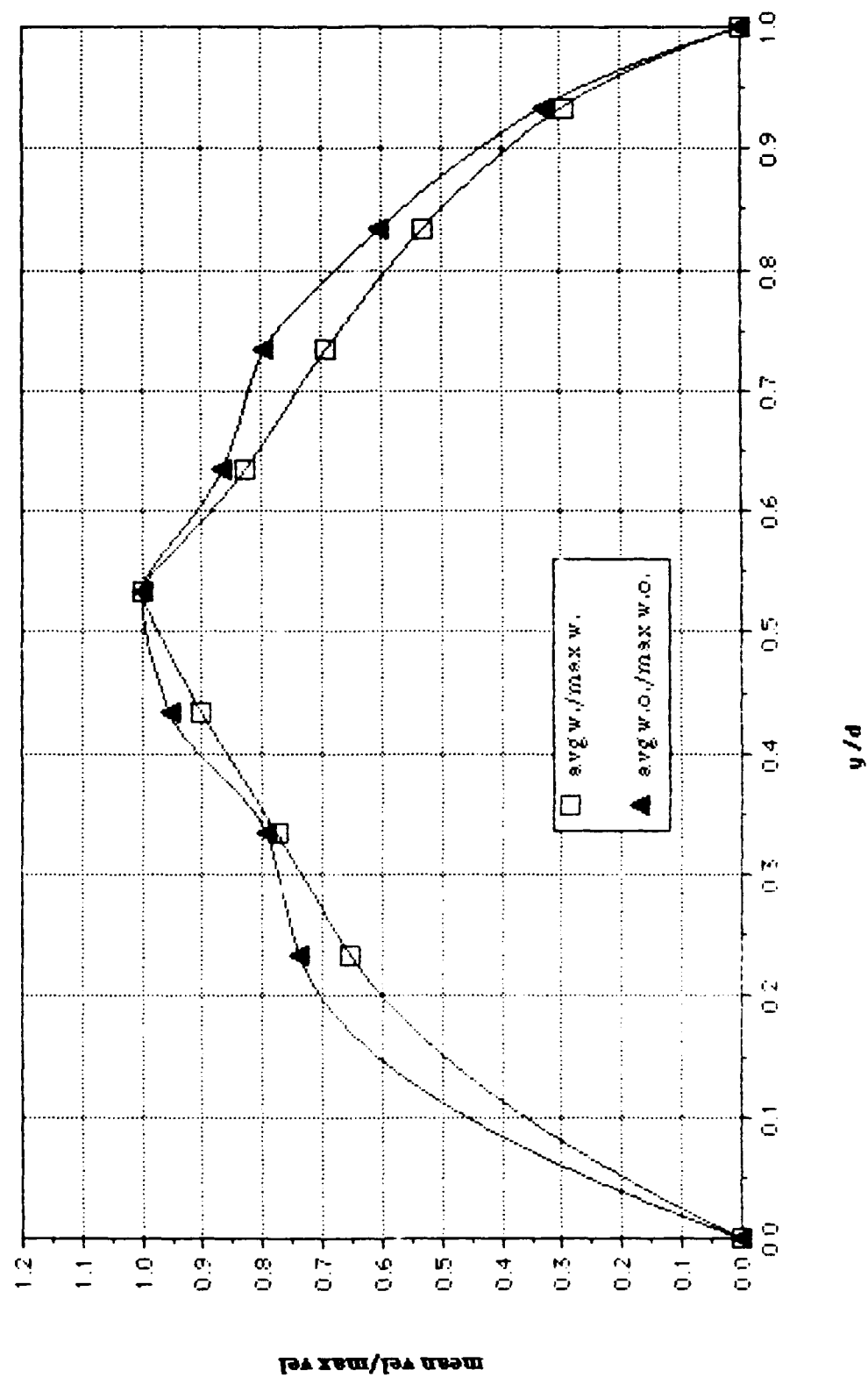


Figure 41.

Mean Velocity Profile at Re No. = 2640  
with 1 Hz Imposed Unsteadiness

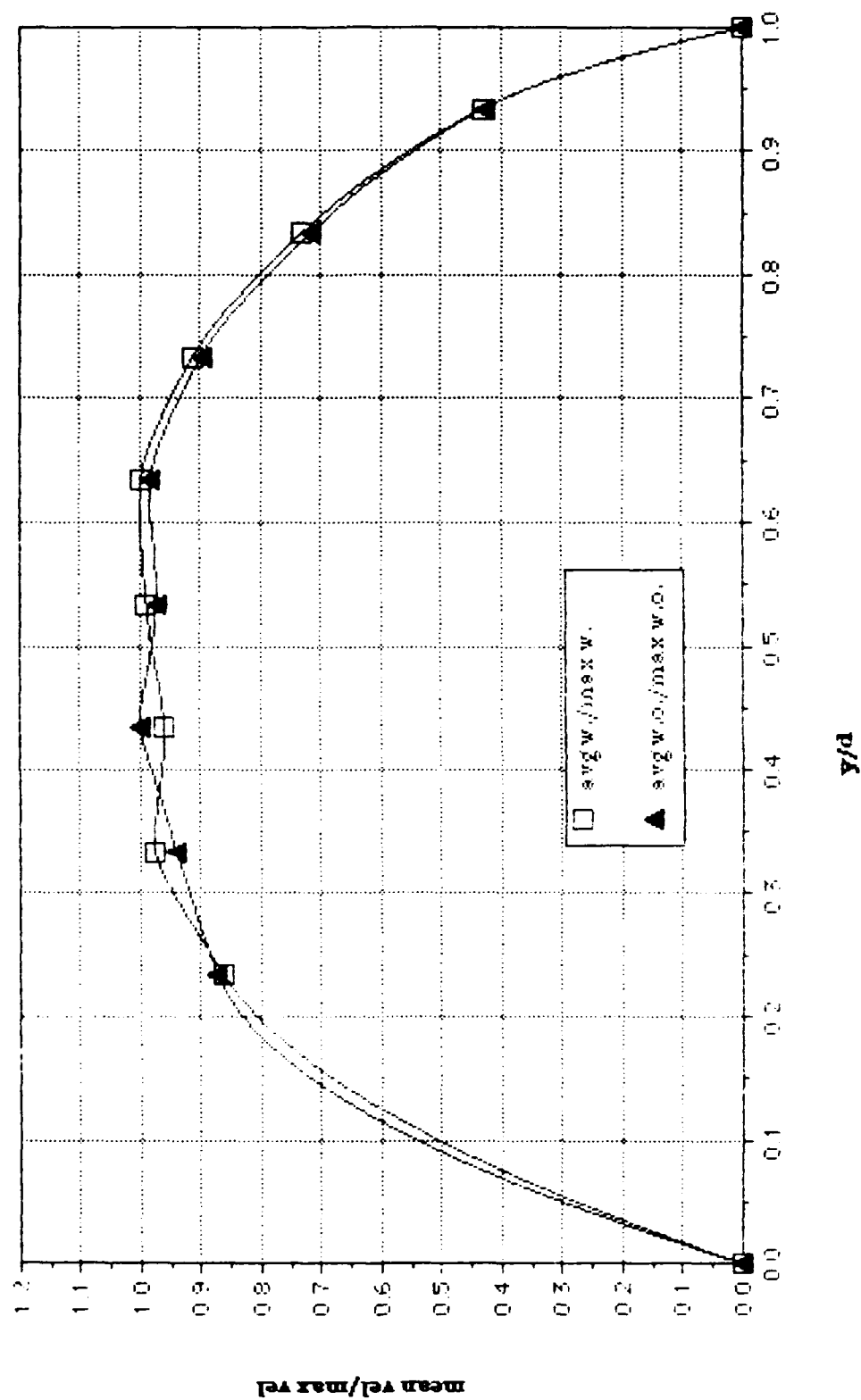


Figure 42.

Peak to Peak Magnitude of Phase Averaged  
Velocity as a Function of  $y/d$

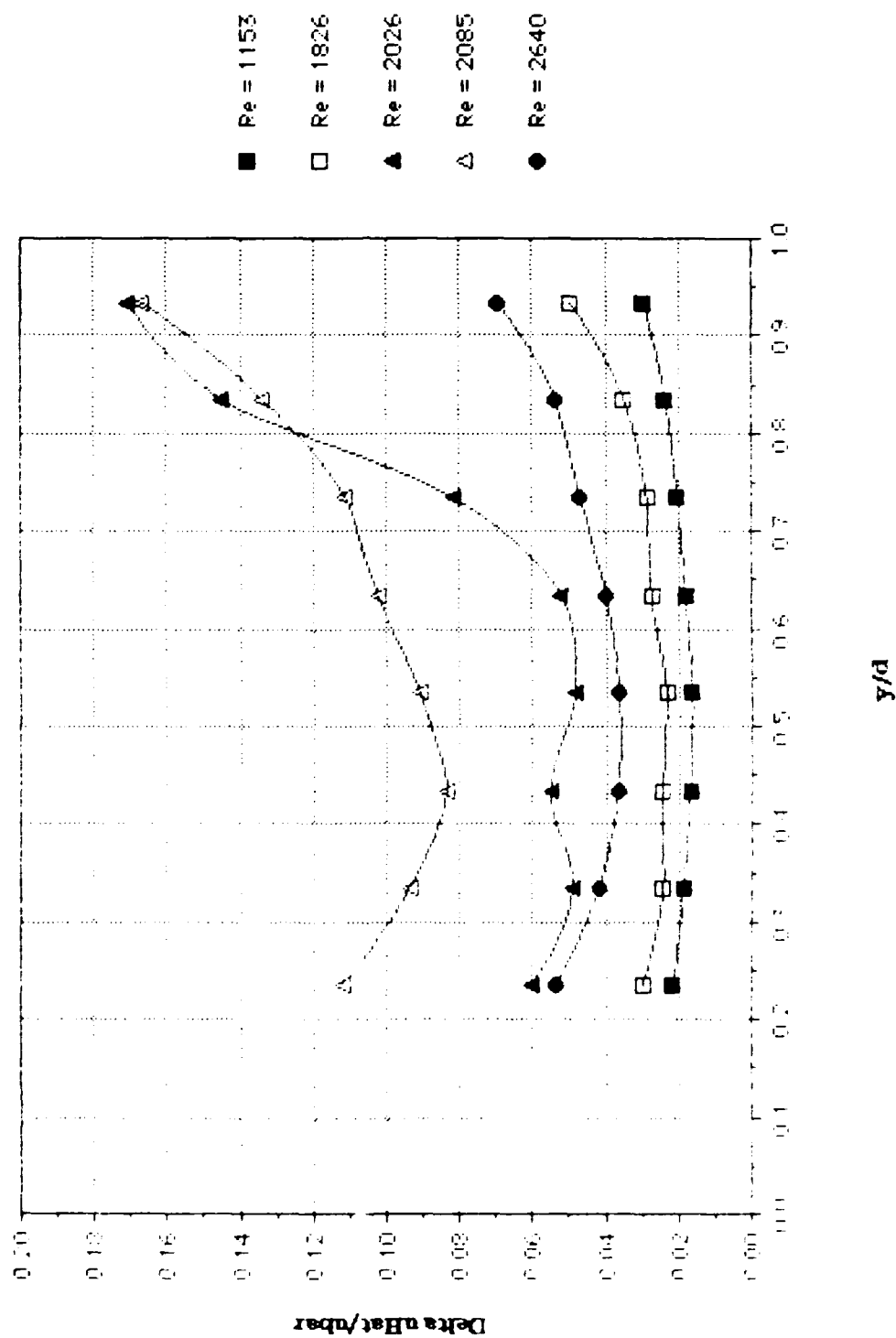


Figure 43.

RUNP1W 280989.2015  
 AVG. VEL. .7033m/s RMS VEL .04045m/s  
 OSC. FREQ. 0Hz STR. # 0  
 BULK VEL. 2.185m/s REY. # 1826

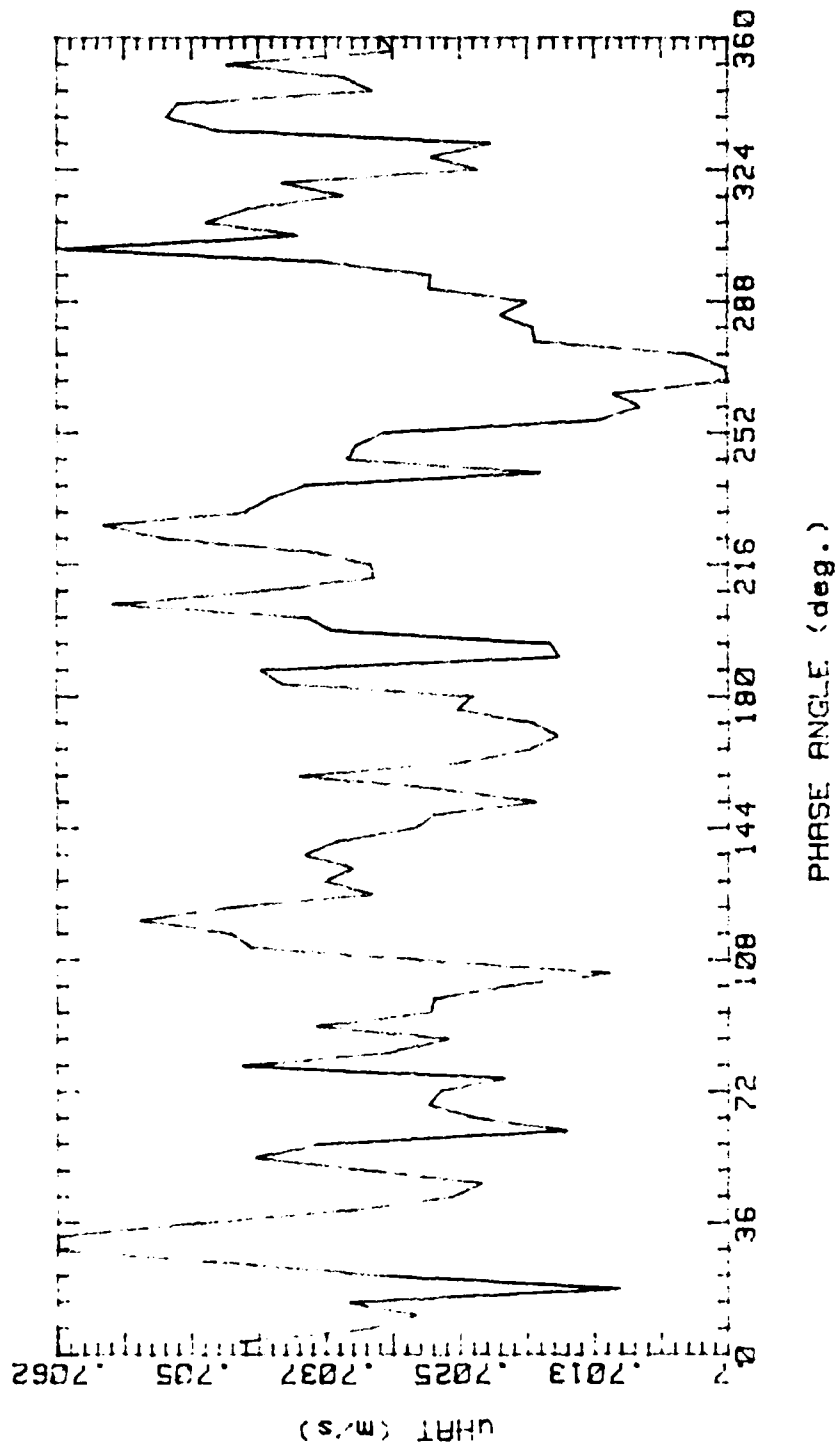


Figure 44.

RUNP1X 280989.2219

AVG. VEL .2632m/s RMS VEL .04593m/s  
OSC. FREQ. 1Hz STR. # .03652  
BULK VEL. 2.185m/s REY. # 1826

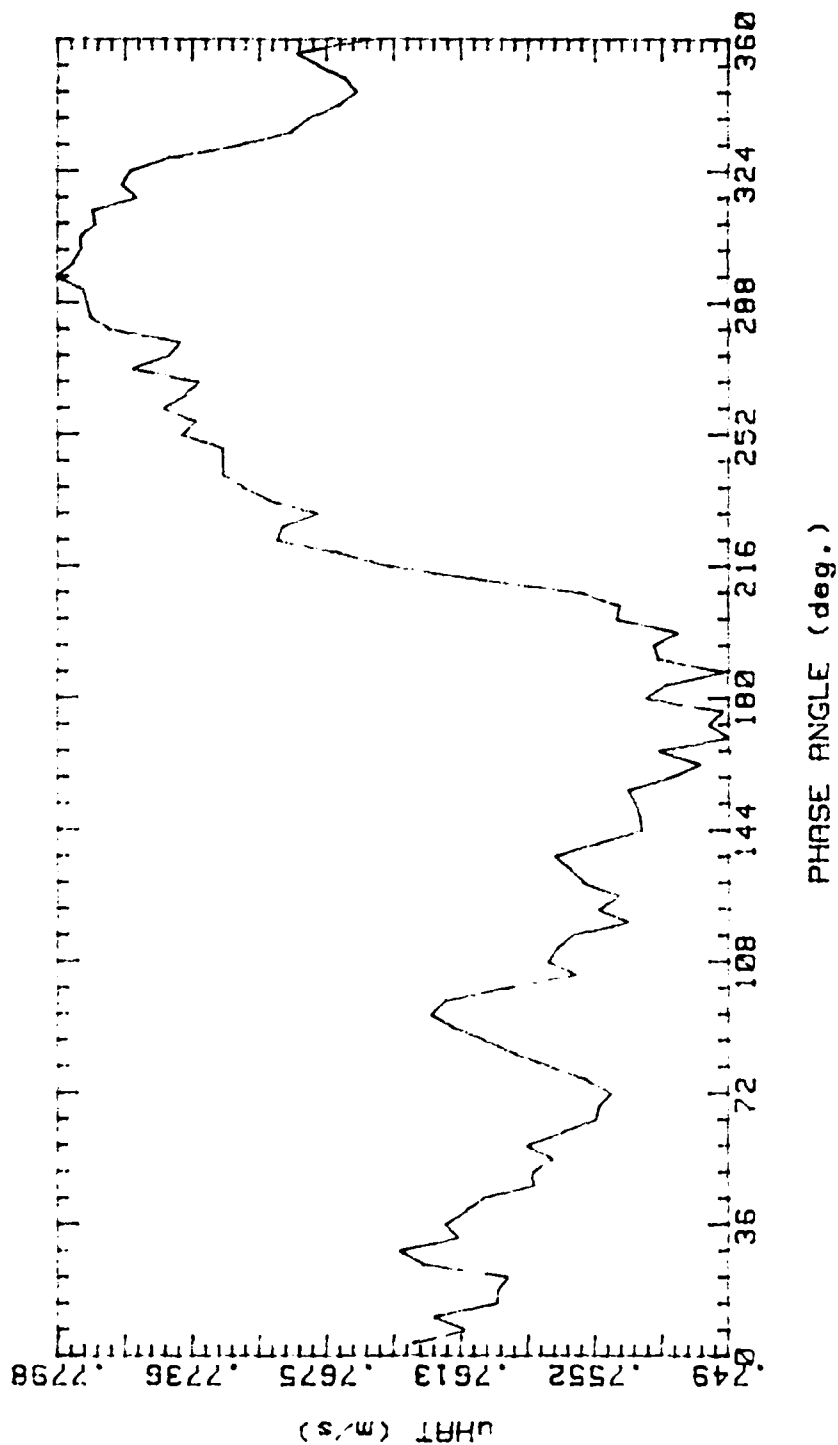


Figure 45.

RUNP2W 280989.2028

AVG. VEL 1.554m/s RMS VEL .09169m/s

OSC. FREQ. QHZ STR. # 0

BULK VEL. 2.185m/s REY. # 1826

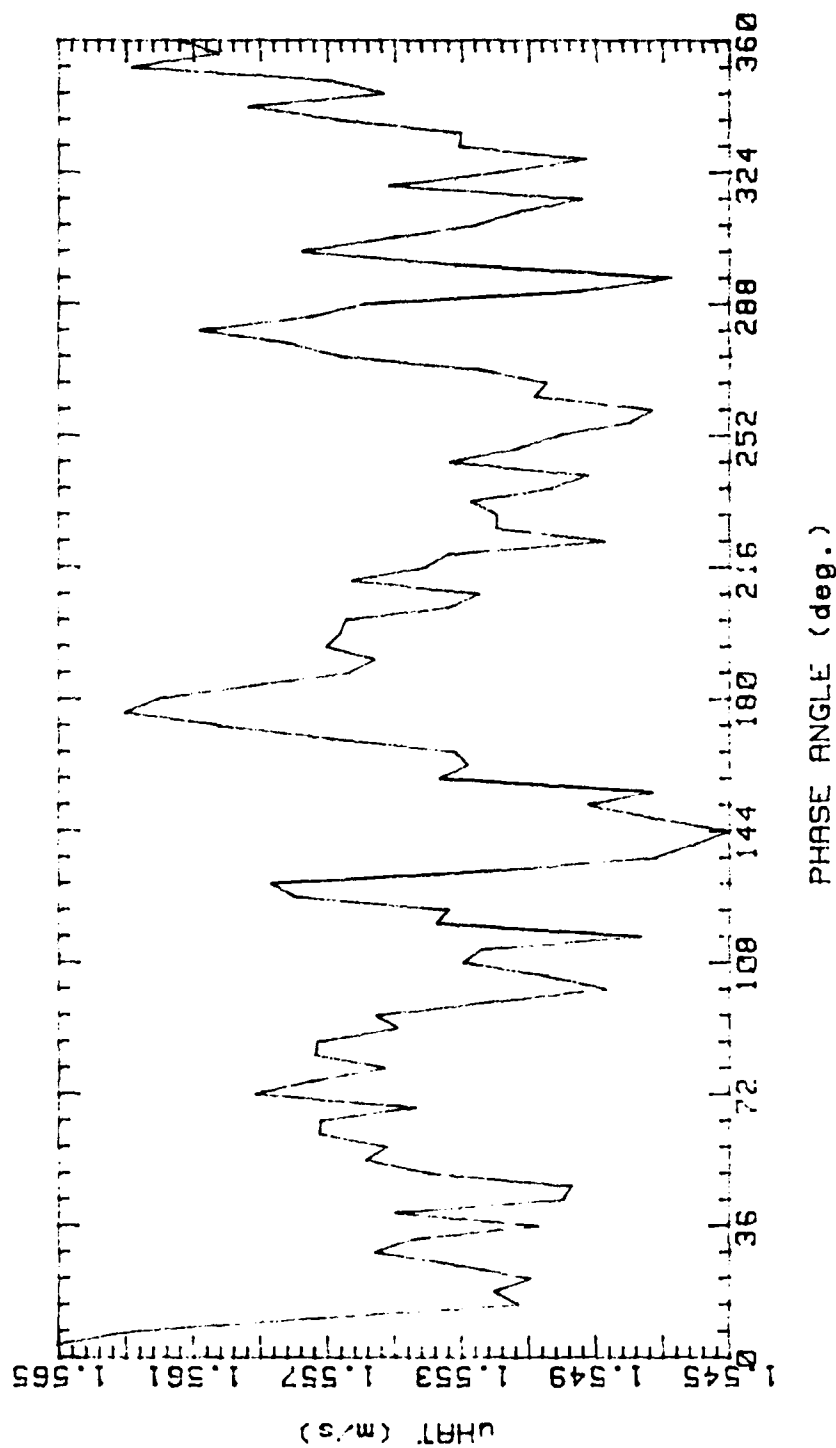


Figure 46.

RUNP2X 280989.2234

AVG. VEL 1.66m/s RMS VEL .0985m/s  
OSC. FREQ. 1Hz STR. # .03652  
BULK VEL. 2.185m/s REY. # 1826

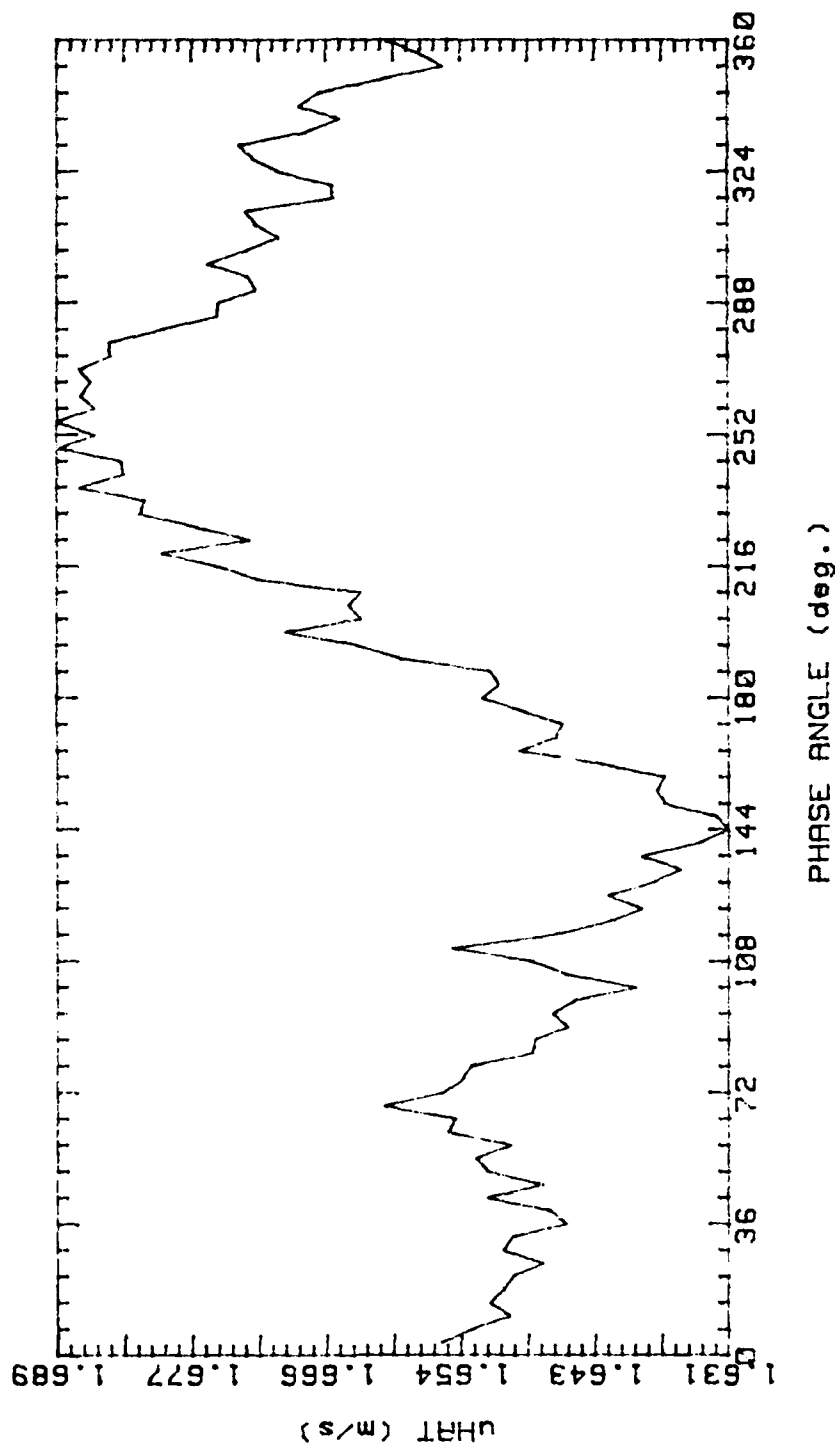


Figure 47.

RUNP3W 280989.2045  
 AVG. VEL 2.47m/s RMS VEL .09151m/s  
 OSC. FREQ. 0Hz STR. # 0  
 BULK VEL. 2.185m/s REY. # 1826

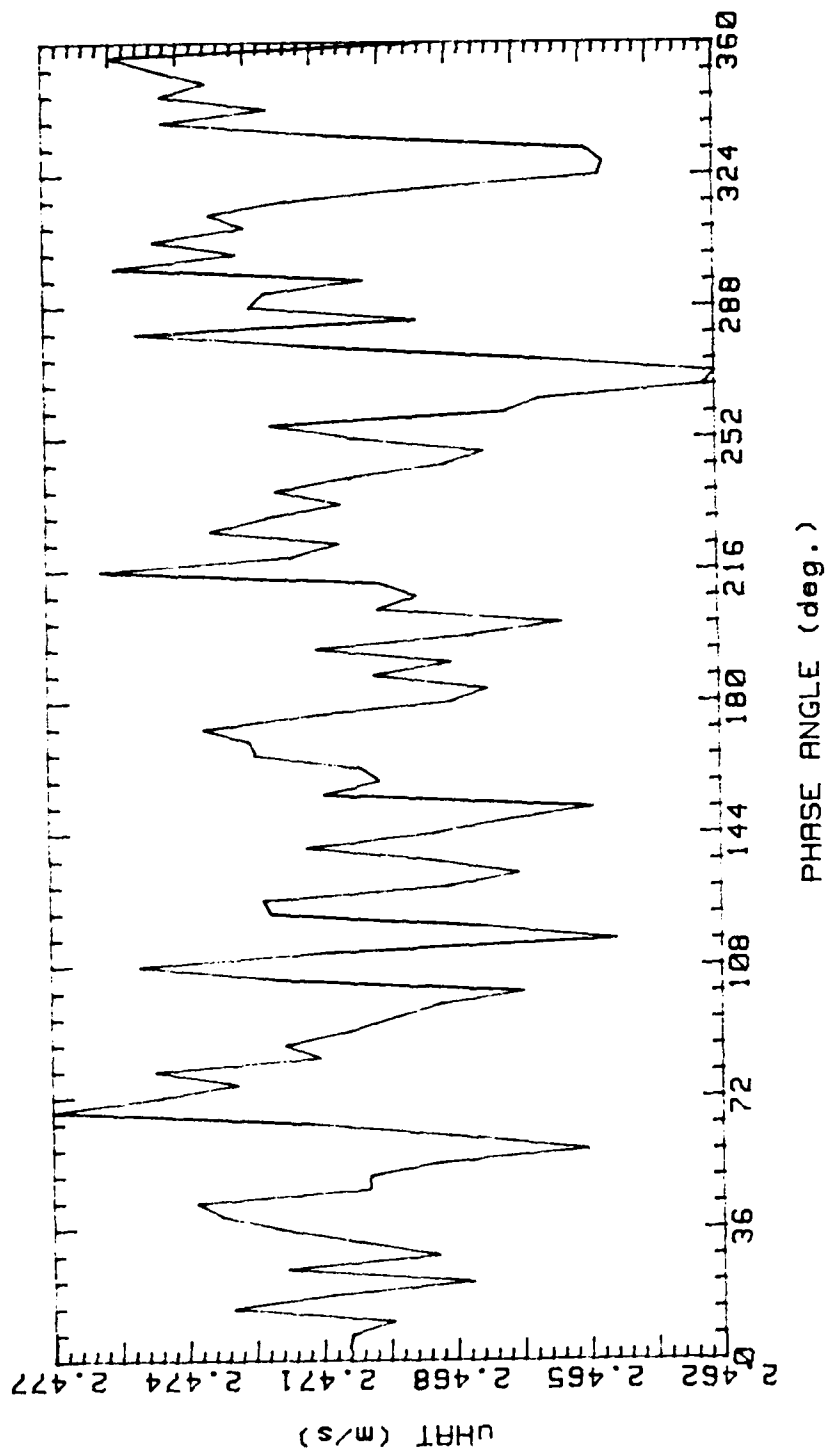


Figure 48.



RUNP3X 280989.2248

AVG. VEL 2.431m/s RMS VEL .09303m/s  
OSC. FREQ. 1Hz STR. # .03652  
BULK VEL. 2.185m/s REY. # 1826

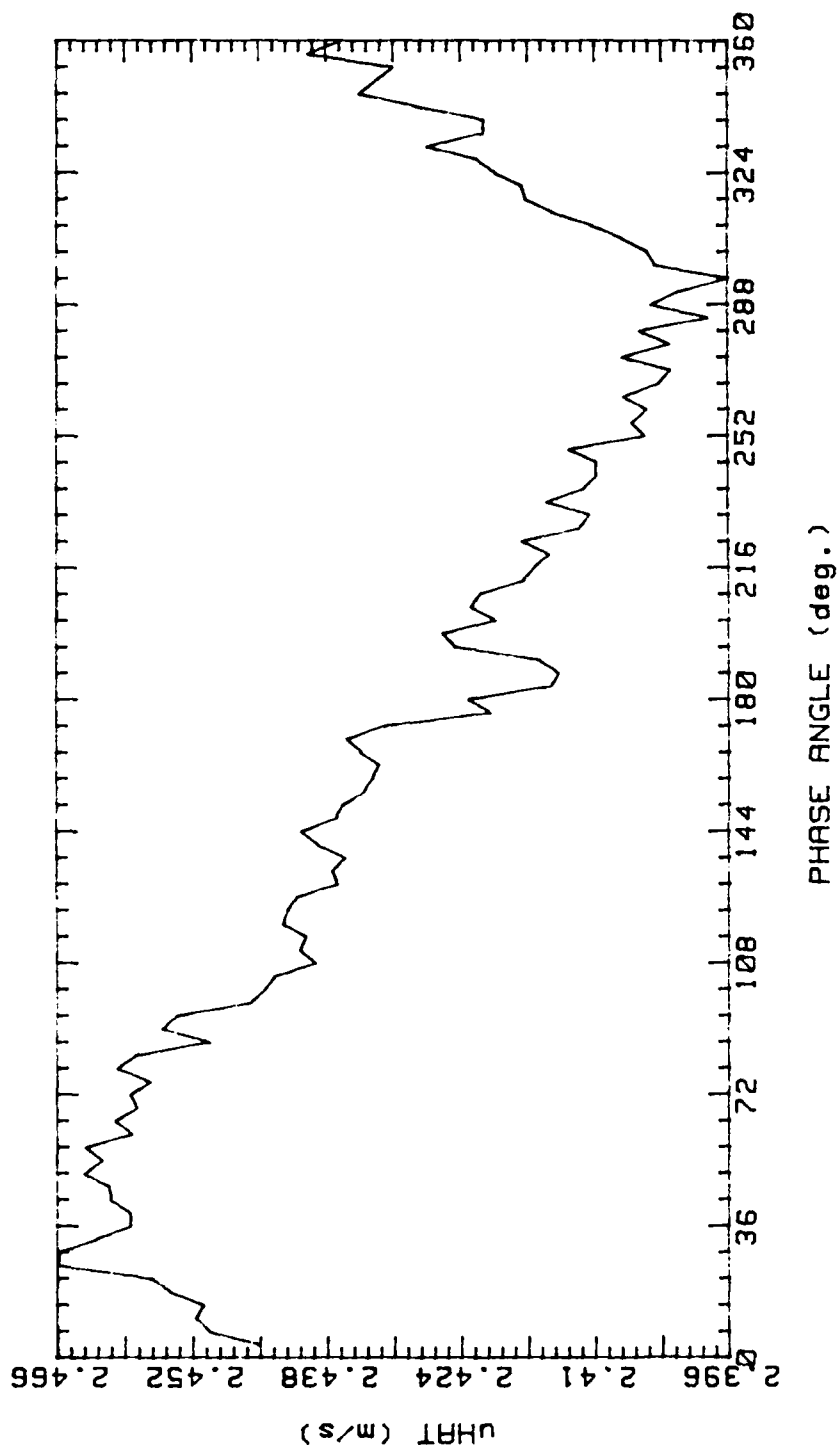


Figure 49.

RUNP4W 280989.2102

AVG. VEL 2.957m/s RMS VEL .1059m/s

OSC. FREQ. 0Hz STR. # 0

BULK VEL. 2.185m/s REY. # 1826

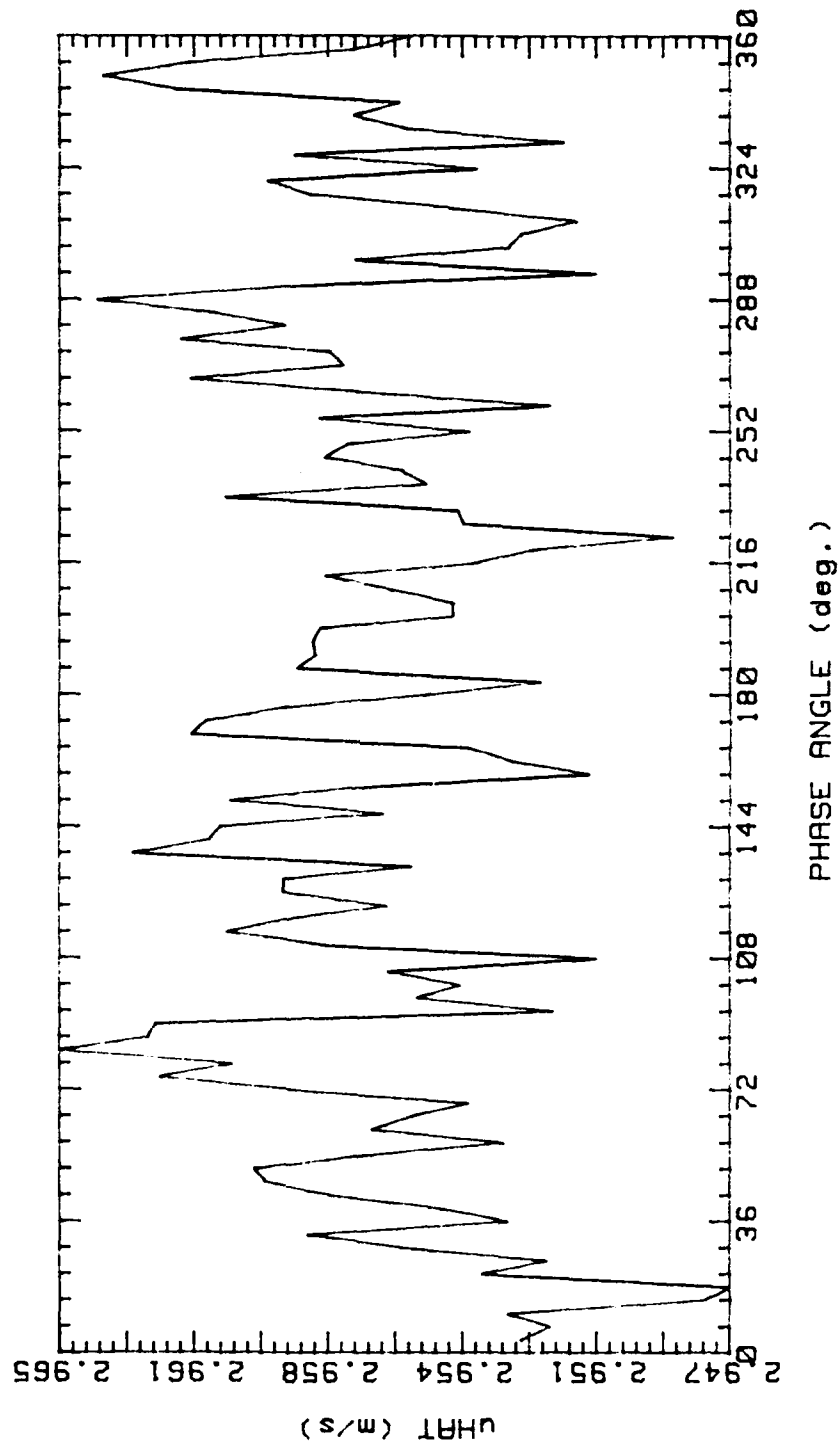


Figure 50.

RUNP4X 280989.2301

AVG. VEL 2.958m/s RMS VEL .1142m/s  
OSC. FREQ. 1Hz STR. # .03652  
BULK VEL. 2.185m/s REY. # 1826

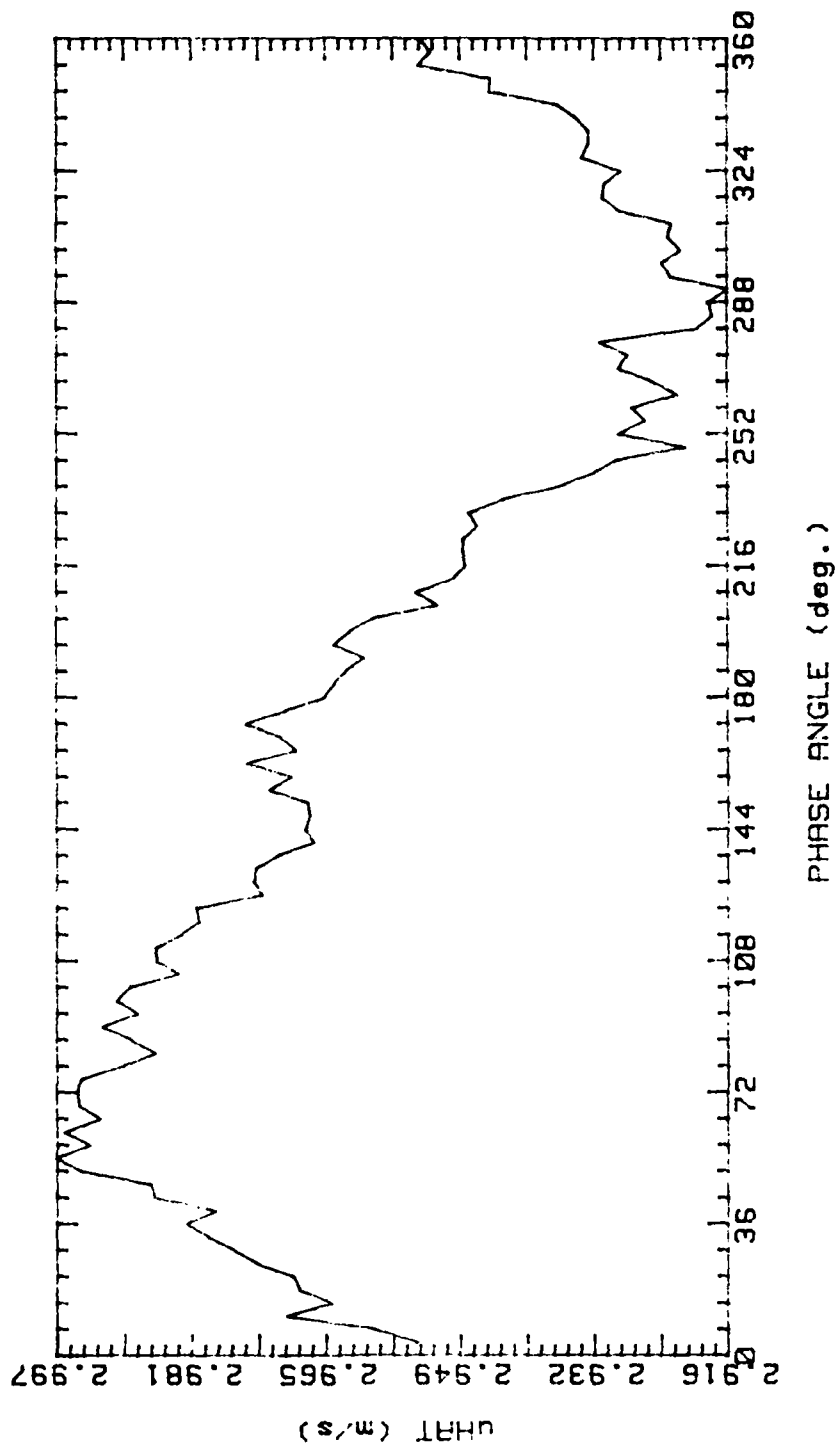


Figure 51.

RUNP5W 280989.2116

AVG. VEL 3.284m/s RMS VEL .1252m/s  
OSC. FREQ. 0Hz STR. # 0  
BULK VEL. 2.185m/s REY. # 1826

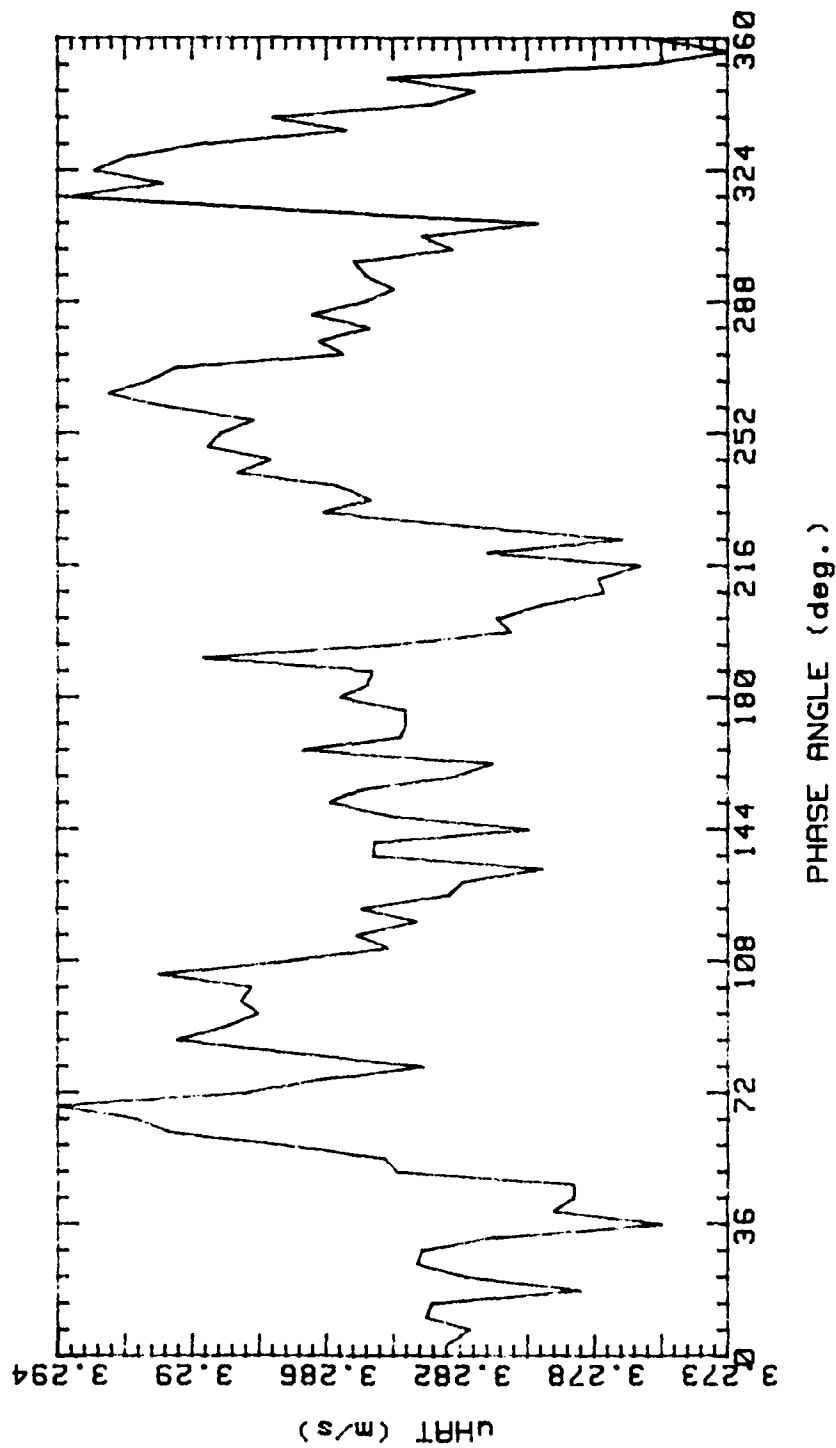


Figure 52.

RUNP5X 280989.2315

AVG. VEL 3.302m/s RMS VEL .1376m/s  
OSC. FREQ. 1Hz STR. # .03652  
BULK VEL. 2.185m/s REY. # 1826

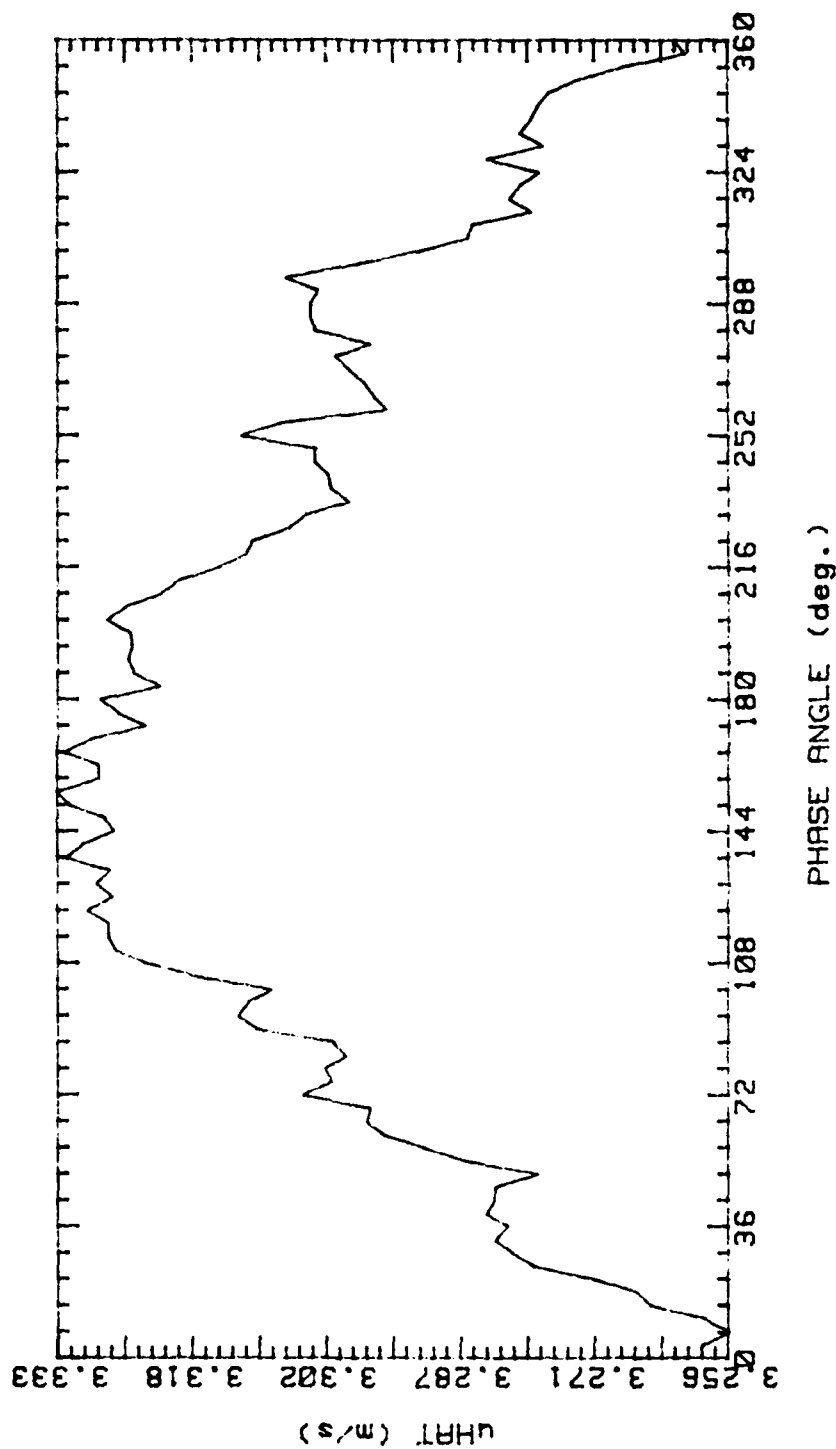


Figure 53.

RUNP6W 280989.2133

AVG. VEL 3.134m/s RMS VEL .1216m/s  
OSC. FREQ. 0Hz STR. # 0  
BULK VEL. 2.185m/s REY. # 1826

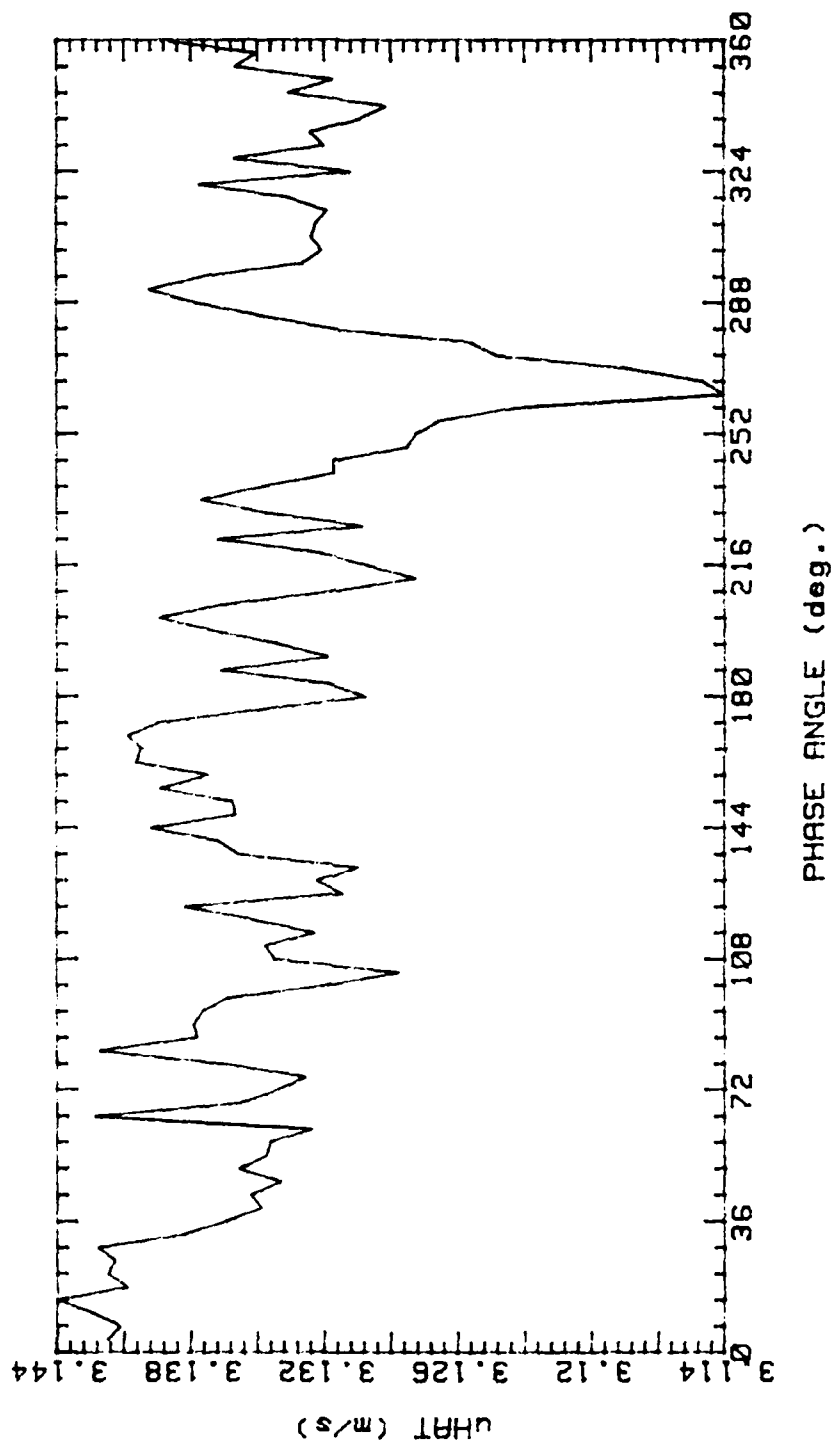


Figure 54.

RUNP6X 280989.2329

AVG. VEL 3.168m/s RMS VEL .1248m/s  
OSC. FREQ. 1Hz STR. # .03652  
BULK VEL. 2.185m/s REY. # 1826

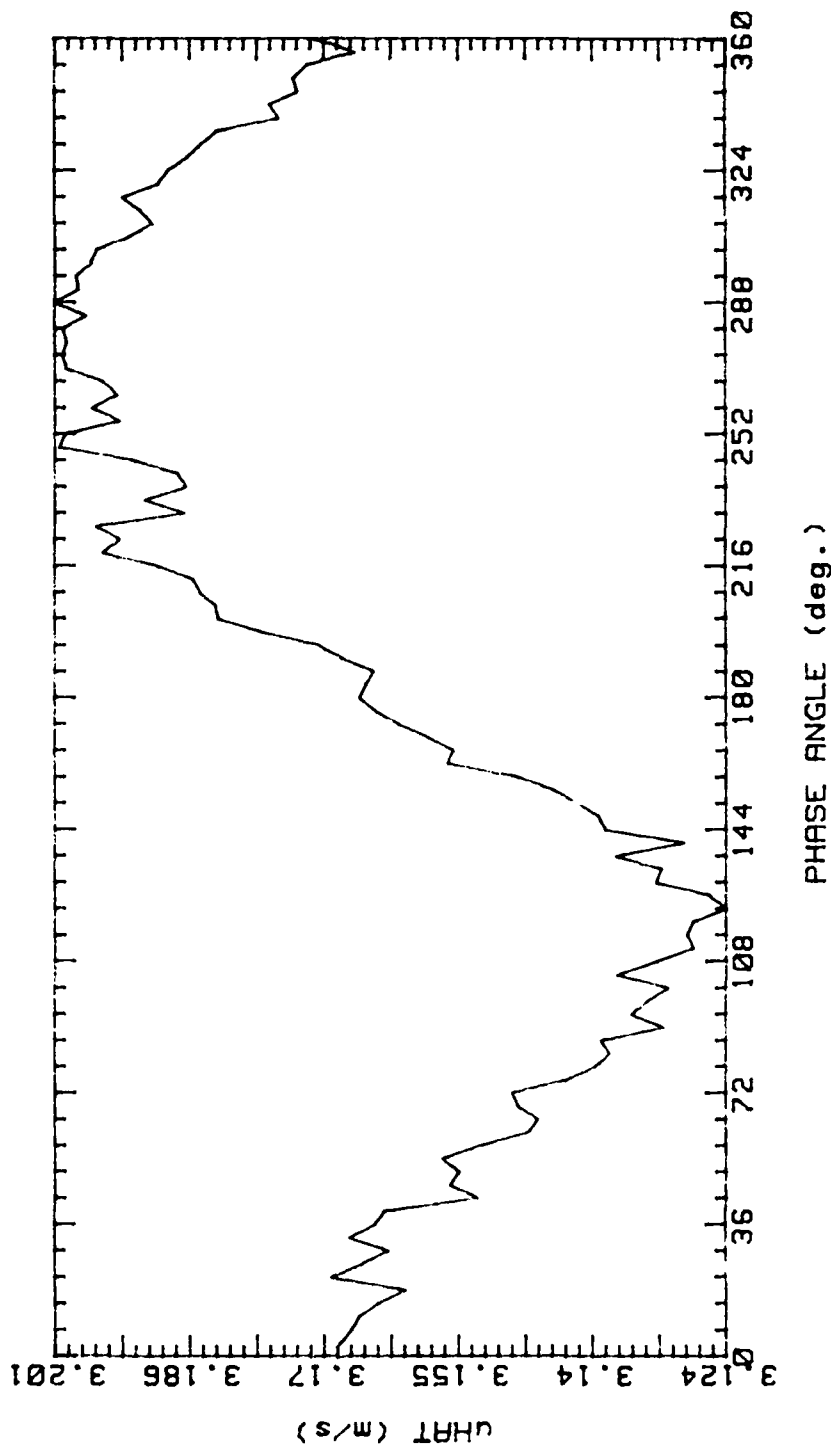


Figure 55.

RUNP7W 280989.2147  
 AVG. VEL 2.811m/s RMS VEL .09981m/s  
 OSC. FREQ. 0Hz STR. # 0  
 BULK VEL. 2.185m/s REY. # 1826

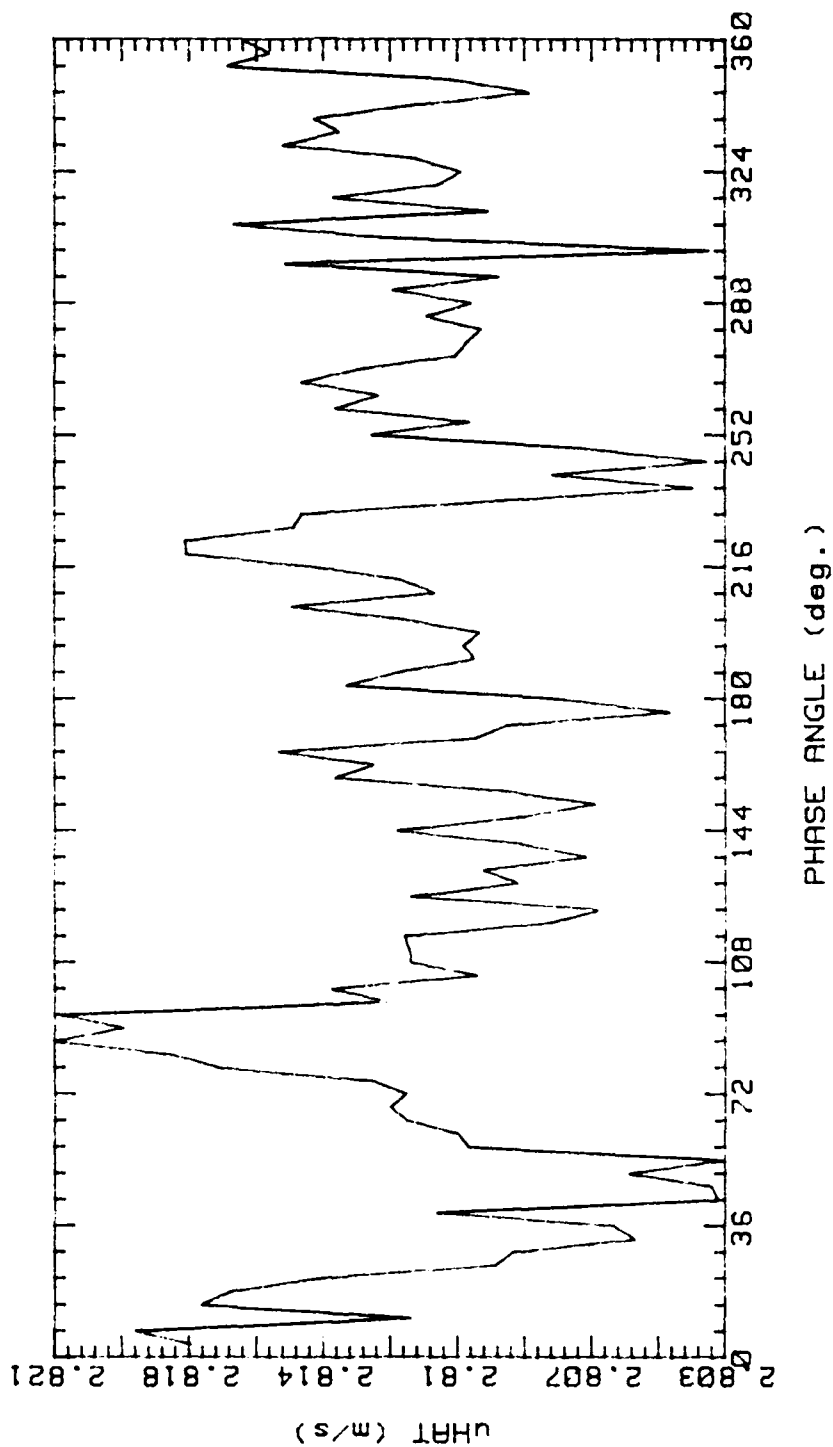


Figure 56.



RUNP7X 280989.2342

AVG. VEL 2.798m/s RMS VEL .1003m/s  
OSC. FREQ. 1Hz STR. # .03652  
BULK VEL. 2.185m/s REY. # 1826

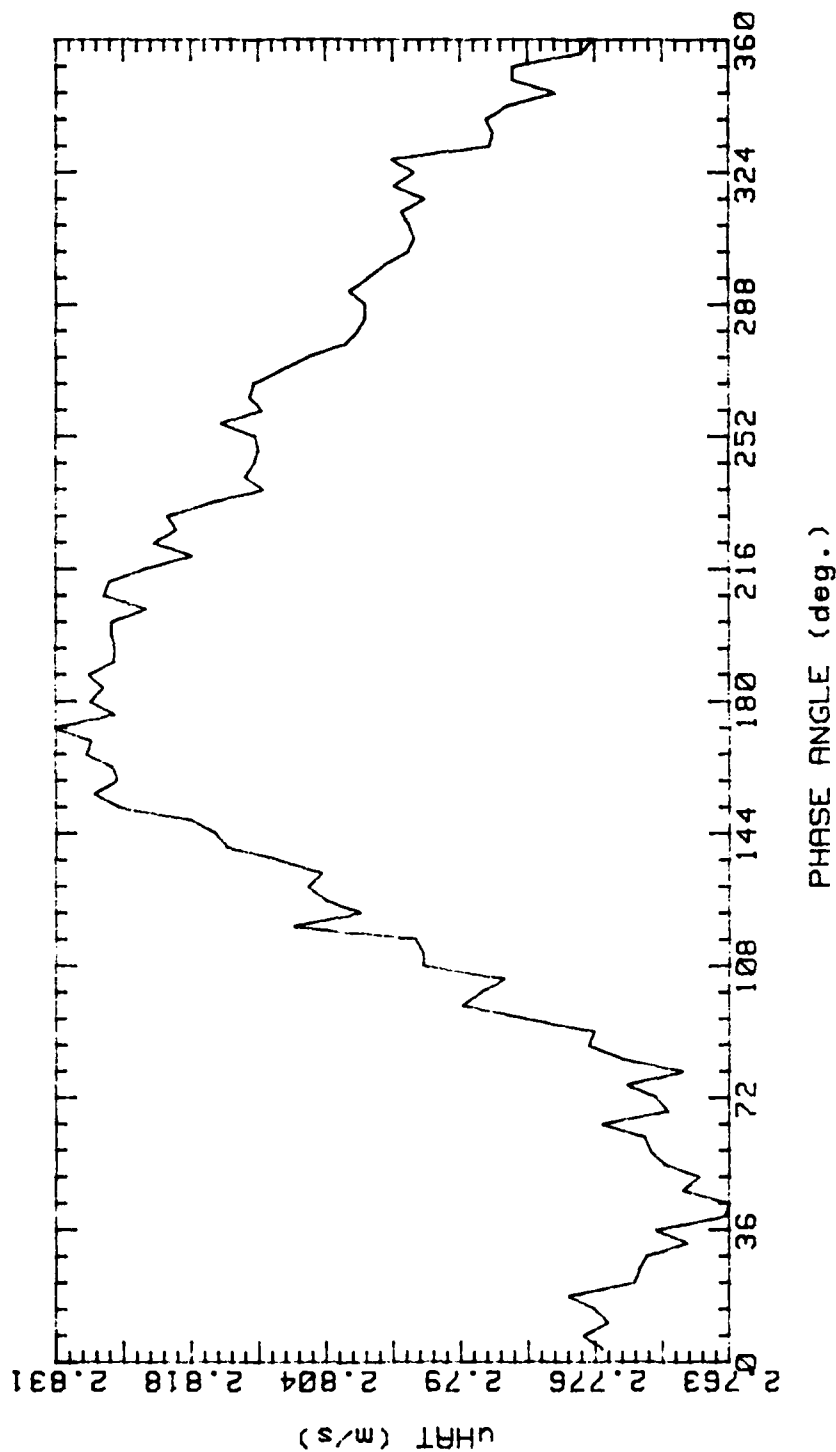


Figure 57.

RUNP8W 280989.2202

AVG. VEL 2.211m/s RMS VEL .09376m/s

OSC. FREQ. 0Hz STR. # 0

BULK VEL. 2.185m/s REY. # 1826

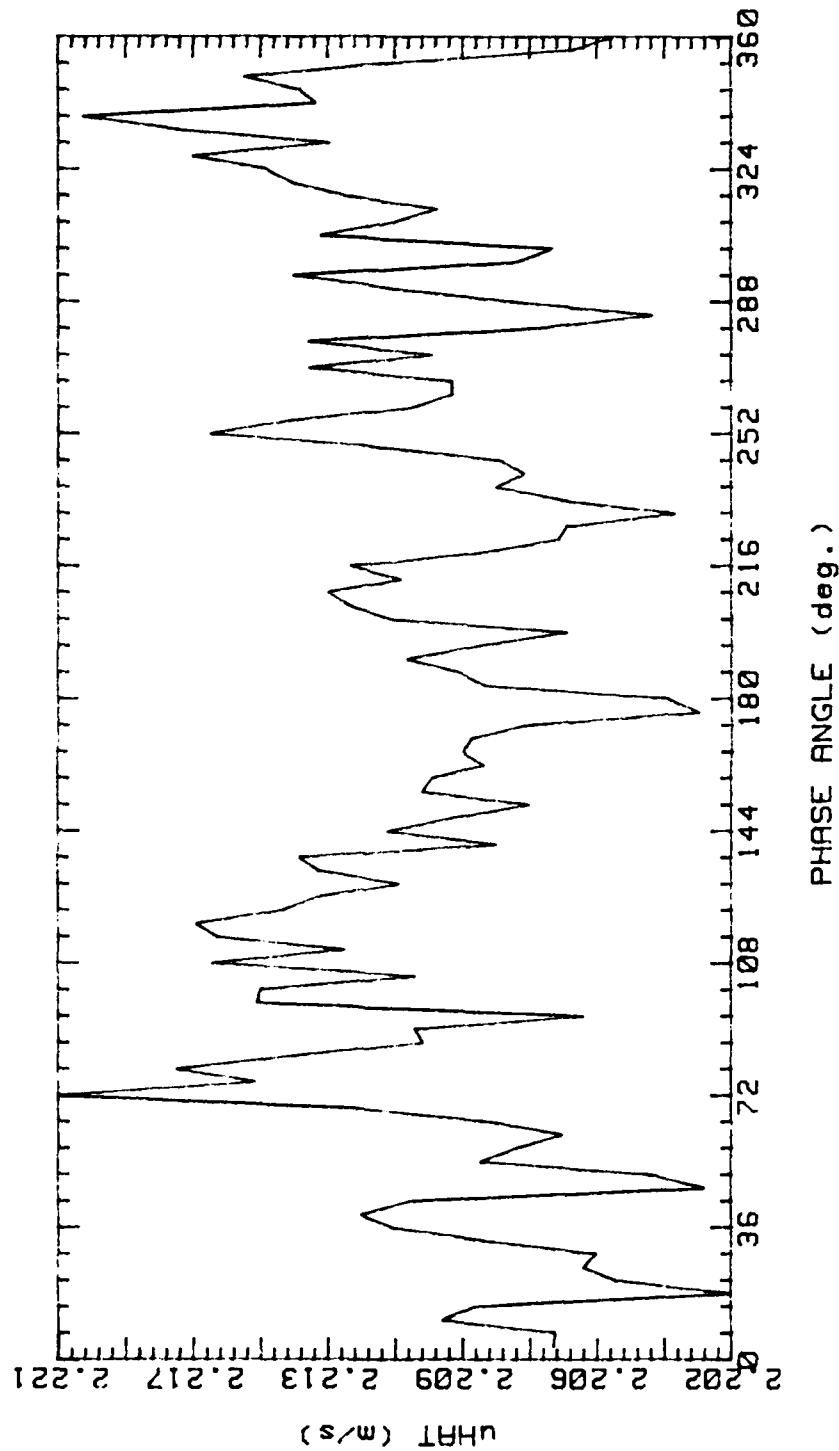


Figure 58.

RUNP8X 280989.2355

AVG. VEL 2.204m/s RMS VEL .09281m/s  
OSC. FREQ. 1Hz STR. # .03652  
BULK VEL. 2.185m/s REY. # 1826

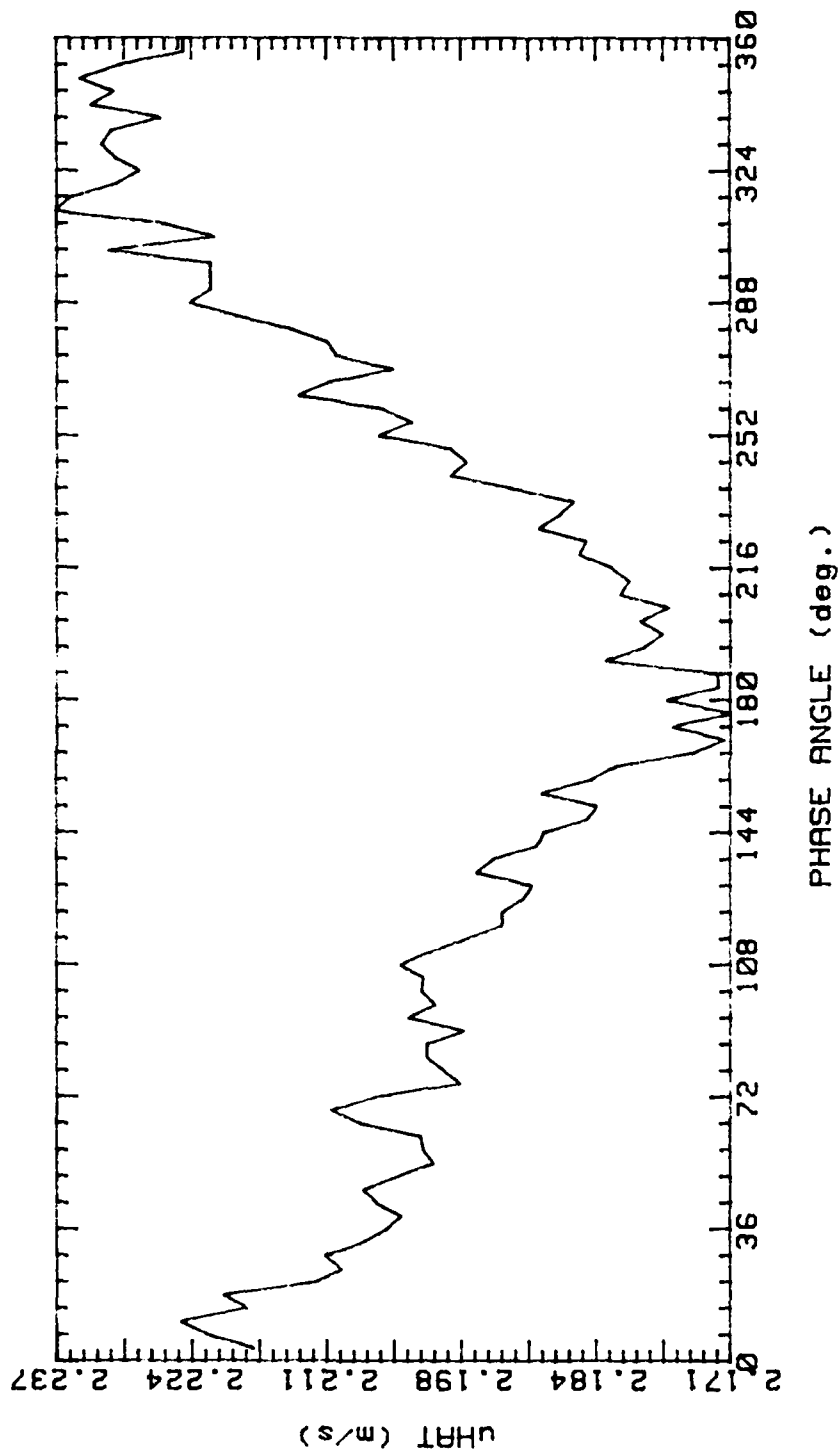


Figure 59.

RUNP1Y 93089.1215

AVG. VEL 1.11m/s RMS VEL .1613m/s

OSC. FREQ. 0Hz STR. # 0

BULK VEL. 2.495m/s REY. # 2085

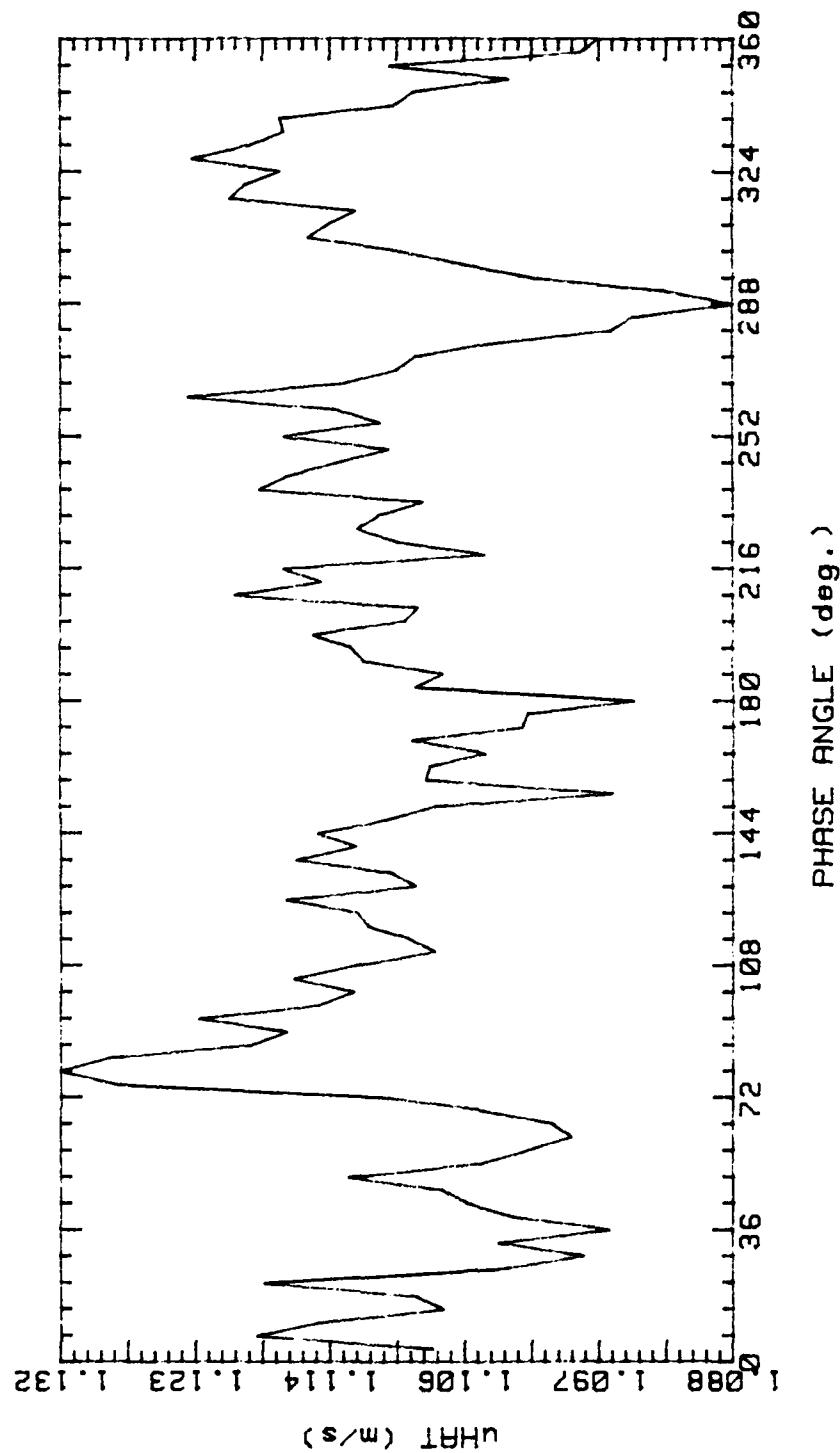


Figure 60.

RUNP1Z 93089.1415

AVG. VEL 1.096m/s RMS VEL .2192m/s

OSC. FREQ. 1Hz STR. # .03198

BULK VEL. 2.495m/s REY. # 2085

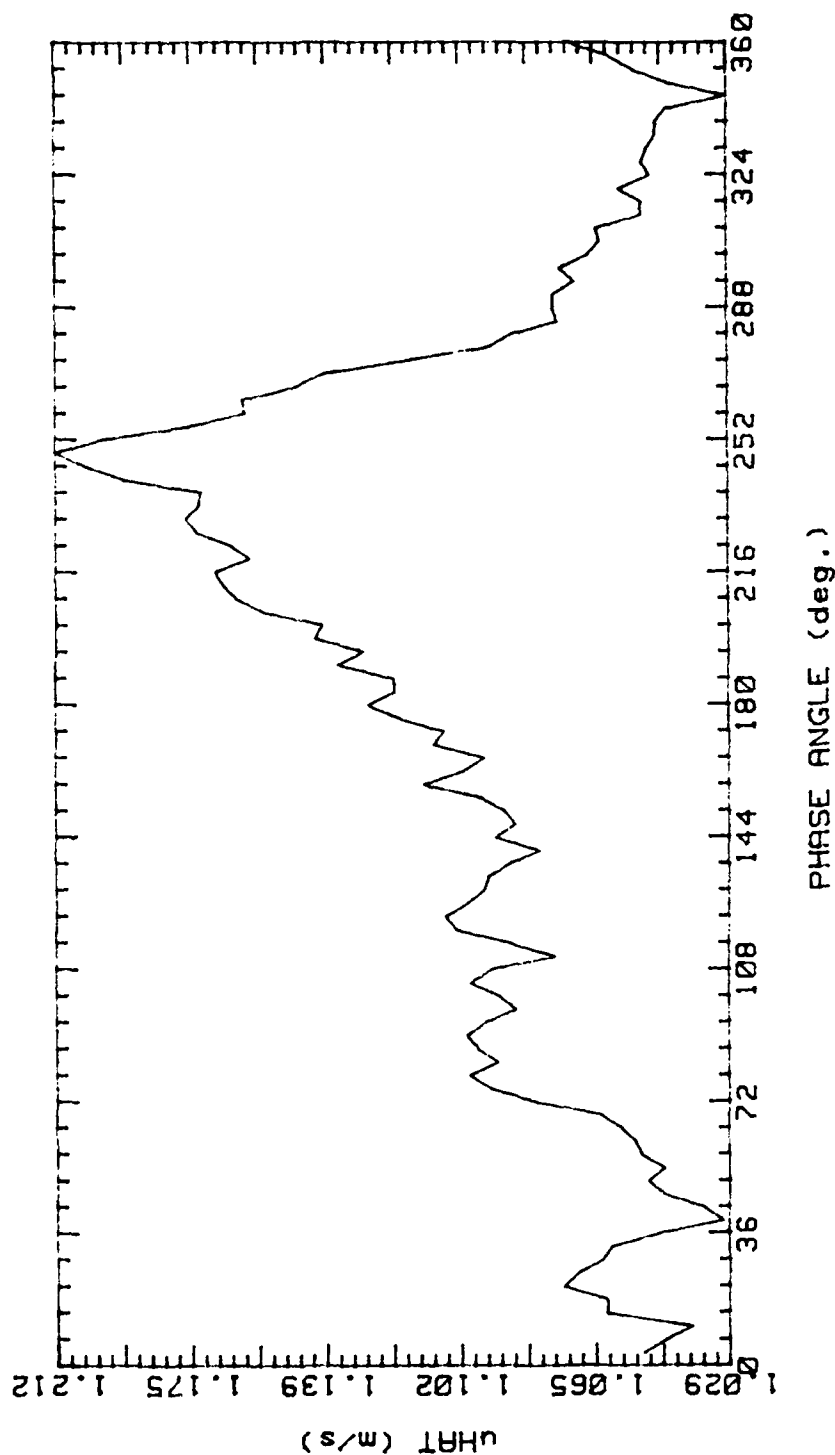


Figure 61.

RUNP2Y 93089.1229

AVG. VEL 2.034m/s RMS VEL .2773m/s

OSC. FREQ. 0Hz STR. # 0

BULK VEL. 2.495m/s REY. # 2085

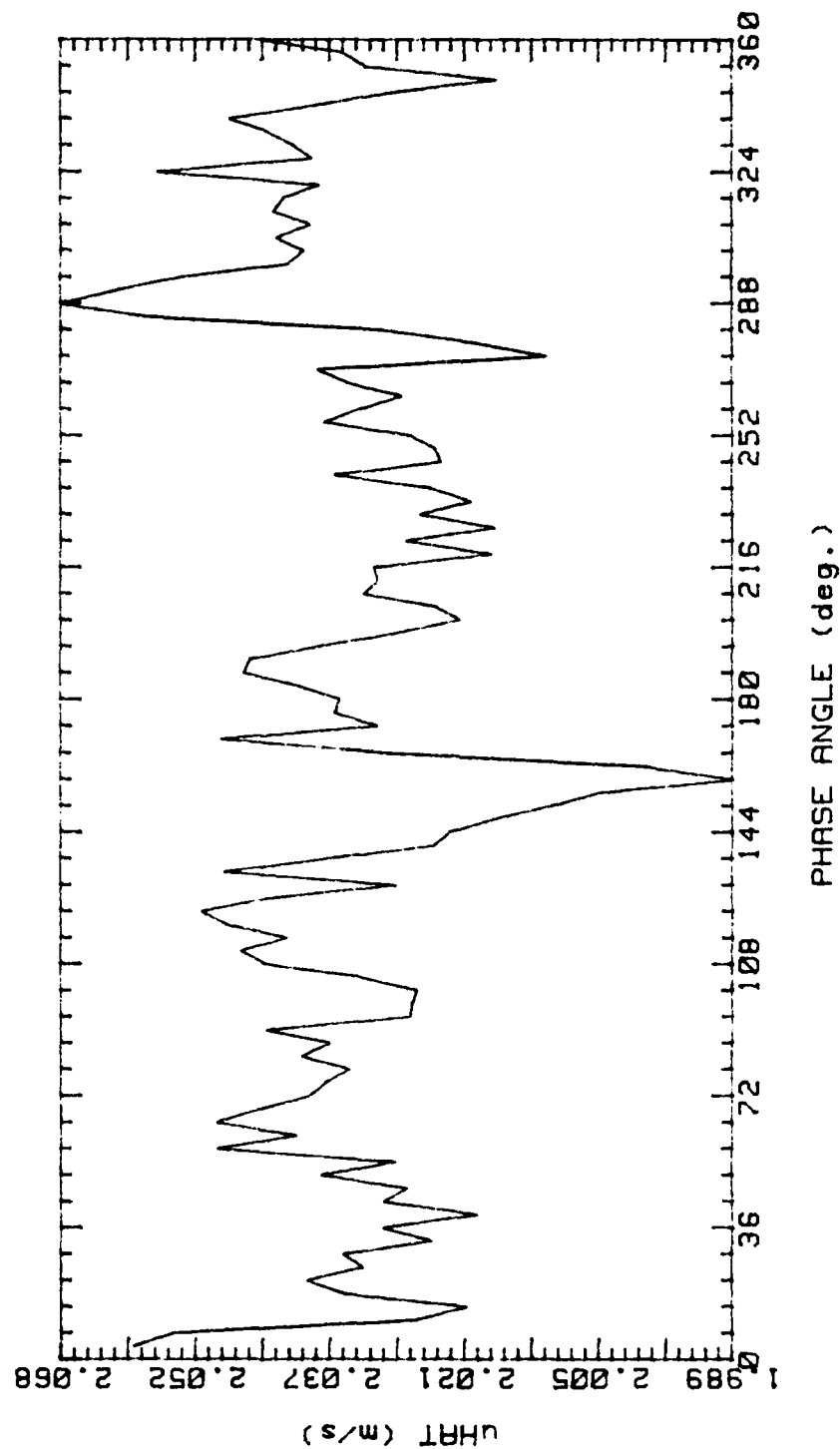


Figure 62.

RUNP2Z 93089.1429

AVG. VEL 1.966m/s RMS VEL .3333m/s  
OSC. FREQ. 1Hz STR. # .03198  
BULK VEL. 2.495m/s REY. # 2085

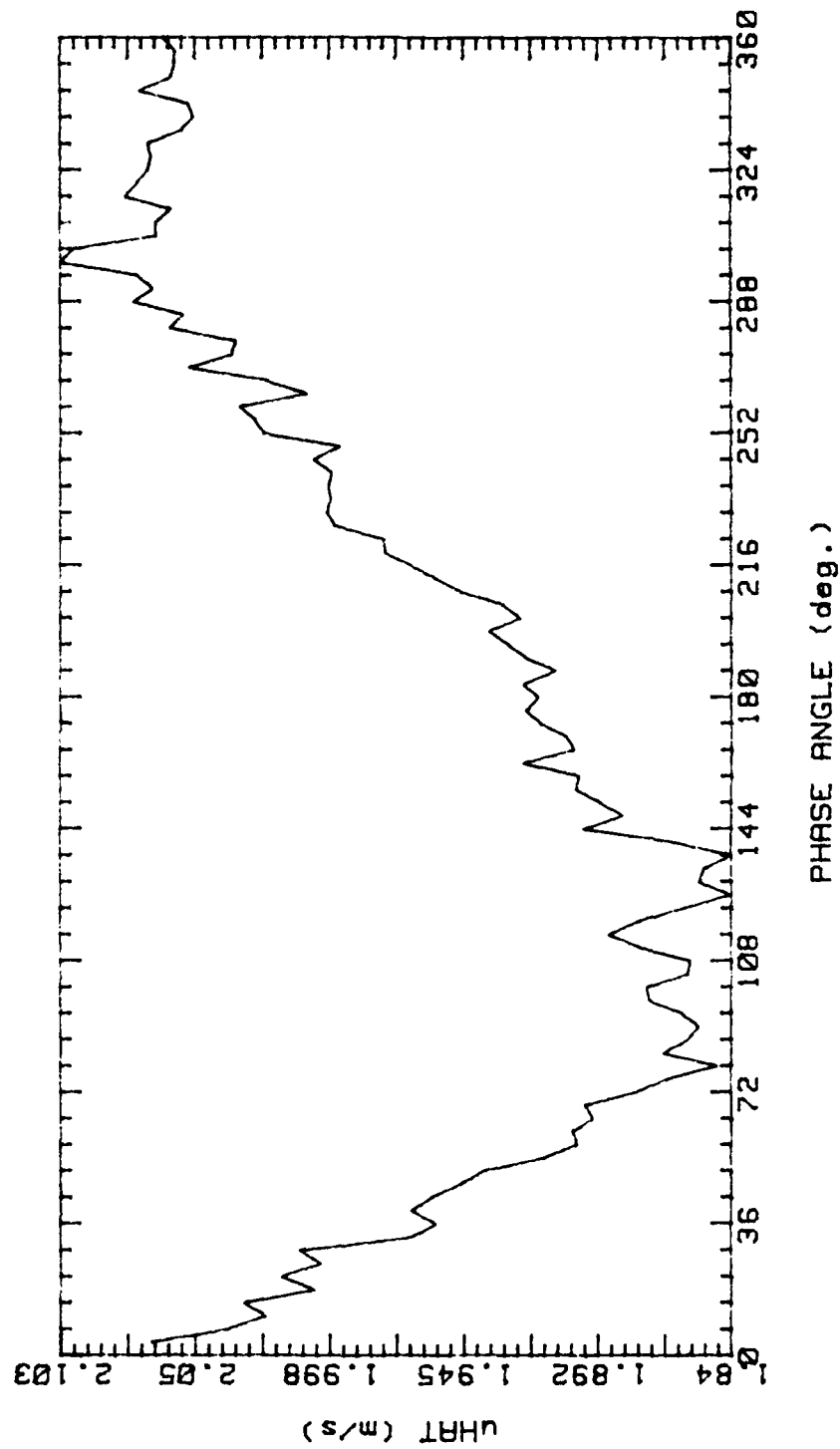


Figure 63

RUNP3Y 93089.1245

AVG. VEL 2.688m/s RMS VEL .2251m/s

OSC. FREQ. 0Hz STR. # 0

BULK VEL. 2.495m/s REY. # 2085

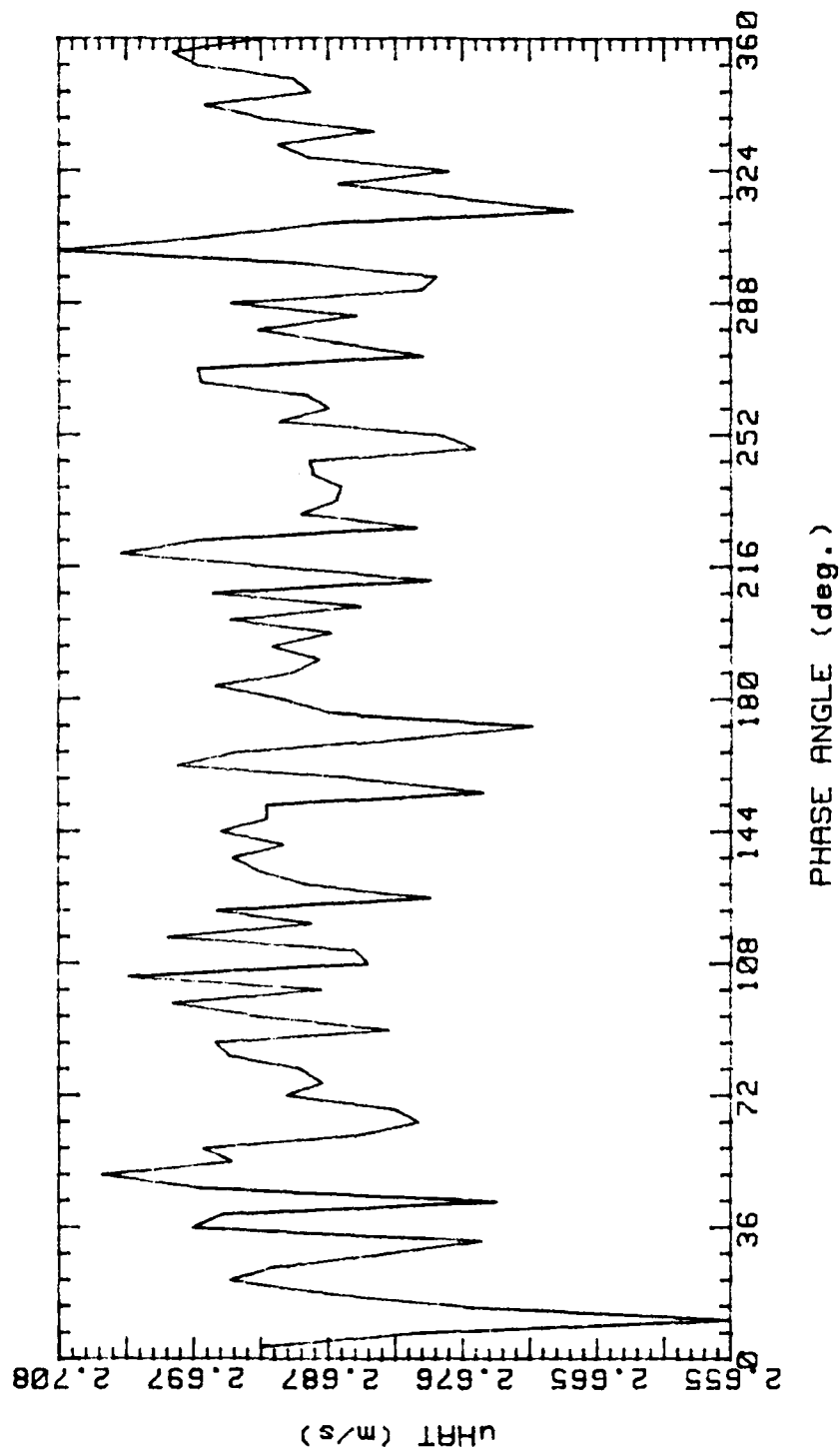


Figure 64.



RUNP3Z 93089.1442

AVG. VEL 2.566m/s RMS VEL .2868m/s  
OSC. FREQ. 1Hz STR. # .03198  
BULK VEL. 2.495m/s REY. # 2085

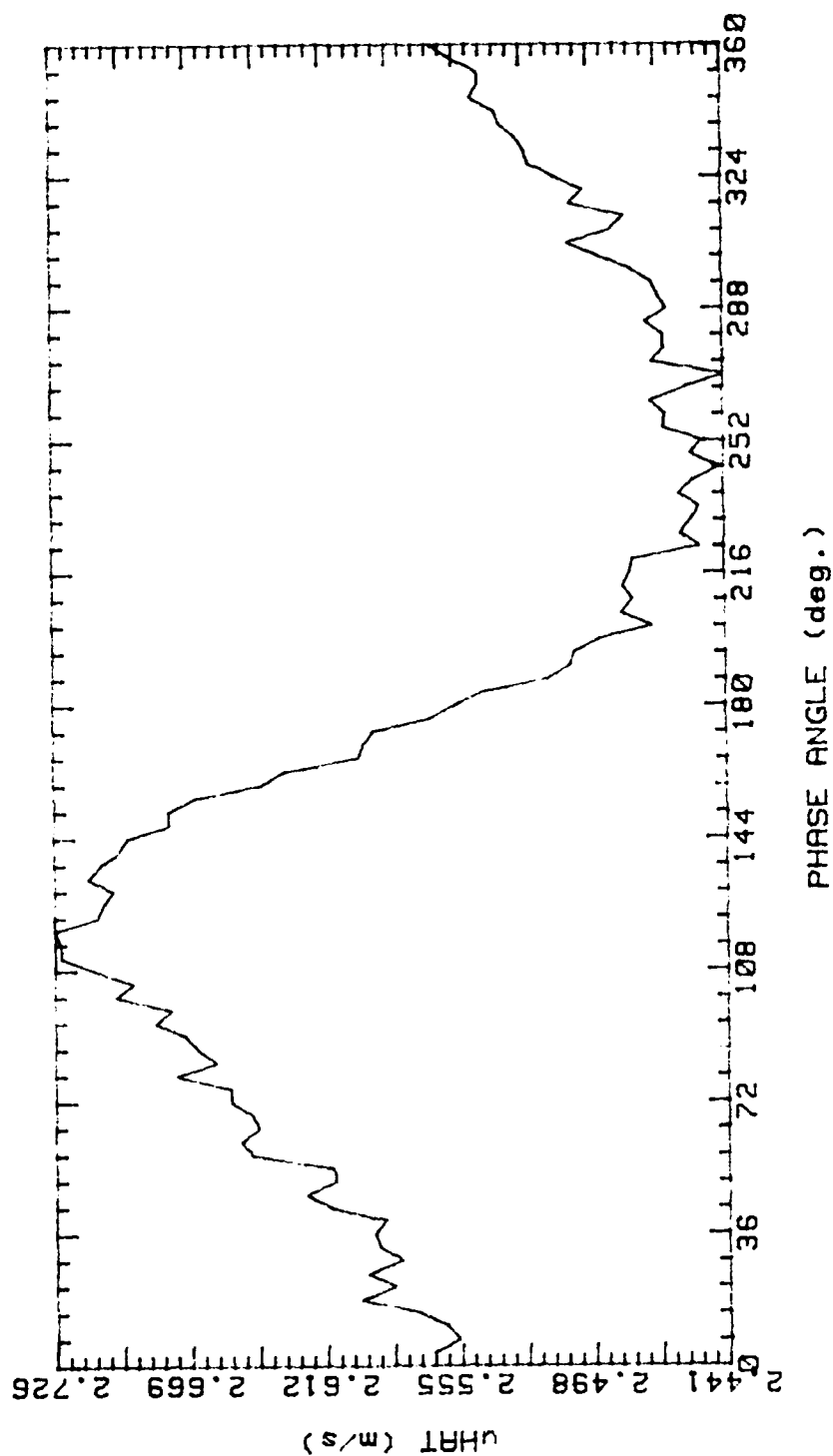


Figure 65.

RUNP4Y 93089.1258

AVG. VEL 2.928m/s RMS VEL .2554m/s

OSC. FREQ. 0Hz STR. # 0

BULK VEL. 2.495m/s REY. # 2085

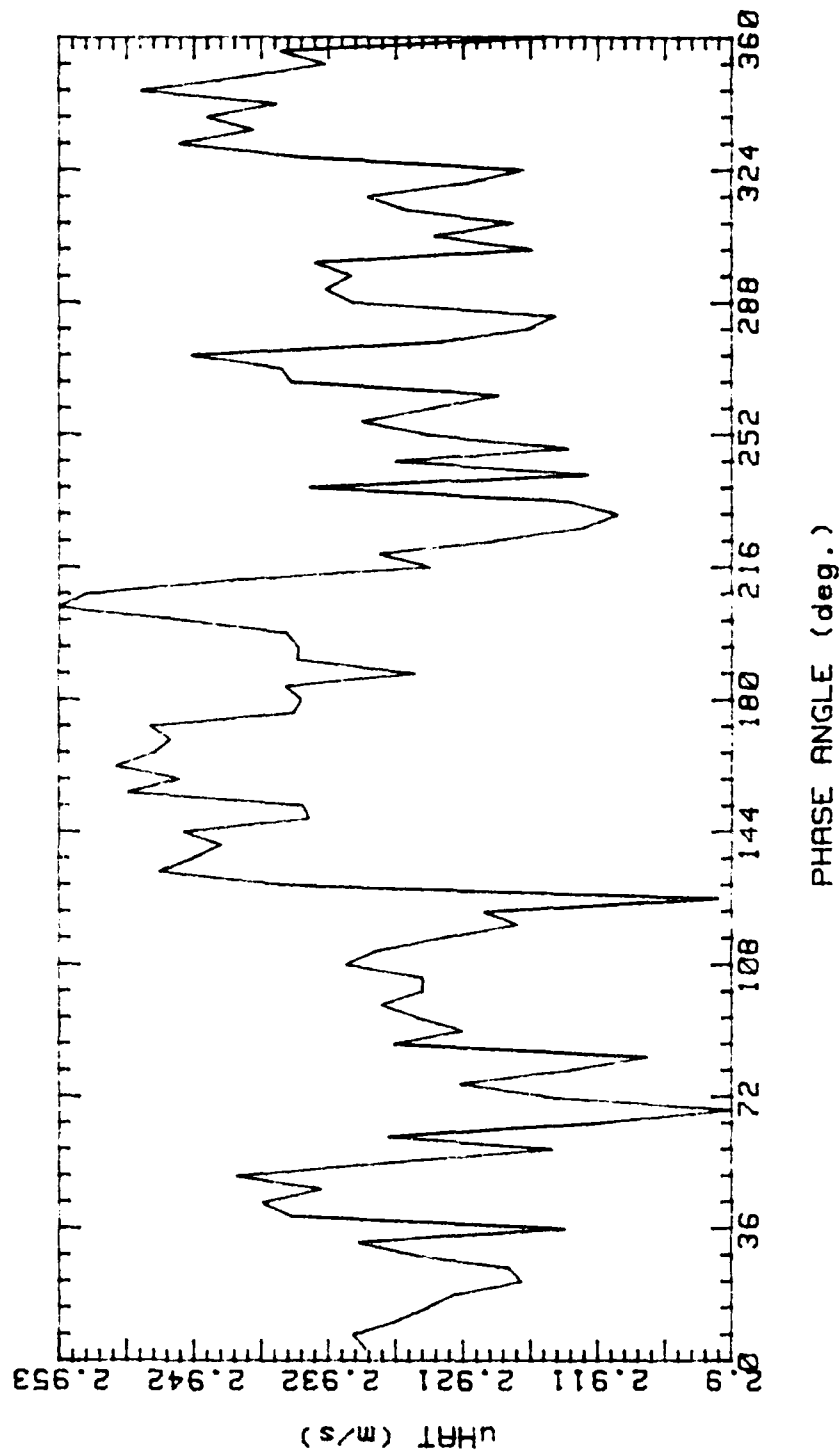


Figure 66.

RUNP4Z 93089.1458

AVG. VEL 3.07m/s RMS VEL .2596m/s  
OSC. FREQ. 1Hz STR. # .03198  
BULK VEL. 2.495m/s REY. # 2085

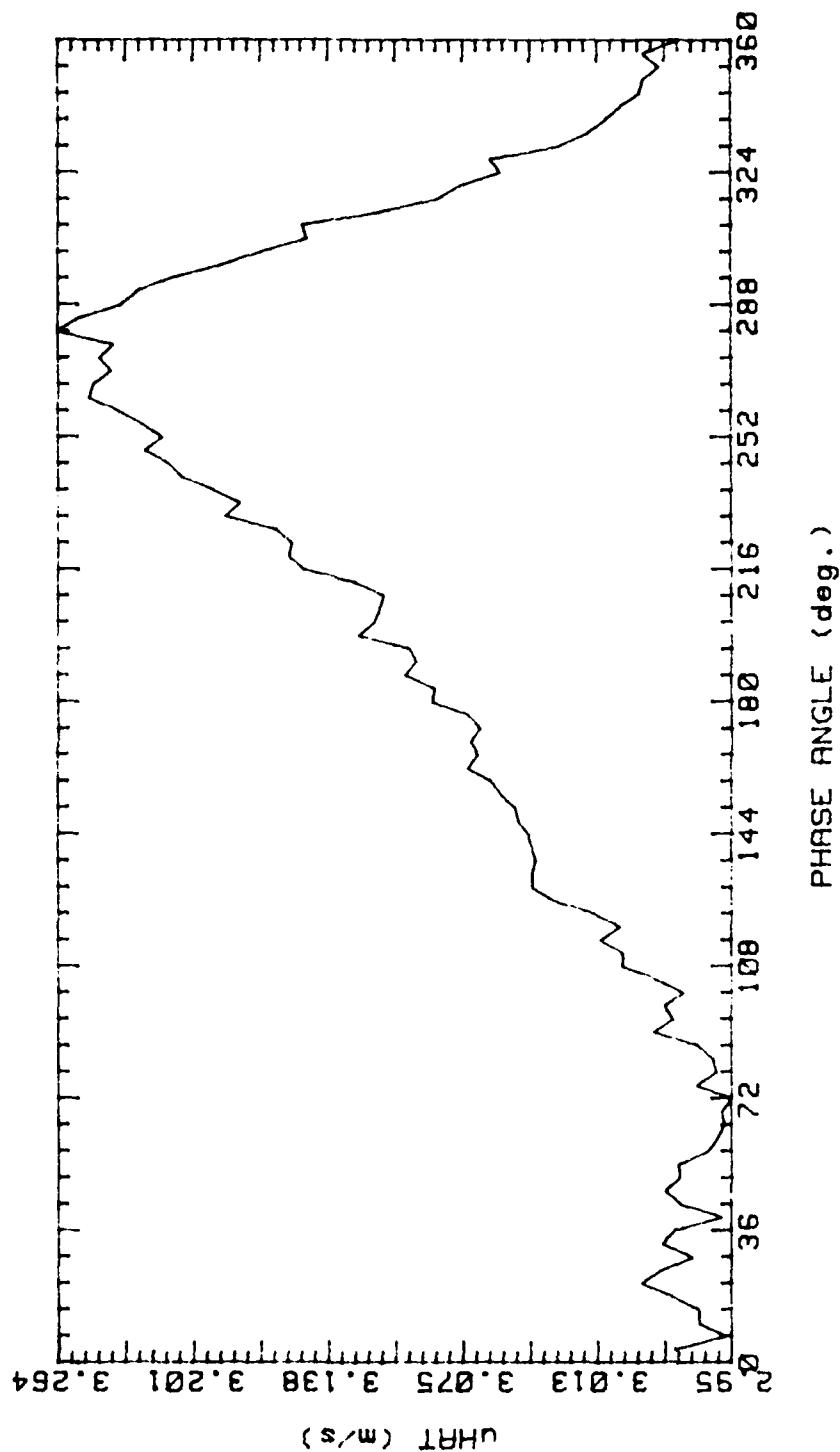


Figure 67.

RUNP5Y 93089.1313

AVG. VEL 3.377m/s RMS VEL .3209m/s

OSC. FREQ. 0Hz STR. # 0

BULK VEL. 2.495m/s REY. # 2085

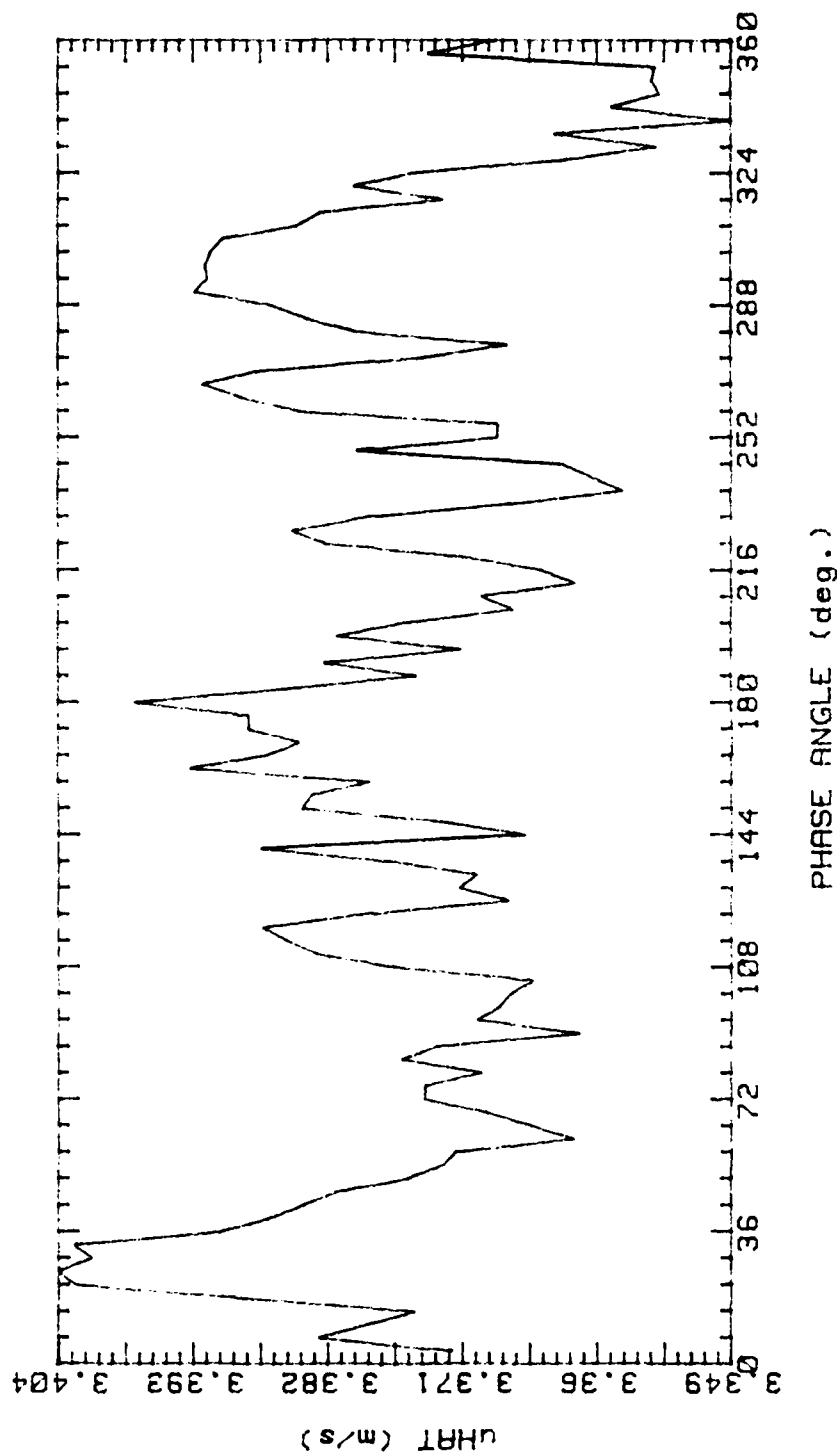


Figure 68.

RUNP5Z 93089.1513  
 AVG. VEL 3.704m/s RMS VEL .2506m/s  
 OSC. FREQ. 1Hz STR. # .03198  
 BULK VEL. 2.495m/s REY. # 2085

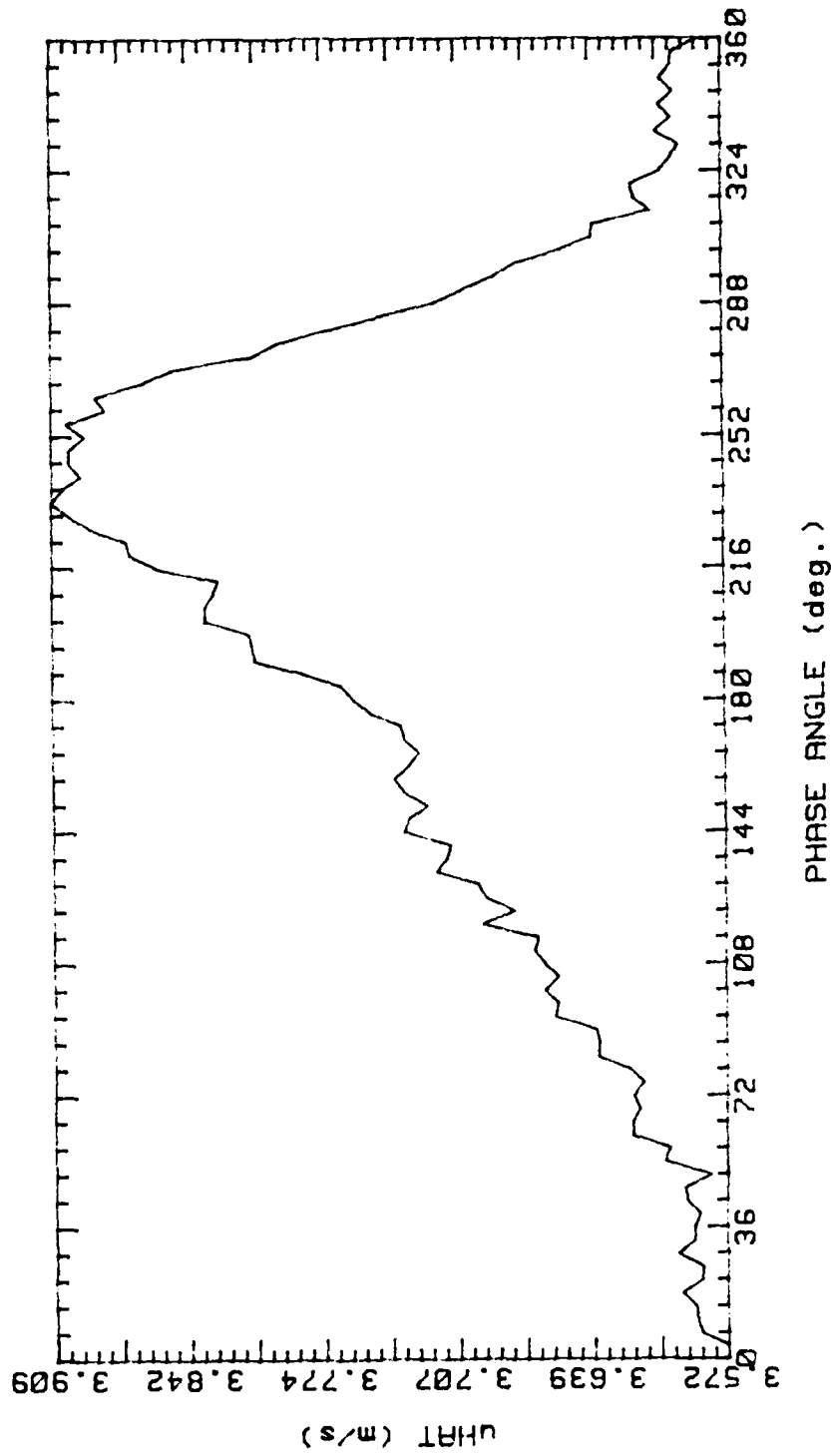


Figure 69.

RUNP6Y 93089.1328

AVG. VEL 3.221m/s RMS VEL .2999m/s

OSC. FREQ. 0Hz STR. # 0

BULK VEL. 2.495m/s REY. # 2085

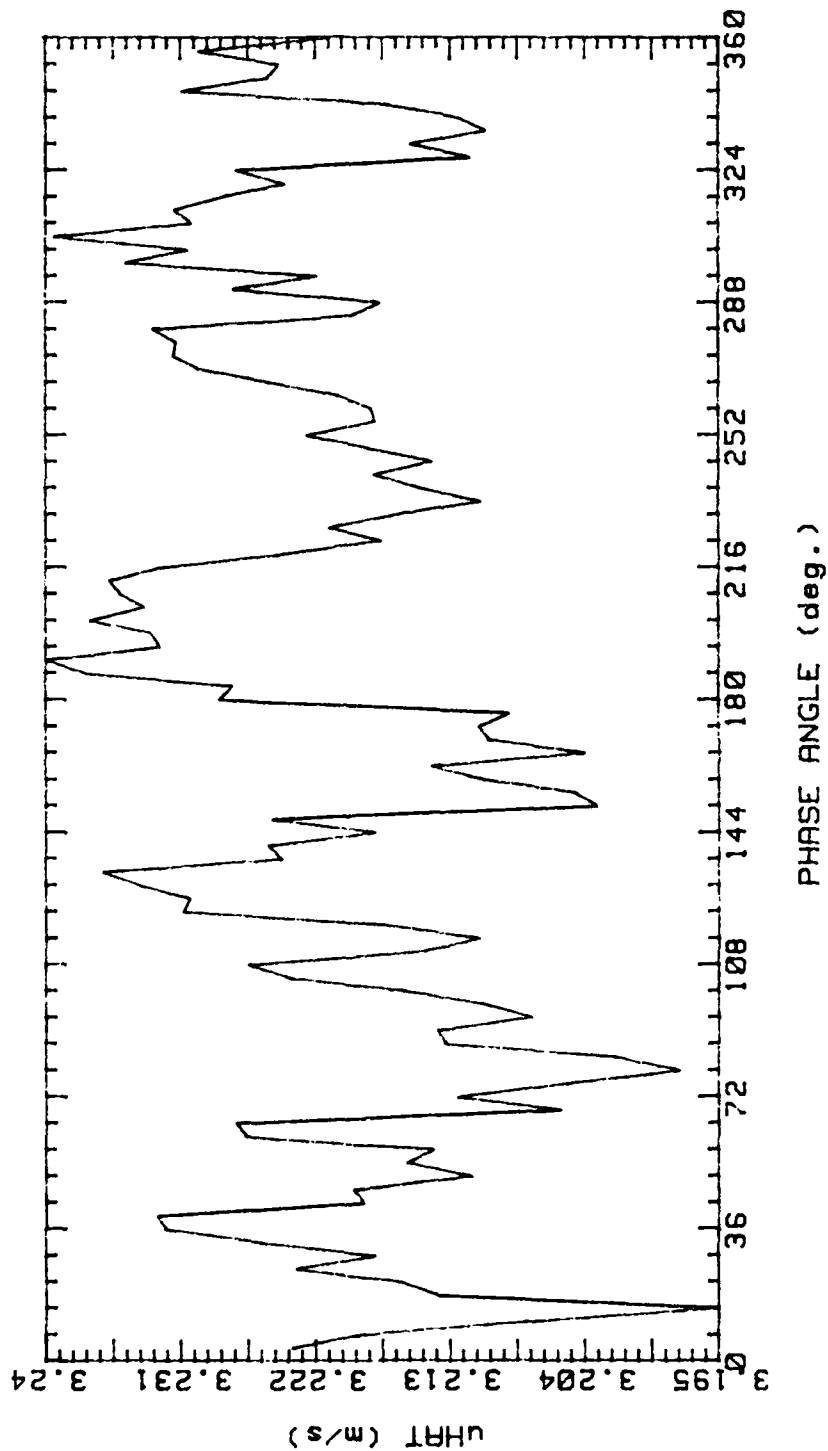


Figure 70.

RUNP6Z 93089.1526  
 AVG. VEL 3.339m/s RMS VEL .2337m/s  
 OSC. FREQ. 1Hz STR. # .03198  
 BULK VEL. 2.495m/s REY. # 2085

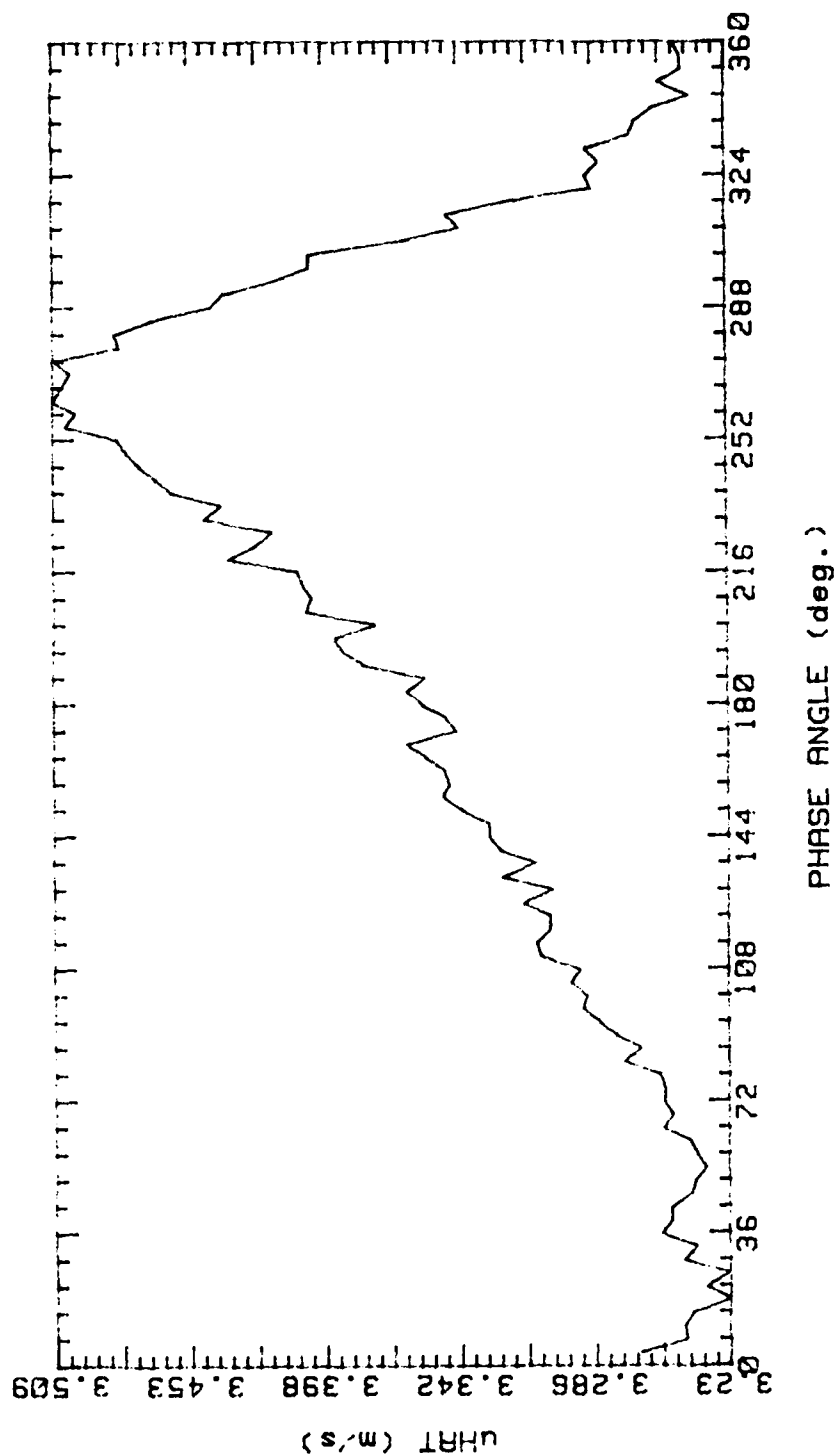


Figure 71.

RUNP7Y 93089.1343

AVG. VEL 2.68m/s RMS VEL .229m/s

OSC. FREQ. 0Hz STR. # 0

BULK VEL. 2.495m/s REY. # 2085

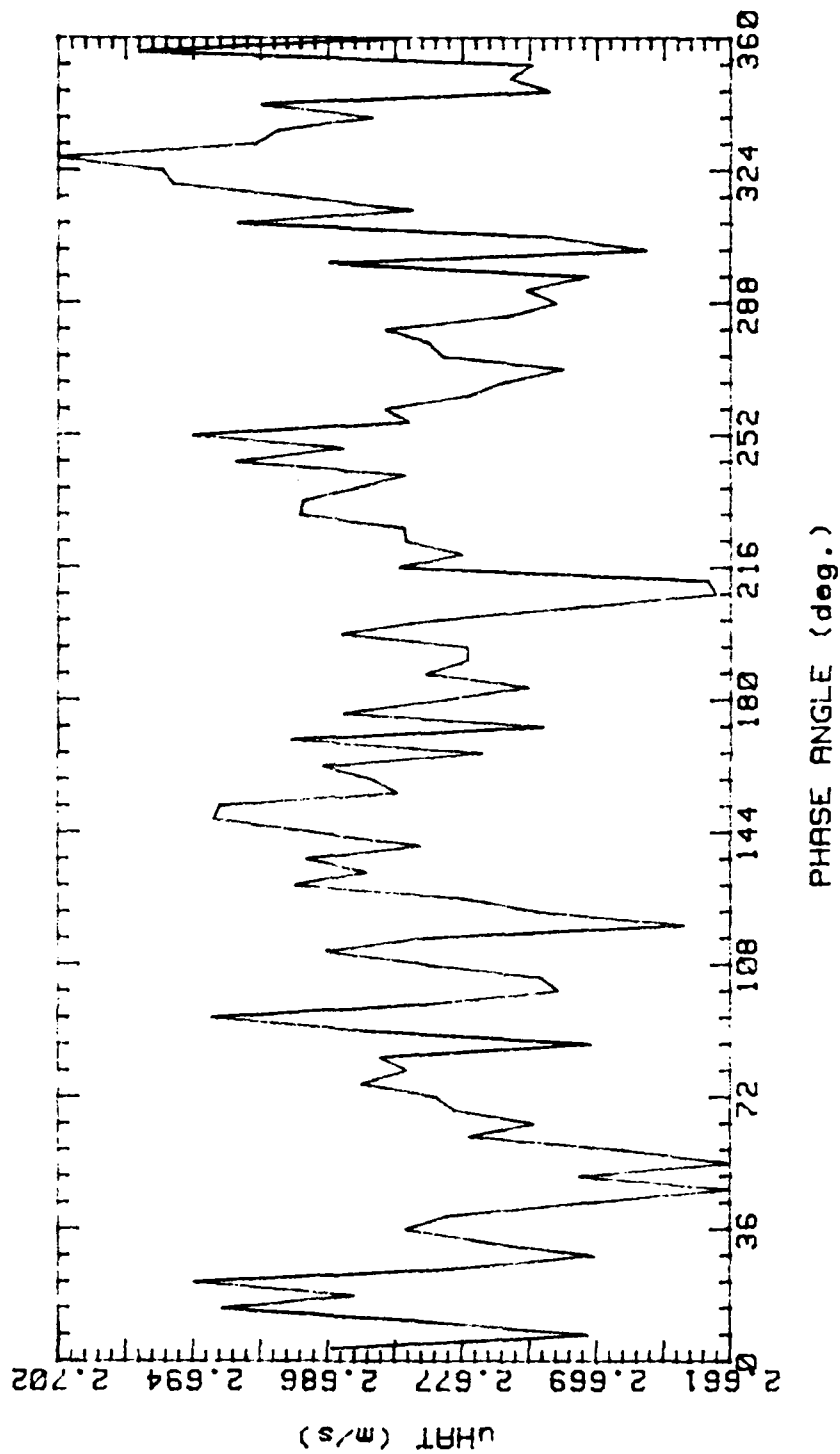


Figure 72.



RUNP7Z 93089.1655

AVG. VEL 2.874m/s RMS VEL .2524m/s

OSC. FREQ. 1Hz STR. # .03198

BULK VEL. 2.495m/s REY. # 2085

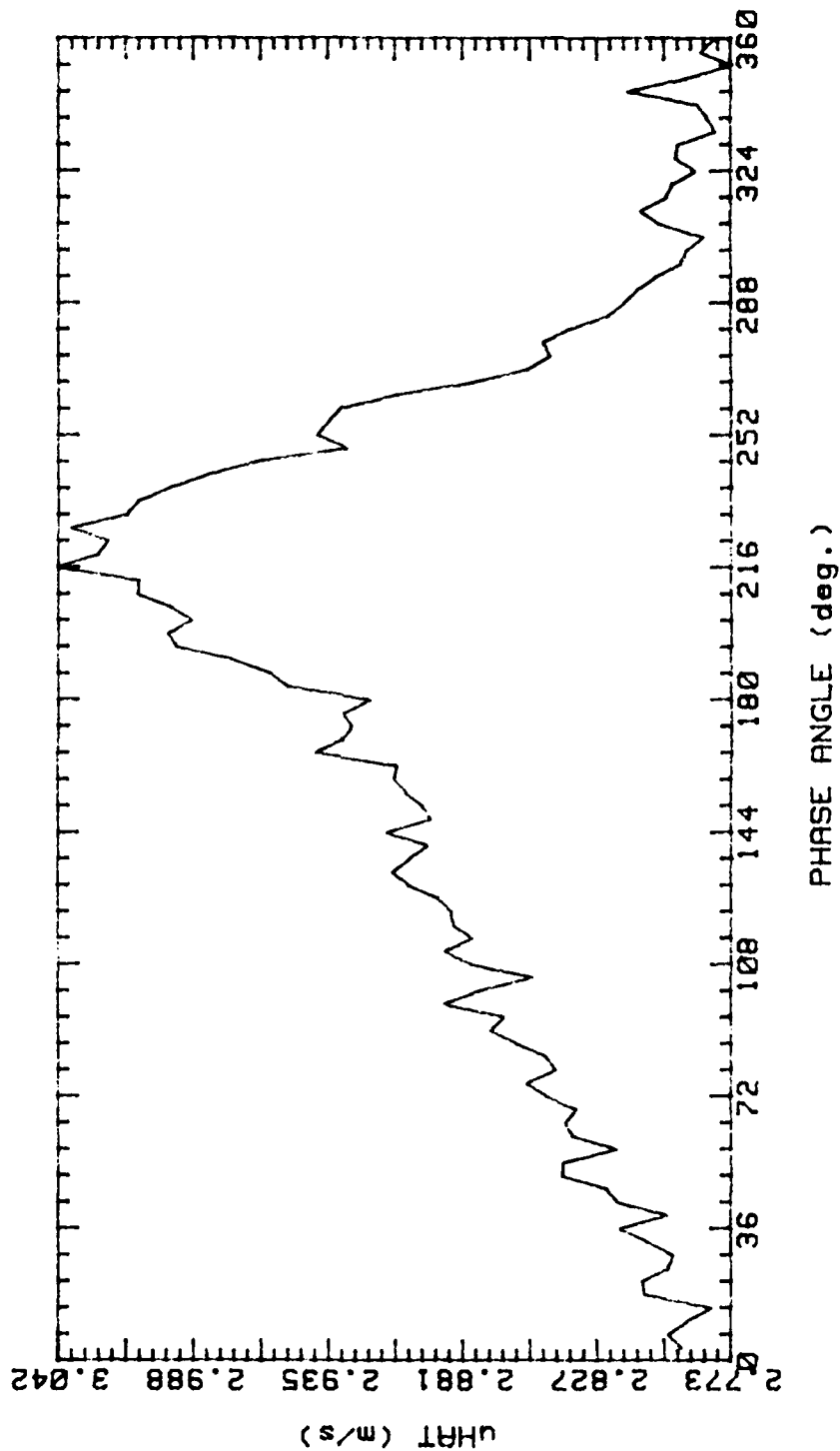


Figure 73.

RUNP8Y 93089.1358  
 AVG. VEL. 2.495m/s RMS VEL. 2.2174m/s  
 OSC. FREQ. 0Hz STR. # 0  
 BULK VEL. 2.495m/s REY. # 2085

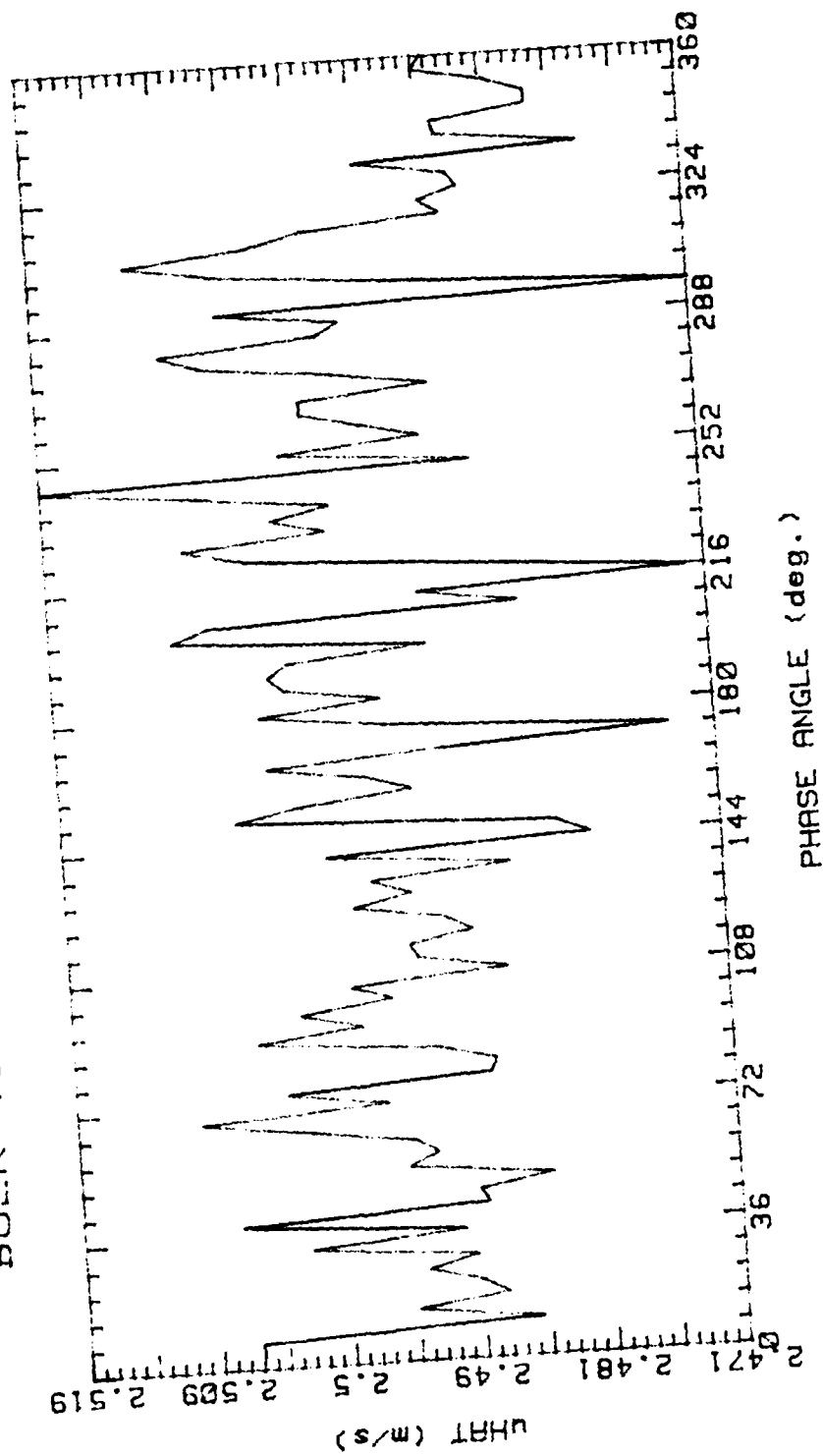


Figure 74.

RUNP8Z 93089.1707

AVG. VEL 2.424m/s RMS VEL .3076m/s

OSC. FREQ. 1Hz STR. # .03198

BULK VEL. 2.495m/s REY. # 2085

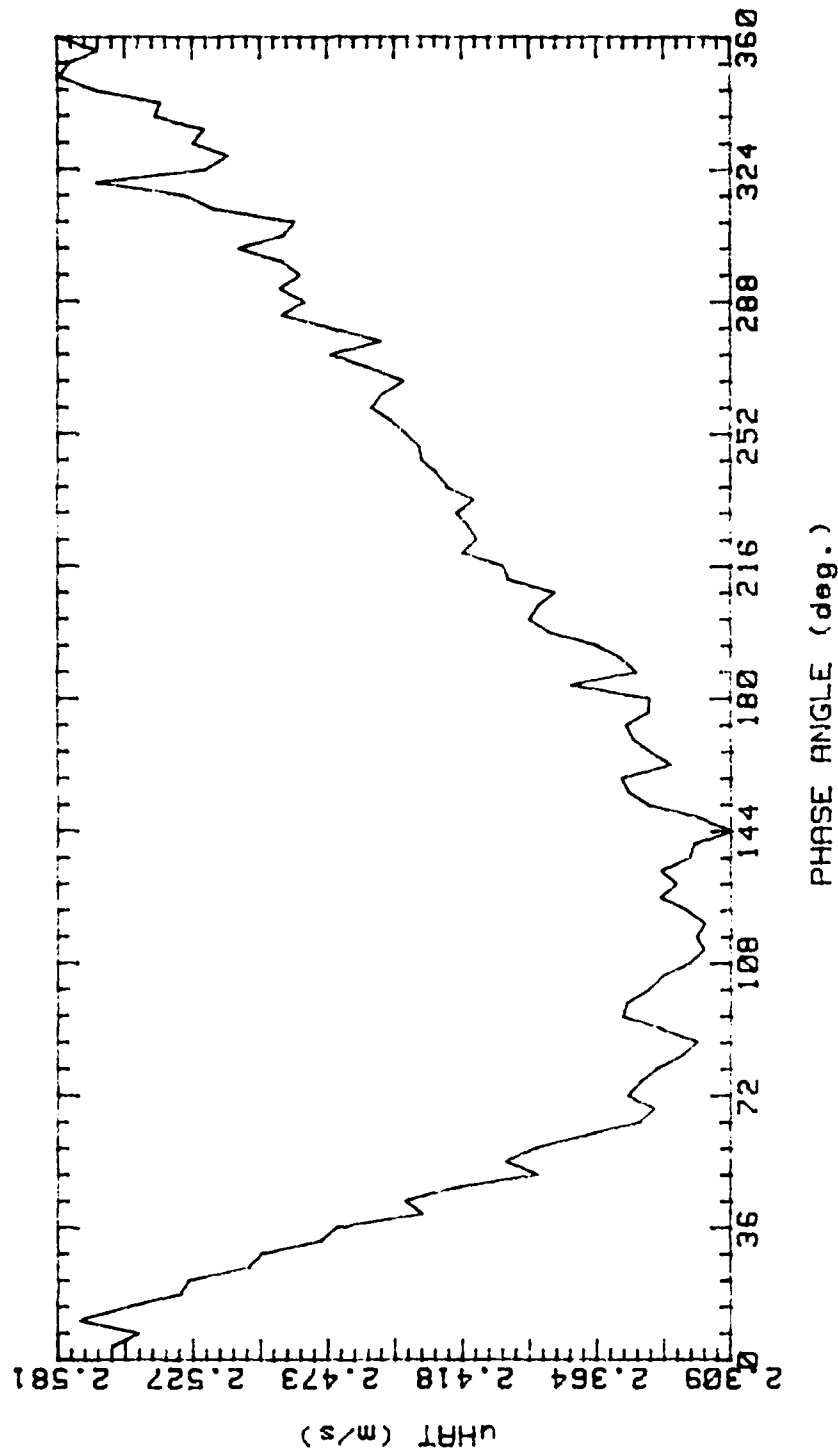


Figure 75.

RUNP1AA 93089.173

AVG. VEL 1.516m/s RMS VEL .3132m/s  
OSC. FREQ. 0Hz STR. # 0  
BULK VEL. 3.16m/s REY. # 2640

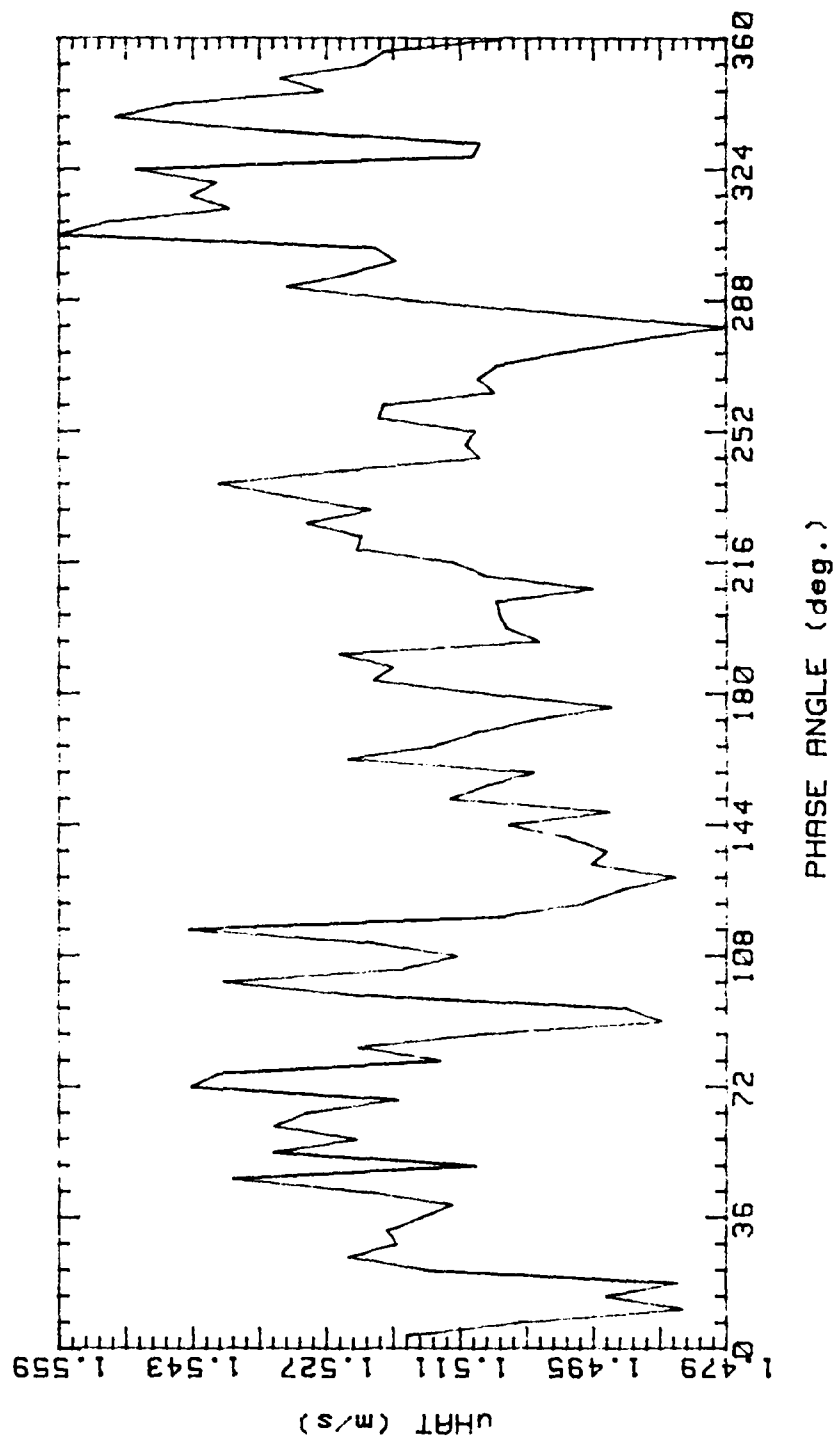


Figure 76.

RUNP1BA 93089.1932

AVG. VEL 1.494m/s RMS VEL .3118m/s  
OSC. FREQ. 1Hz STR. # .02525  
BULK VEL. 3.16m/s REY. # 2640

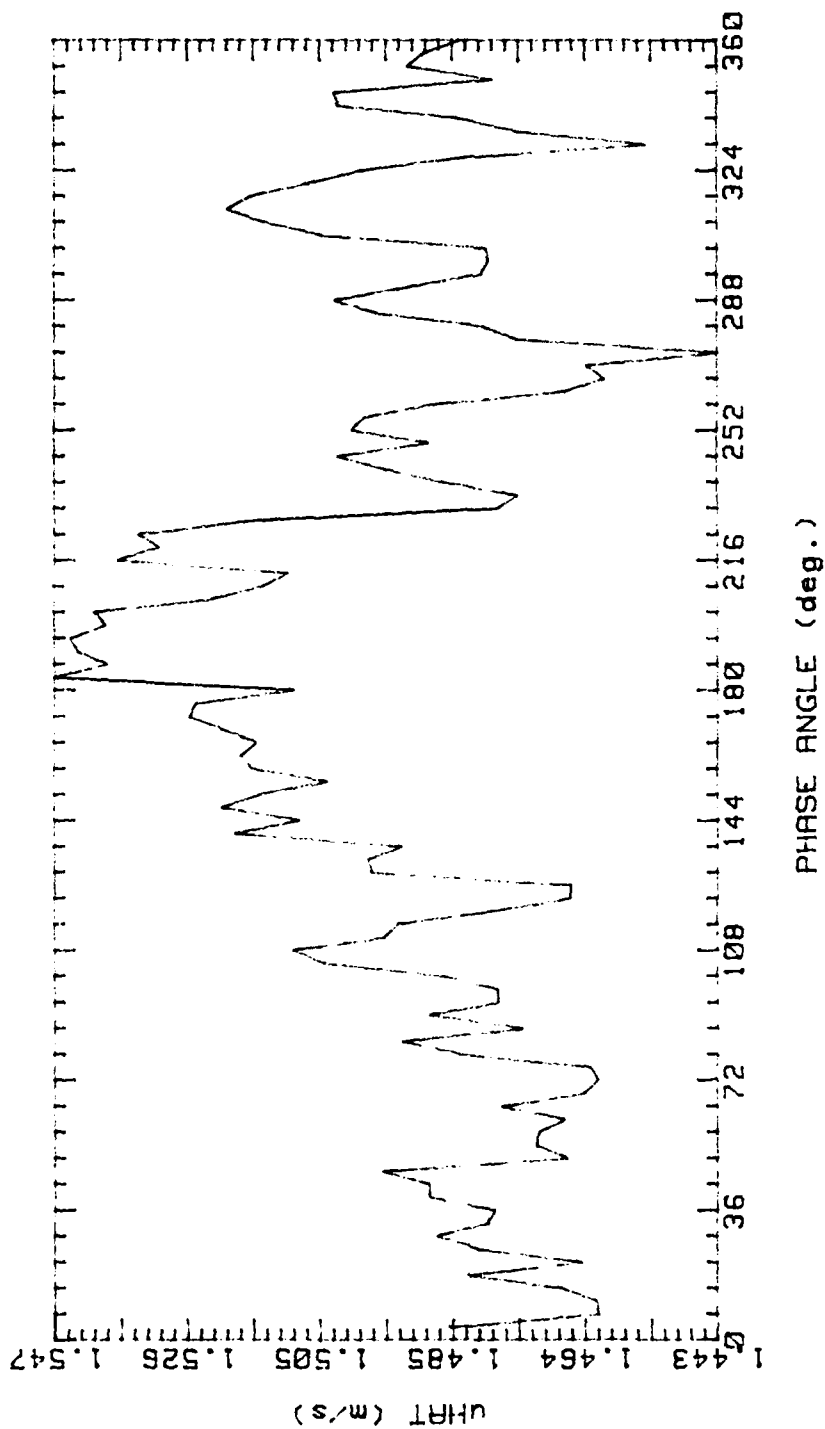


Figure 77.

RUNP2AA 93089.1745

AVG. VEL 2.538m/s RMS VEL .3974m/s

OSC. FREQ. 0Hz STR. # 0

BULK VEL. 3.16m/s REY. # 2640

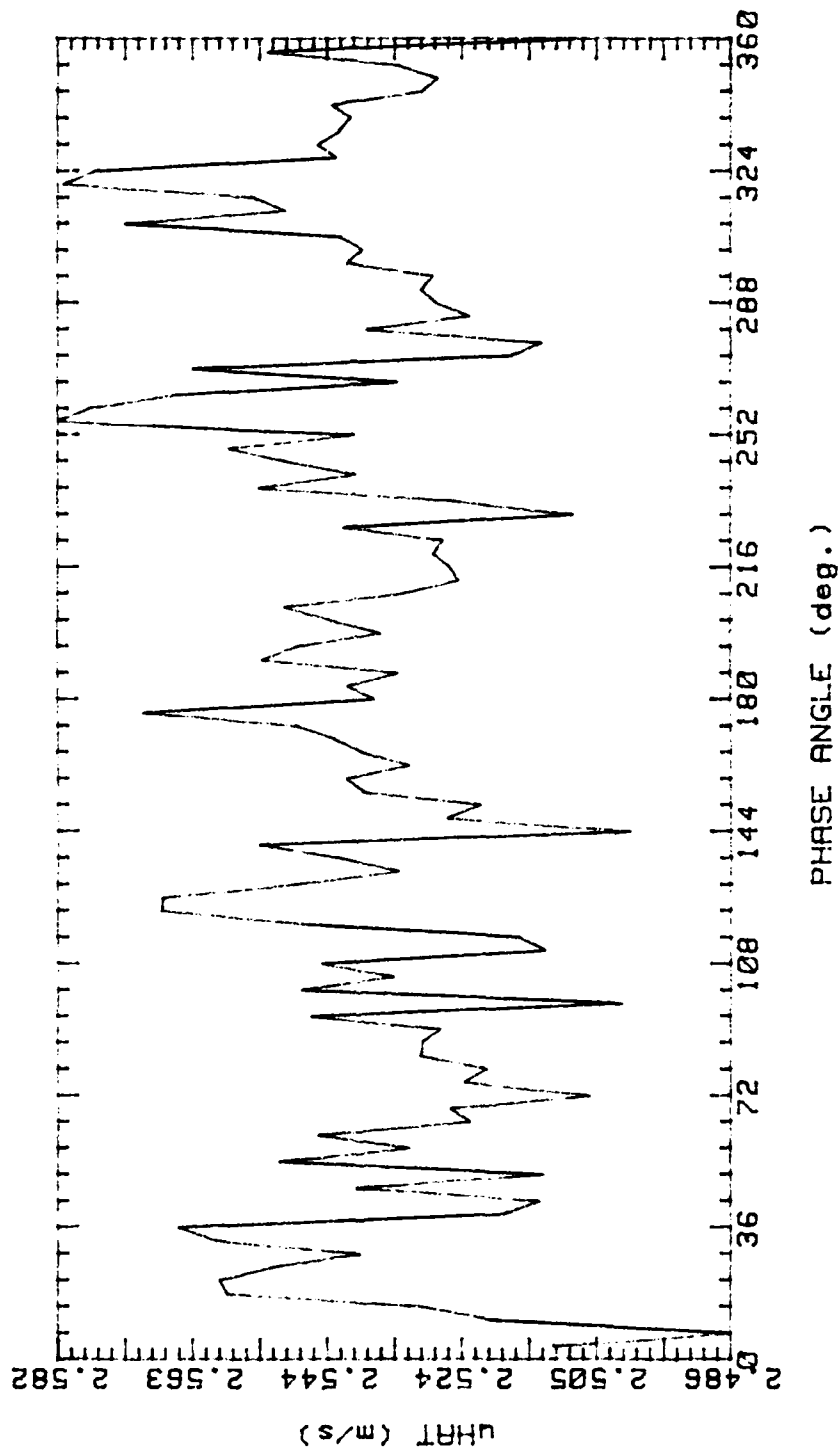


Figure 78.

RUNP2BA 93089.1947

AVG. VEL 2.539m/s RMS VEL .3974m/s  
OSC. FREQ. 1Hz STR. # .02525  
BULK VEL. 3.16m/s REY. # 2640

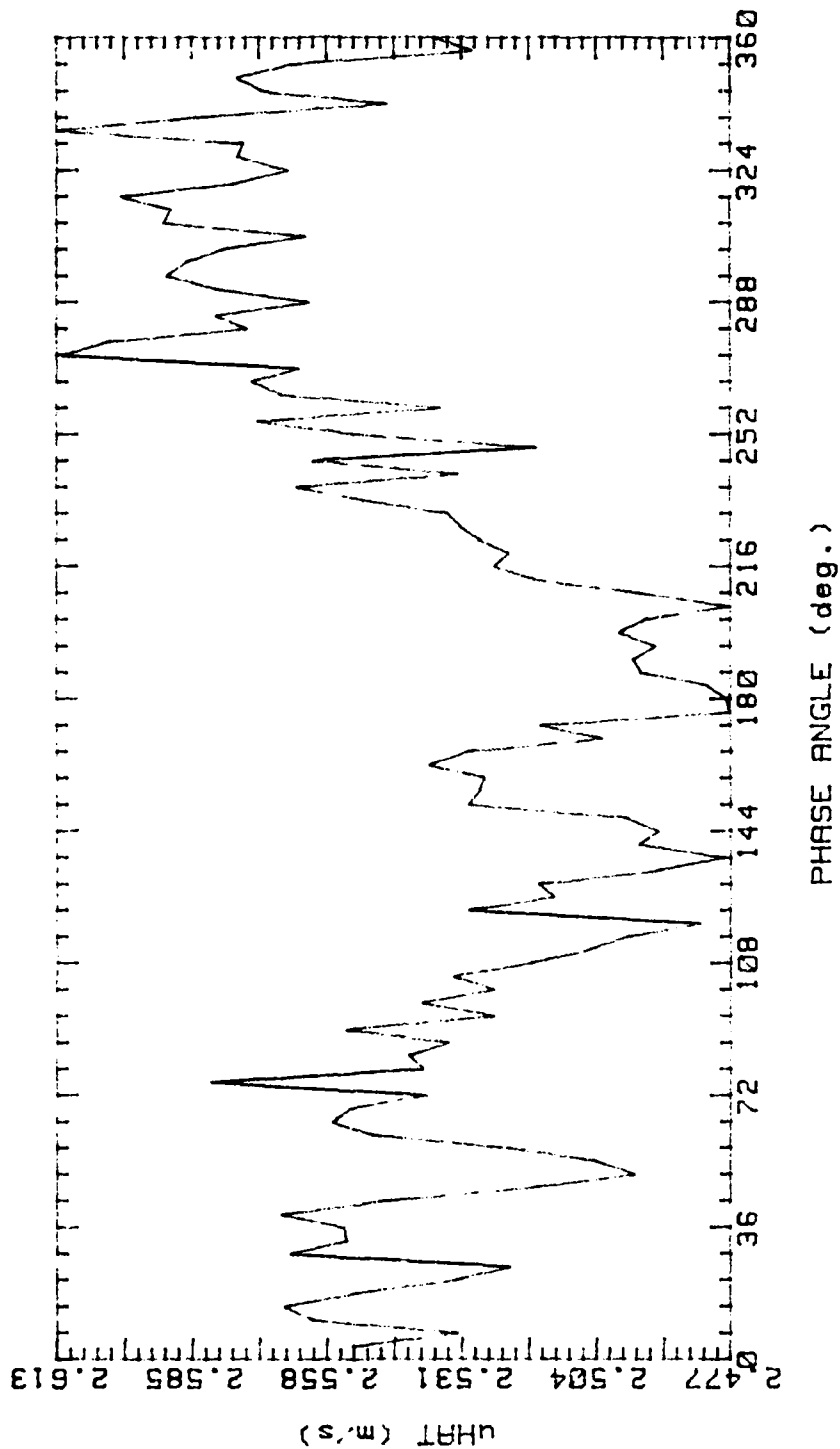


Figure 79.

RUNP3AA 93089.1801  
 AVG. VEL 3.183m/s RMS VEL .3148m/s  
 OSC. FREQ. 0Hz STR. # 0  
 BULK VEL. 3.16m/s REY. # 2640

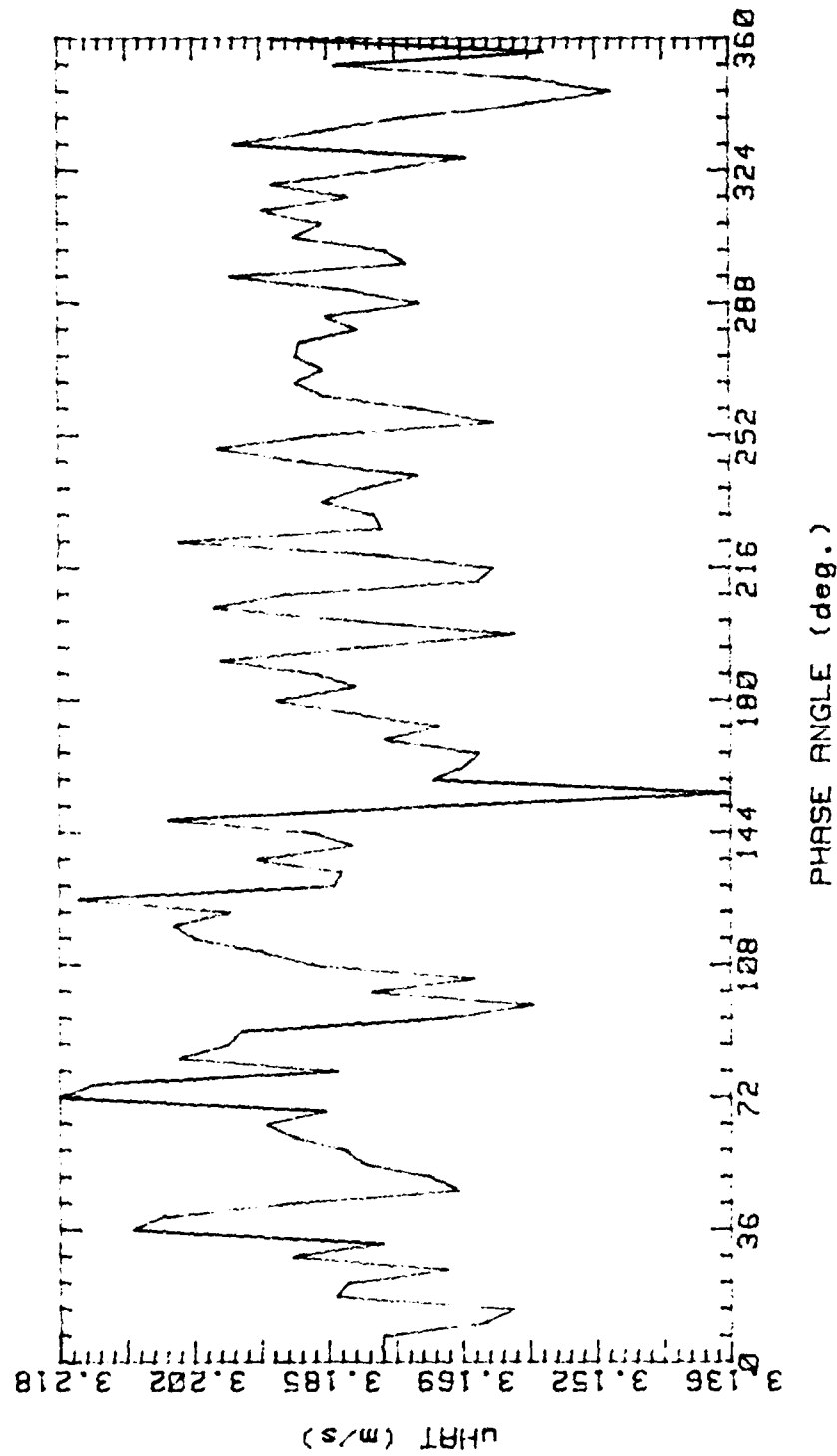


Figure 80.



RUNP3BA 93089.2001

AVG. VEL 3.168m/s RMS VEL .3107m/s  
OSC. FREQ. 1Hz STR. # .02525  
BULK VEL. 3.16m/s REY. # 2640

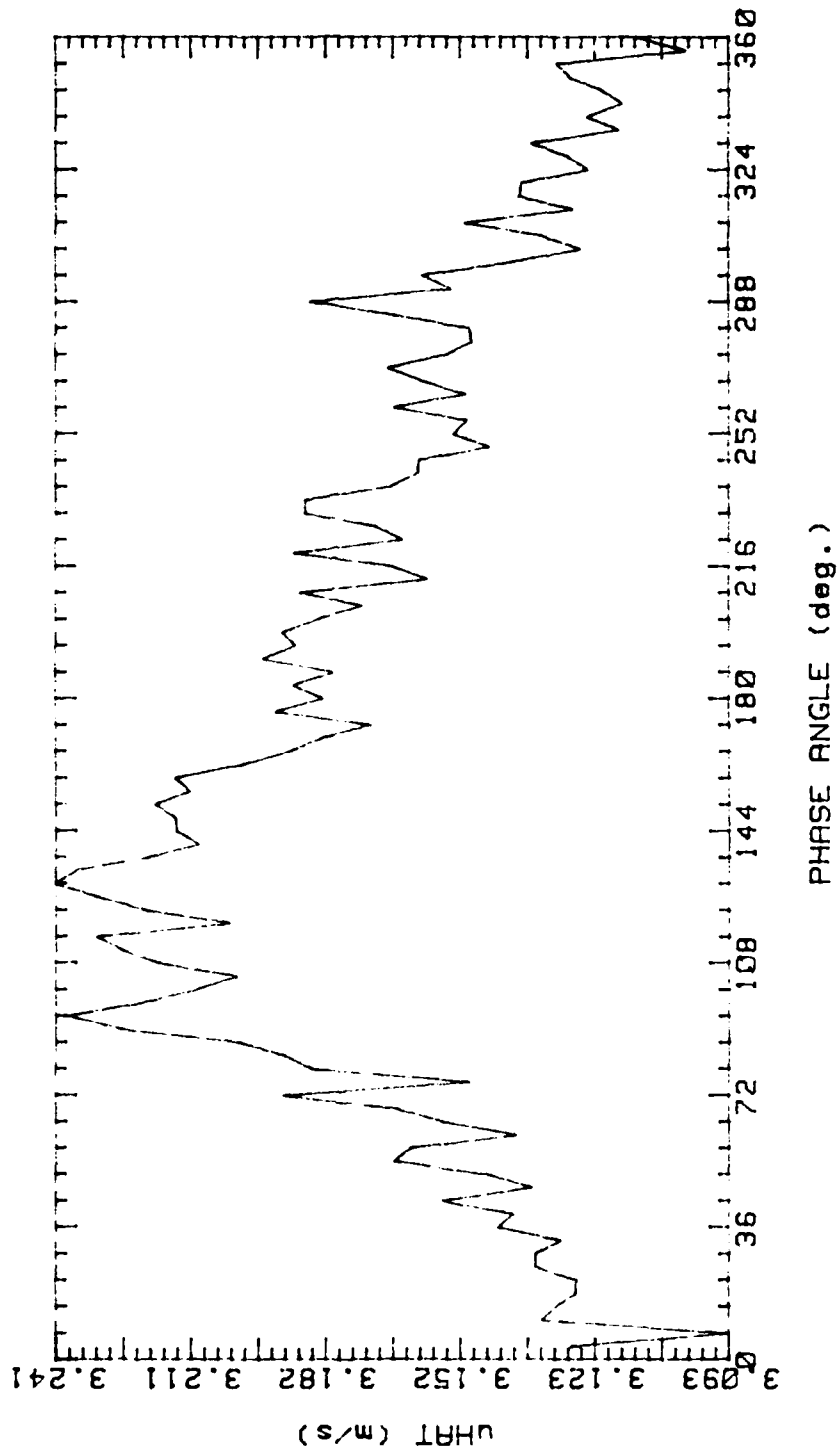


Figure 81.

RUNP4AA 93089.1815  
 AVG. VEL 3.48m/s RMS VEL .239m/s  
 OSC. FREQ. 0Hz STR. # 0  
 BULK VEL. 3.16m/s REY. # 2640

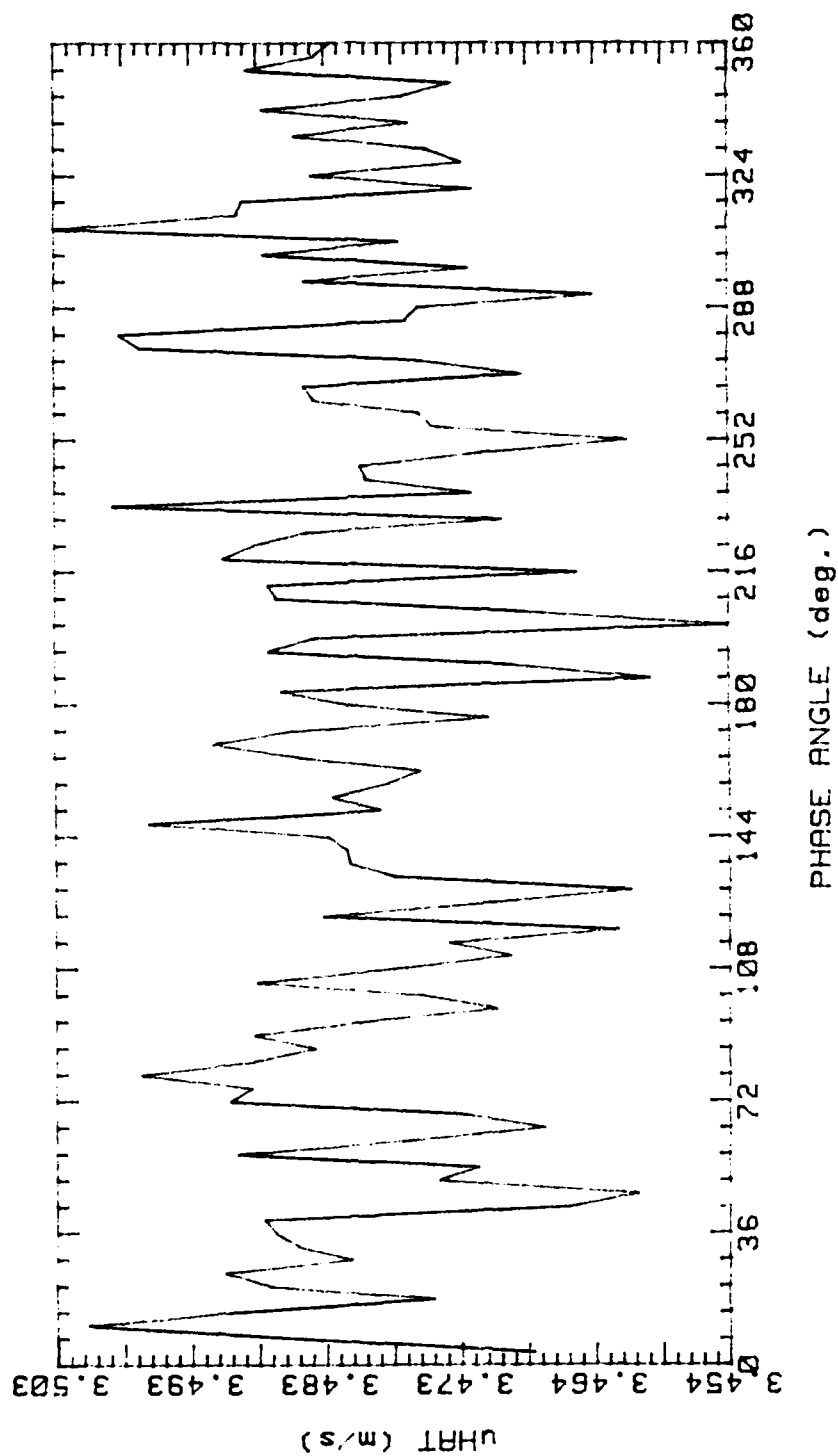


Figure 82.

RUNP4BA 93089.2014

AVG. VEL 3.468m/s RMS VEL .2407m/s  
OSC. FREQ. 1Hz STR. # .02525  
BULK VEL. 3.16m/s REY. # 2640

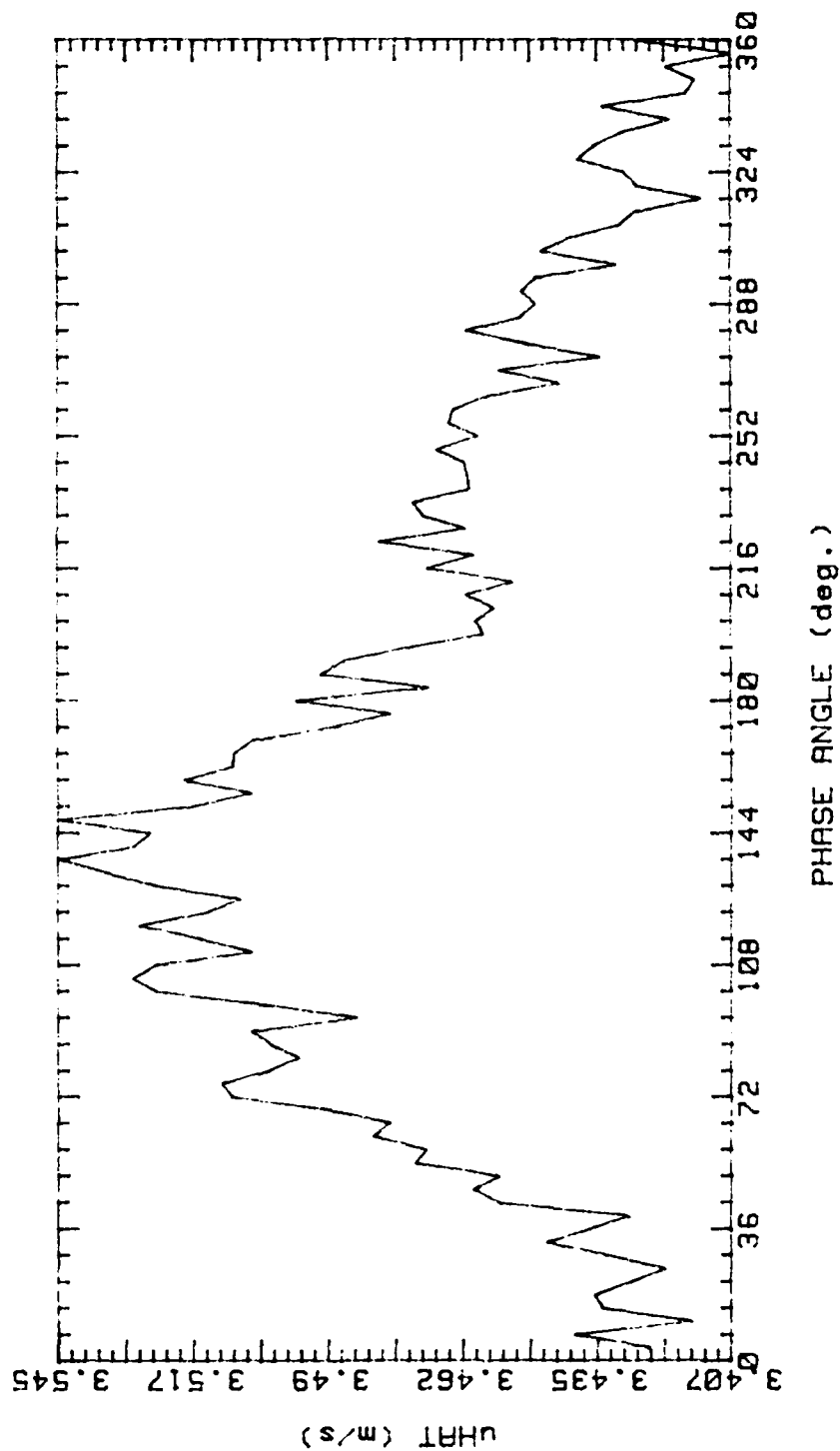


Figure 83.

RUNPSAA 93089.1831

AVG. VEL 3.445m/s RMS VEL .1782m/s

OSC. FREQ. 0Hz STR. # 0

BULK VEL. 3.16m/s REY. # 2640

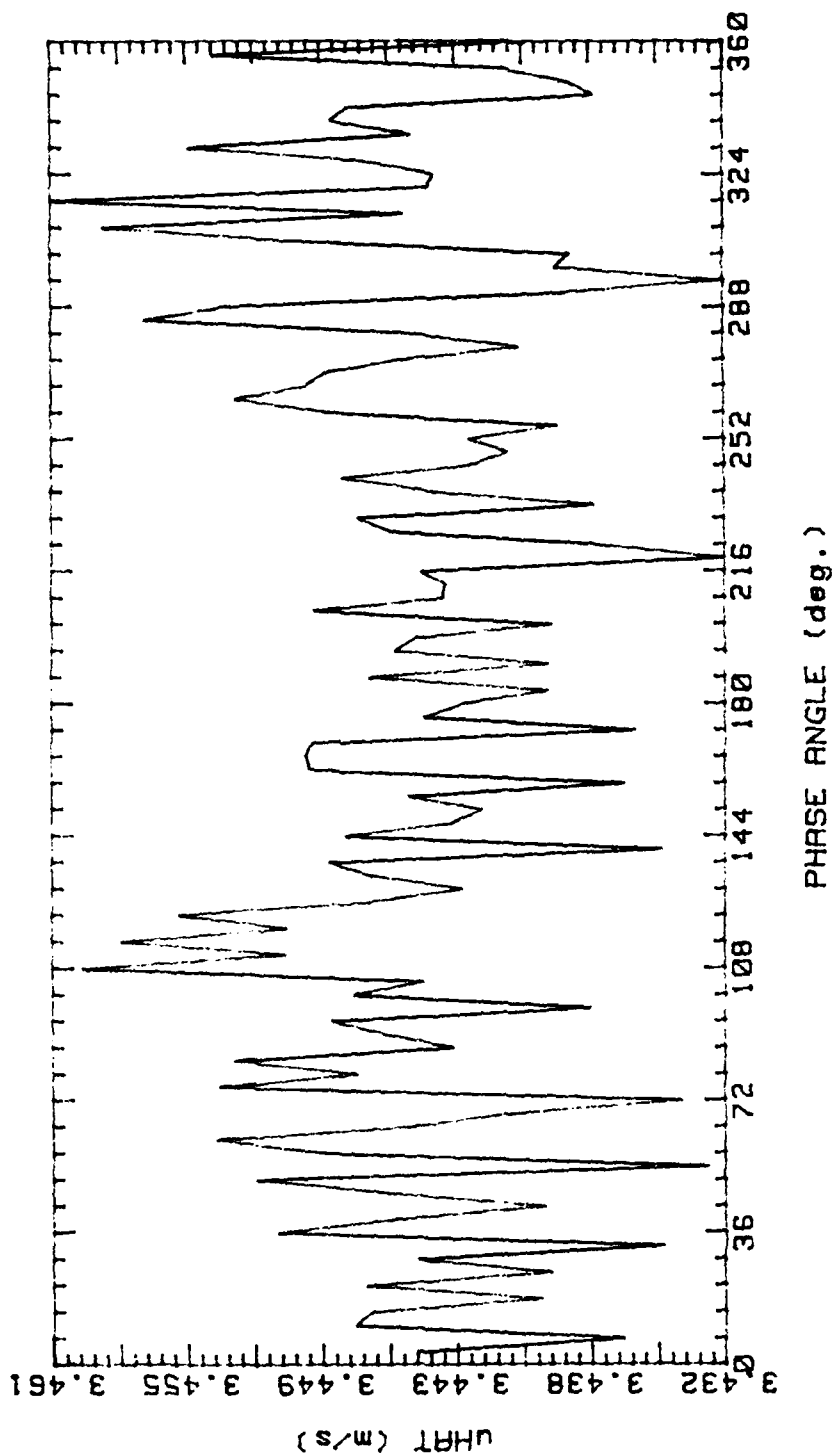


Figure 84.

RUNP5BA 93089.2027

AVG. VEL 3.434m/s RMS VEL .1786m/s  
OSC. FREQ. 1Hz STR. # .02525  
BULK VEL. 3.16m/s REY. # 2640

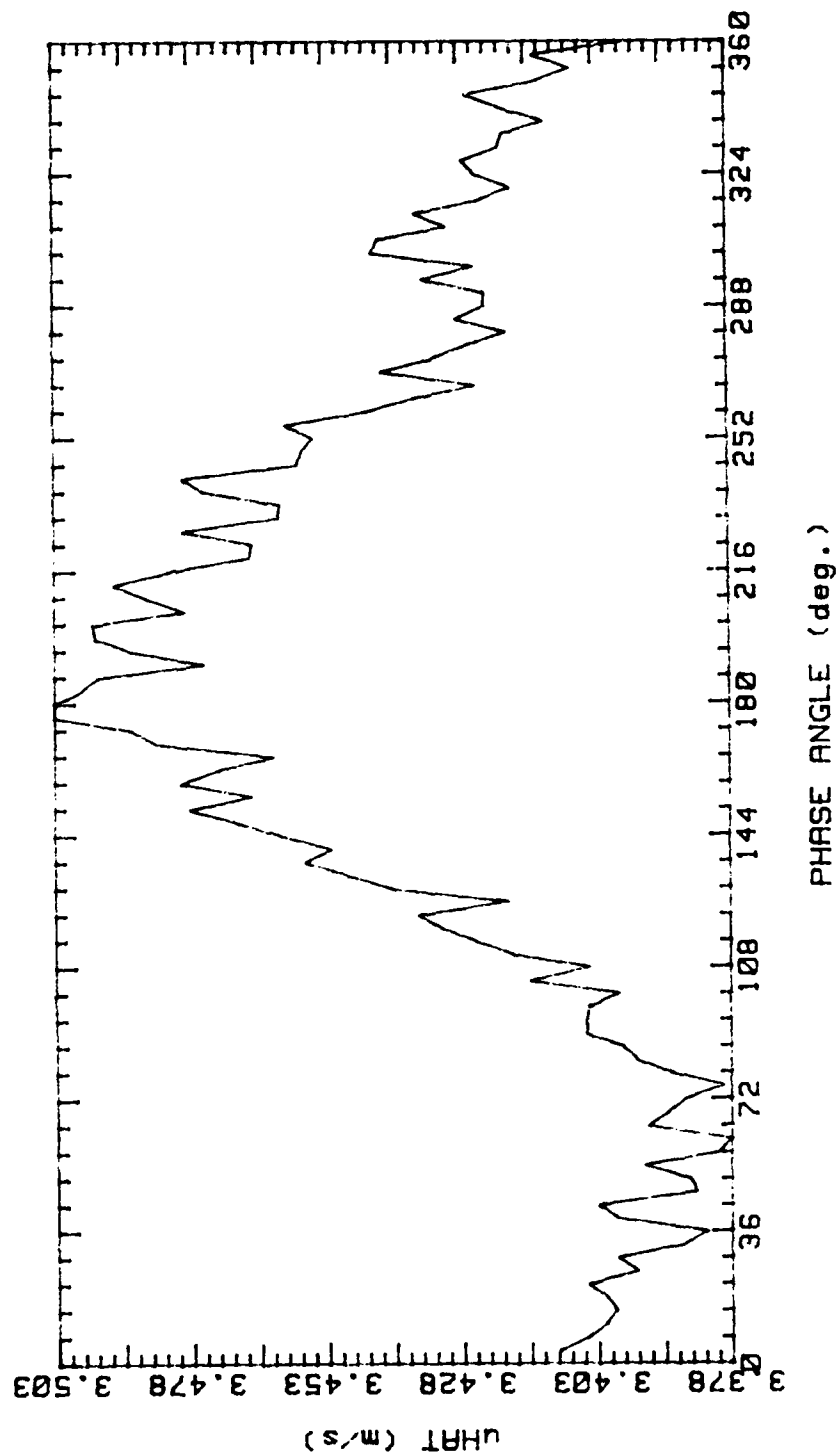


Figure 85.

RUNP6AA 93089.1845  
 AVG. VEL 3.538m/s RMS VEL .198m/s  
 OSC. FREQ. 0Hz STR. # 0  
 BULK VEL. 3.16m/s REY. # 2640

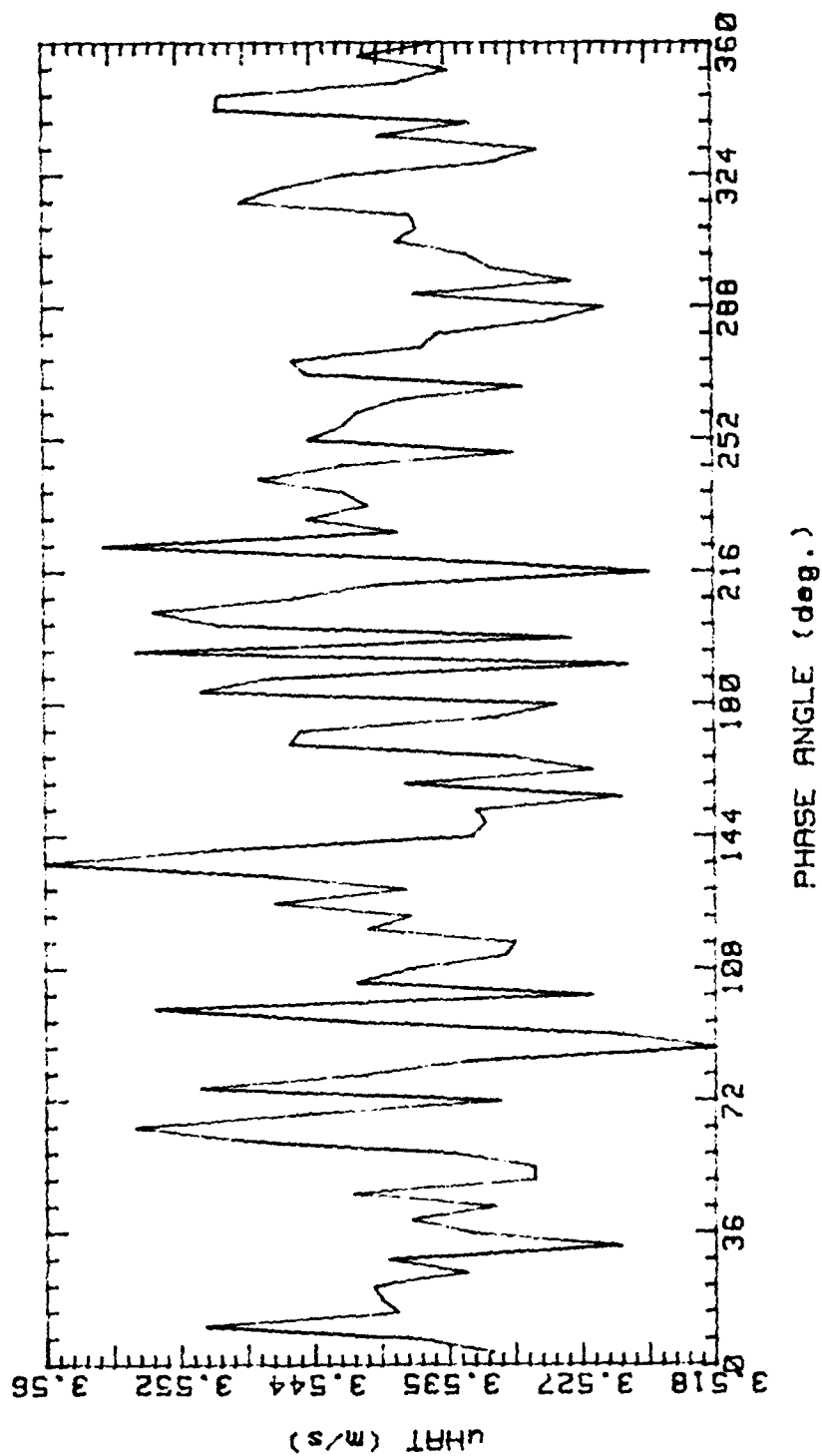


Figure 86.

RUNP6BA 93089.2041

AVG. VEL 3.332m/s RMS VEL .1892m/s  
OSC. FREQ. 1Hz STR. # .02525  
BULK VEL. 3.16m/s REY. # 2640

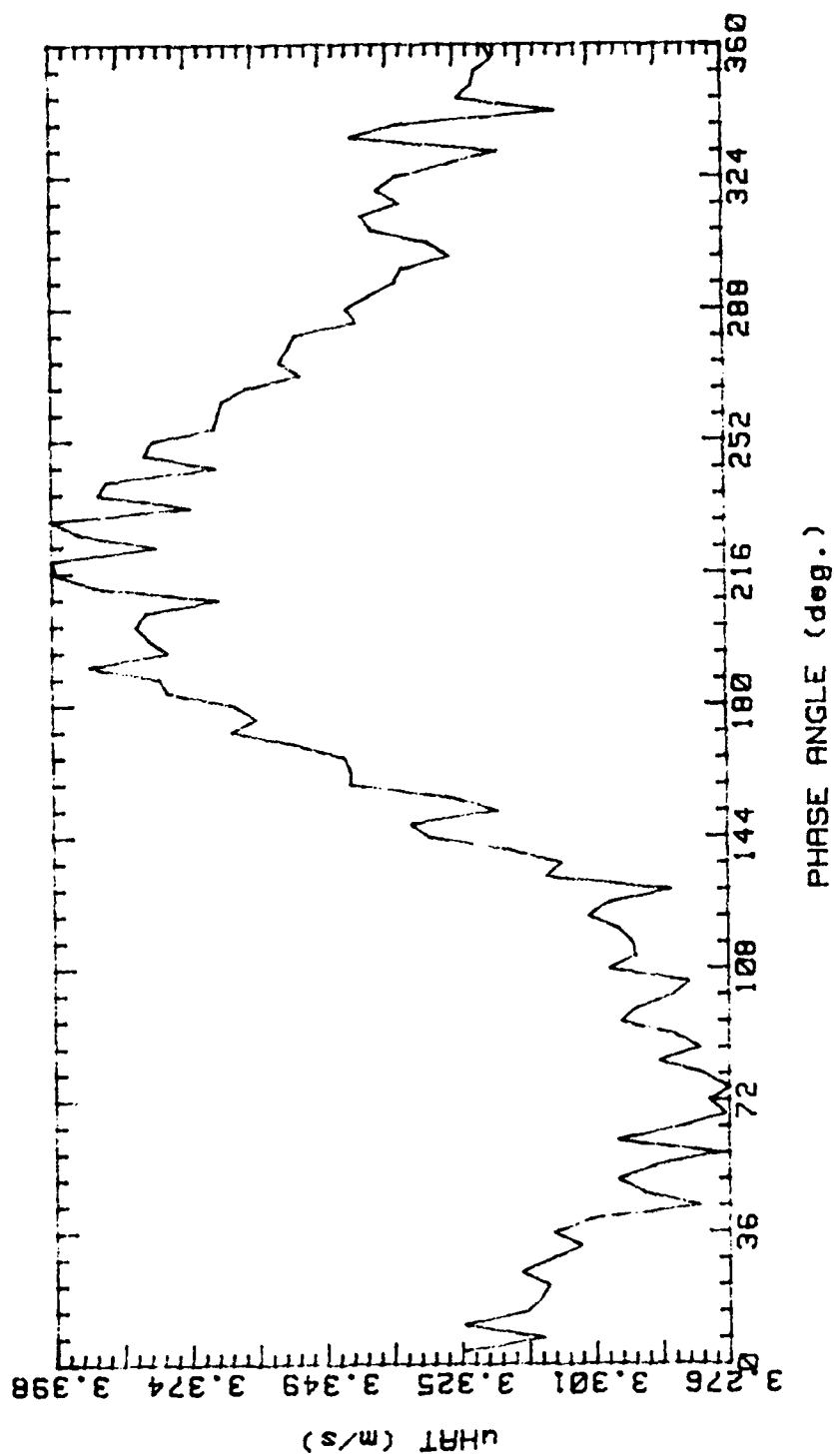


Figure 87.

RUNP7AA 93089.1901  
 AVG. VEL 3.327m/s RMS VEL .2572m/s  
 OSC. FREQ. 0Hz STR. # 0  
 BULK VEL. 3.16m/s REY. # 2640

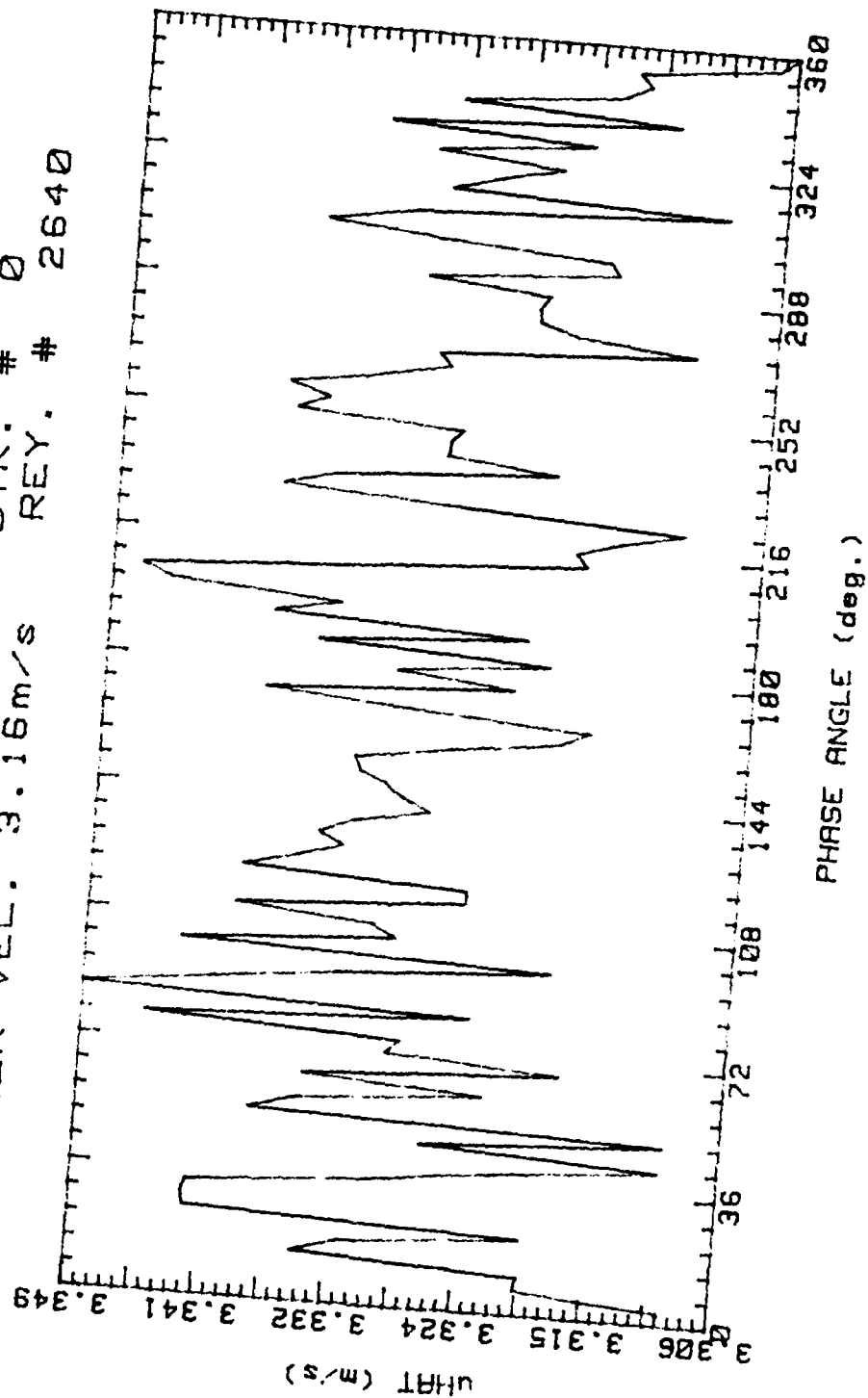


Figure 88.



RUNP7BA 93089.2053

AVG. VEL 3.386m/s RMS VEL .2623m/s  
OSC. FREQ. 1Hz STR. # .02525  
BULK VEL. 3.16m/s REY. # 2640

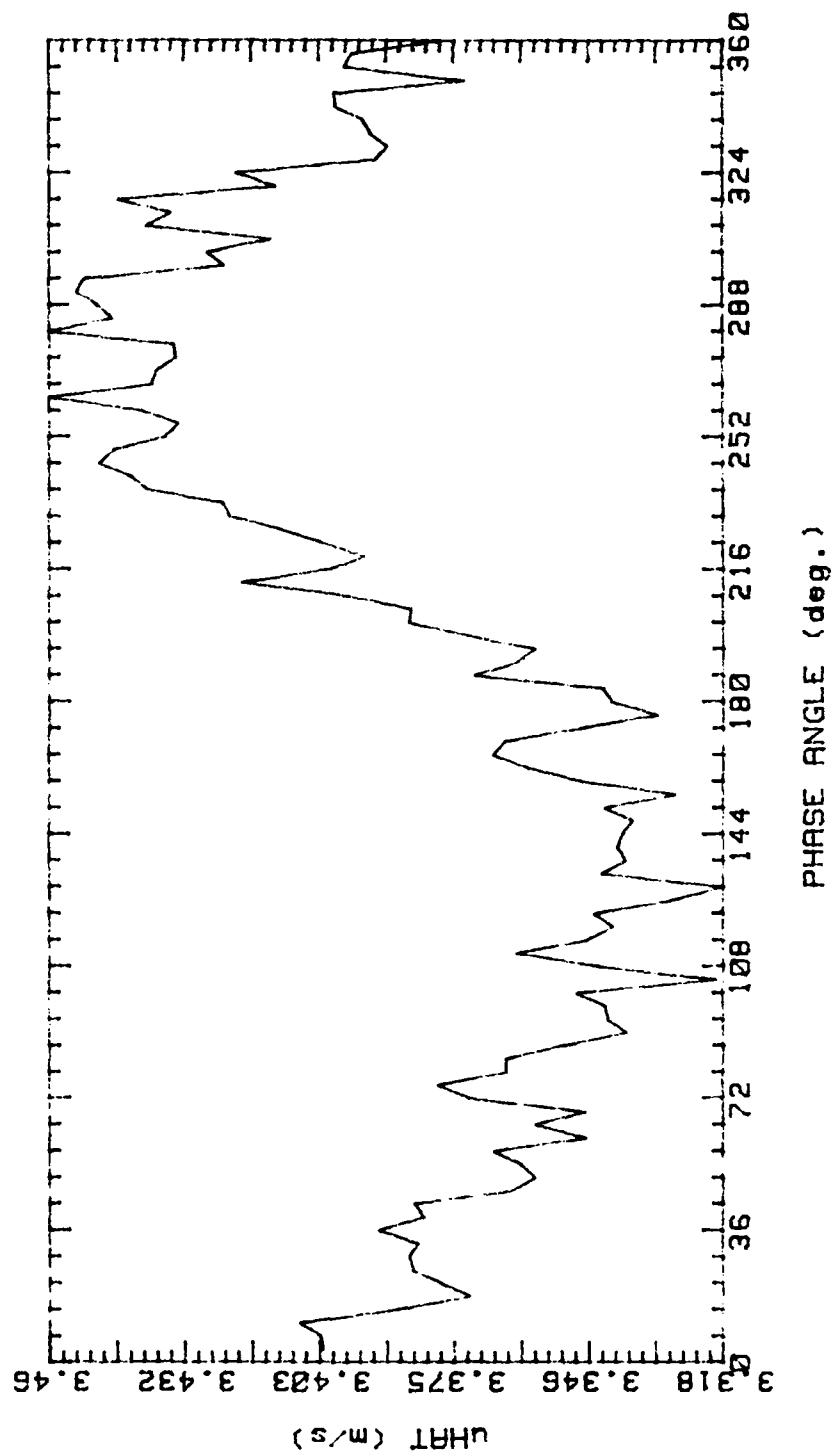


Figure 89.

RUNP8AA 93089.1917

AVG. VEL 3.088m/s RMS VEL .3464m/s

OSC. FREQ. 0Hz STR. # 0

BULK VEL. 3.16m/s REY. # 2640

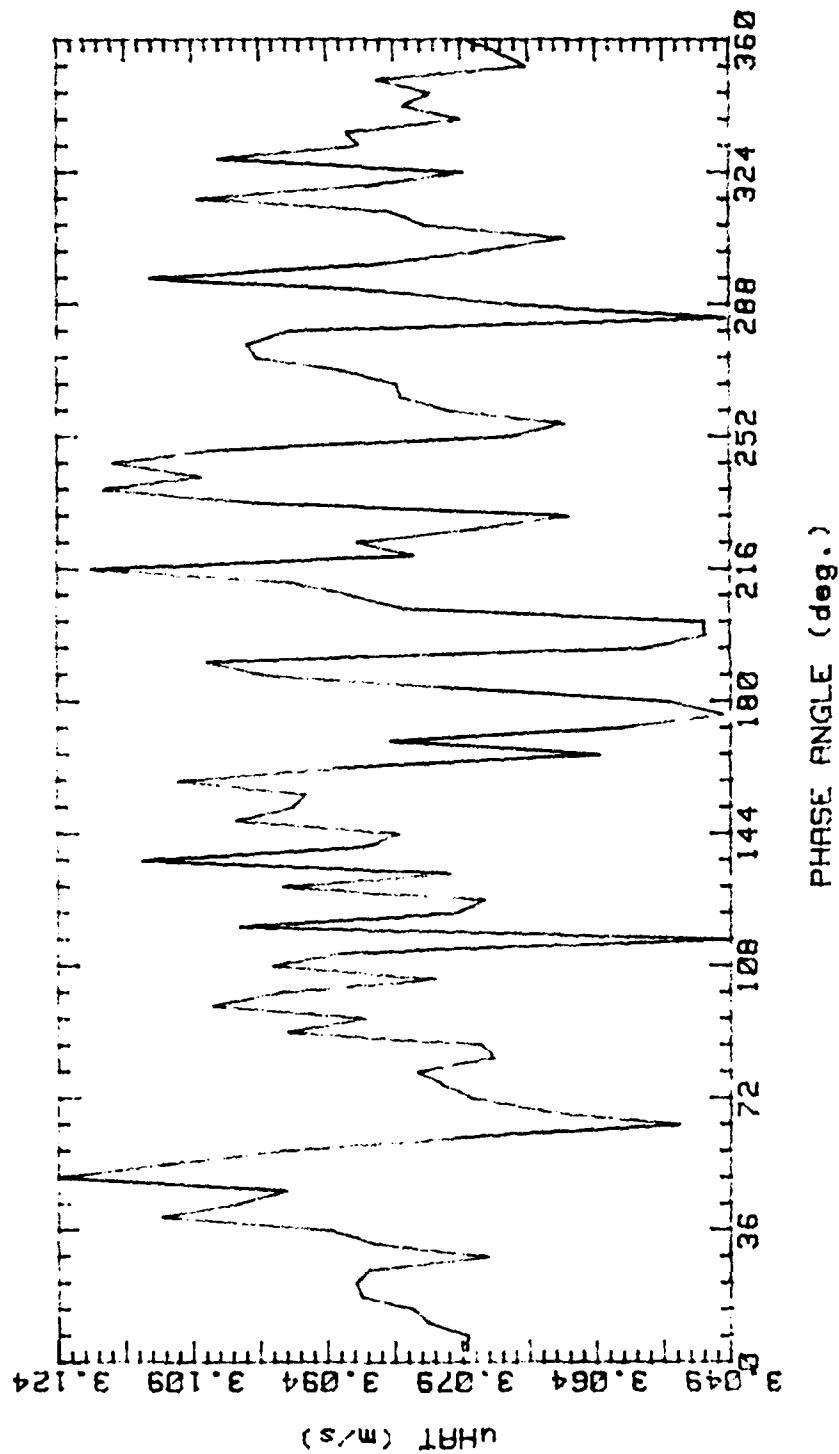


Figure 90.

RUNP8BA 93089.2106

AVG. VEL. 2.991m/s RMS VEL .3459m/s  
OSC. FREQ. 1Hz STR. # .02525  
BULK VEL. 3.16m/s REY. # 2640

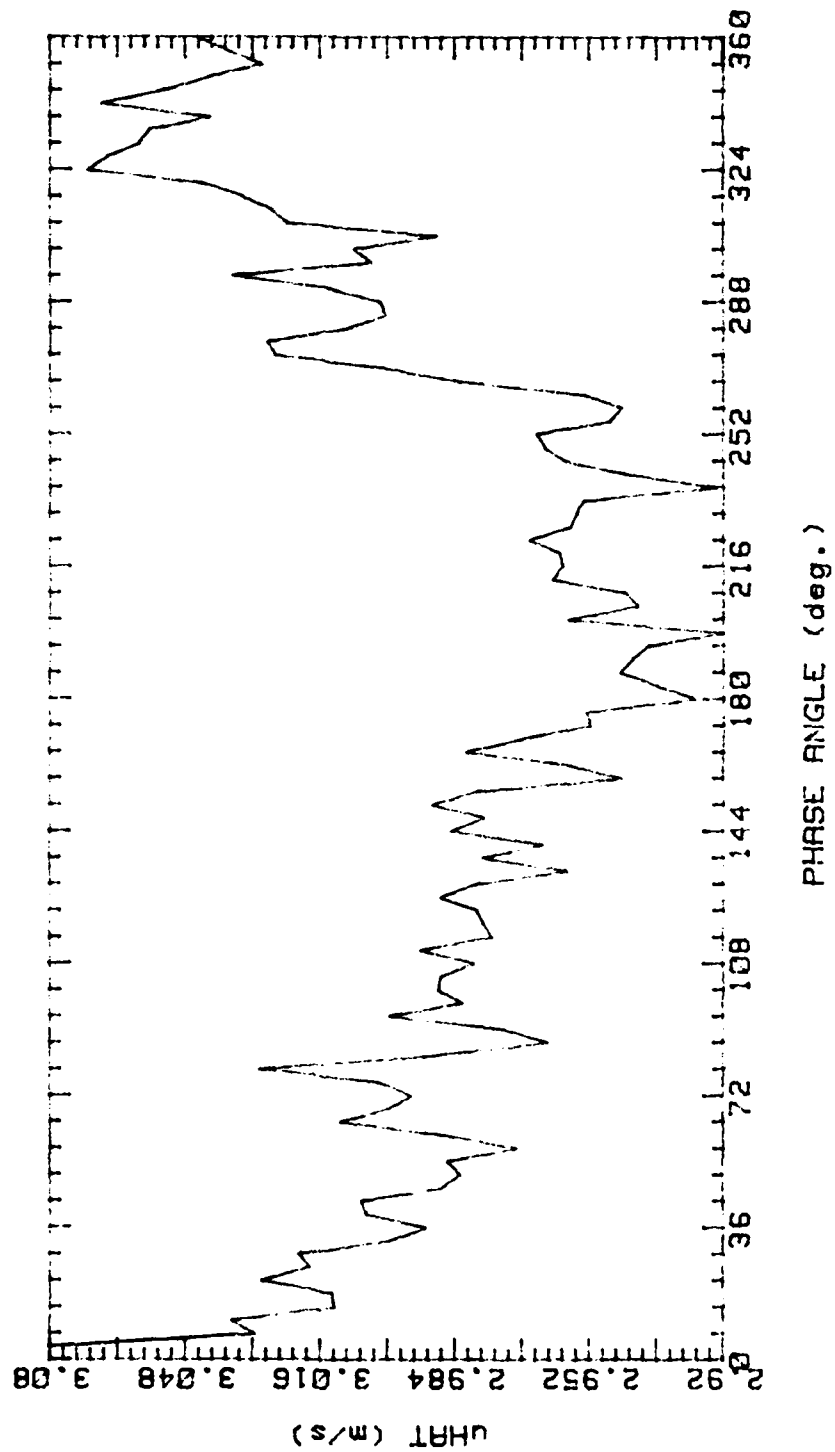


Figure 91.

RMS Velocity Profile Development  
with No Imposed Unsteadiness

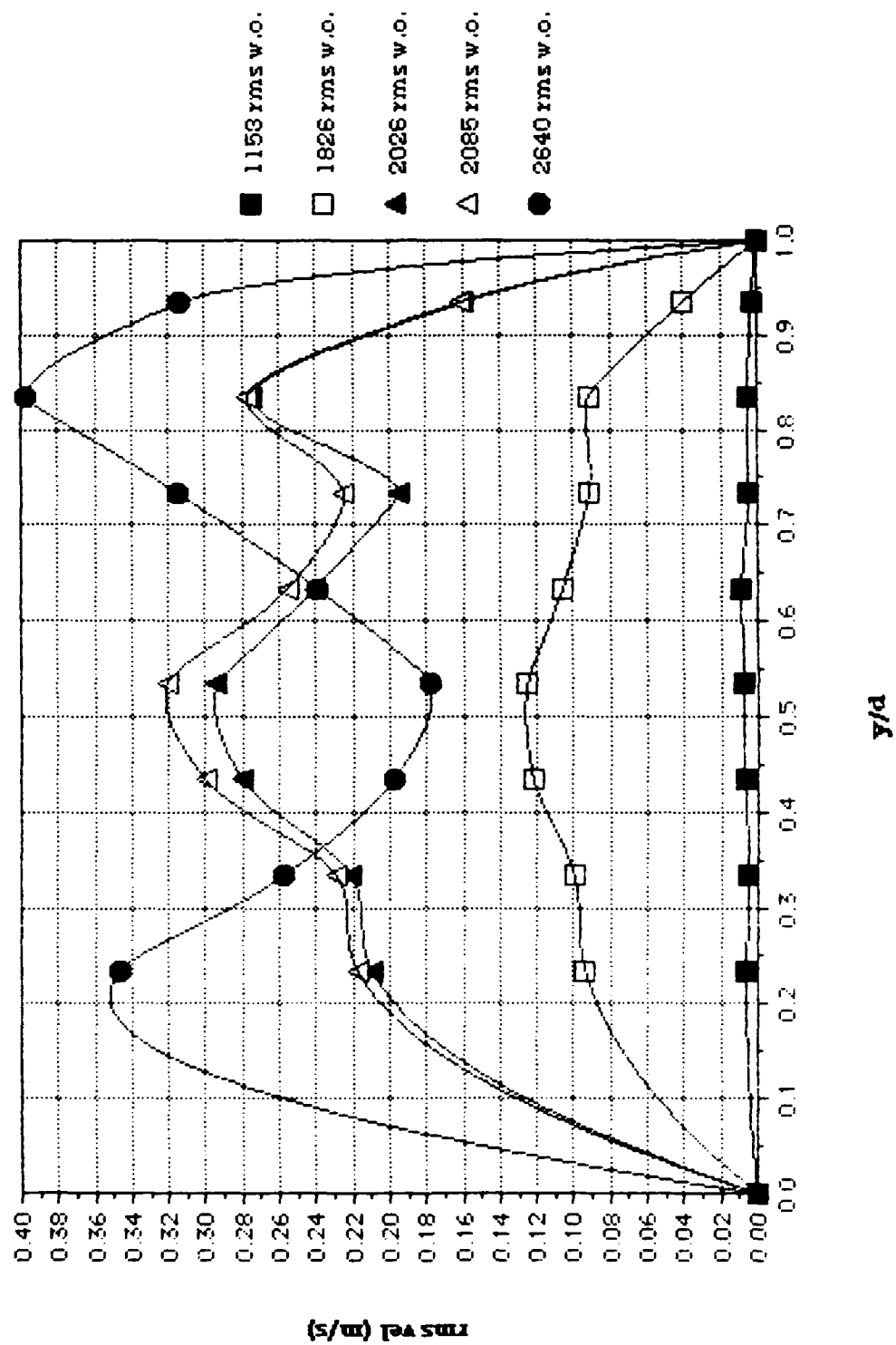


Figure 92.

RMS Velocity Profile Development  
with 1 Hz Imposed Unsteadiness

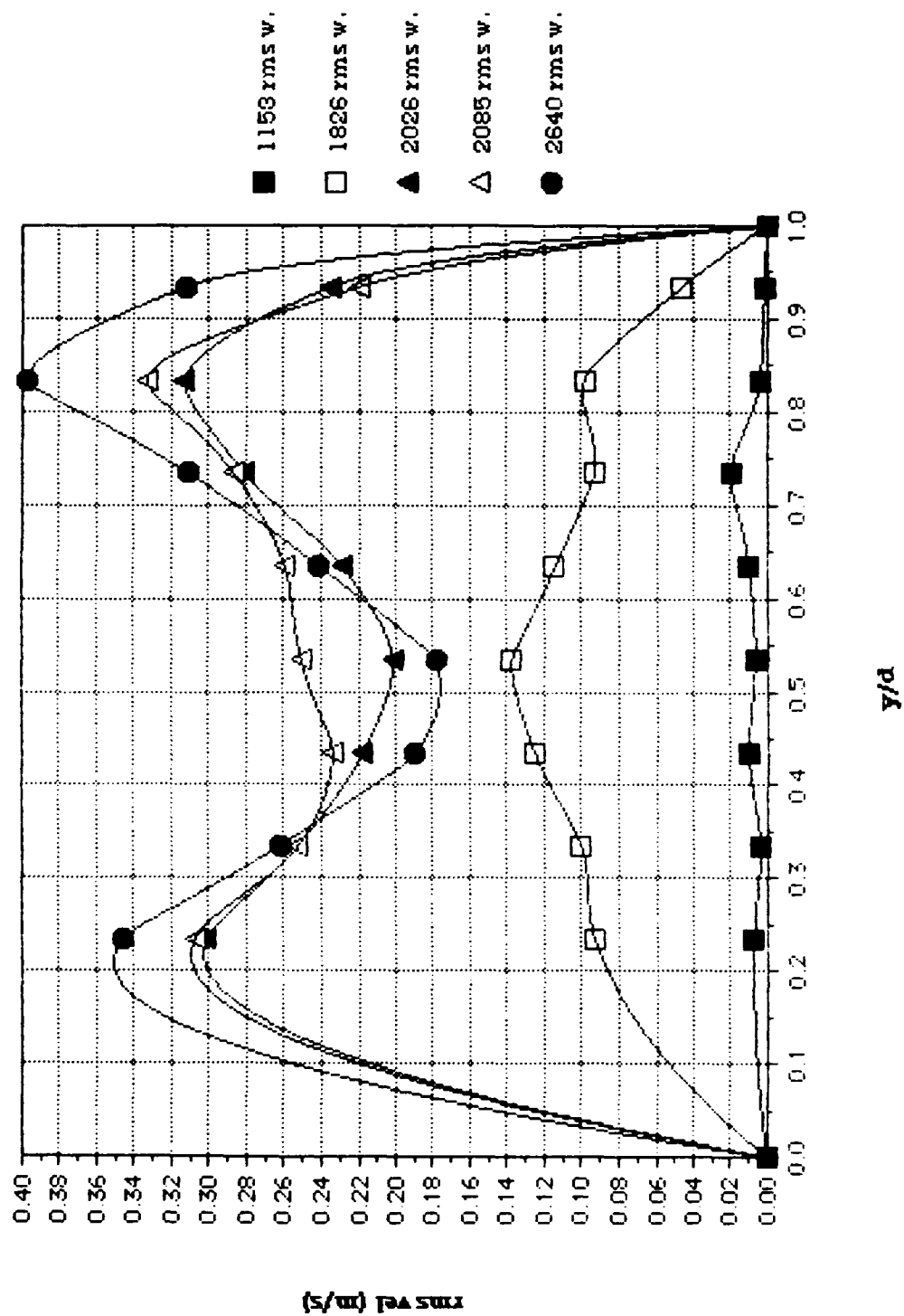


Figure 93.

RMS Velocity Profile at Re No. = 1153  
with 1 Hz Imposed Unsteadiness

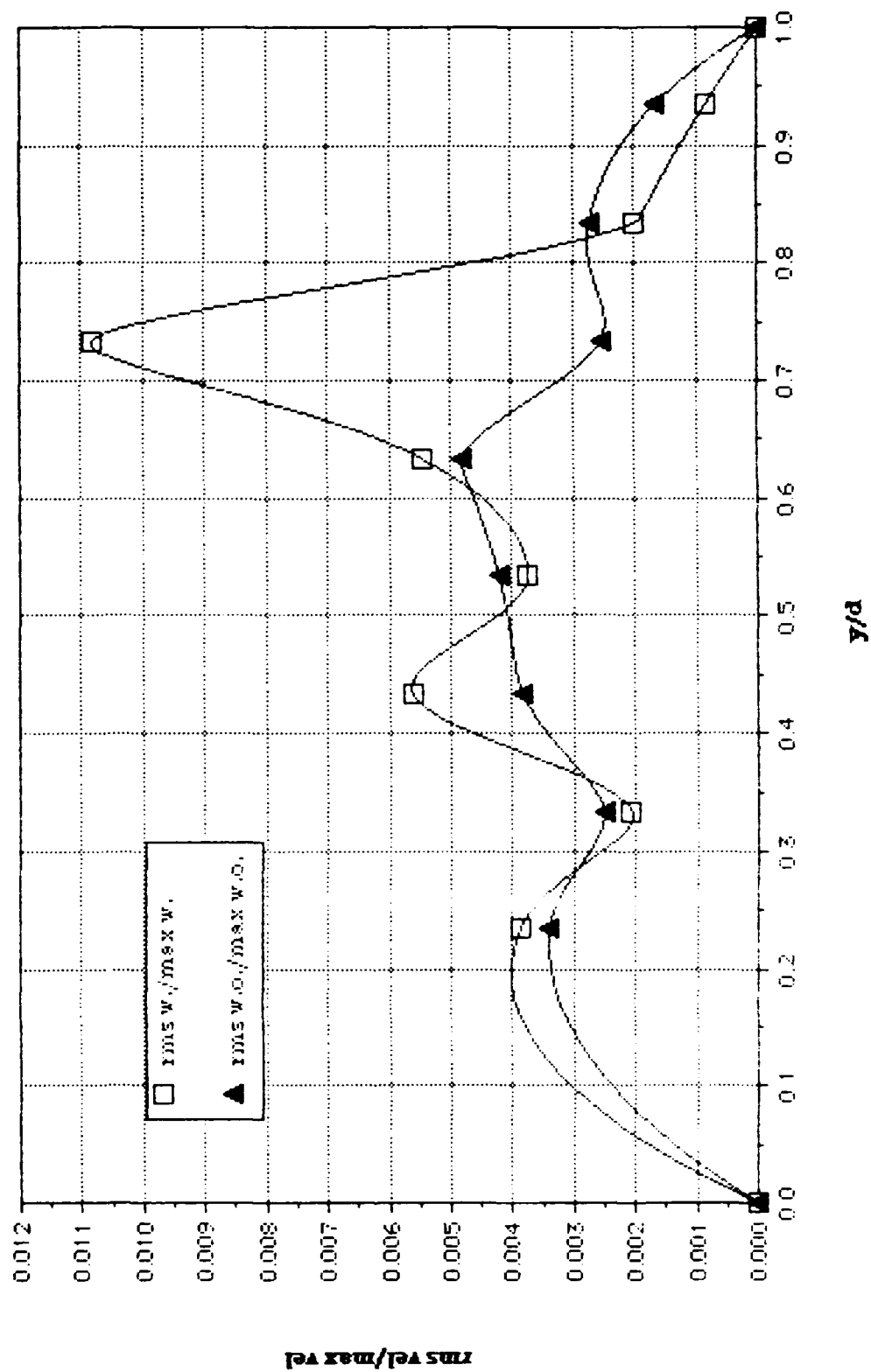


Figure 94.

RMS Velocity Profile at Re No. = 1826  
with 1 Hz Imposed Unsteadiness

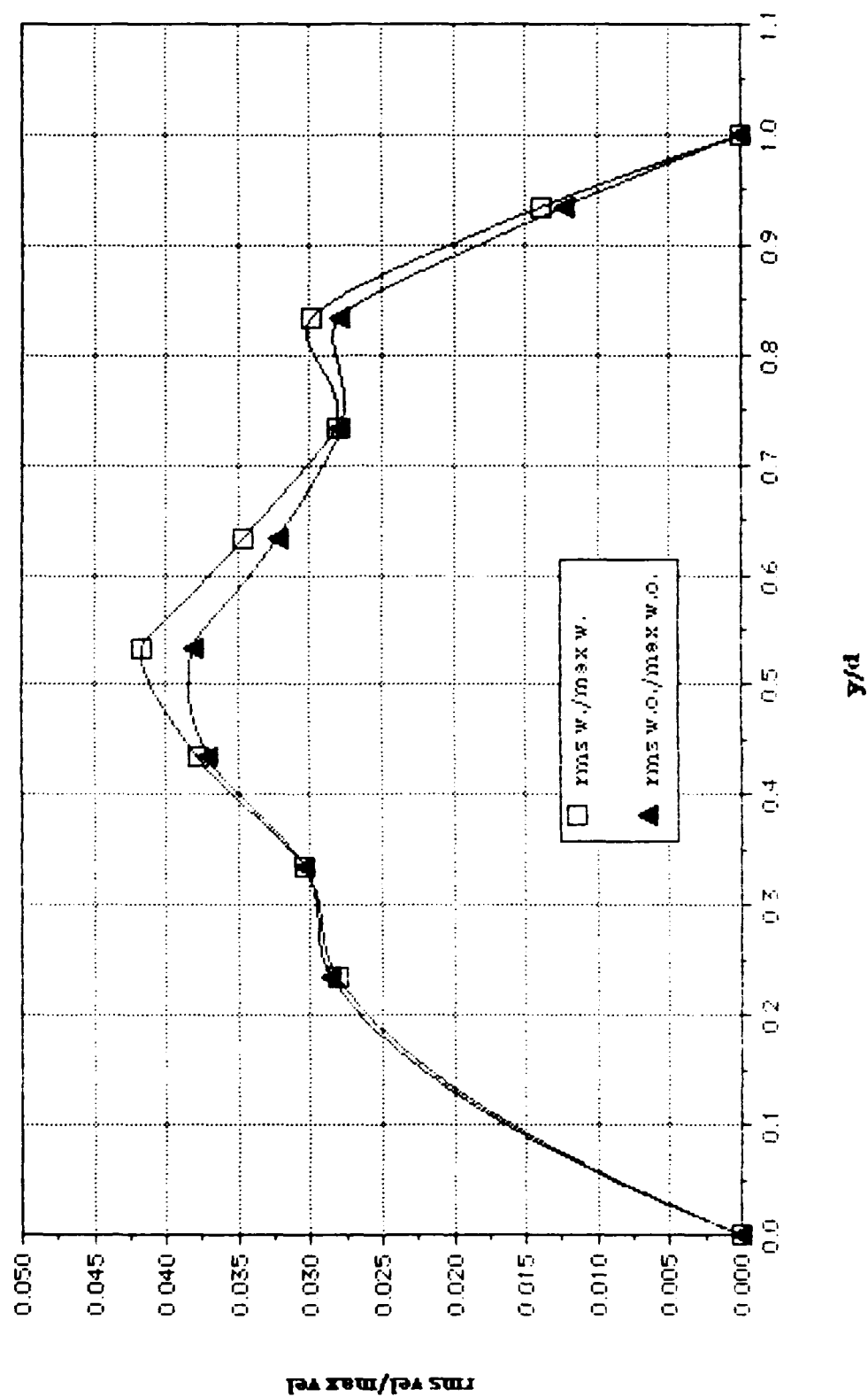


Figure 95.

RMS Velocity Profile at Re No. = 2026  
with 1 Hz Imposed Unsteadiness

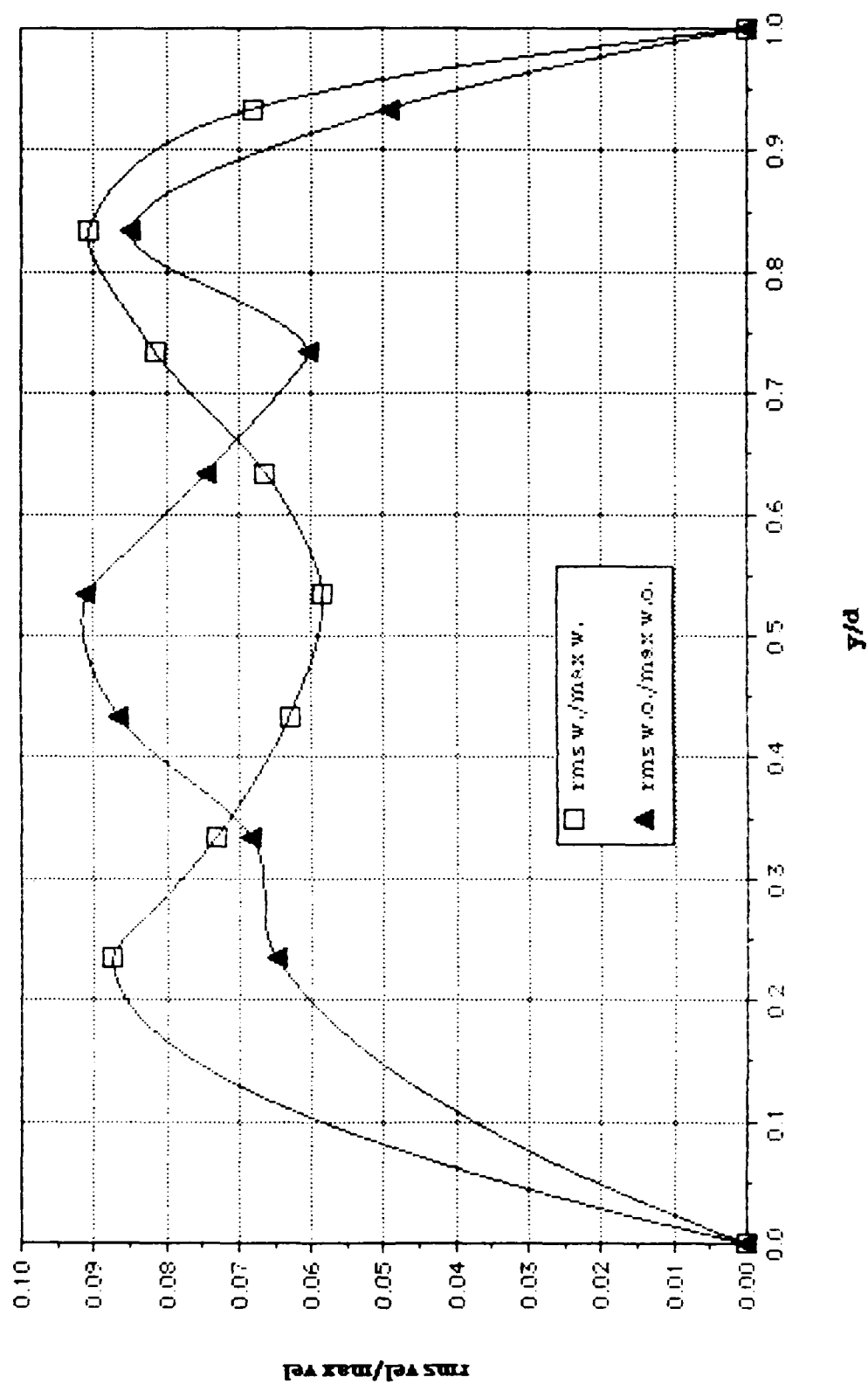


Figure 96.



RMS Velocity Profile at Re No. = 2085  
with 1 Hz Imposed Unsteadiness

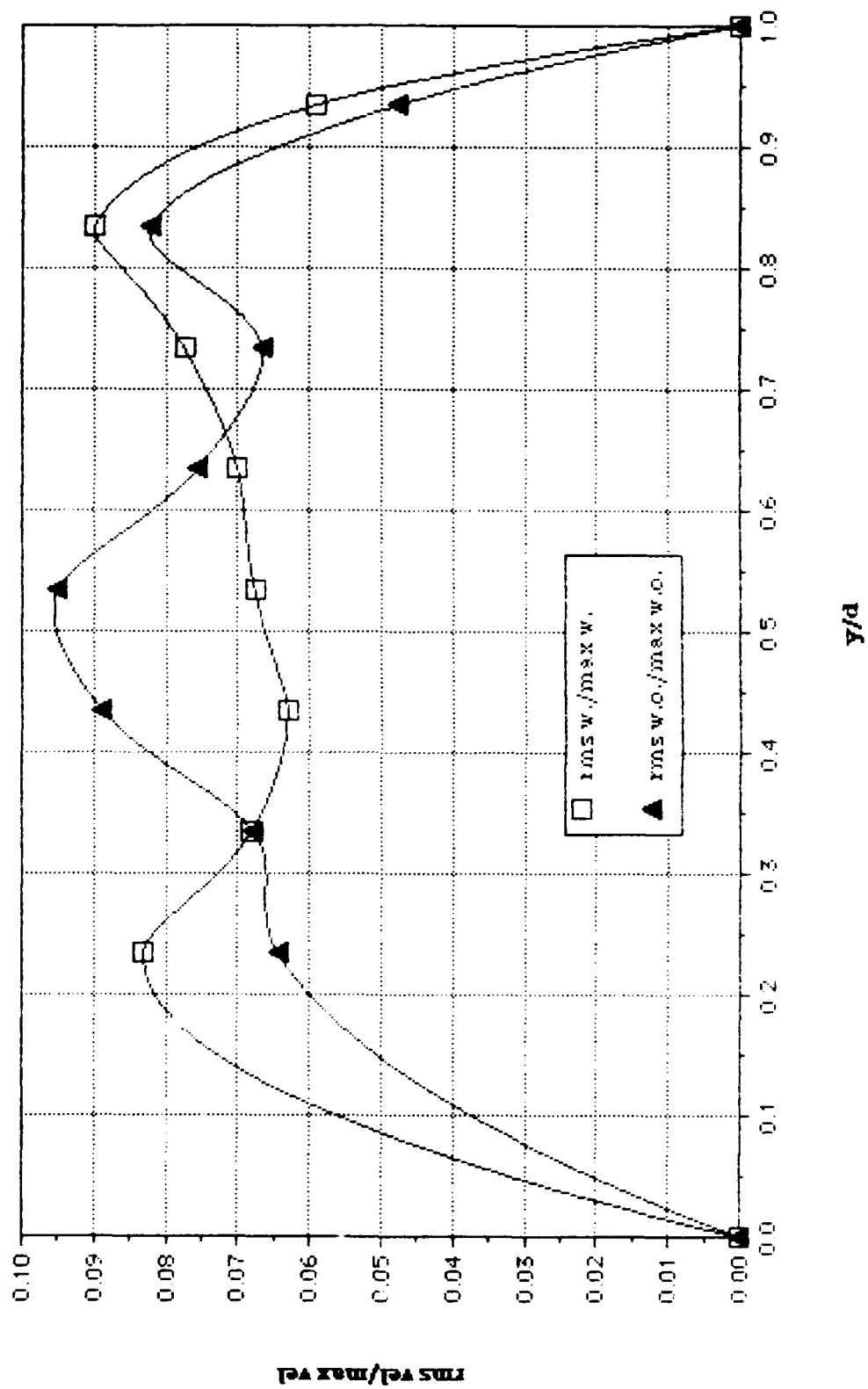


Figure 97.

**RMS Velocity Profile at Re No. = 2640  
with 1 Hz Imposed Unsteadiness**

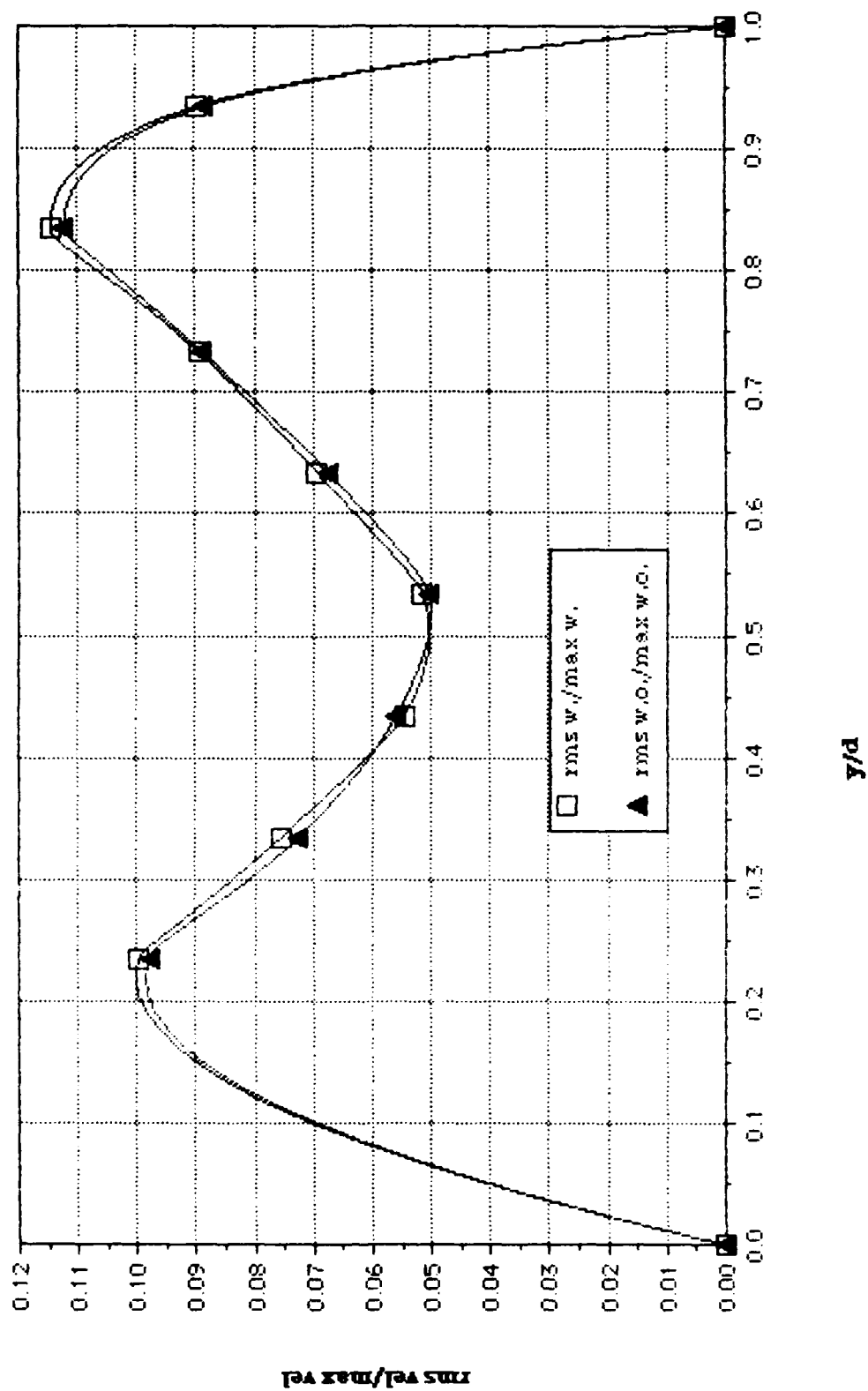


Figure 98.

RUNP1W 280989.2015

AVG. VEL .7033m/s RMS VEL .04045m/s  
OSC. FREQ. 0Hz STR. # 0  
BULK VEL. 2.185m/s REY. # 1826

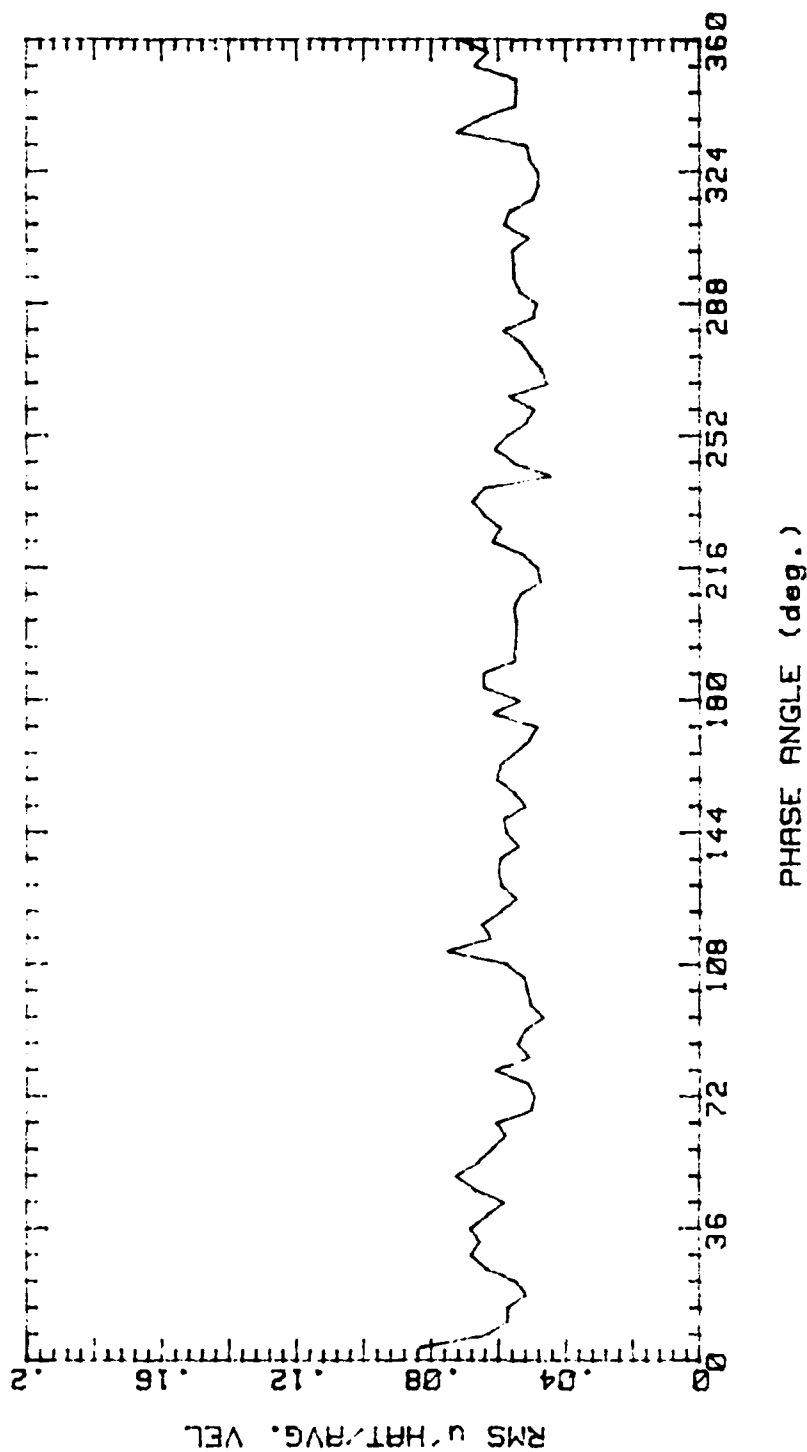
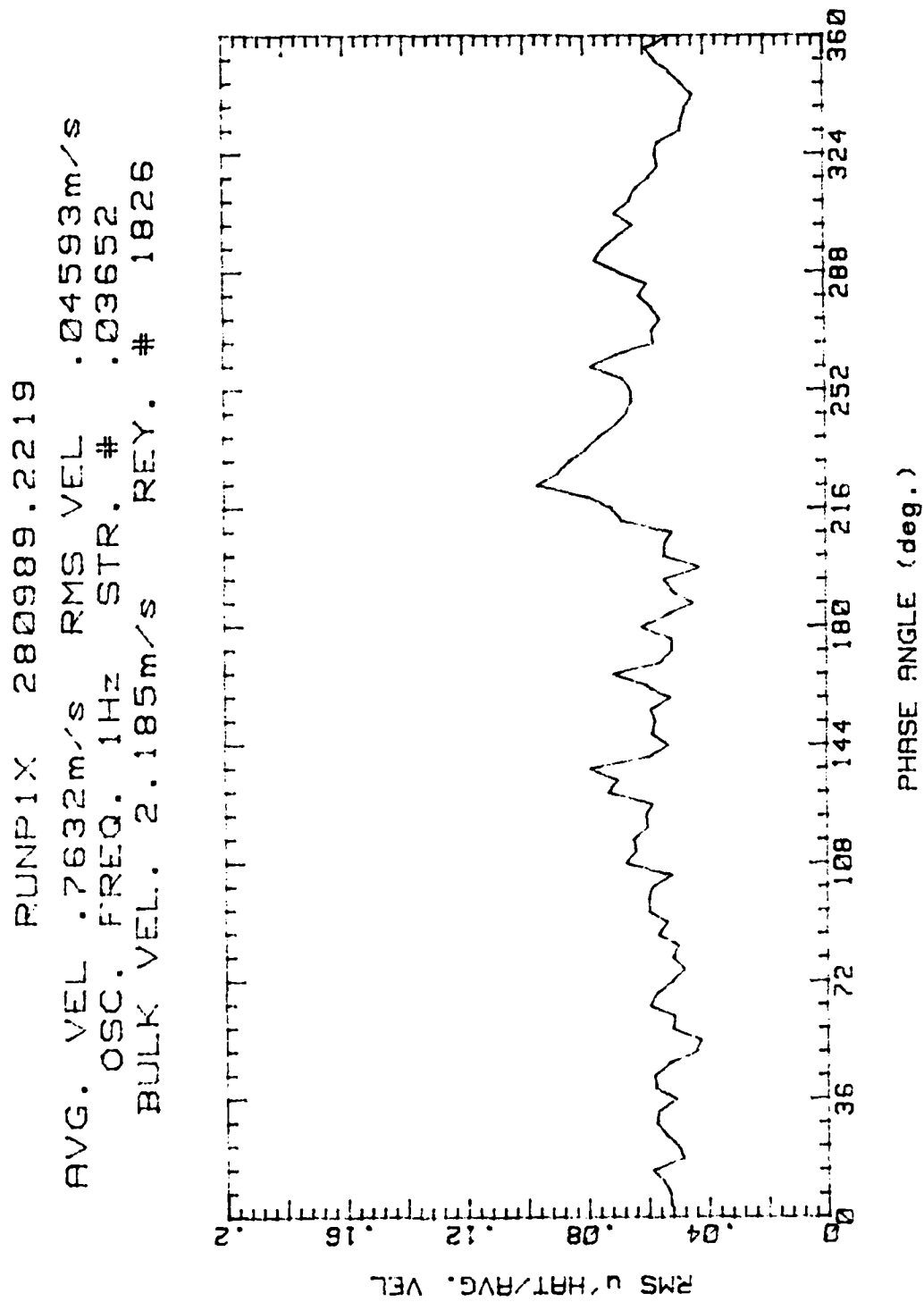


Figure 99.

Figure 100.



RUNP2W 280989.2028

AVG. VEL 1.554m/s RMS VEL .09169m/s  
OSC. FREQ. 0Hz STR. # 0  
BULK VEL. 2.185m/s REY. # 1826

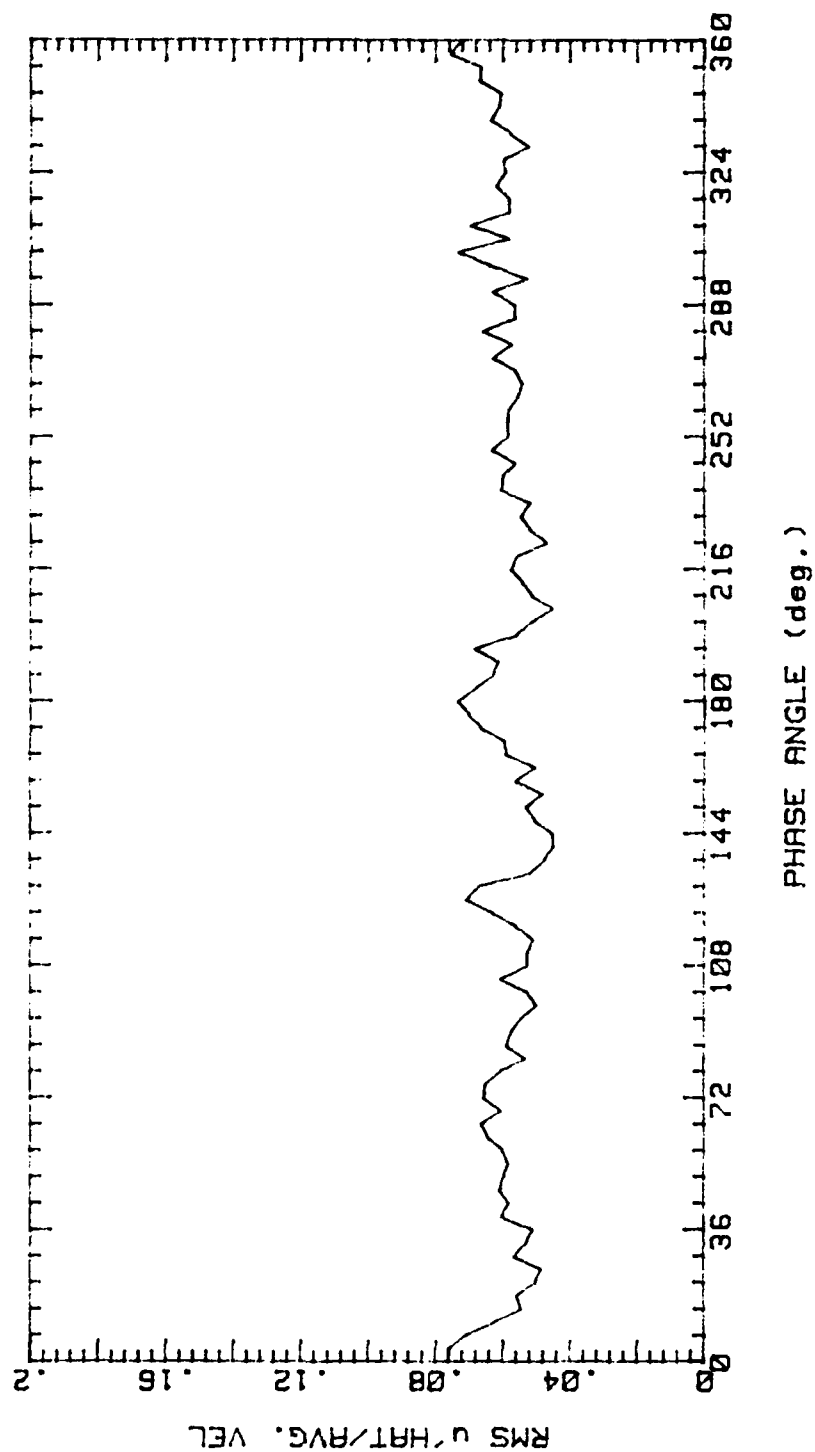


Figure 101.

RUNP2X 280989.2234  
 AVG. VEL 1.66m/s RMS VEL .0985m/s  
 OSC. FREQ. 1Hz STR. # .03652  
 BULK VEL. 2.185m/s REY. # 1026

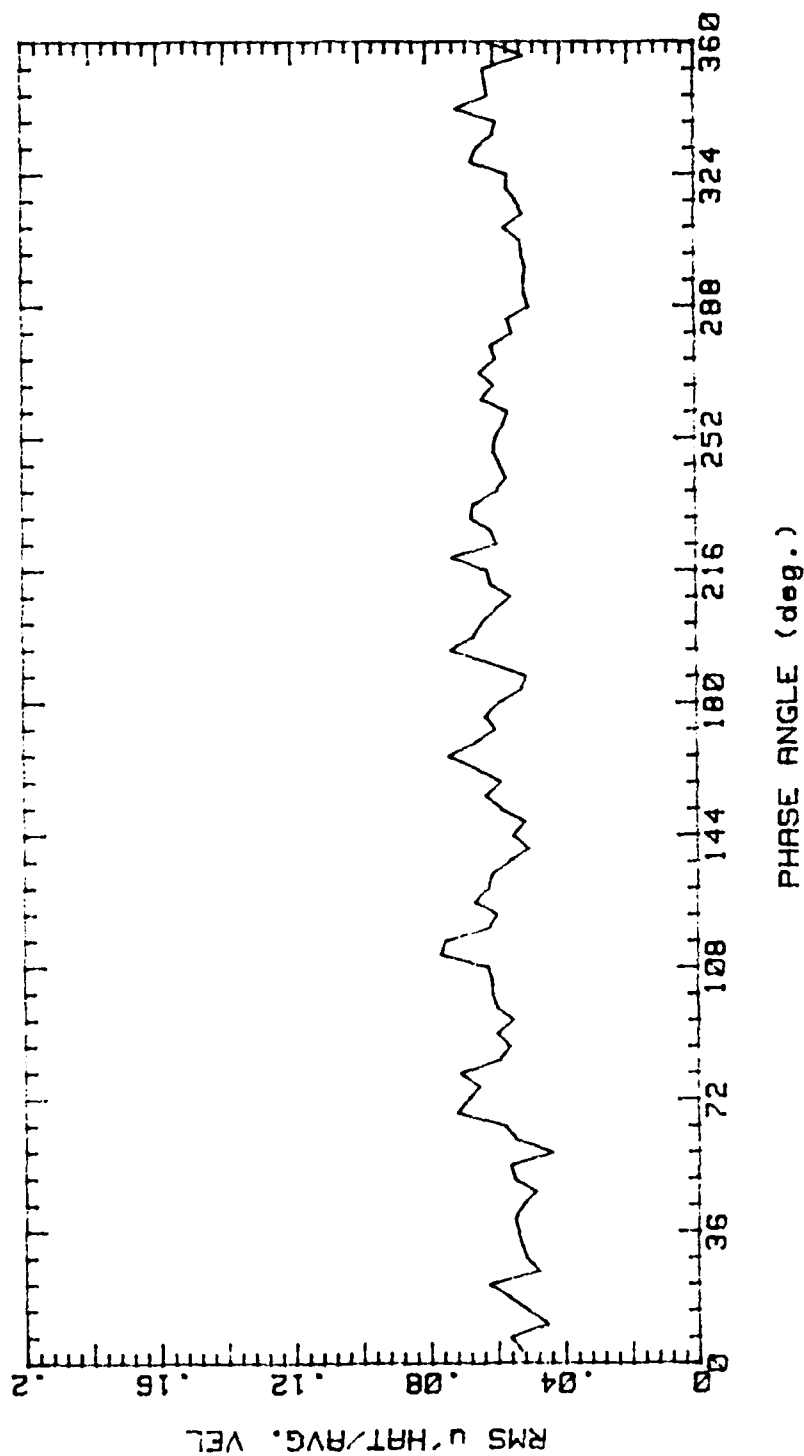


Figure 102.

RUNP3W 280989.2045

AVG. VEL 2.47m/s RMS VEL .09151m/s  
OSC. FREQ. 0Hz STR. # 0  
BULK VEL. 2.185m/s REY. # 1826

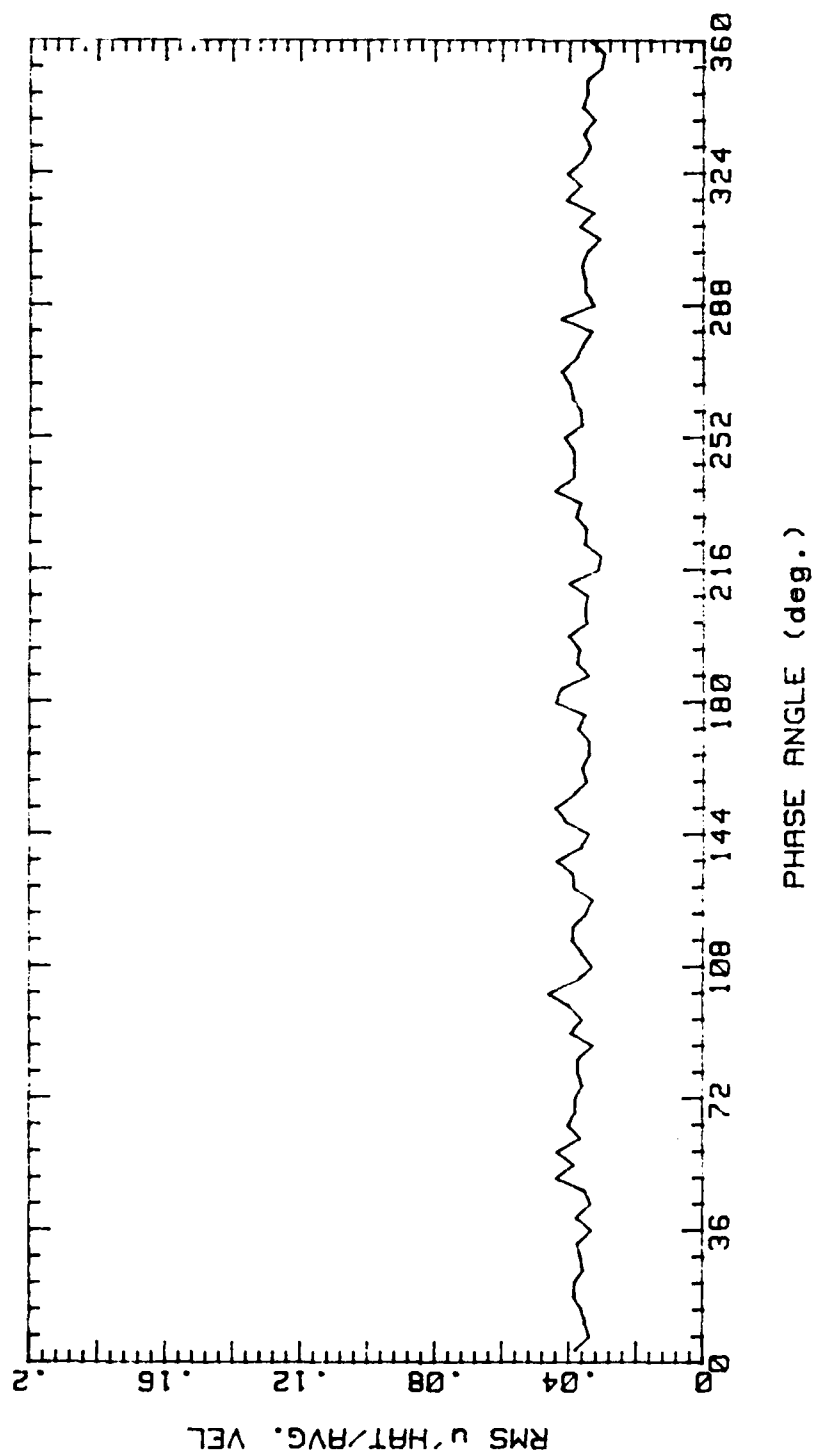


Figure 103.

RUNP3X 280989.2248

AVG. VEL 2.431m/s RMS VEL .09303m/s  
OSC. FREQ. 1Hz STR. # .03652  
BULK VEL. 2.185m/s REY. # 1826

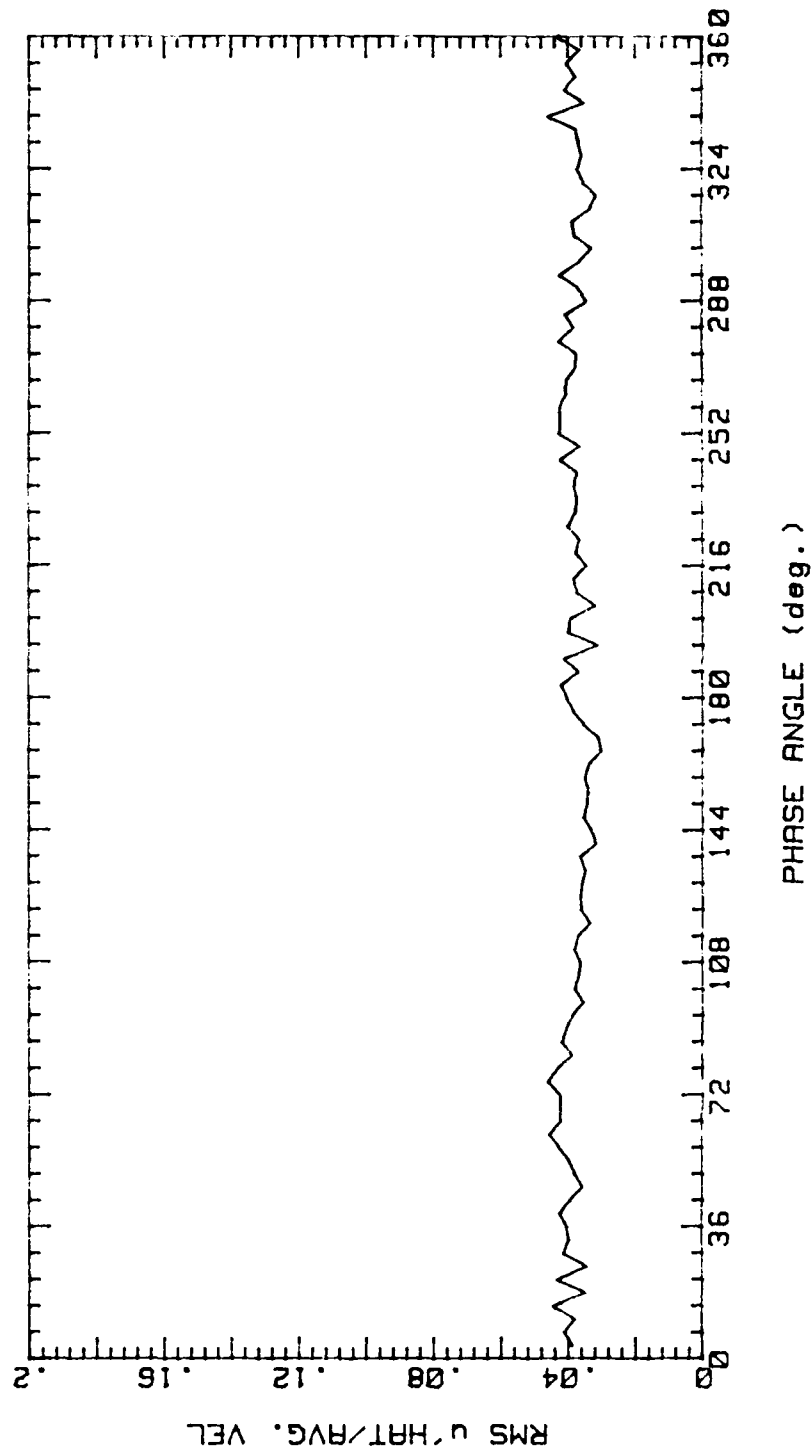


Figure 104.



RUNP4W 280989.2102

AVG. VEL. 2.957m/s RMS VEL. .1059m/s  
OSC. FREQ. 0Hz STR. # 0  
BULK VEL. 2.185m/s REY. # 1826

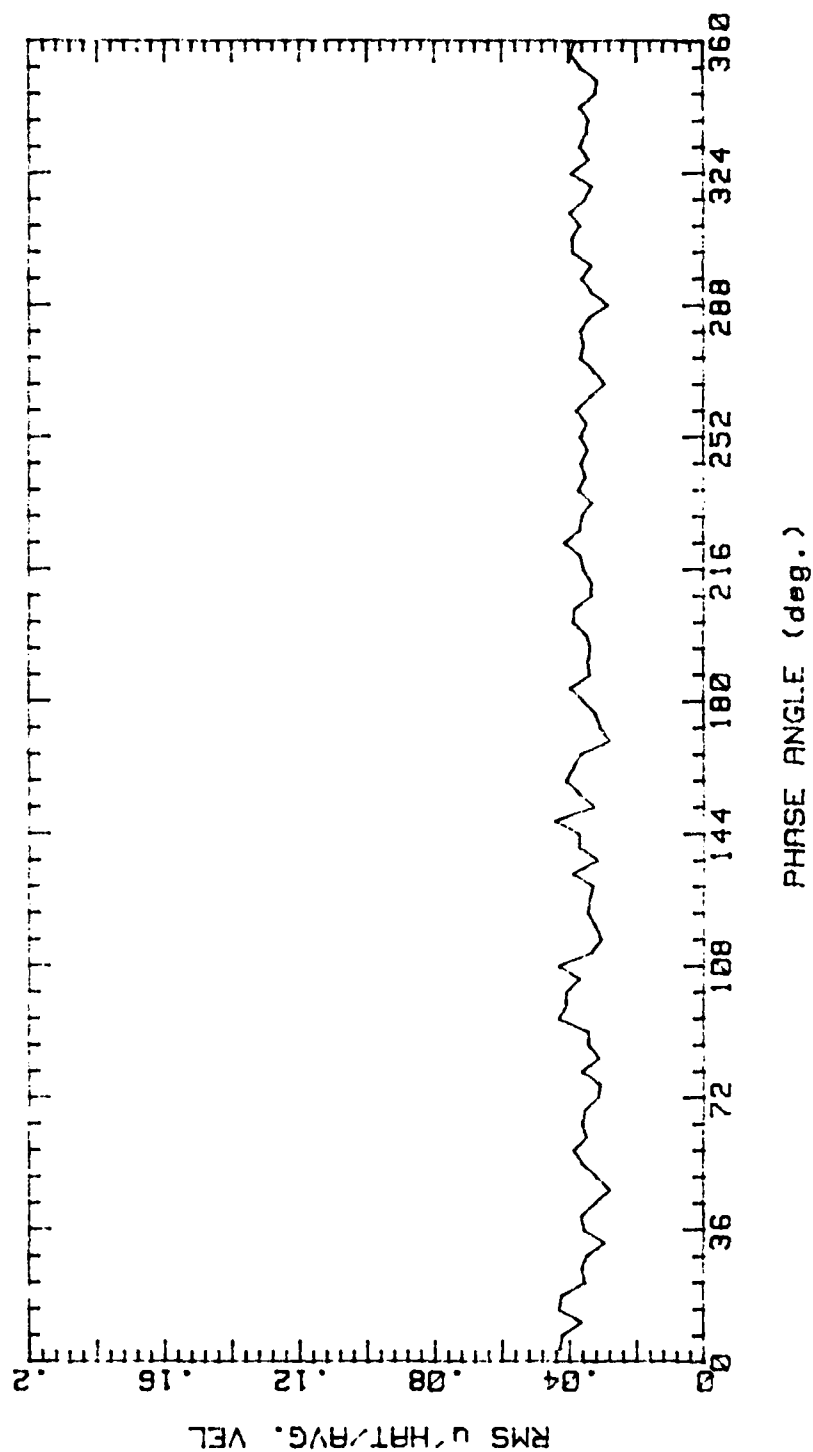


Figure 105.

RUNP4X 280989.2301

AVG. VEL 2.958m/s RMS VEL .1142m/s  
OSC. FREQ. 1Hz STR. # .03652  
BULK VEL. 2.185m/s REY. # 1826

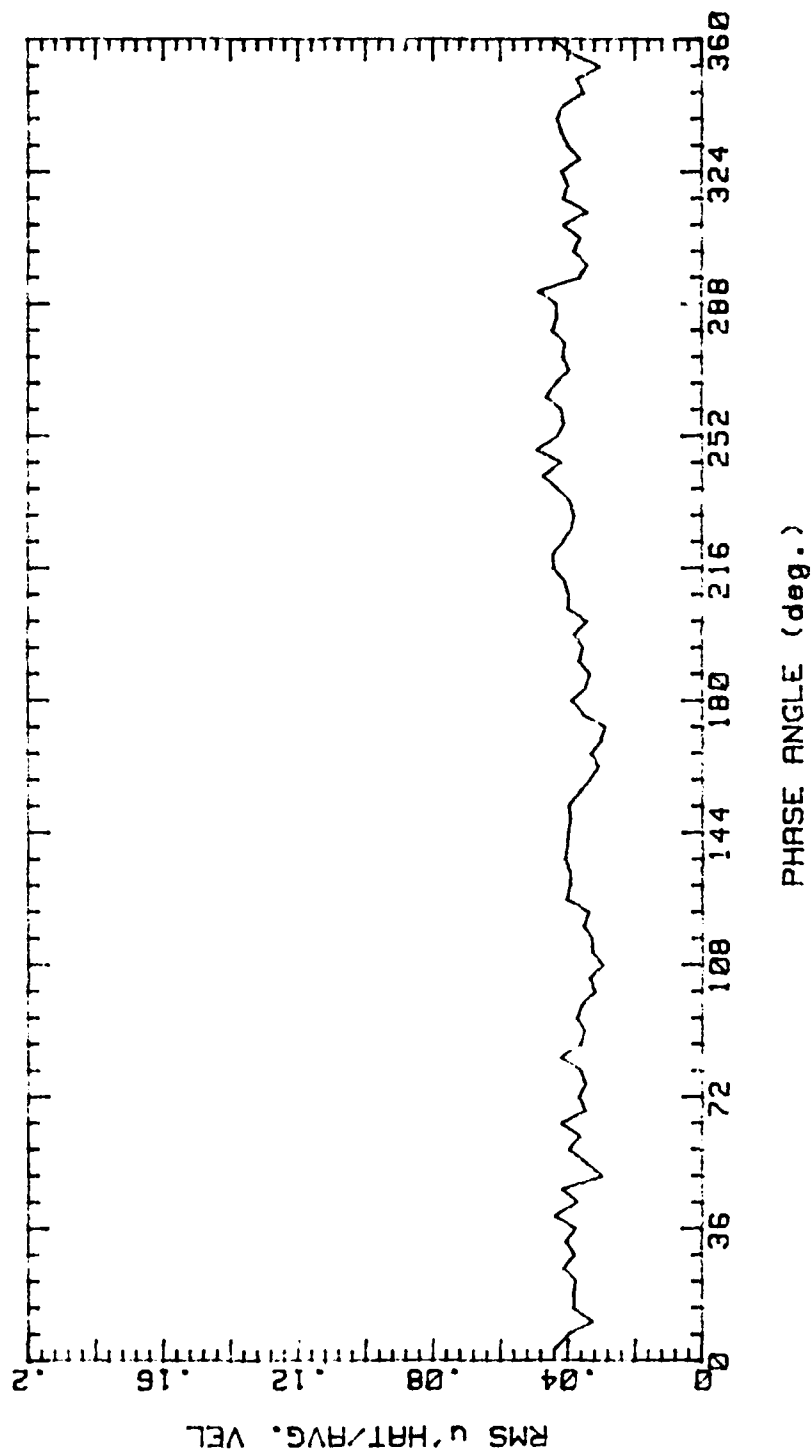


Figure 106.

RUNP5W 280989.2116

AVG. VEL 3.284m/s RMS VEL .1252m/s

OSC. FREQ. 0Hz STR. # 0

BULK VEL. 2.185m/s REY. # 1826

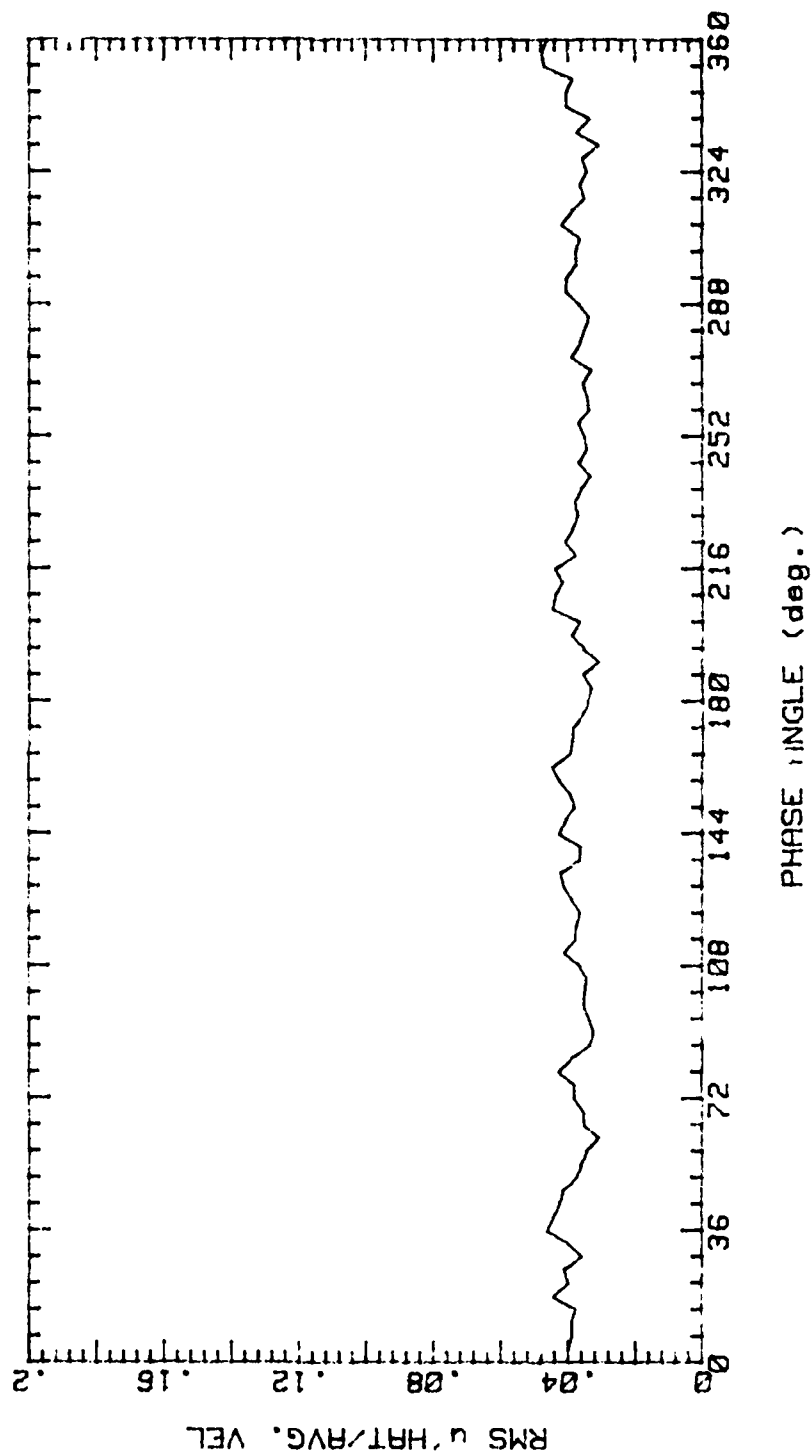


Figure 107.

RUNP5X 280989.2315

AVG. VEL 3.302m/s RMS VEL .1376m/s  
OSC. FREQ. 1Hz STR. # .03652  
BULK VEL. 2.185m/s REY. # 1826

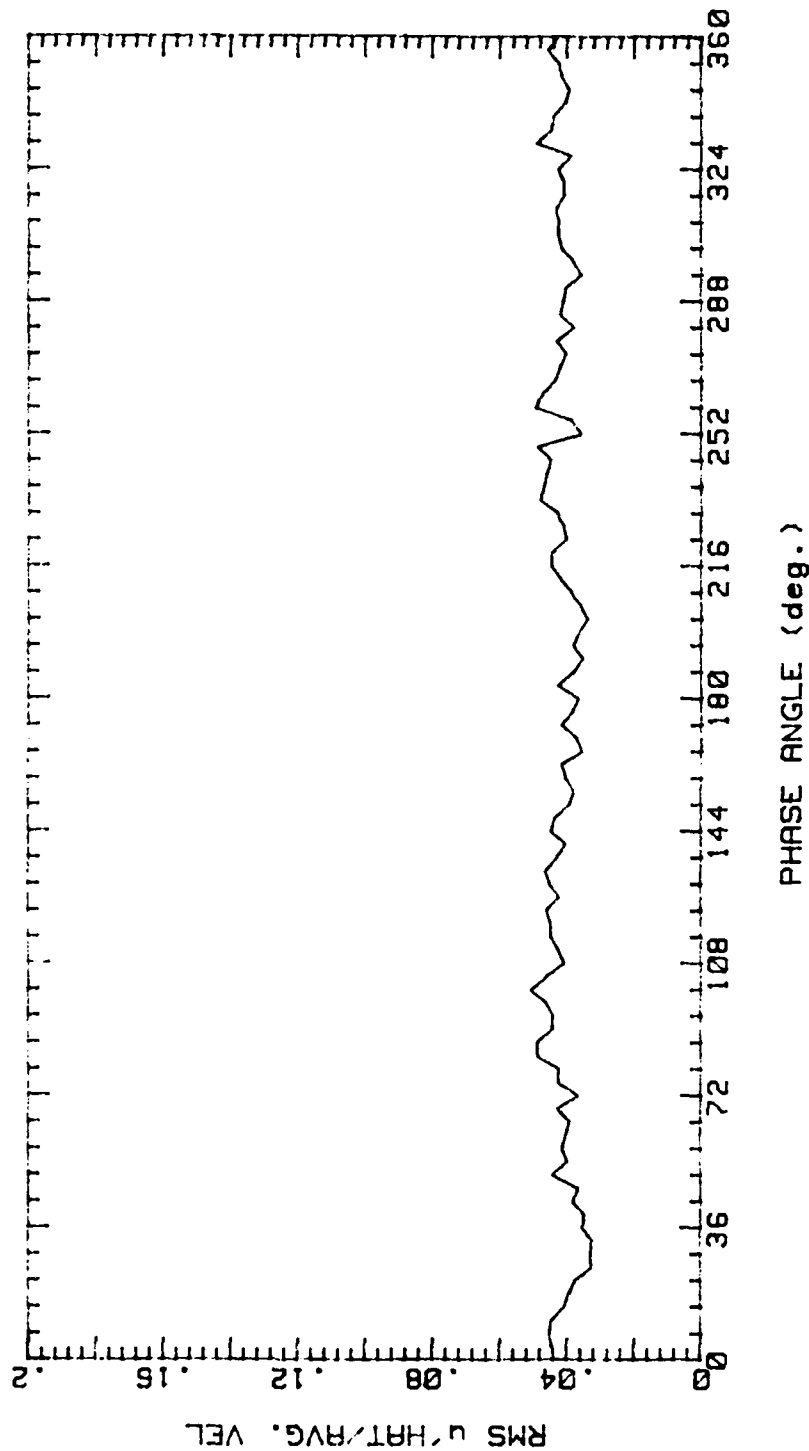


Figure 108.

RUNP6W 280989.2133  
 AVG. VEL 3.134m/s RMS VEL .1216m/s  
 OSC. FREQ. 0Hz STR. # 0  
 BULK VEL. 2.185m/s REY. # 1826

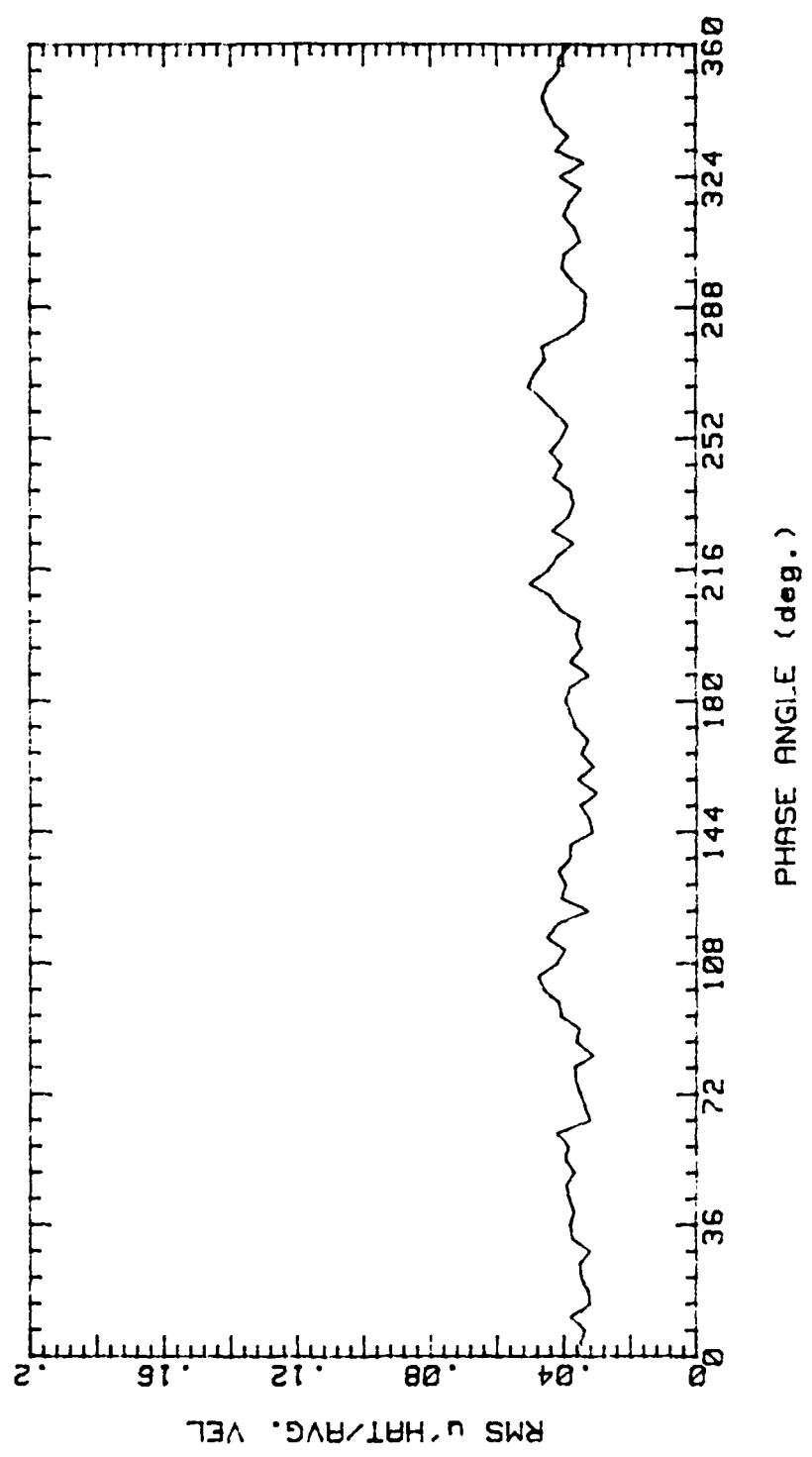


Figure 109.

RUNP6X 280989.2329

AVG. VEL 3.168m/s RMS VEL .1248m/s

OSC. FREQ. 1Hz STR. # .03652

BULK VEL. 2.185m/s REY. # 1826

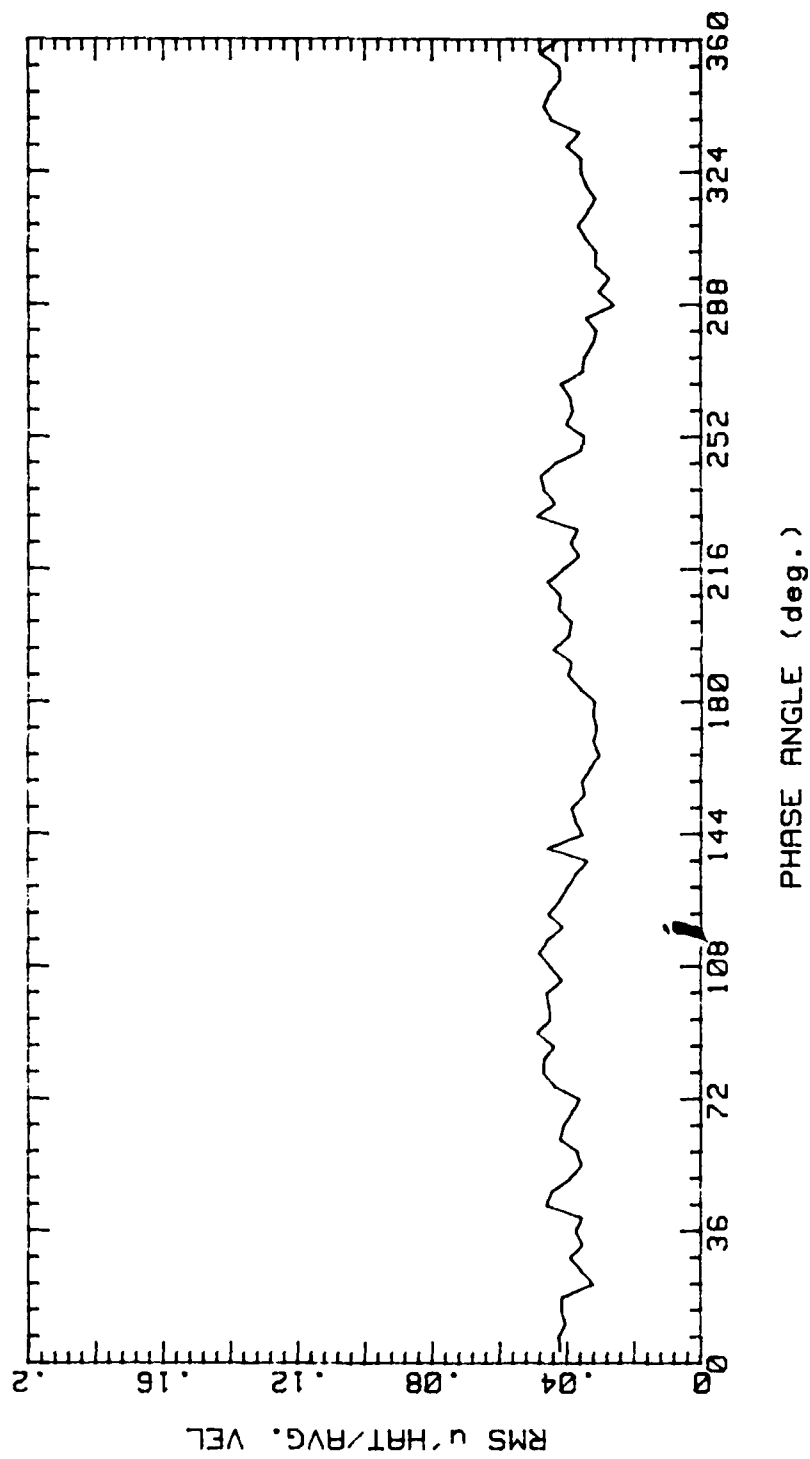


Figure 110.

RUNP7W 280989.2147

AVG. VEL 2.811m/s RMS VEL .09981m/s

OSC. FREQ. 0Hz STR. # 0

BULK VEL. 2.185m/s REY. # 1826

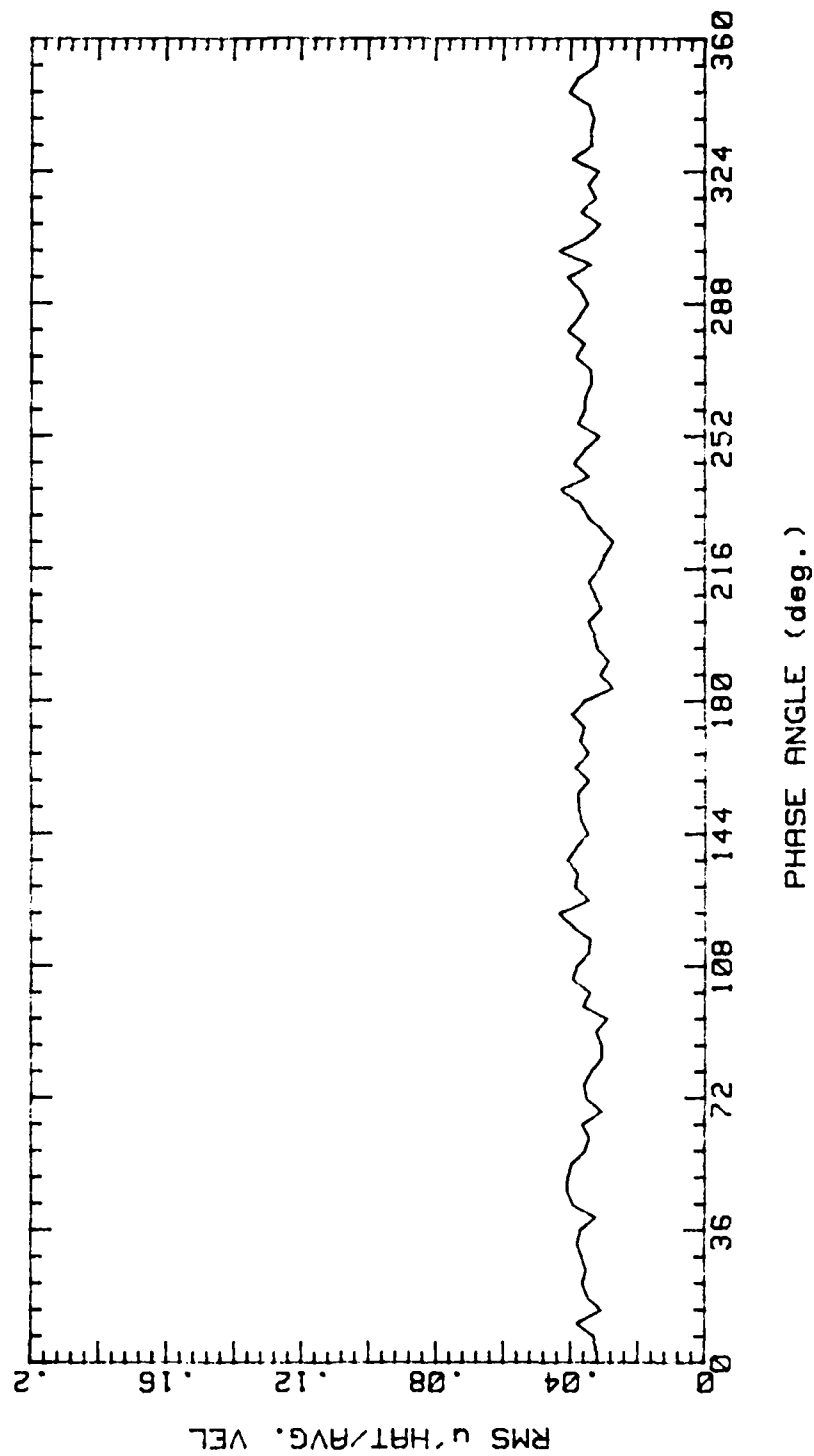


Figure 111.

RUNP7X 280989.2342

AVG. VEL 2.798m/s RMS VEL .1003m/s  
OSC. FREQ. 1Hz STR. # .03652  
BULK VEL. 2.185m/s REY. # 1826

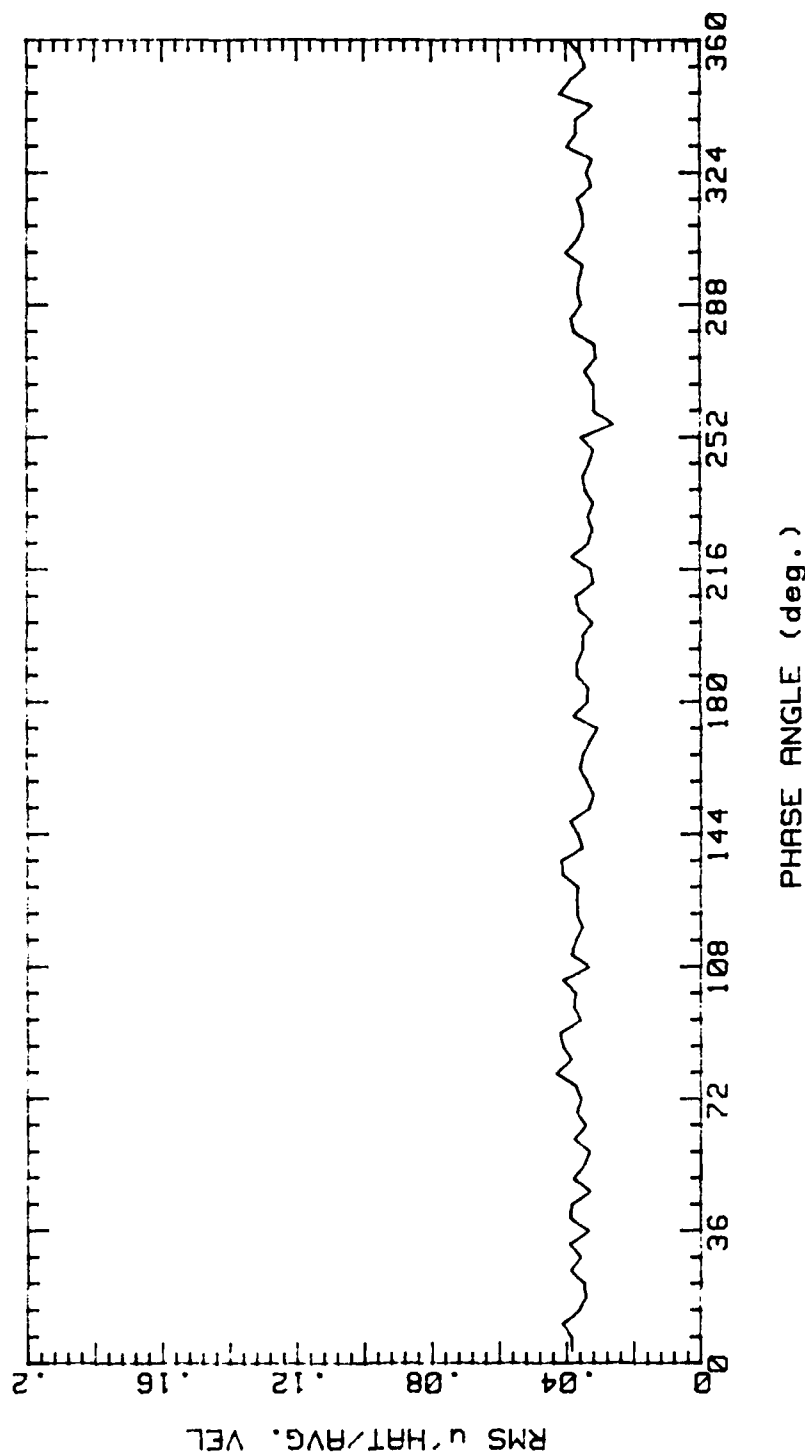


Figure 112.



RUNP8W 280989.2202

AVG. VEL 2.211m/s RMS VEL .09376m/s

OSC. FREQ. 0Hz STR. # 0

BULK VEL. 2.185m/s REY. # 1826

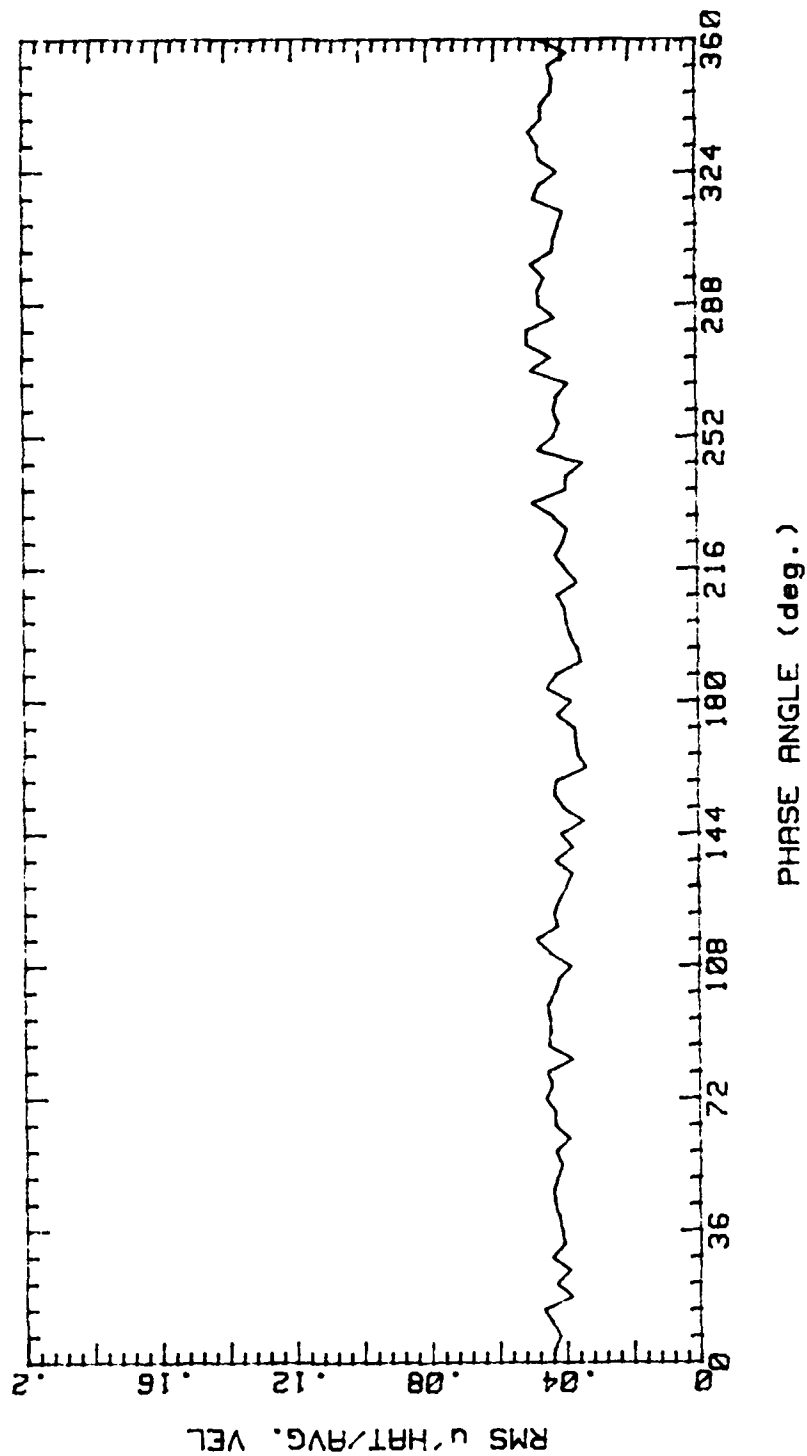


Figure 113.

RUNP8X 280989.2355

AVG. VEL 2.204m/s RMS VEL .09281m/s  
OSC. FREQ. 1Hz STR. # .03652  
BULK VEL. 2.185m/s REY. # 1826

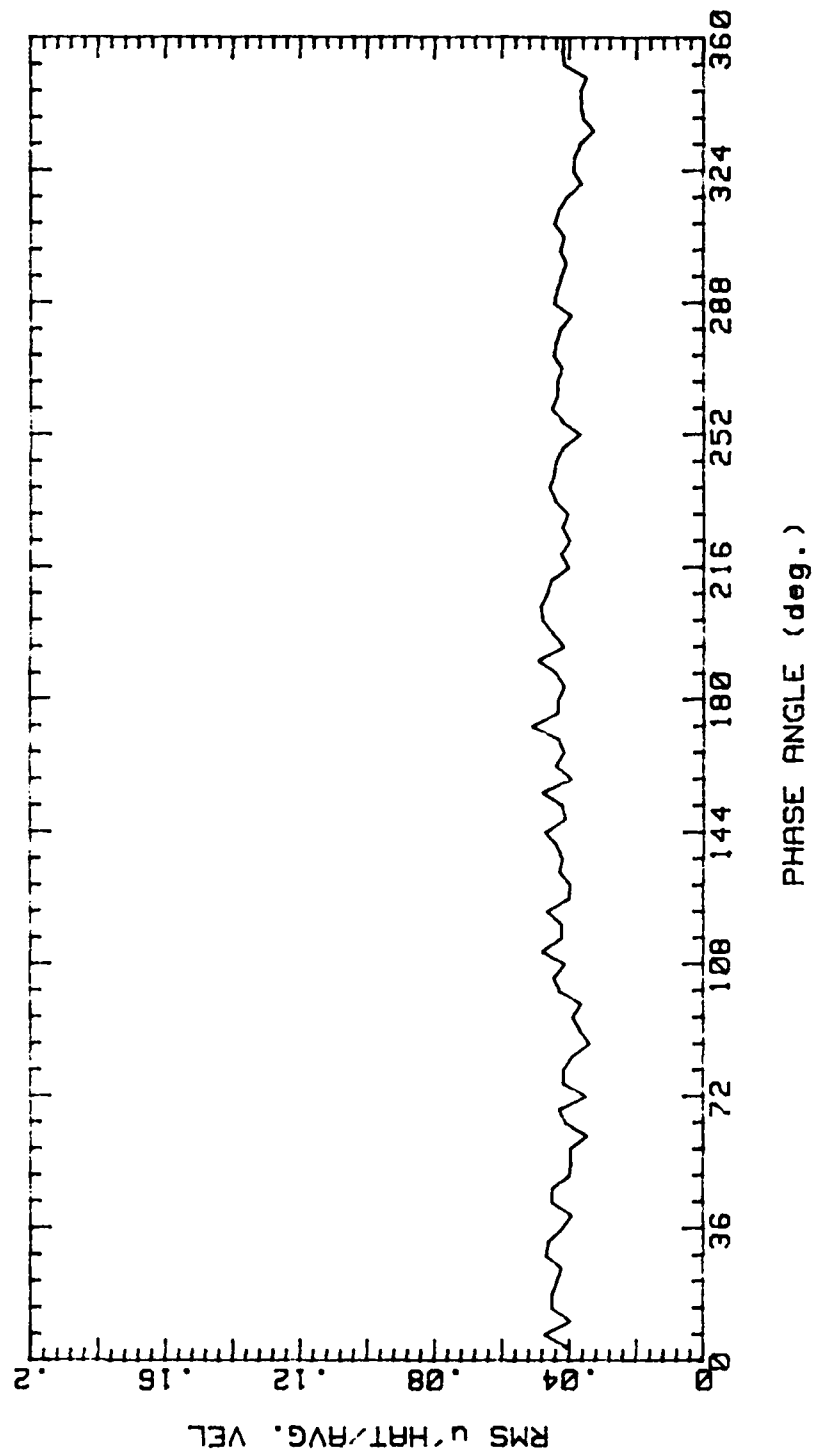


Figure 114.

RUNP1Y 93089.1215  
 AVG. VEL. 1.11m/s RMS VEL .1613m/s  
 OSC. FREQ. 0Hz STR. # 0  
 BULK VEL. 2.495m/s REY. # 2085

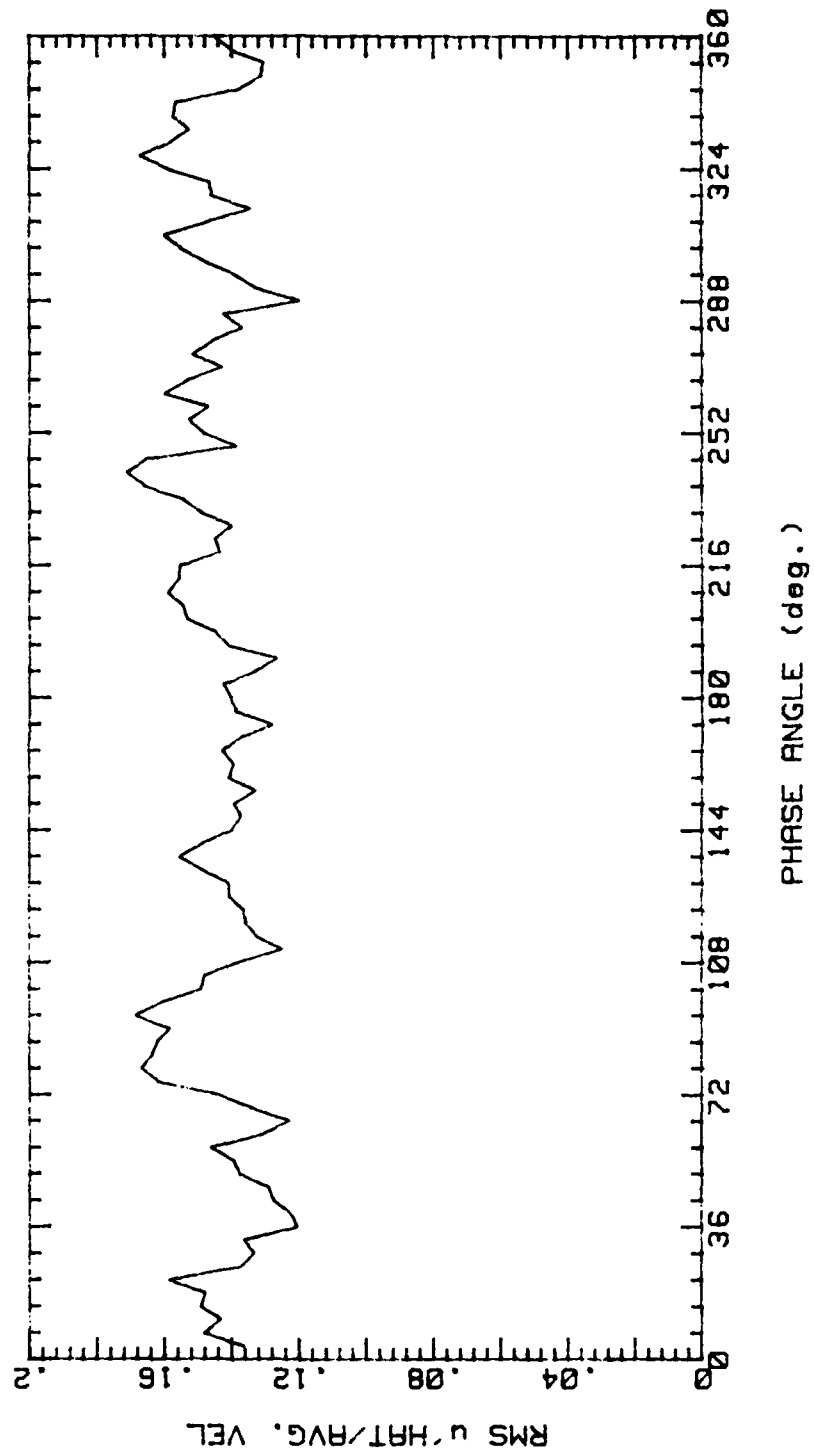


Figure 115.

RUNP1Z 93089.1415

AVG. VEL 1.096m/s RMS VEL .2192m/s

OSC. FREQ. 1Hz STR. # .03198

BULK VEL. 2.495m/s REY. # 2085

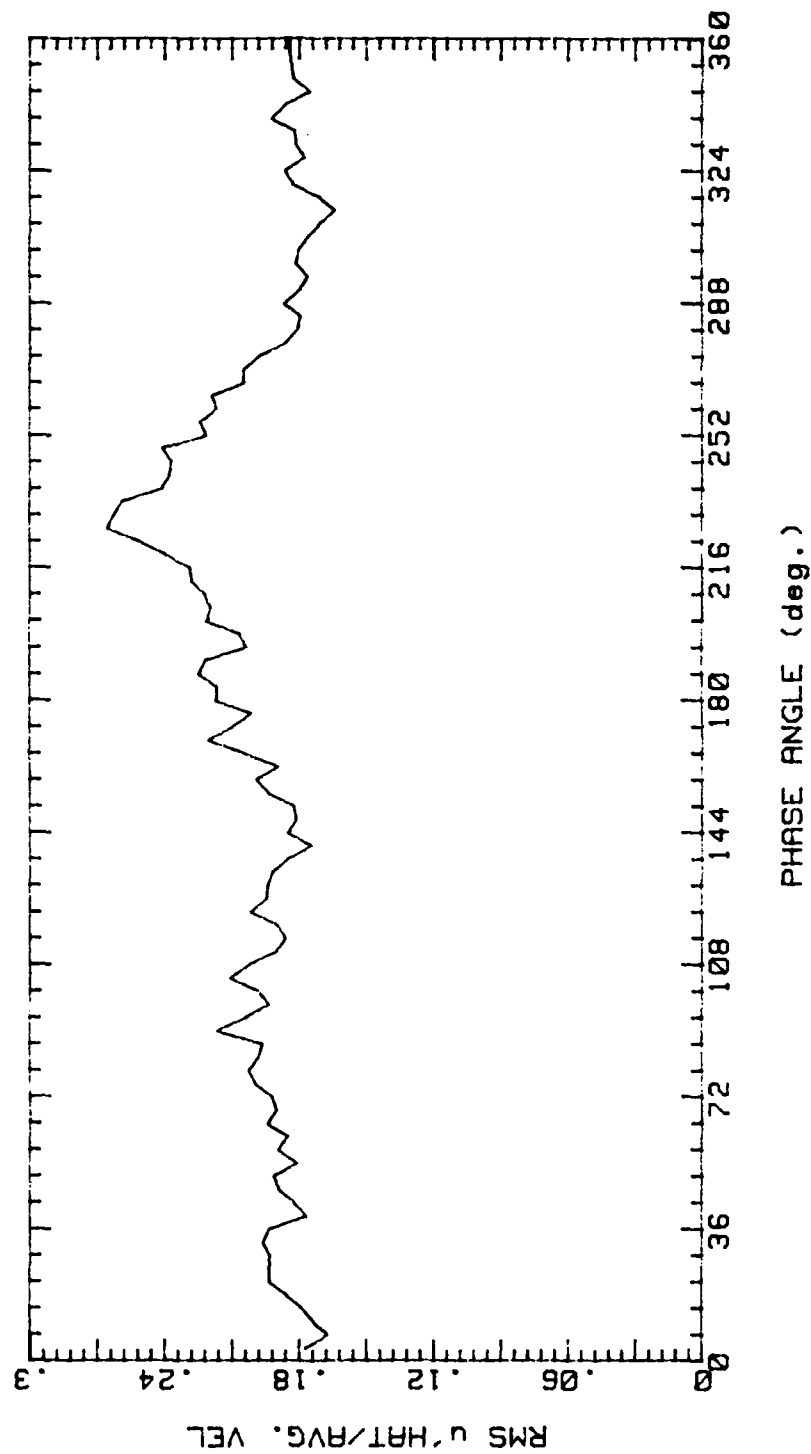


Figure 116.

RUNP2Y 93089.1229

AVG. VEL 2.034m/s RMS VEL .2773m/s  
OSC. FREQ. 0Hz STR. # 0  
BULK VEL. 2.495m/s REY. # 2085

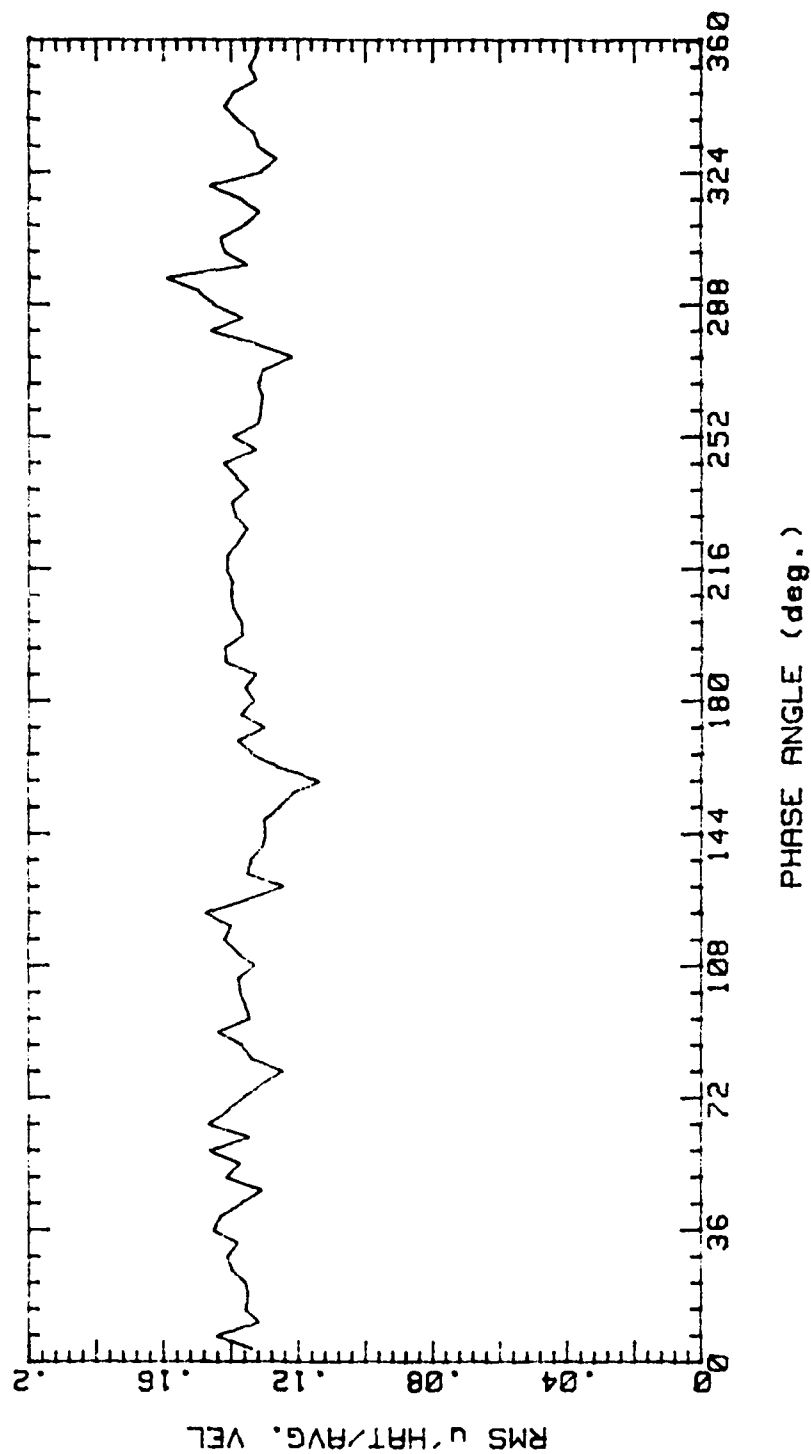


Figure 117.

RUNP2Z 93089.1429  
 AVG. VEL 1.966m/s RMS VEL .3333m/s  
 OSC. FREQ. 1Hz STR. # .03198  
 BULK VEL. 2.495m/s REY. # 2085

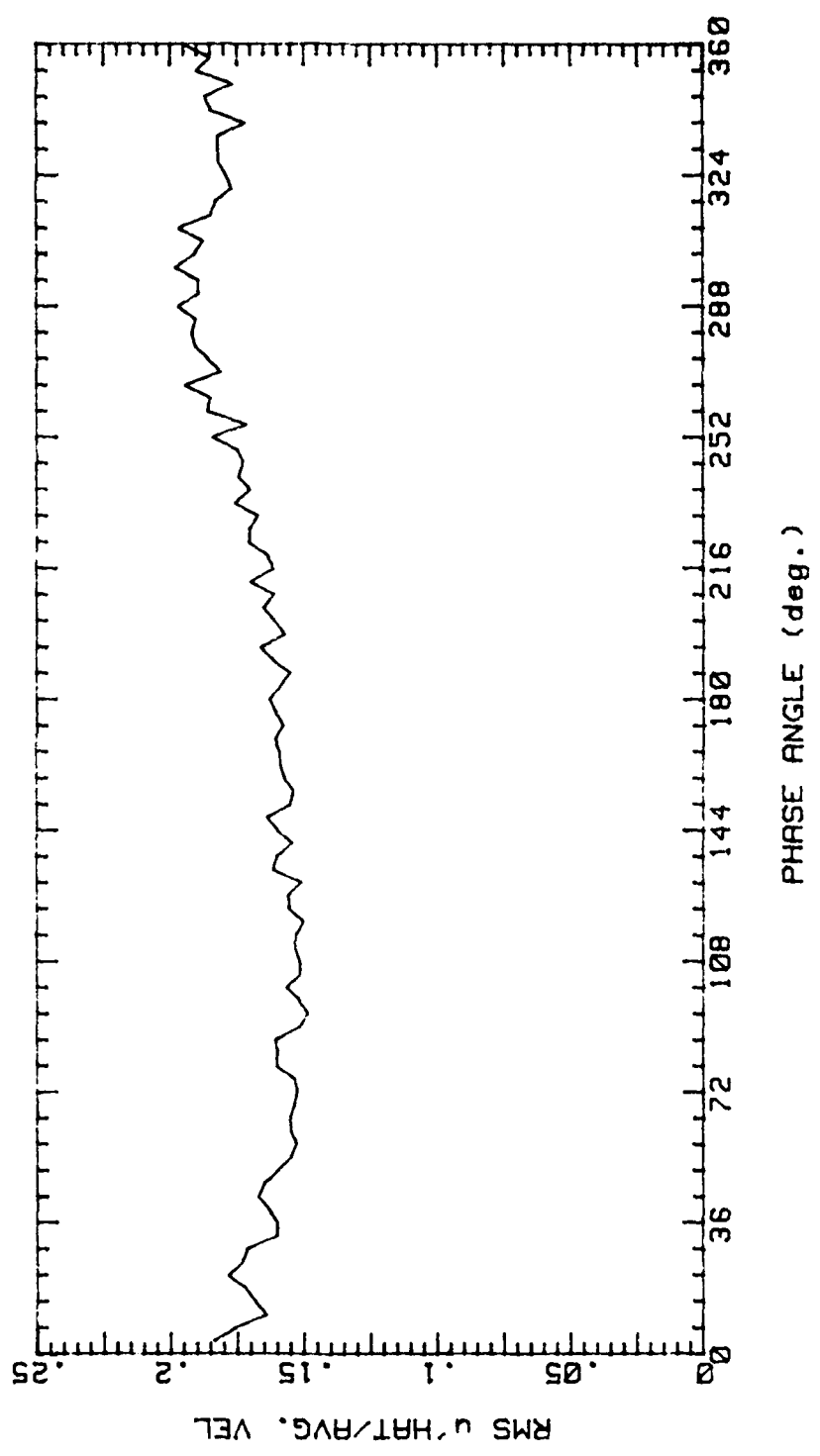


Figure 118.

RUNP3Y 93089.1245

AVG. VEL 2.688m/s RMS VEL .2251m/s  
OSC. FREQ. 0Hz STR. # 0  
BULK VEL. 2.495m/s REY. # 2085

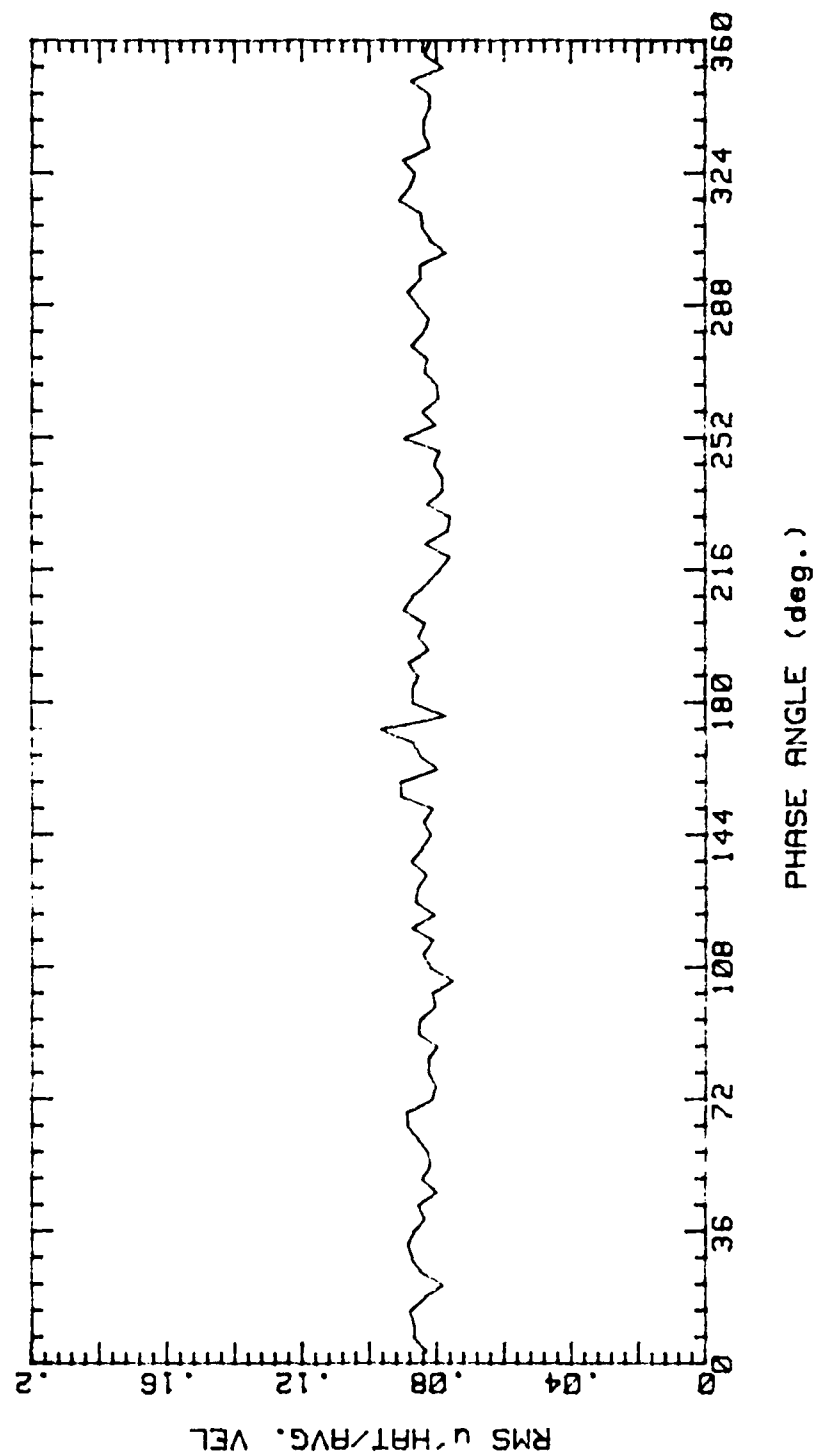


Figure 119.

RUNP3Z 93089.1442  
 AVG. VEL 2.566m/s RMS VEL .2868m/s  
 OSC. FREQ. 1Hz STR. # .03198  
 BULK VEL. 2.495m/s REY. # 2085

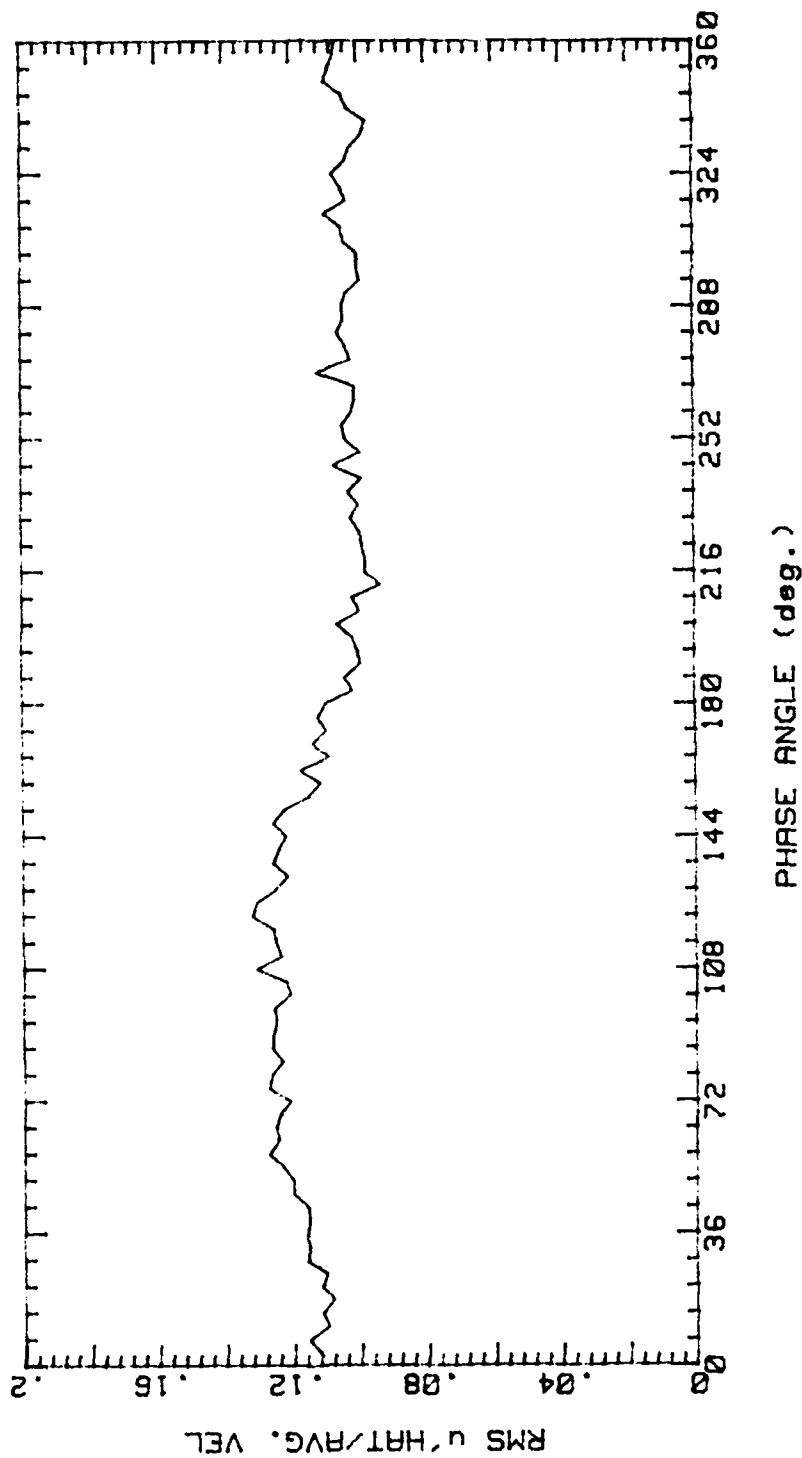


Figure 120.



RUNP4Y 93089.1258

AVG. VEL 2.928m/s RMS VEL .2554m/s

OSC. FREQ. 0Hz STR. # 0

BULK VEL. 2.495m/s REY. # 2085

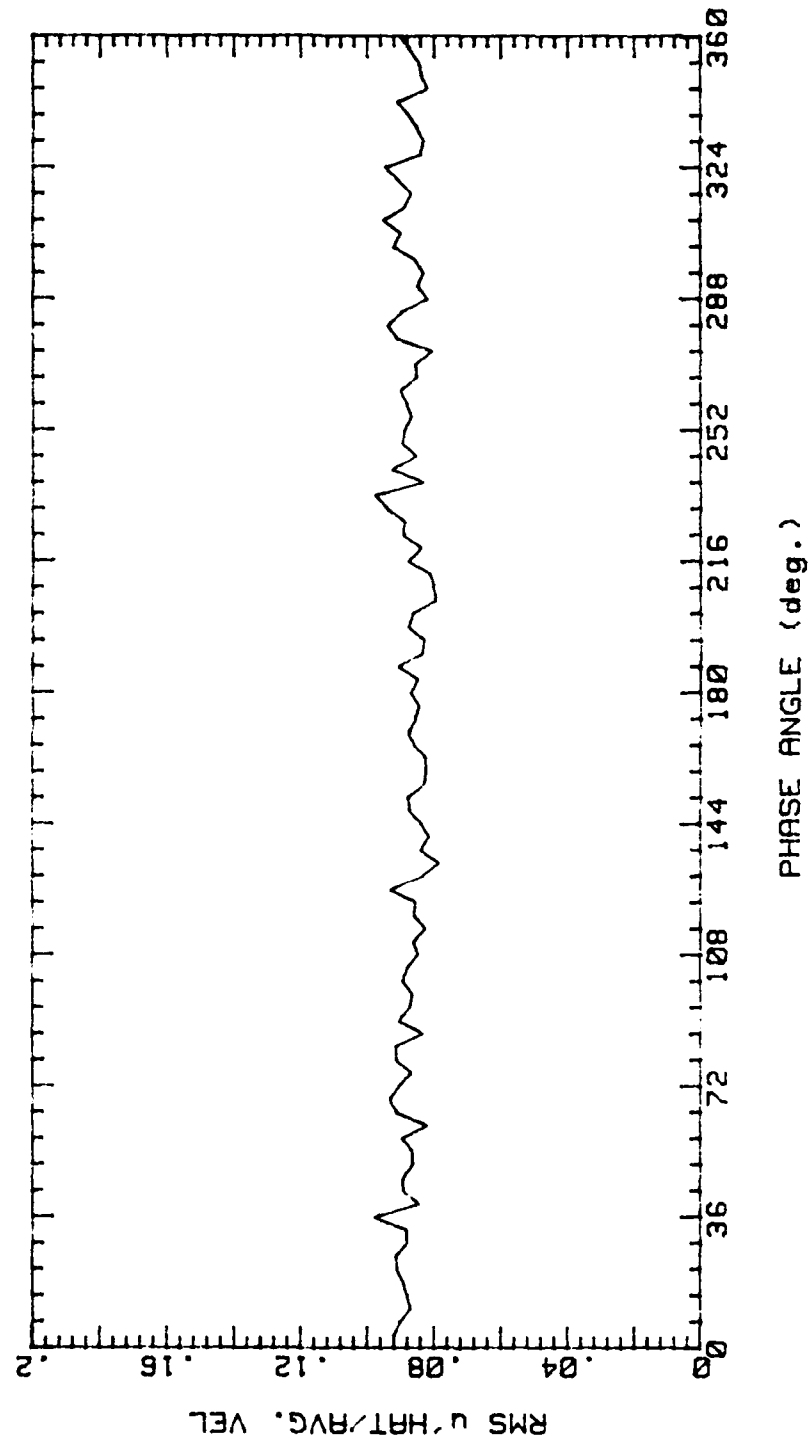


Figure 121.

RUNP4Z 93089.1458

AVG. VEL 3.07m/s RMS VEL .2596m/s  
OSC. FREQ. 1Hz STR. # .03198  
BULK VEL. 2.495m/s REY. # 2085

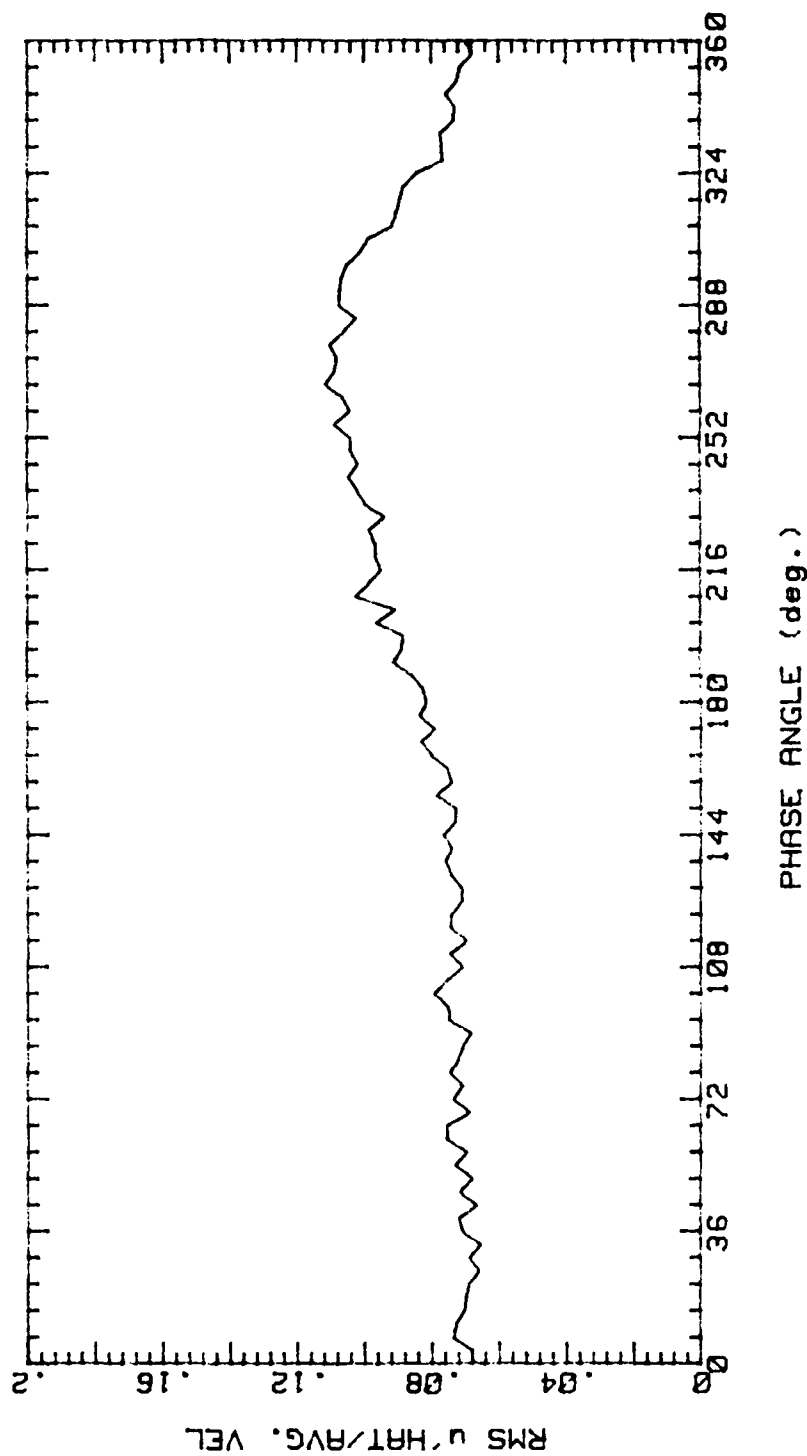


Figure 122.

RUNP5Y 93089.1313

AVG. VEL 3.377m/s RMS VEL .3209m/s

OSC. FREQ. 0Hz STR. # 0

BULK VEL. 2.495m/s REY. # 2085

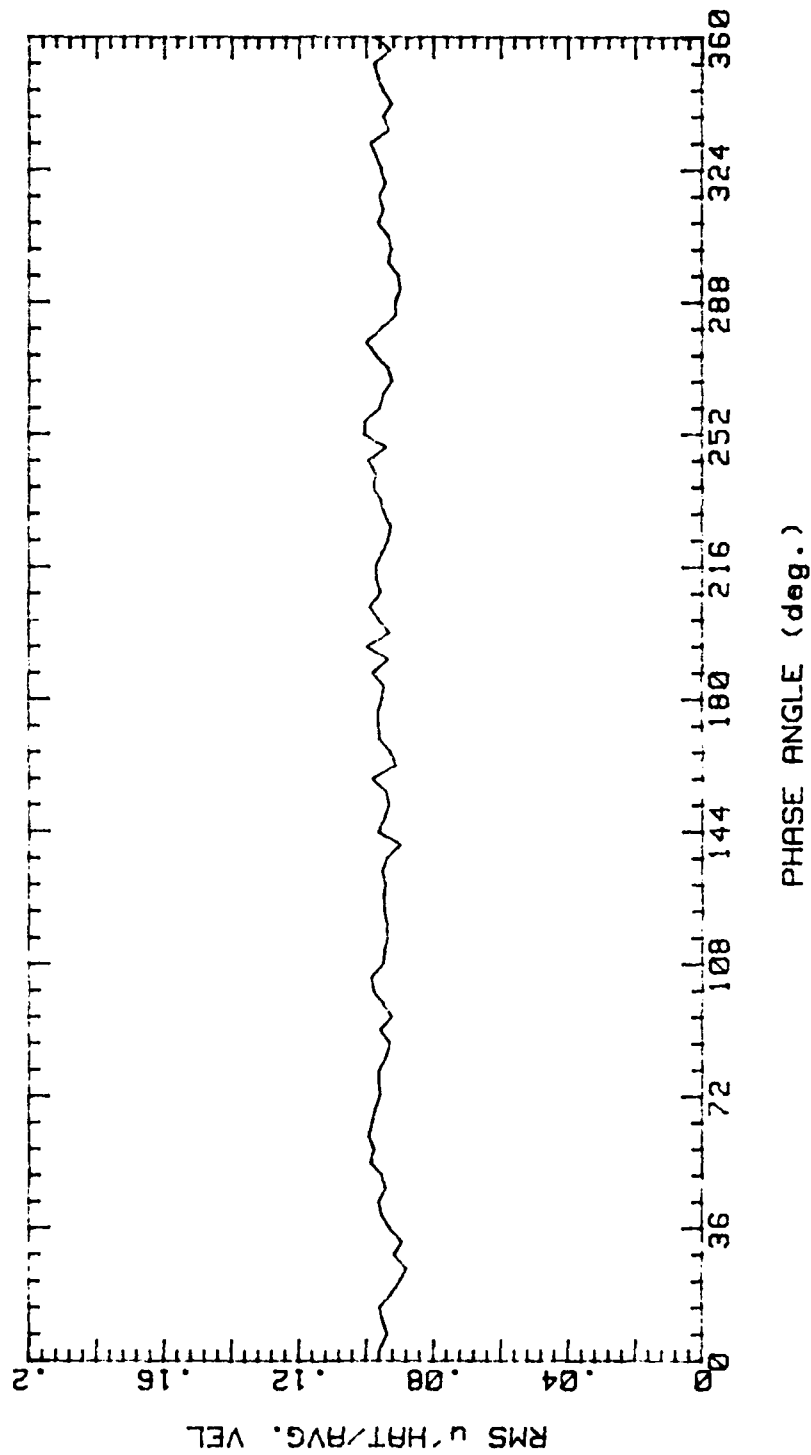


Figure 123.

RUNP5Z 93089.1513  
 AVG. VEL 3.704m/s RMS VEL .2506m/s  
 OSC. FREQ. 1Hz STR. # .03198  
 BULK VEL. 2.495m/s REY. # 2085

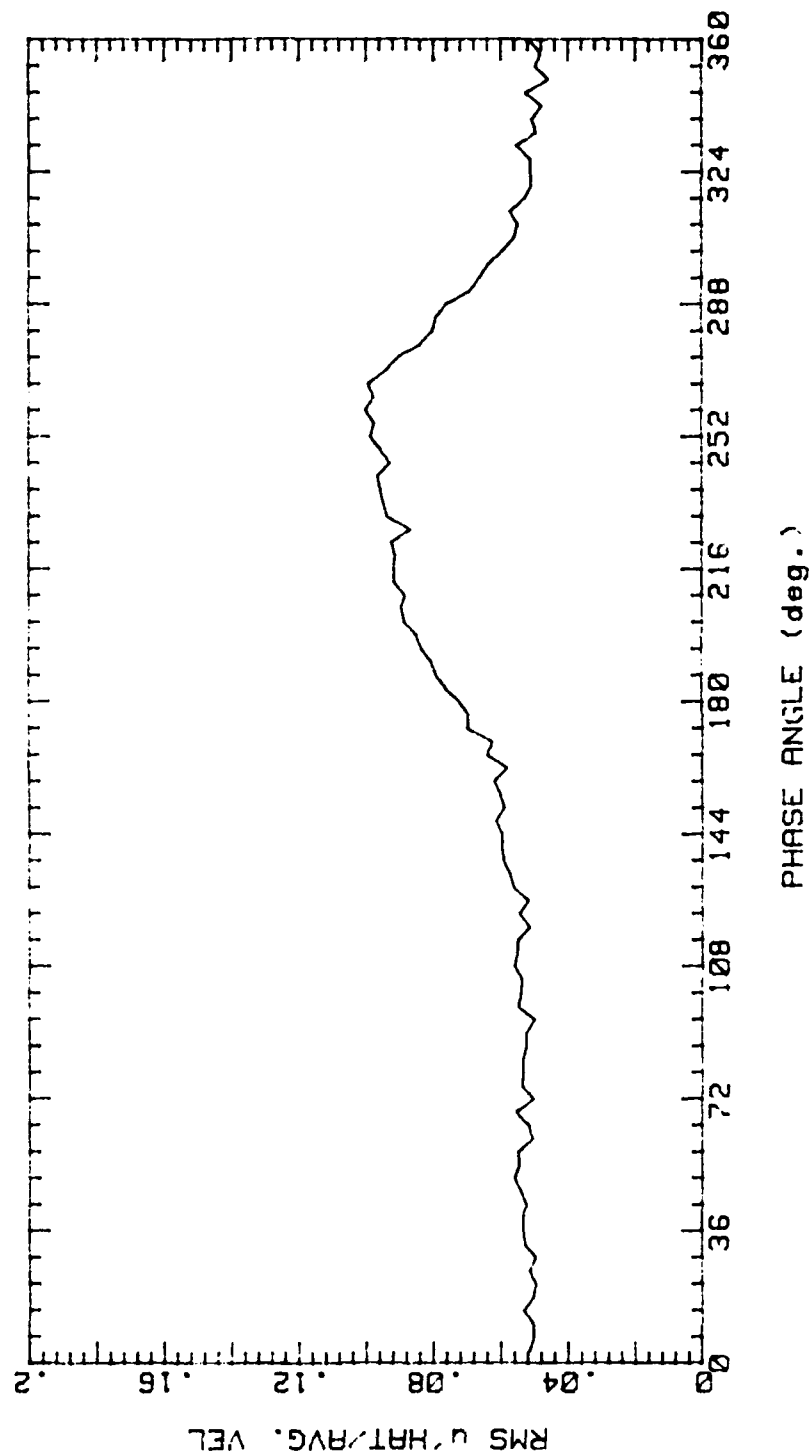


Figure 124.

RUNP6Y 93089.1328

AVG. VEL 3.221m/s RMS VEL .2999m/s  
OSC. FREQ. 0Hz STR. # 0  
BULK VEL. 2.495m/s REY. # 2085

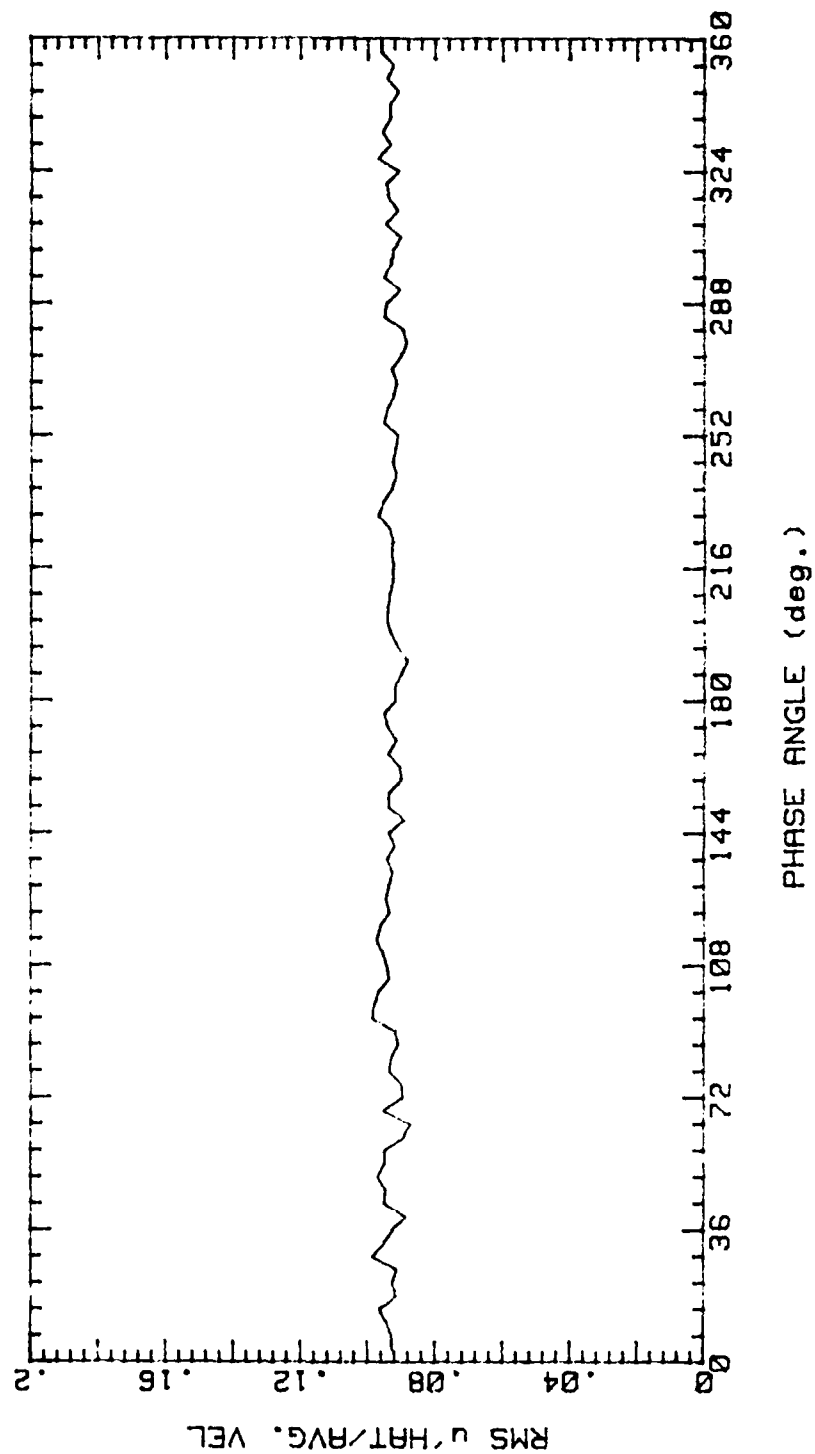


Figure 125.

RUNP6Z 93089.1526

AVG. VEL 3.339m/s RMS VEL .2337m/s  
OSC. FREQ. 1Hz STR. # .03198  
BULK VEL. 2.495m/s REY. # 2085

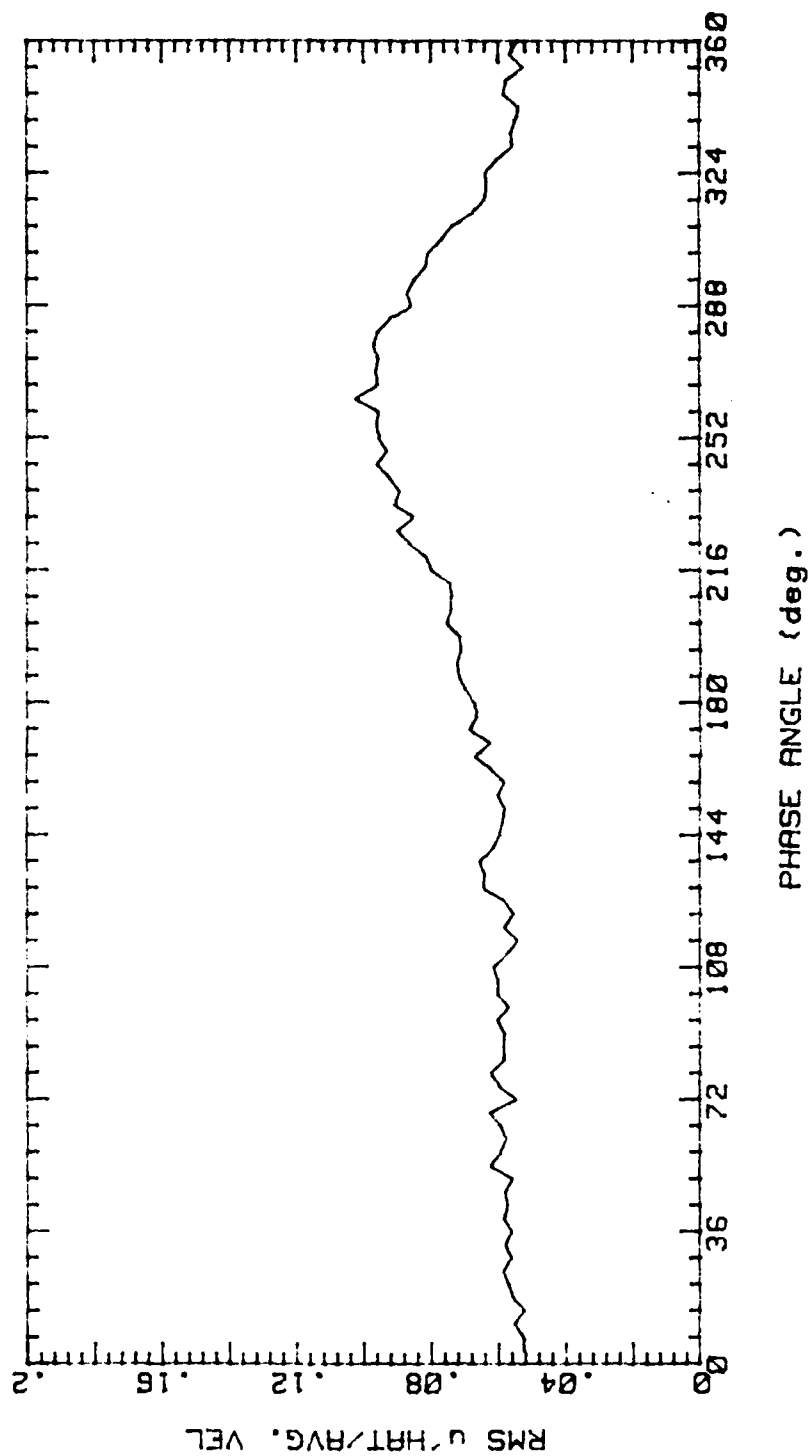


Figure 126.

RUNP7Y 93089.1343

AVG. VEL 2.68m/s RMS VEL .229m/s

OSC. FREQ. 0Hz STR. # 0

BULK VEL. 2.495m/s REY. # 2085

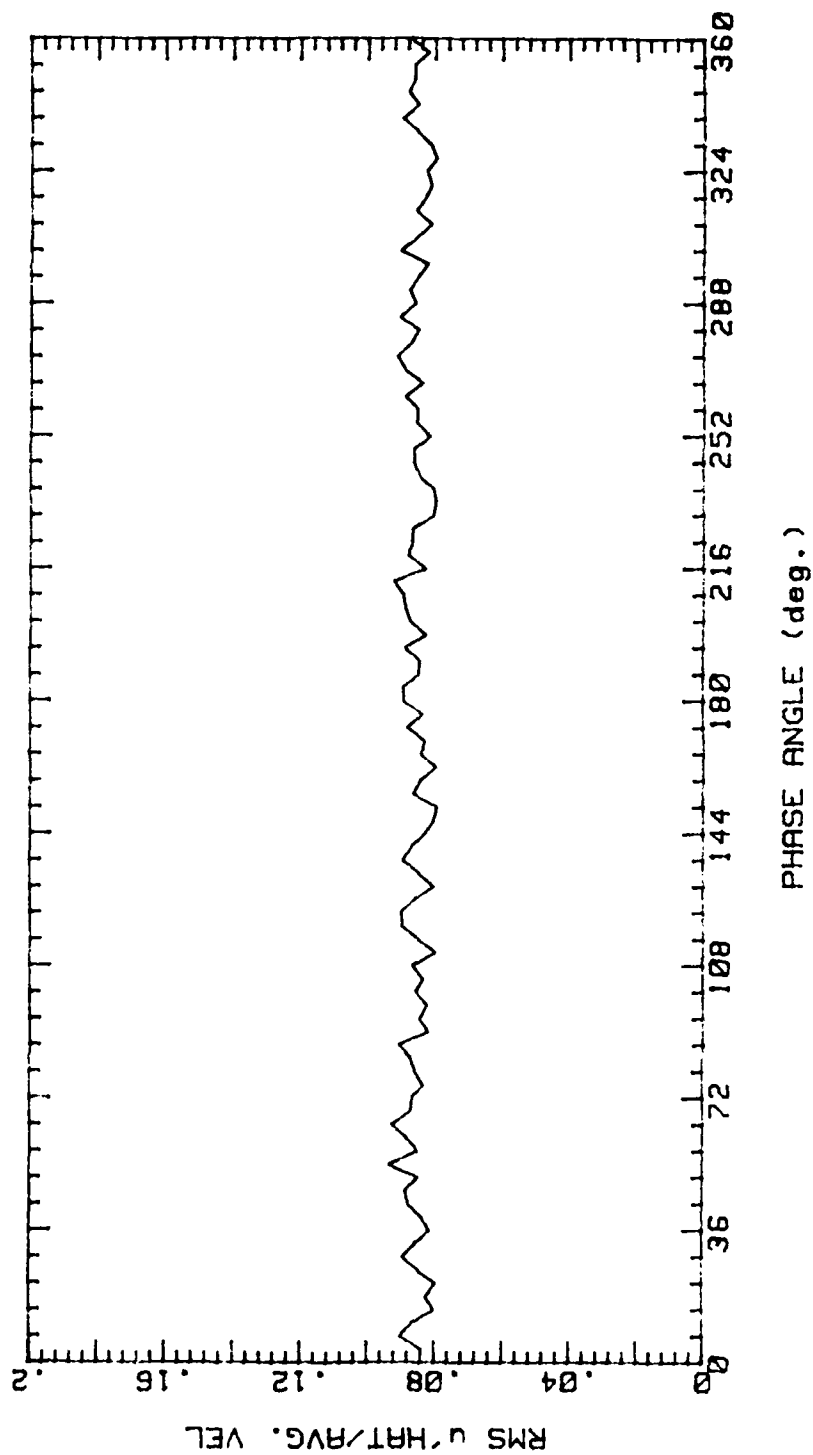


Figure 127.

RUNP7Z 93089.1655  
 AVG. VEL 2.874m/s RMS VEL .2524m/s  
 OSC. FREQ. 1Hz STR. # .03198  
 BULK VEL. 2.495m/s REY. # 2085

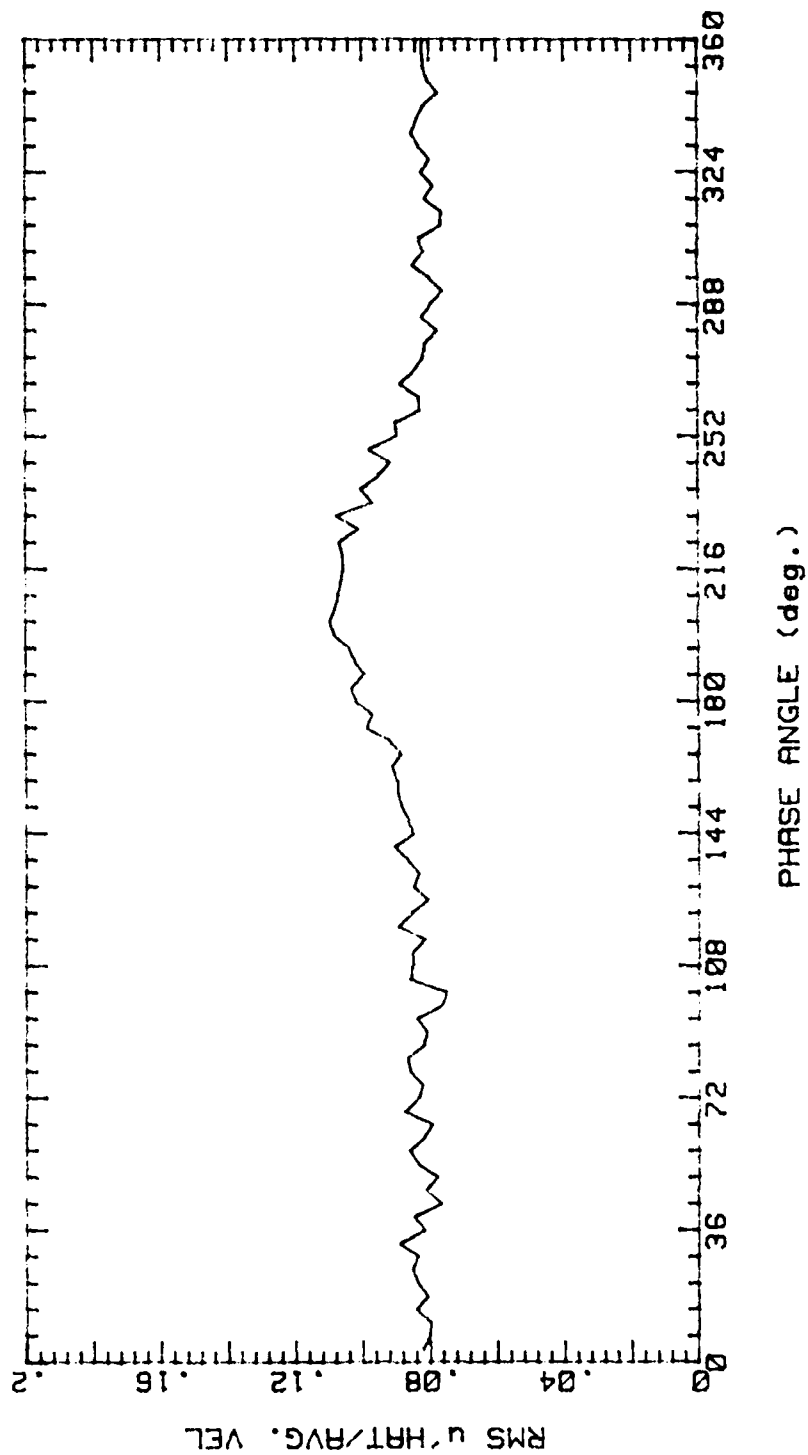


Figure 128.



RUNP8Y 93089.1358  
 AVG. VEL 2.495m/s RMS VEL .2174m/s  
 OSC. FREQ. 0Hz STR. # 0  
 BULK VEL. 2.495m/s REY. # 2085

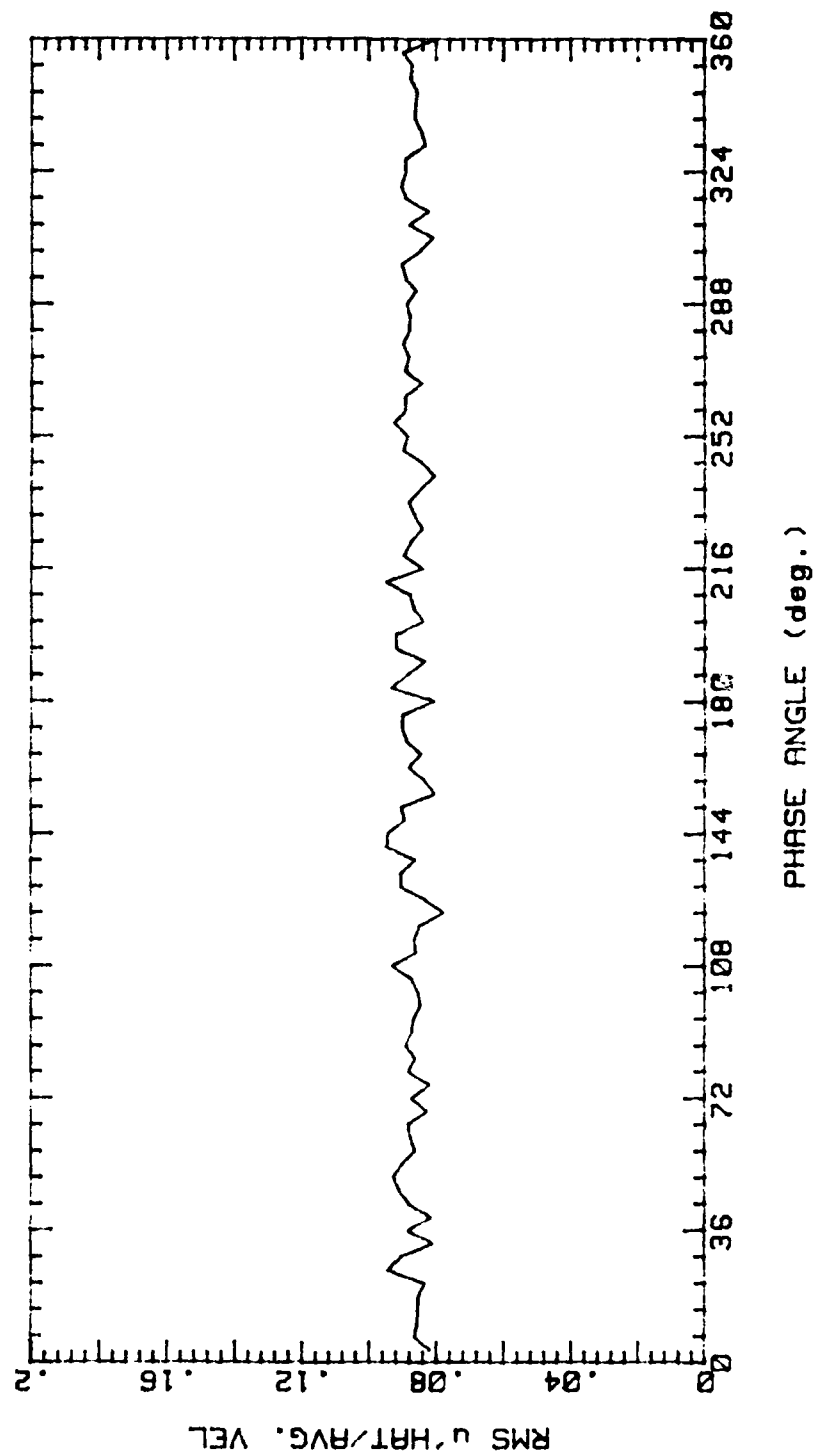


Figure 129.

RUNP8Z 93089.1707

AVG. VEL 2.424m/s RMS VEL .3076m/s  
OSC. FREQ. 1Hz STR. # .03198  
BULK VEL. 2.495m/s REY. # 2085

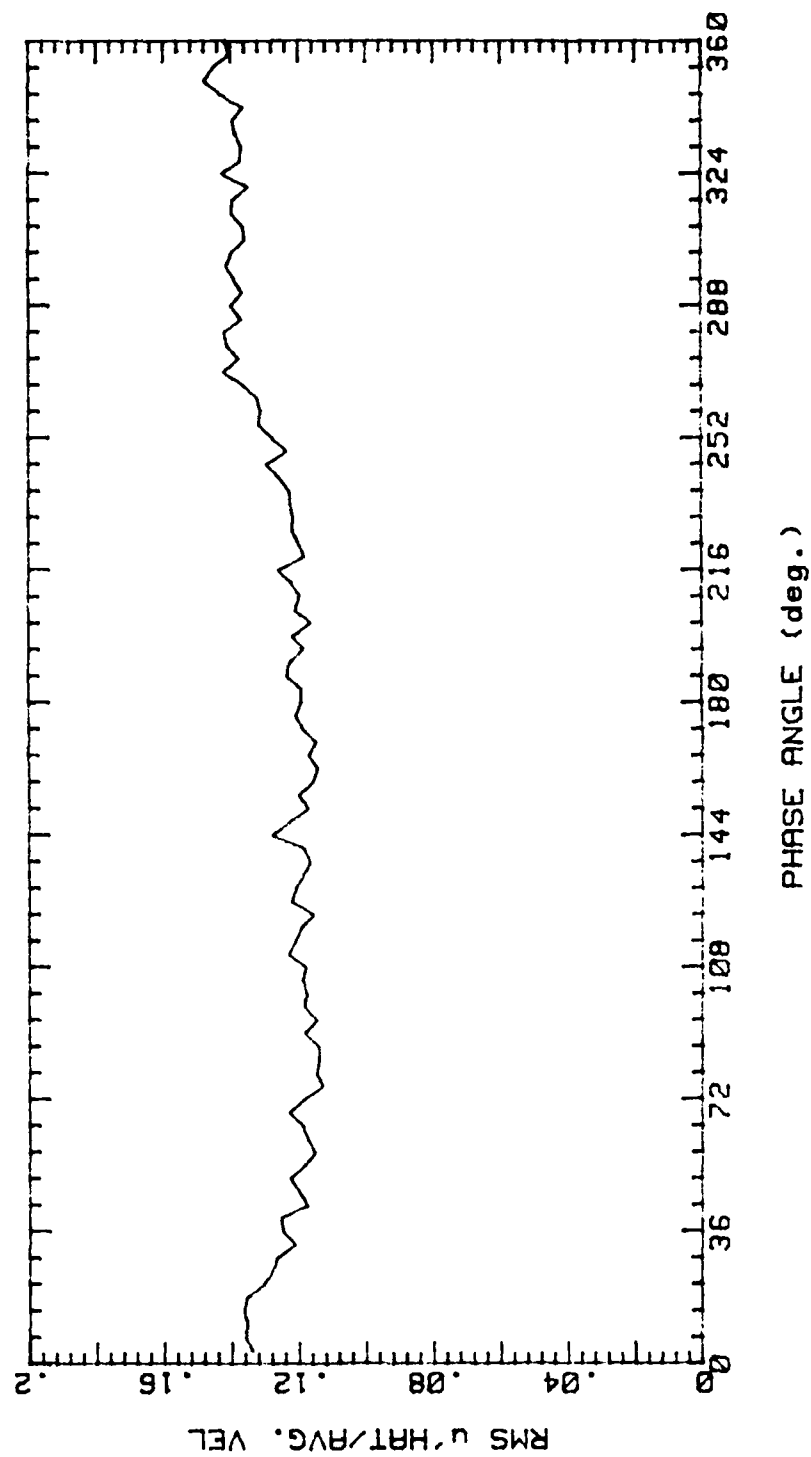


Figure 130.

RUNP1AA 93089.173

AVG. VEL 1.516m/s RMS VEL .3132m/s

OSC. FREQ. 0Hz STR. # 0

BULK VEL. 3.16m/s REY. # 2640

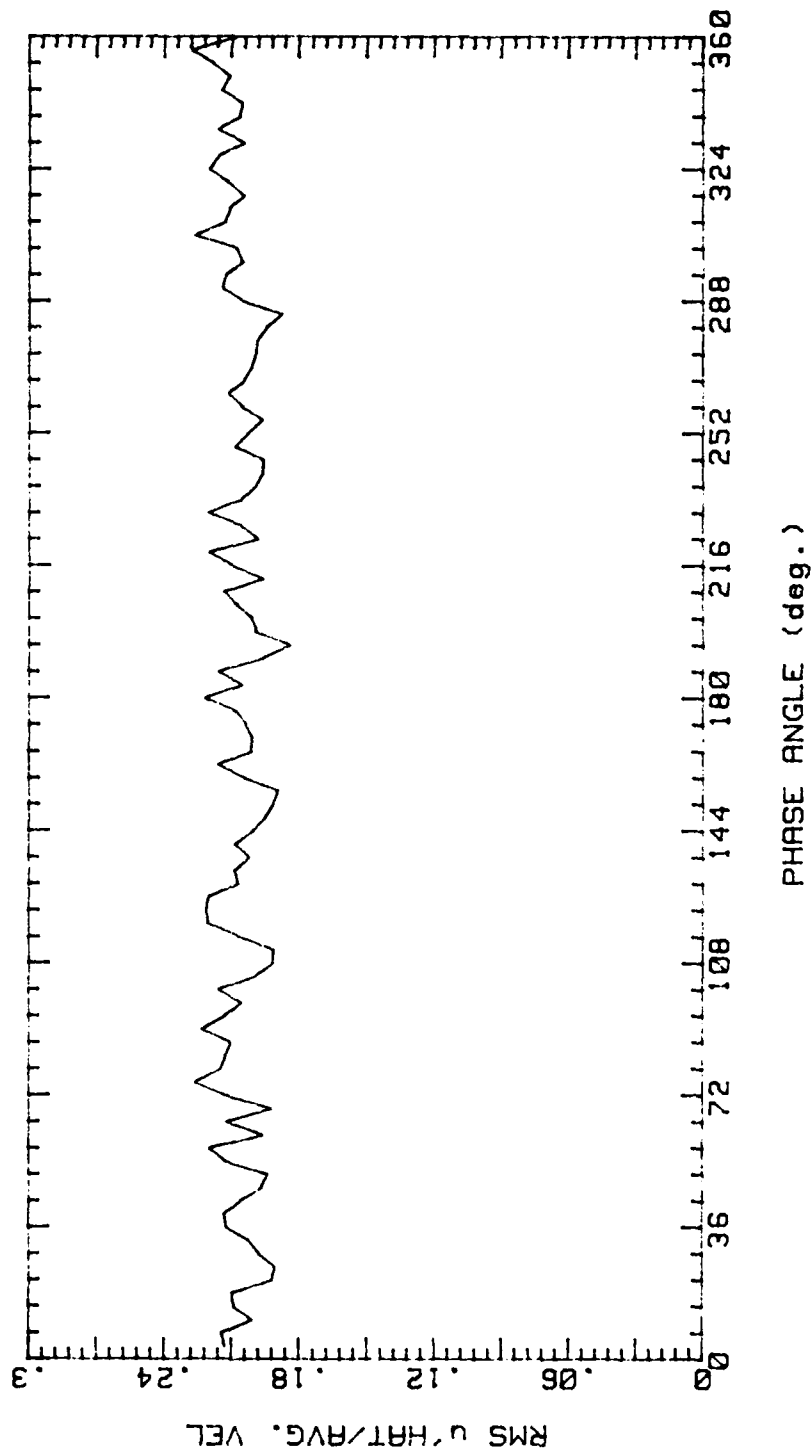


Figure 131.

RUNP1BA 93089.1932  
 AVG. VEL. 1.494m/s RMS VEL. .3118m/s  
 OSC. FREQ. 1Hz STR. # .02525  
 BULK VEL. 3.16m/s REY. # 2640

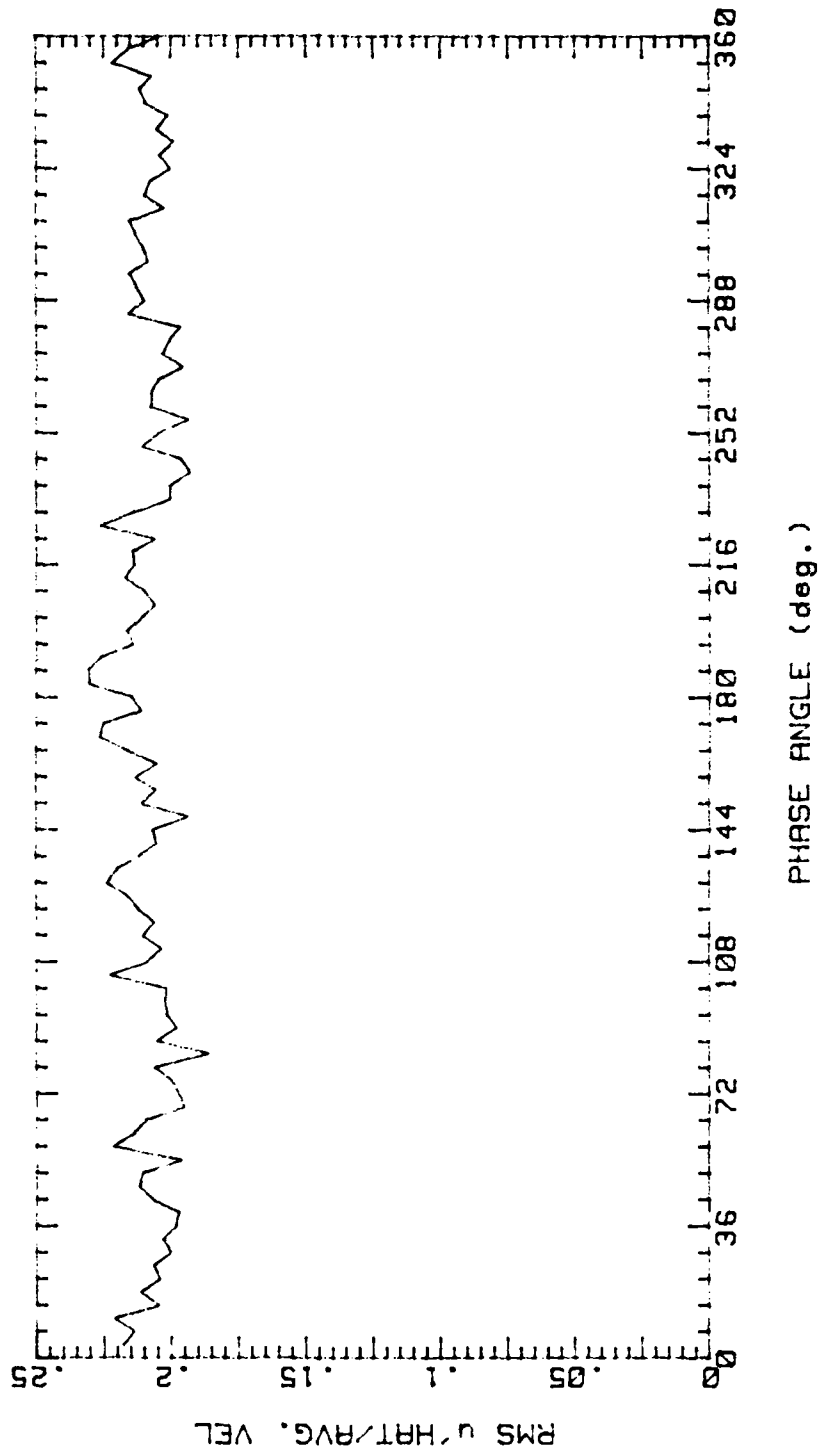


Figure 132.

RUNP2AA 93089.1745

AVG. VEL 2.538m/s RMS VEL .3974m/s  
OSC. FREQ. 0Hz STR. # 0  
BULK VEL. 3.16m/s REY. # 2640

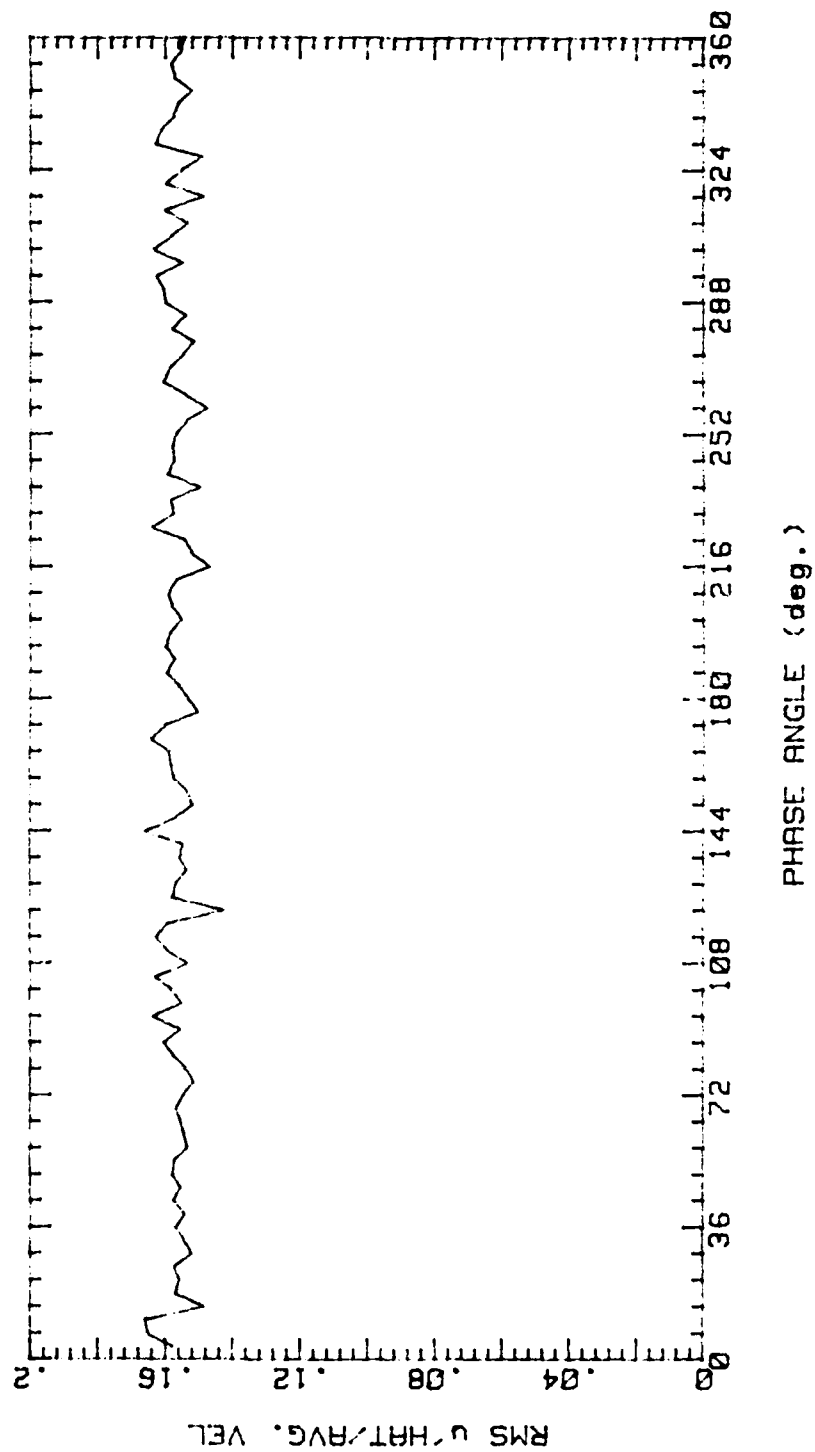


Figure 133.

RUNP2BA 93089.1947  
 AVG. VEL 2.539m/s RMS VEL .3974m/s  
 OSC. FREQ. 1Hz STR. # .02525  
 BULK VEL. 3.16m/s REY. # 2640

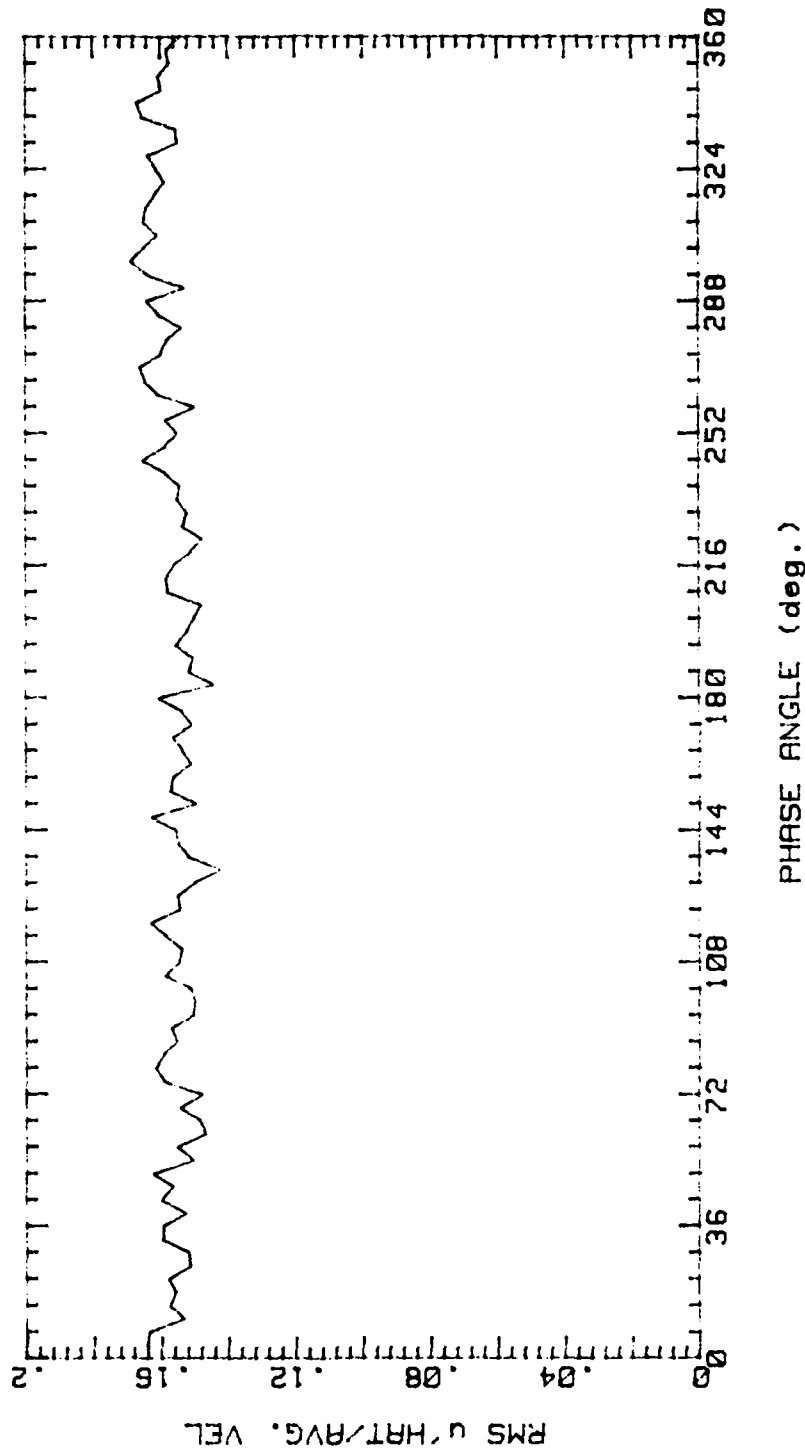


Figure 134.

RUNP3AA 93089.1801

AVG. VEL 3.183m/s RMS VEL .3148m/s  
OSC. FREQ. 0Hz STR. # 0  
BULK VEL. 3.16m/s REY. # 2640

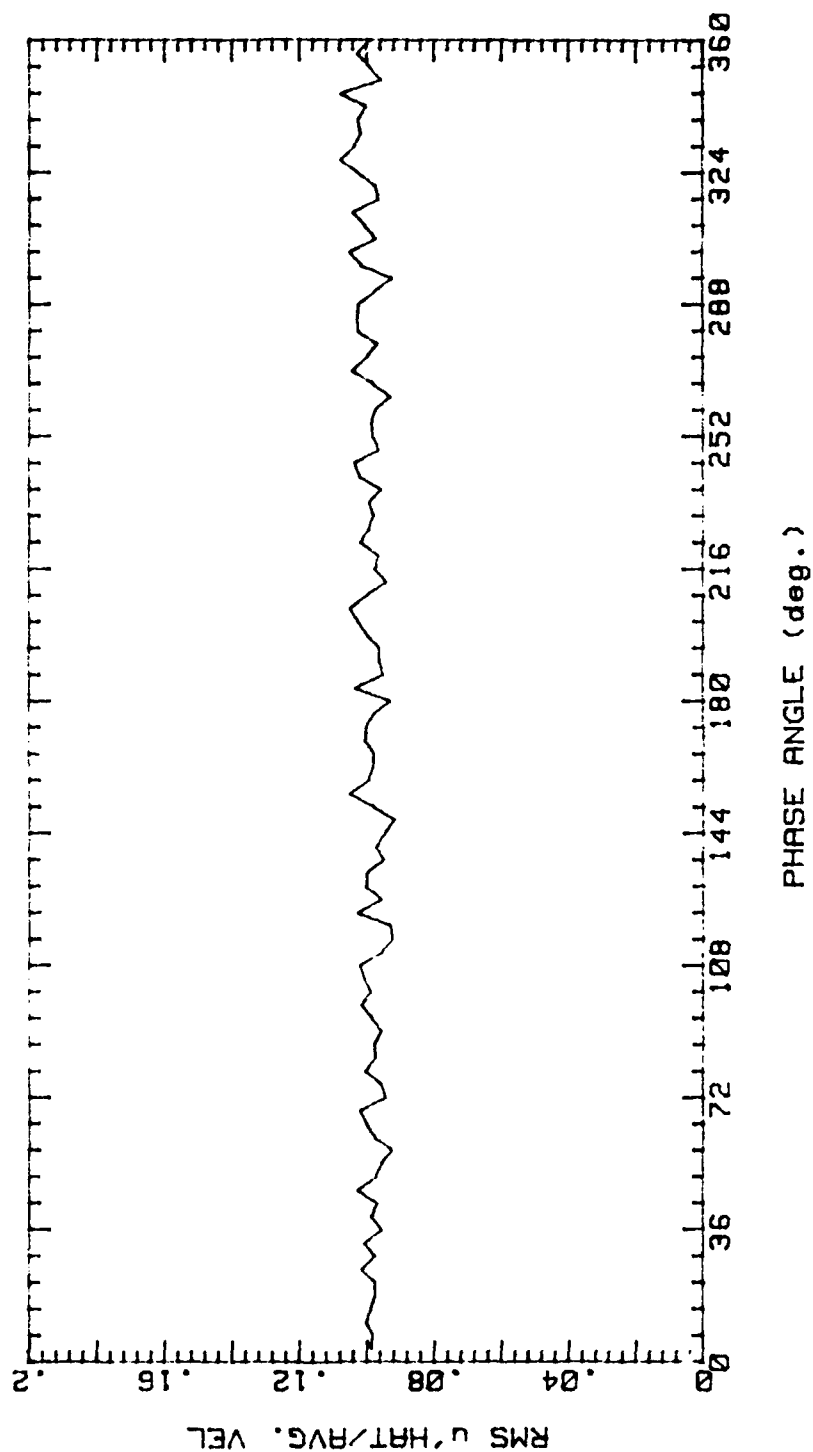


Figure 135.

RUNP3BA 93089.2001  
 AVG. VEL 3.168m/s RMS VEL .3107m/s  
 OSC. FREQ. 1Hz STR. # .02525  
 BULK VEL. 3.16m/s REY. # 2640

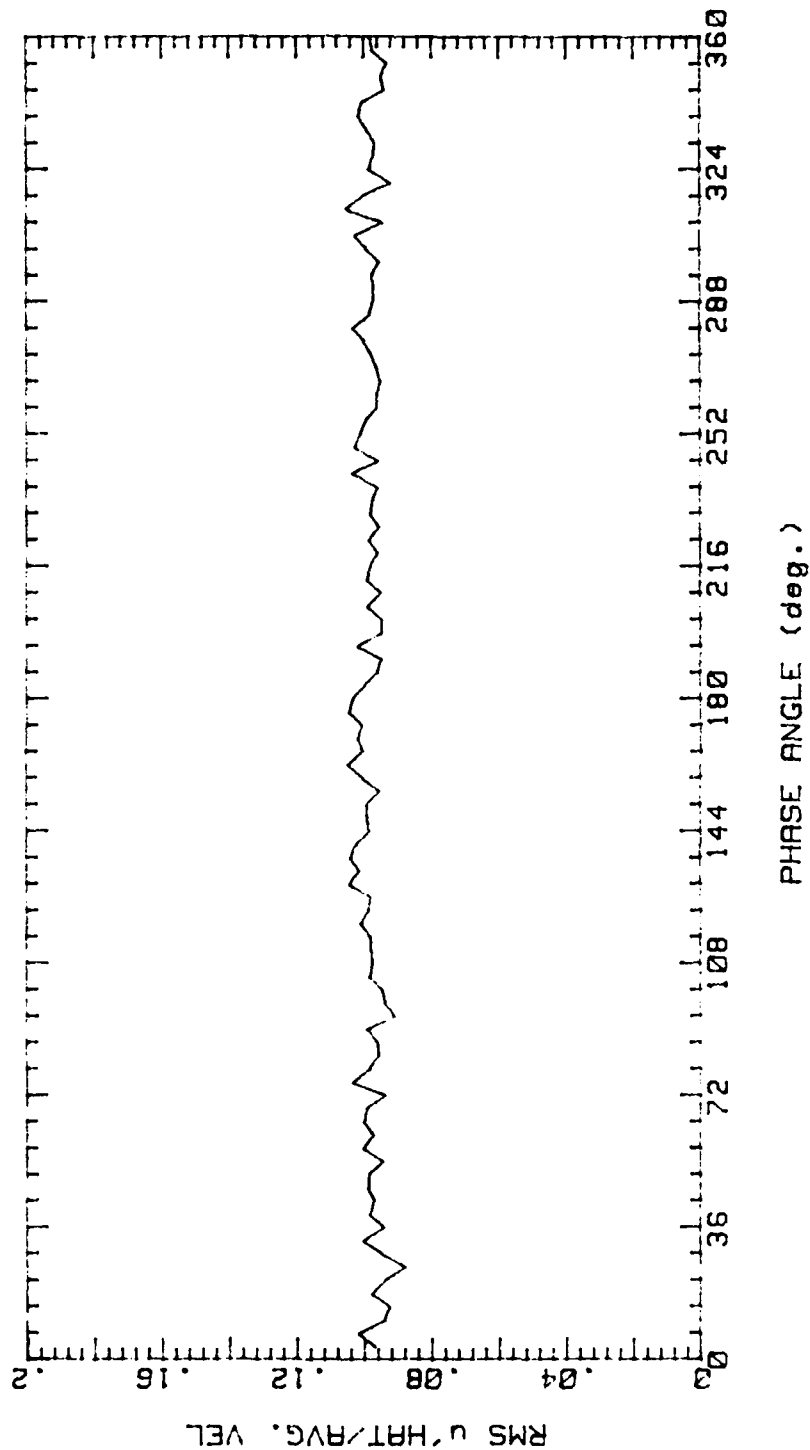


Figure 136.



RUNP4AA 93089.1815

AVG. VEL 3.48m/s RMS VEL .239m/s  
OSC. FREQ. 0Hz STR. # 0  
BULK VEL. 3.16m/s REY. # 2640

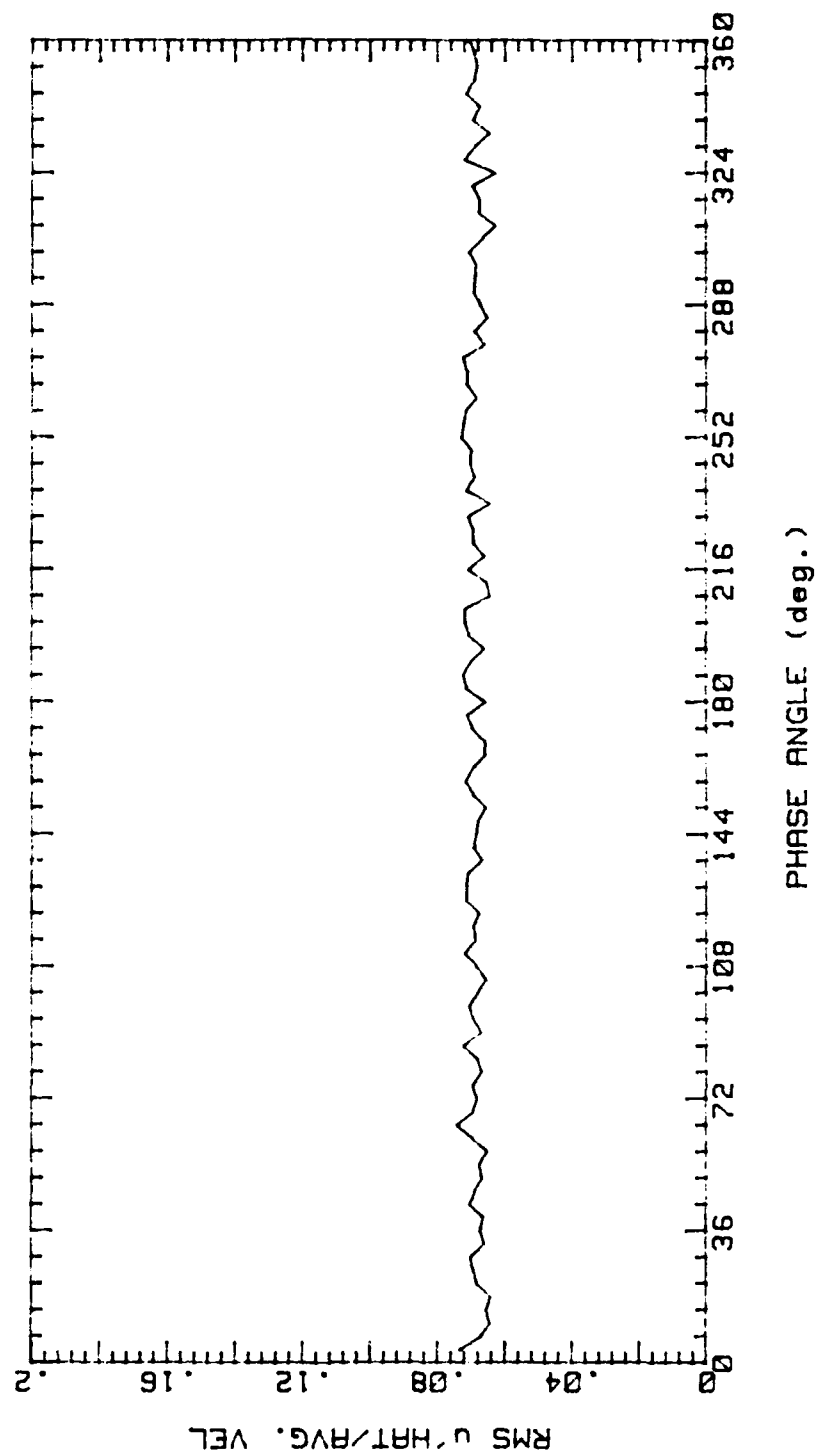


Figure 137.

RUNP4BA 93089.2014  
 AVG. VEL 3.468m/s RMS VEL .2407m/s  
 OSC. FREQ. 1Hz STR. # .02525  
 BULK VEL. 3.16m/s REY. # 2640

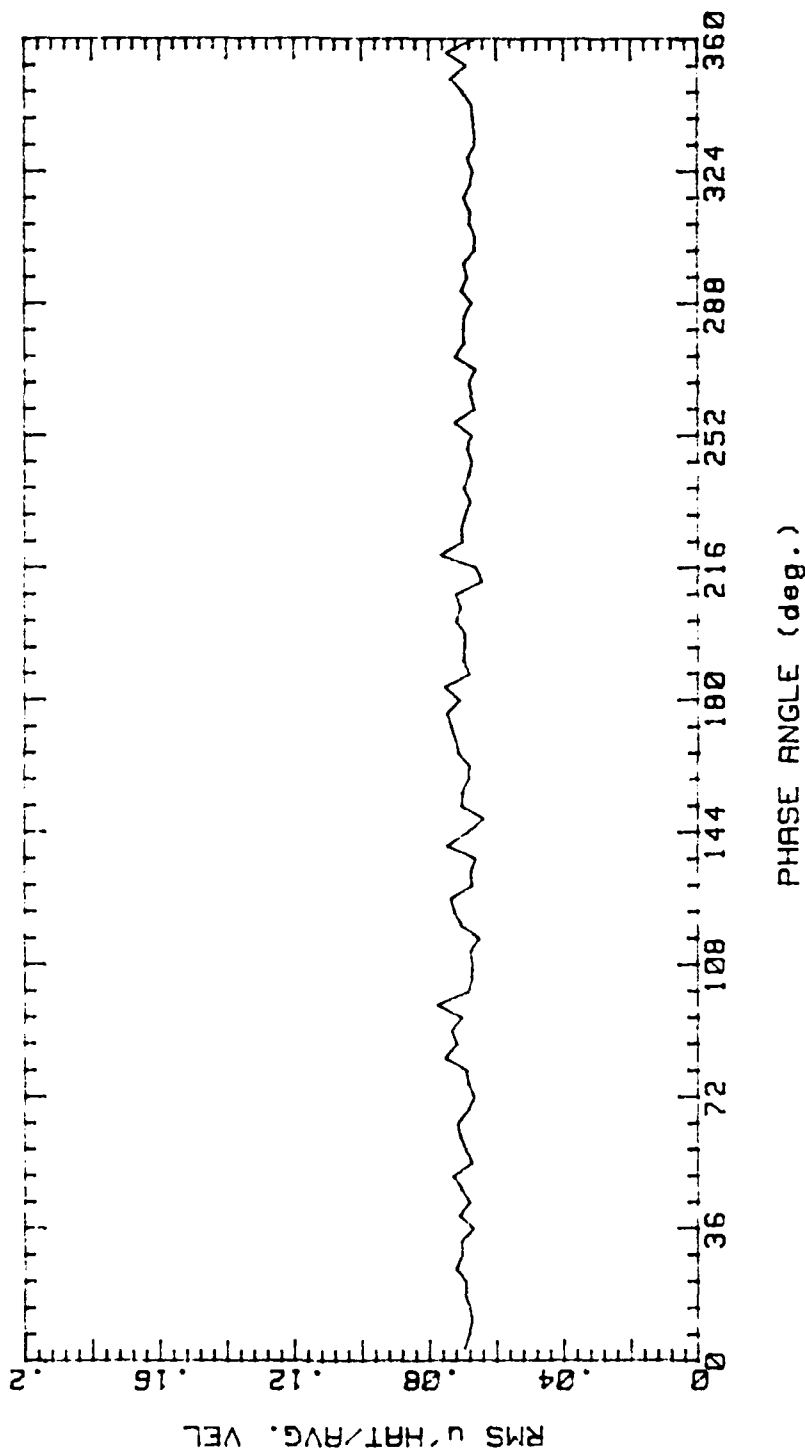


Figure 138.

RUNP5AA 93089.1831

AVG. VEL 3.445m/s RMS VEL .1782m/s  
OSC. FREQ. 0Hz STR. # 0  
BULK VEL. 3.16m/s REY. # 2640

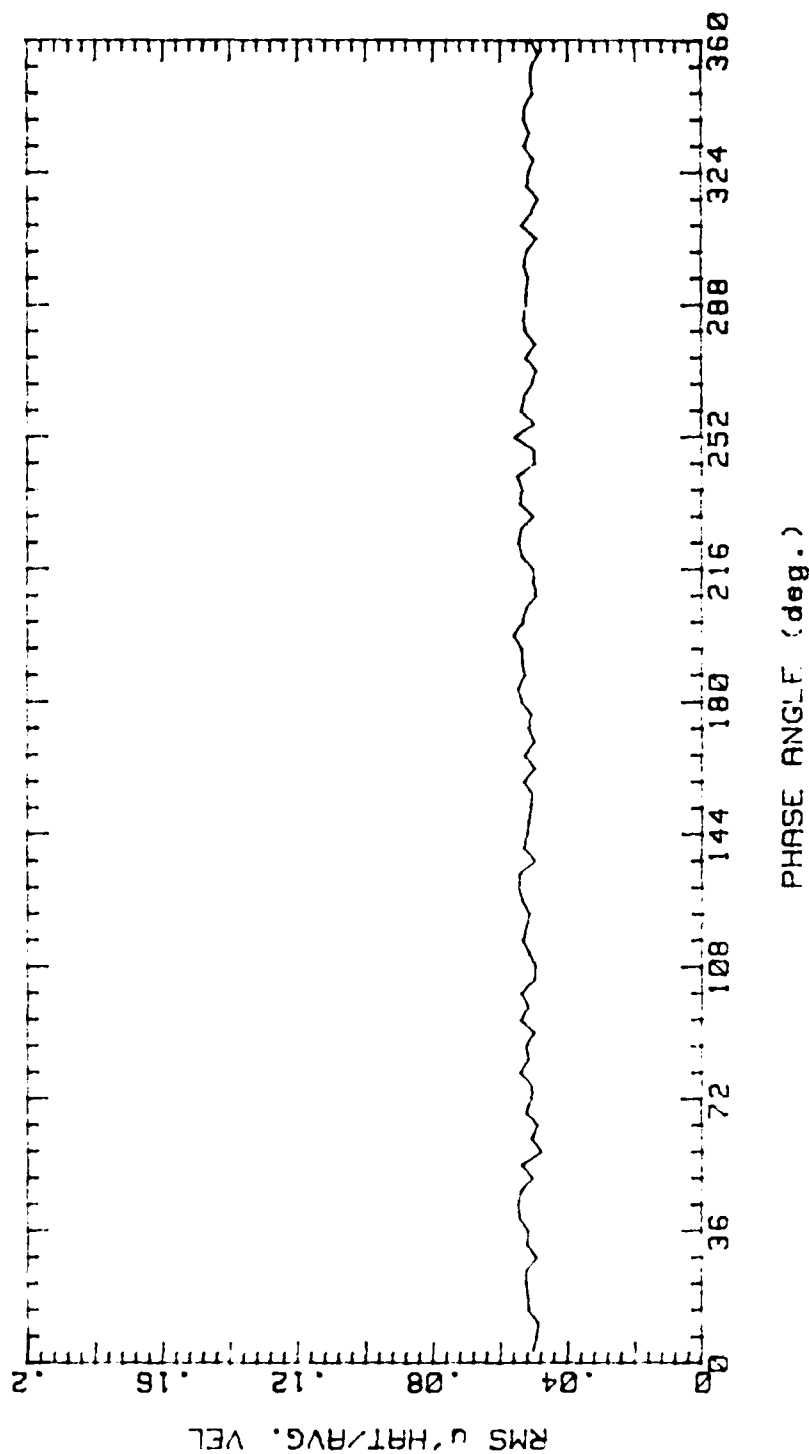


Figure 139.

RUNP5BA 93089.2027

AVG. VEL 3.434m/s RMS VEL .1786m/s  
OSC. FREQ. 1Hz STR. # .02525  
BULK VEL. 3.16m/s REY. # 2640

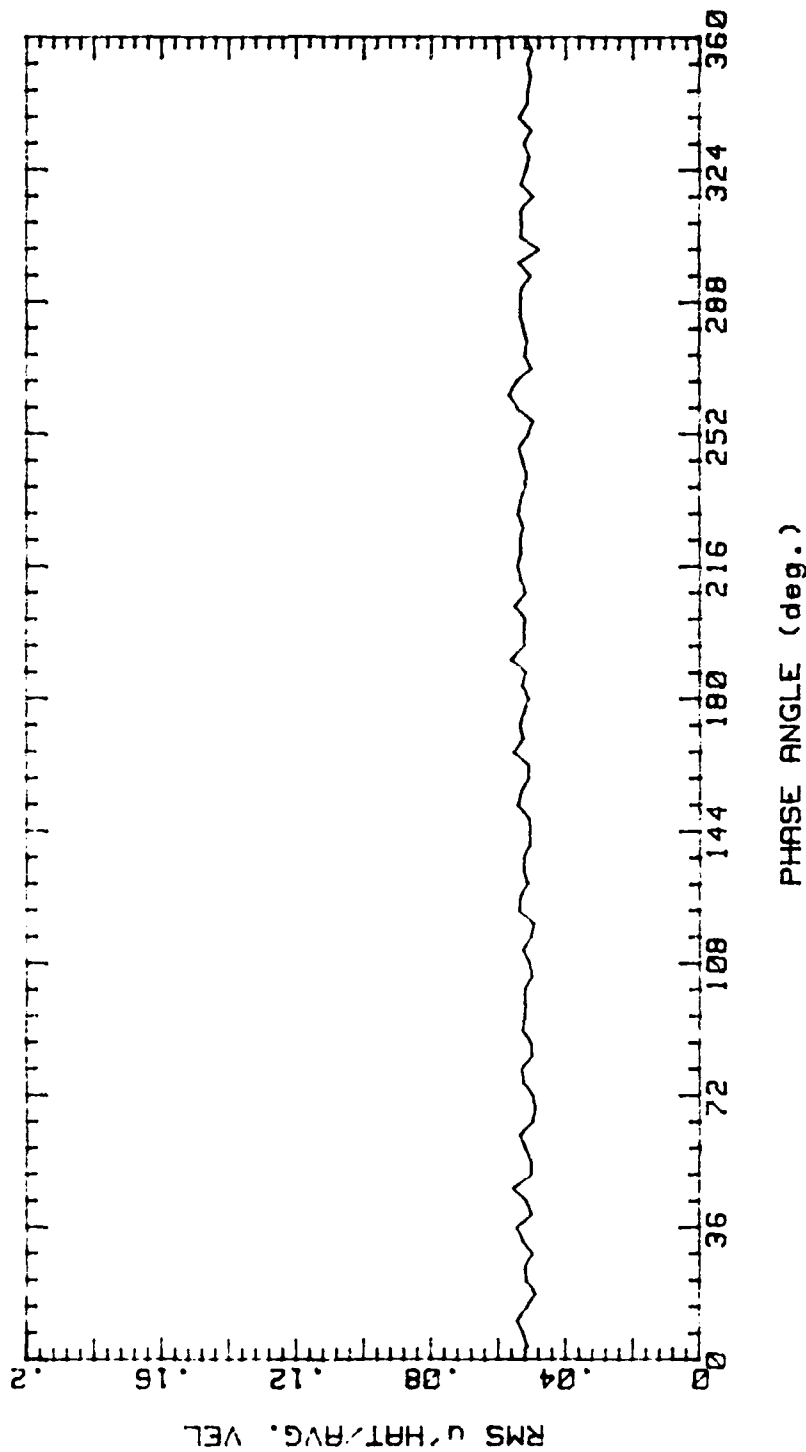


Figure 140.

RUNP6AA 93089.1845

AVG. VEL 3.538m/s RMS VEL .198m/s  
OSC. FREQ. 0Hz STR. # 0  
BULK VEL. 3.16m/s REY. # 2640

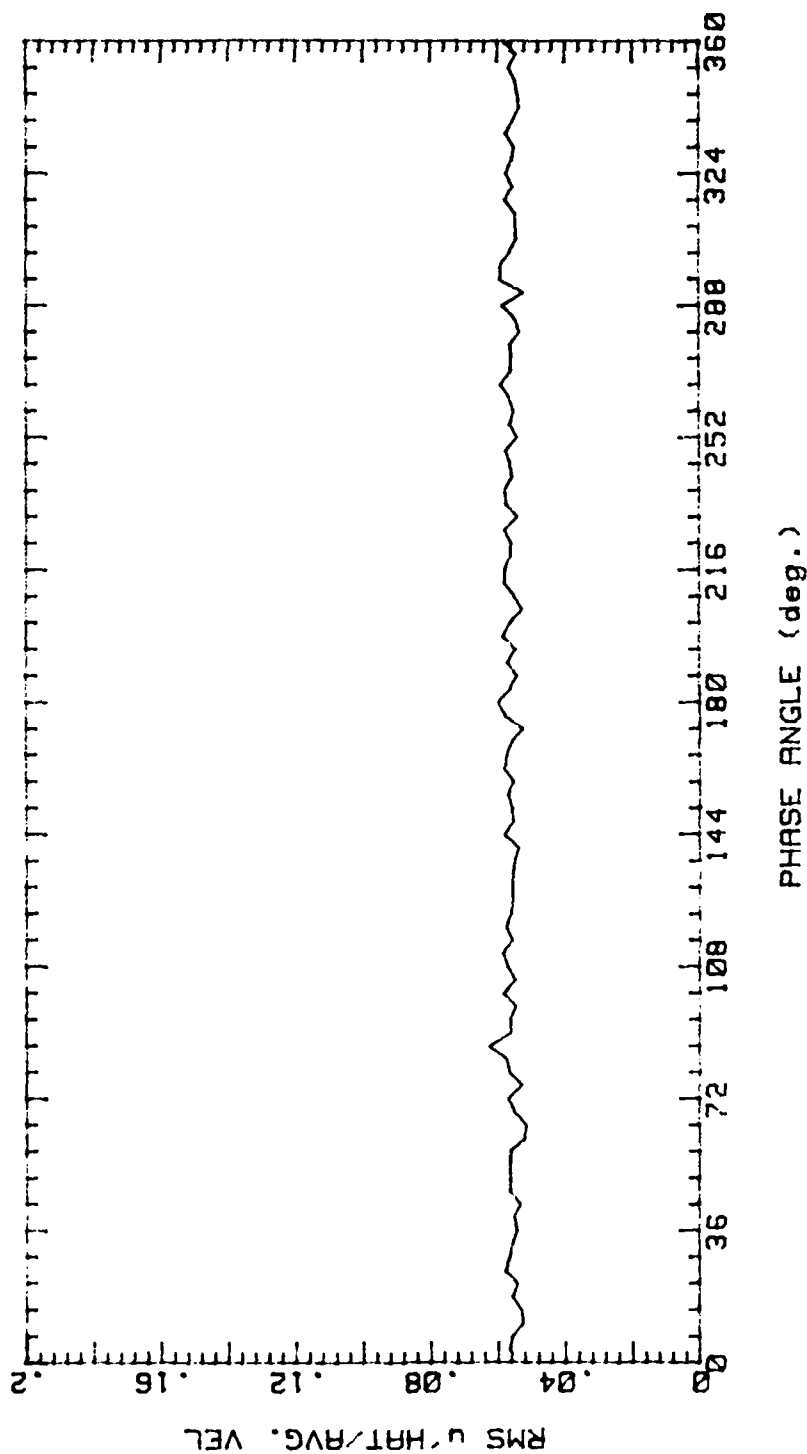


Figure 141.

RUNP6BA 93089.2041

AVG. VEL 3.332m/s RMS VEL .1892m/s  
OSC. FREQ. 1Hz STR. # .02525  
BULK VEL. 3.16m/s REY. # 2640

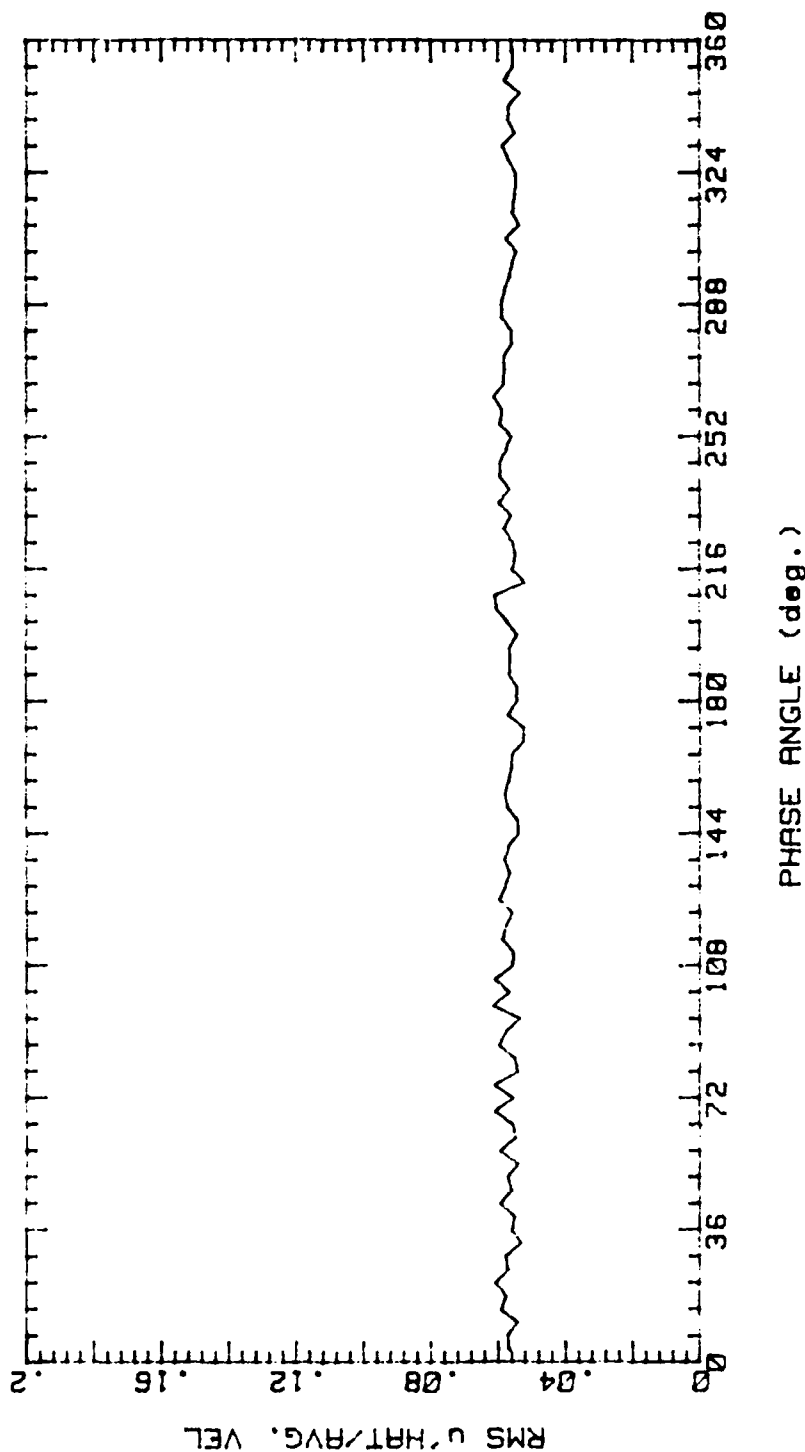


Figure 142.

RUNP7AA 93089.1901

AVG. VEL 3.327m/s RMS VEL .2572m/s  
OSC. FREQ. 0Hz STR. # 0  
BULK VEL. 3.16m/s REY. # 2640

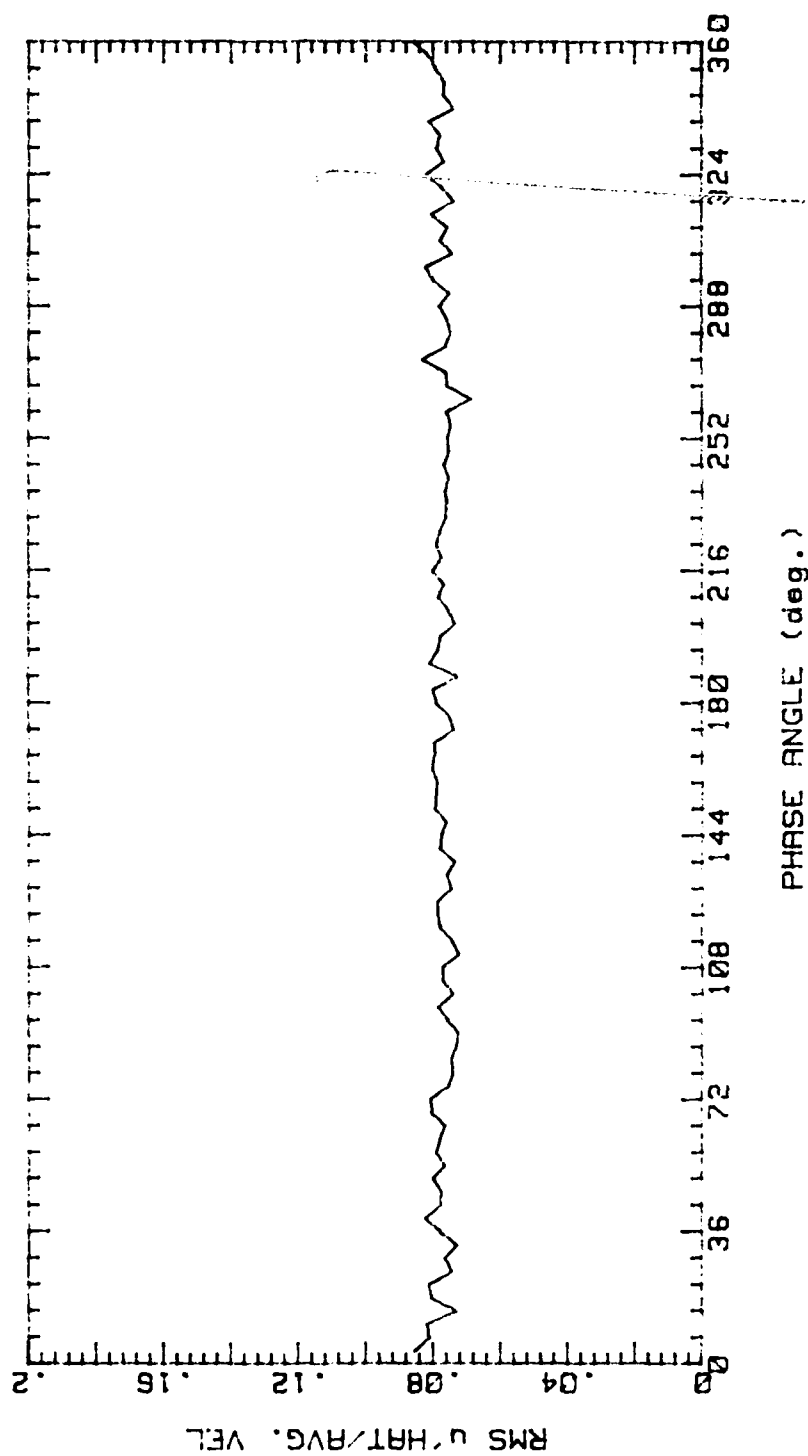


Figure 143.

RUNP7BA 93089.2053

AVG. VEL 3.386m/s RMS VEL .2623m/s  
OSC. FREQ. 1Hz STR. # .02525  
BULK VEL. 3.16m/s REY. # 2640

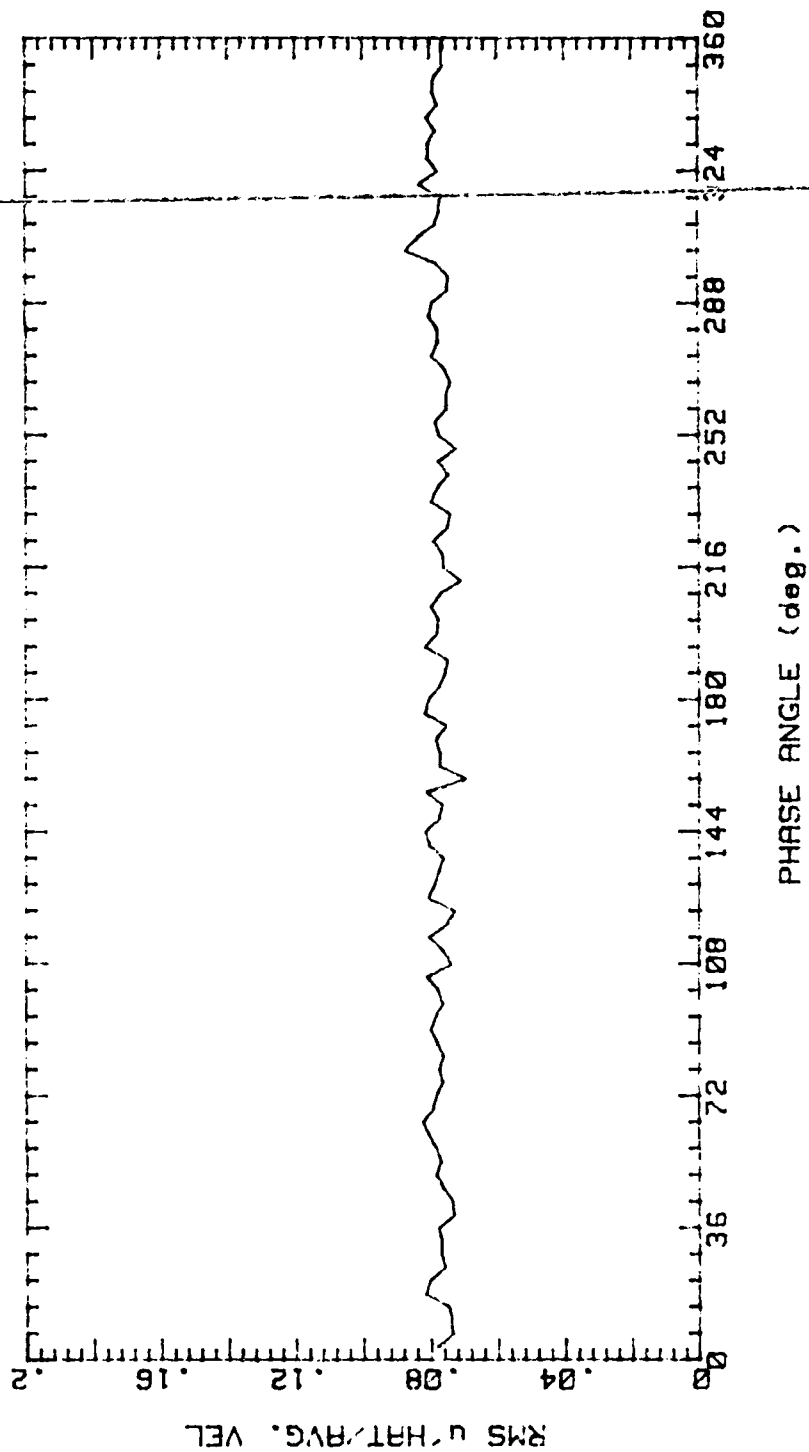


Figure 144.



RUNP8AA 93089.1917  
 AVG. VEL 3.088m/s RMS VEL .3464m/s  
 OSC. FREQ. 0Hz STR. # 0  
 BULK VEL. 3.16m/s REY. # 2640

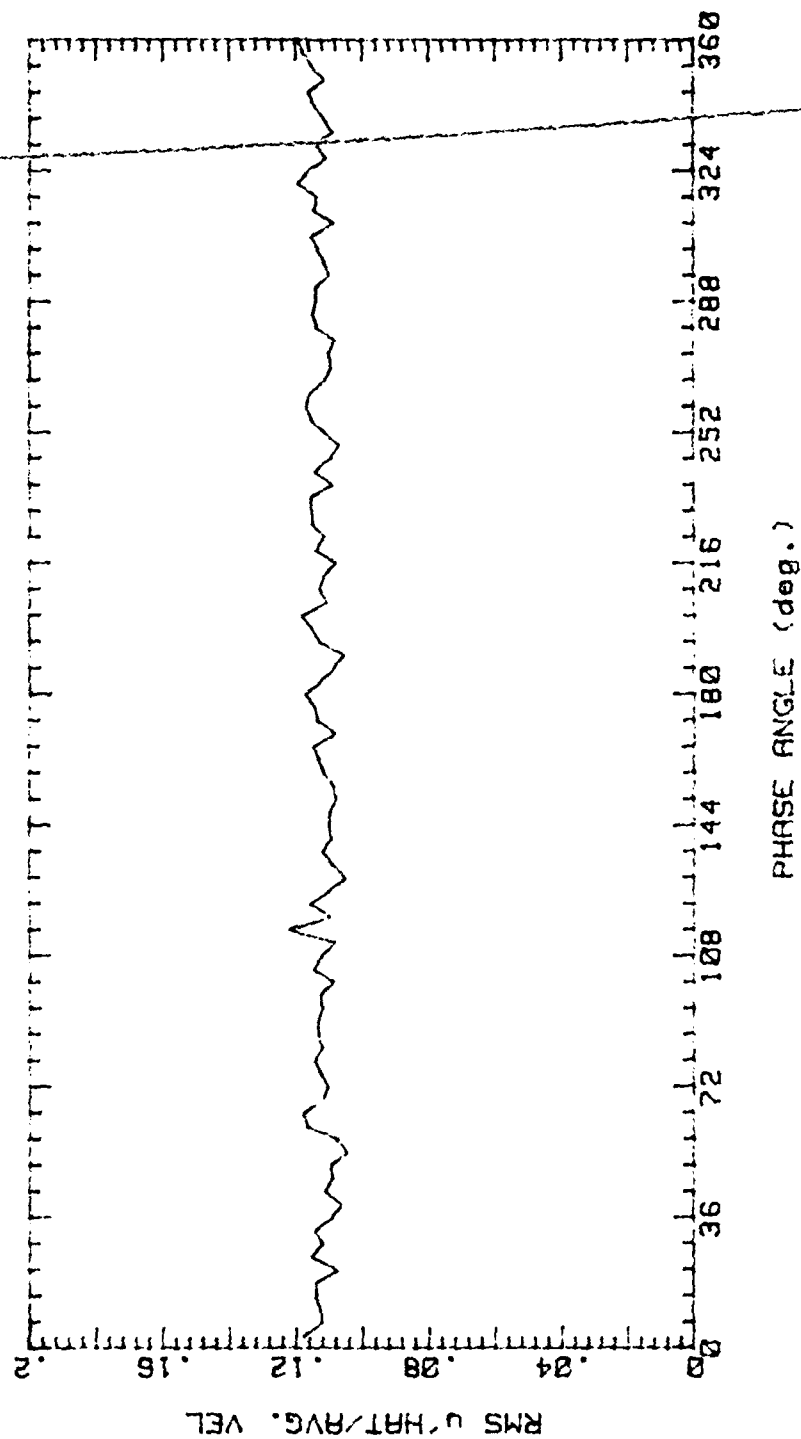


Figure 145.

RUNP8BA 93089.2106

AVG. VEL 2.991m/s RMS VEL .3459m/s  
OSC. FREQ. 1Hz STR. # .02525  
BULK VEL. 3.16m/s REY. # 2640

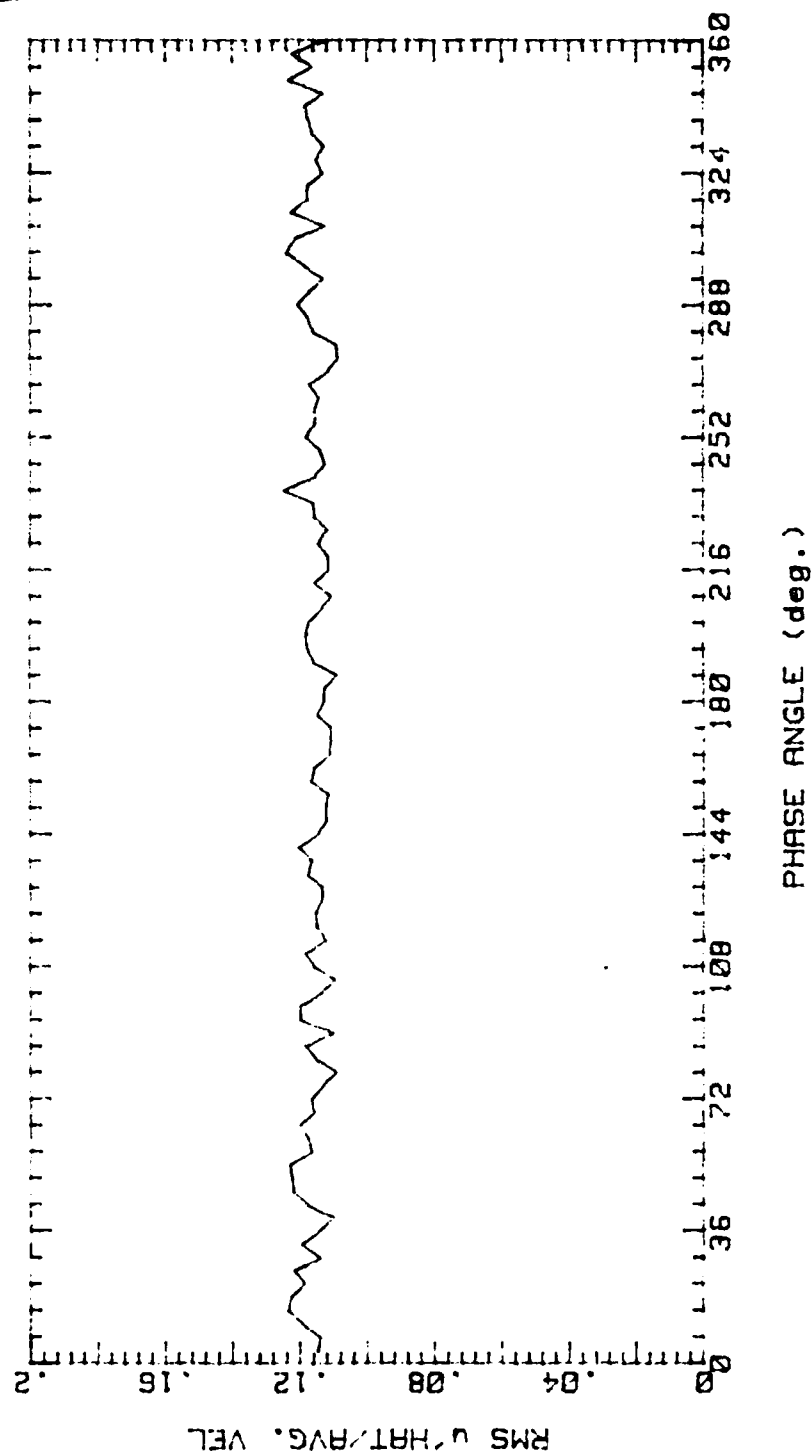


Figure 146.

Peak to Peak Magnitude of Phase Average  
RMS Velocity as a Function of  $y/d$

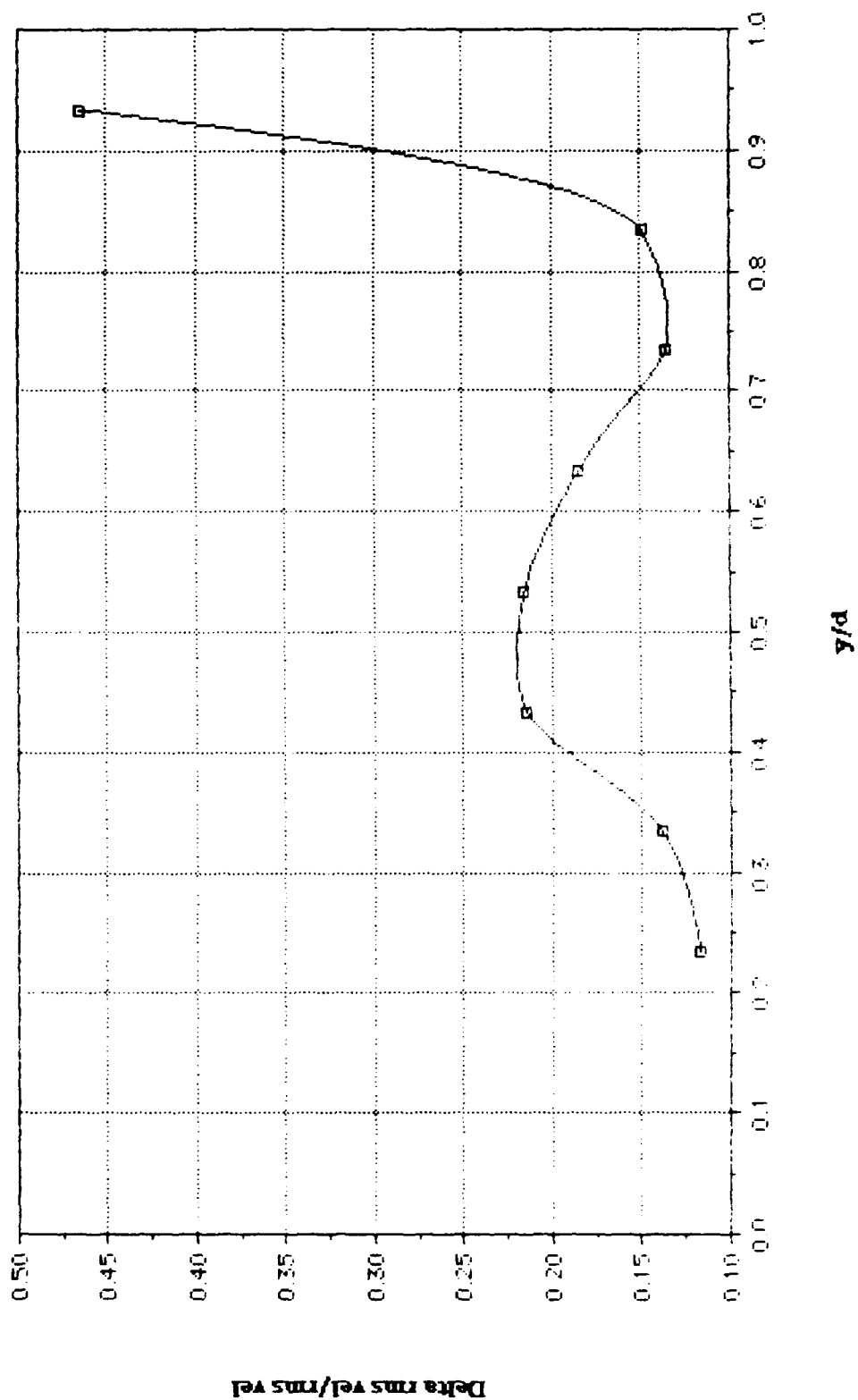


Figure 147.

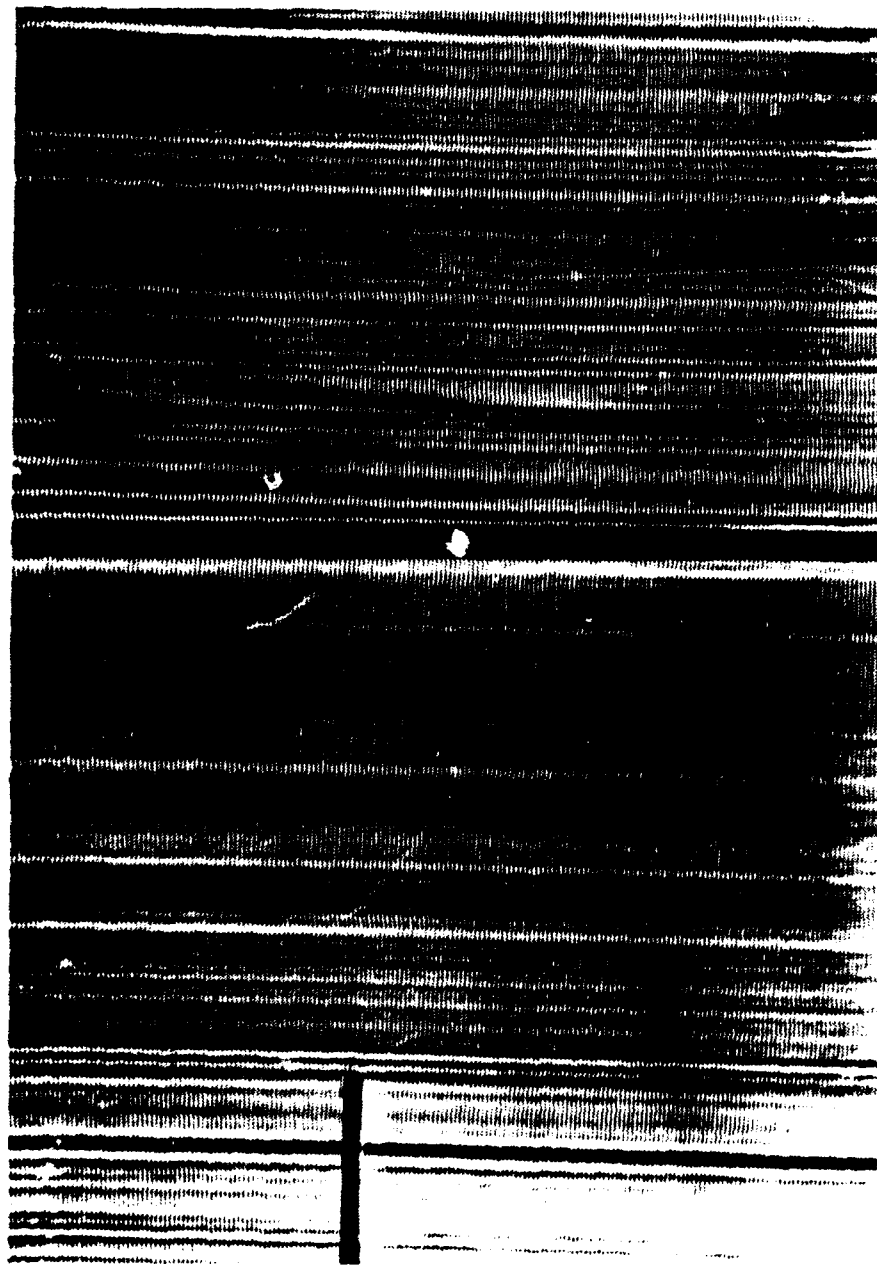


Figure 148.  $Re = 1136$

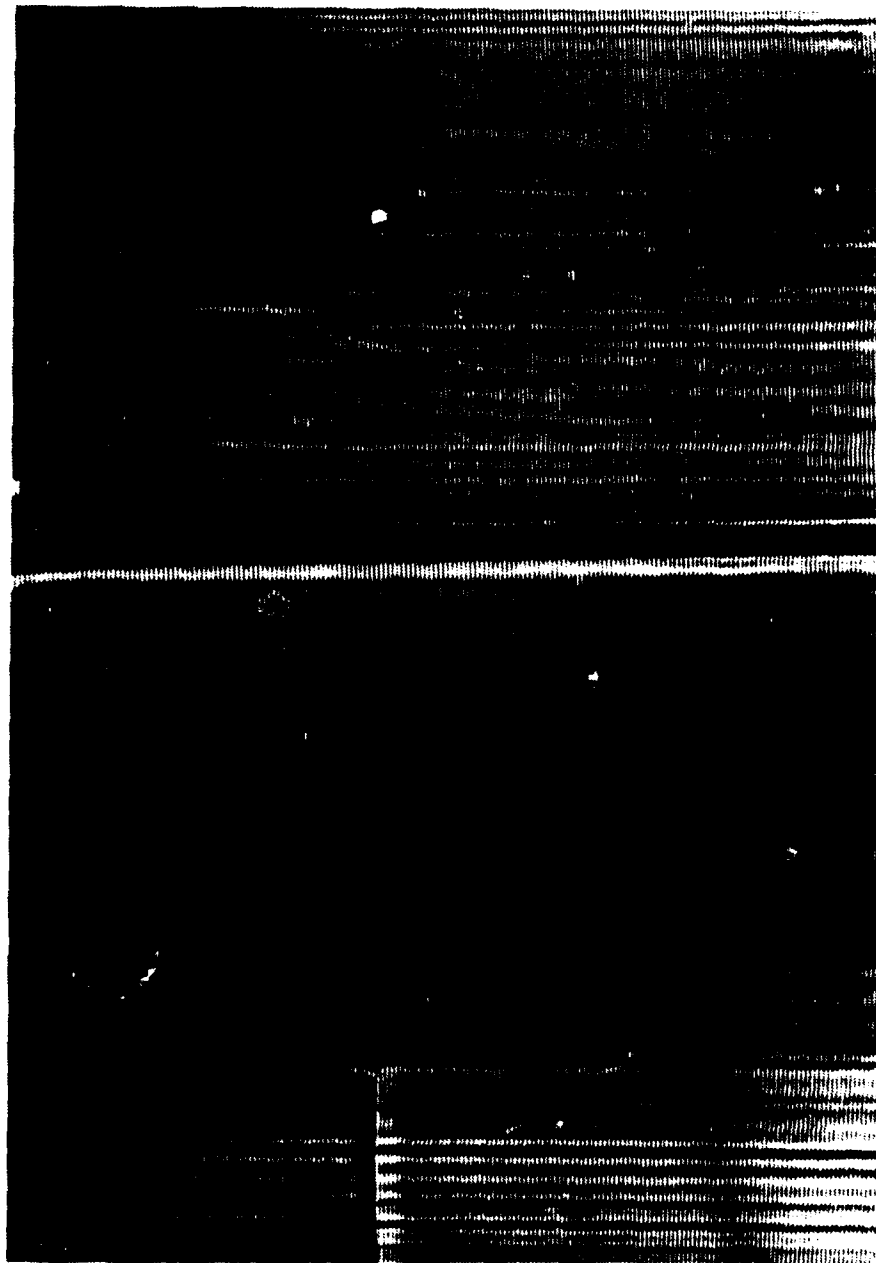


Figure 149.  $Re = 1153$

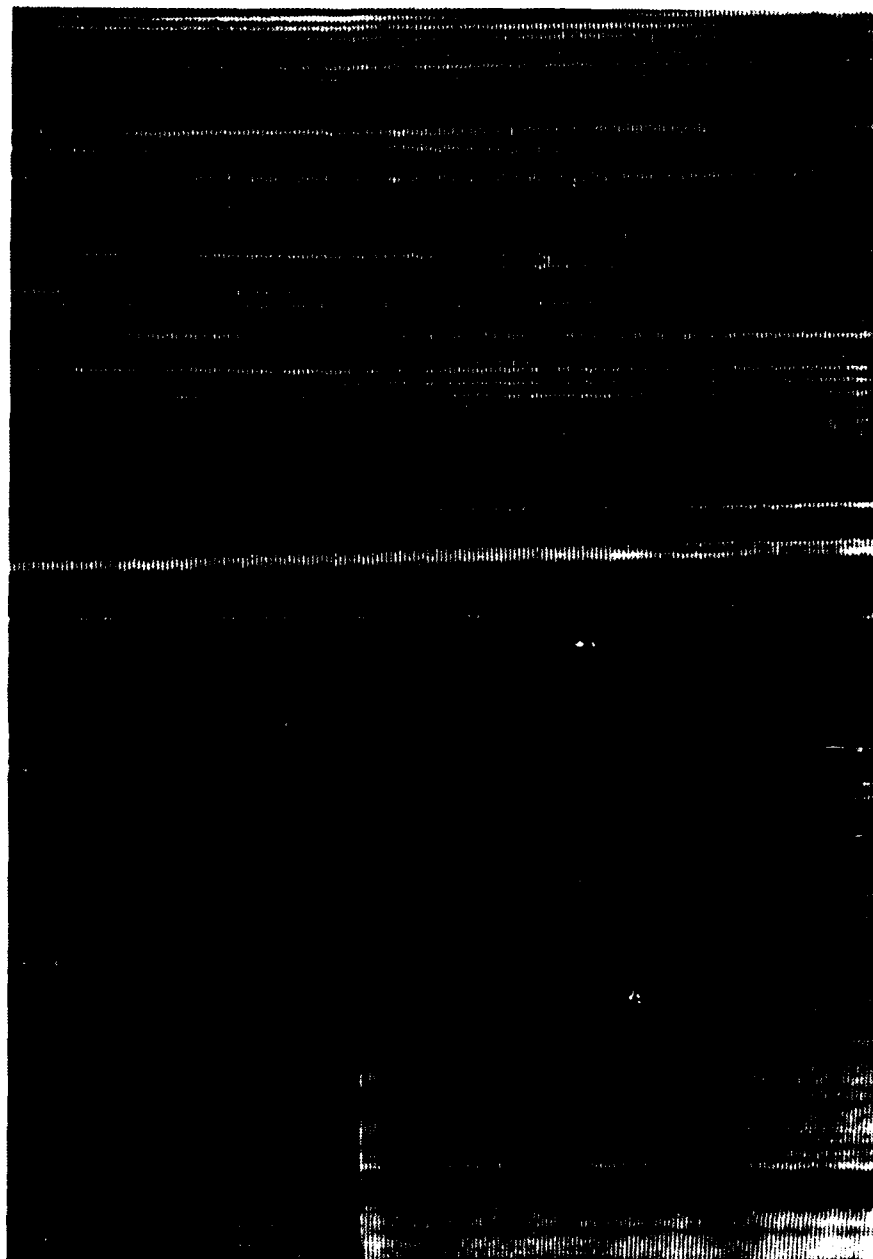


Figure 150.  $Re = 1278$

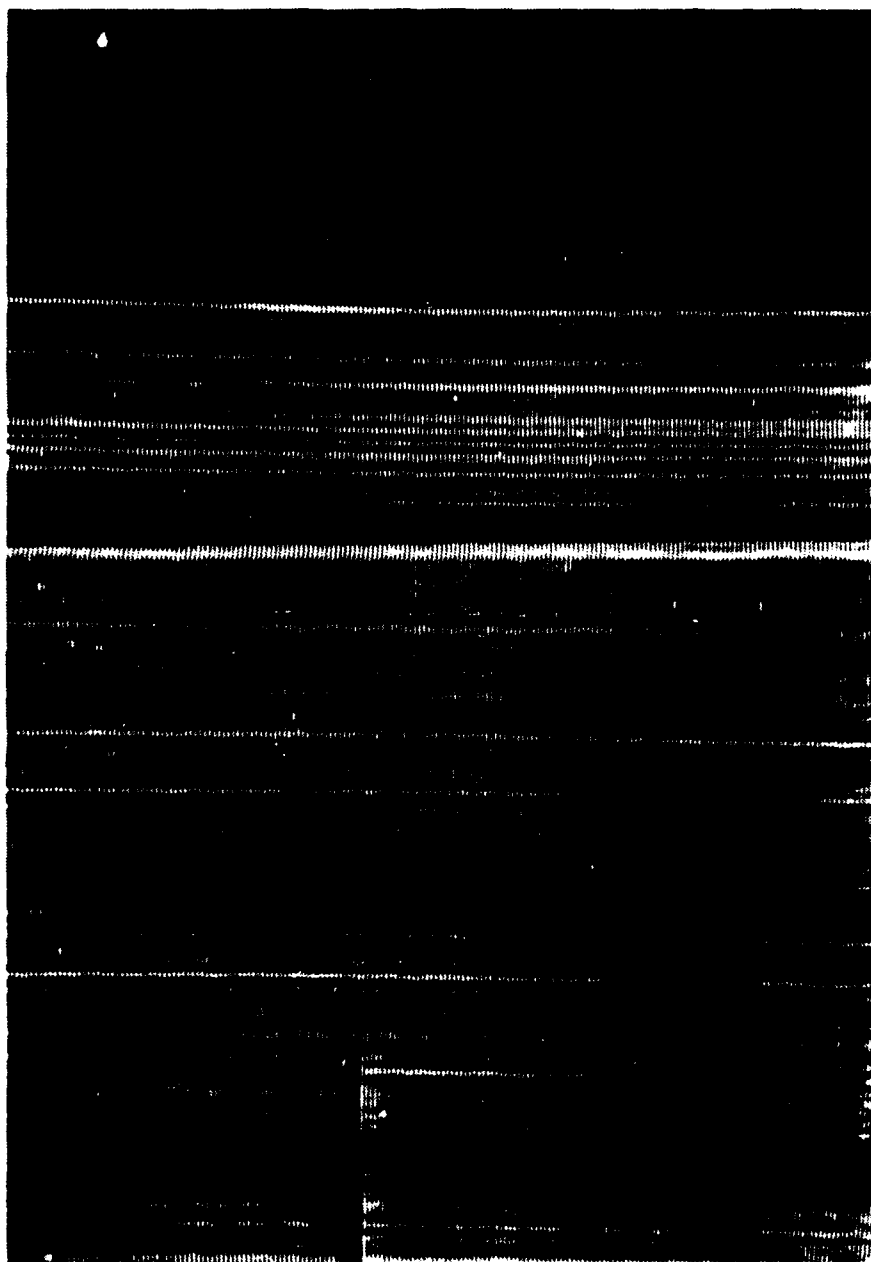


Figure 151.  $Re = 1328$



Figure 152.  $Re = 1395$



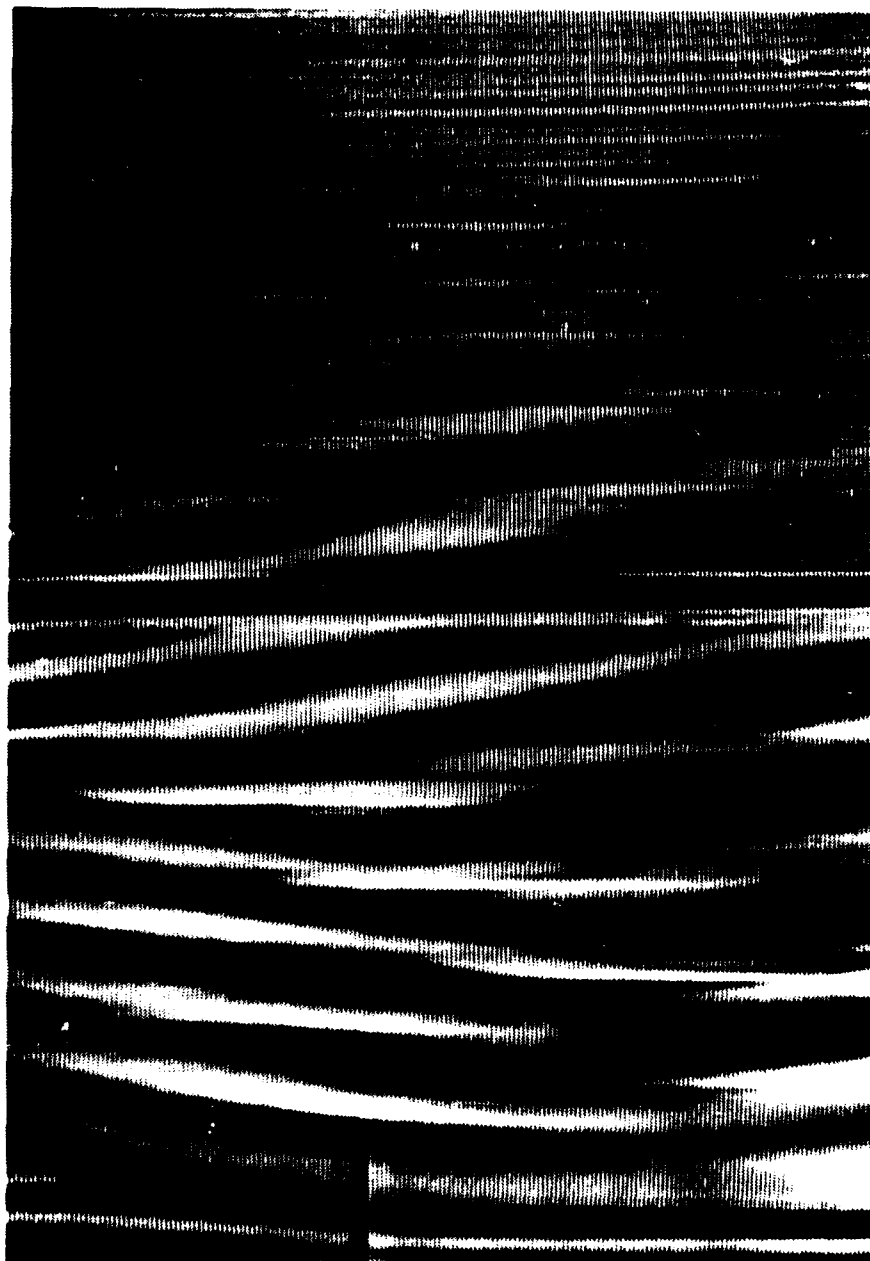


Figure 153.  $Re = 1395$

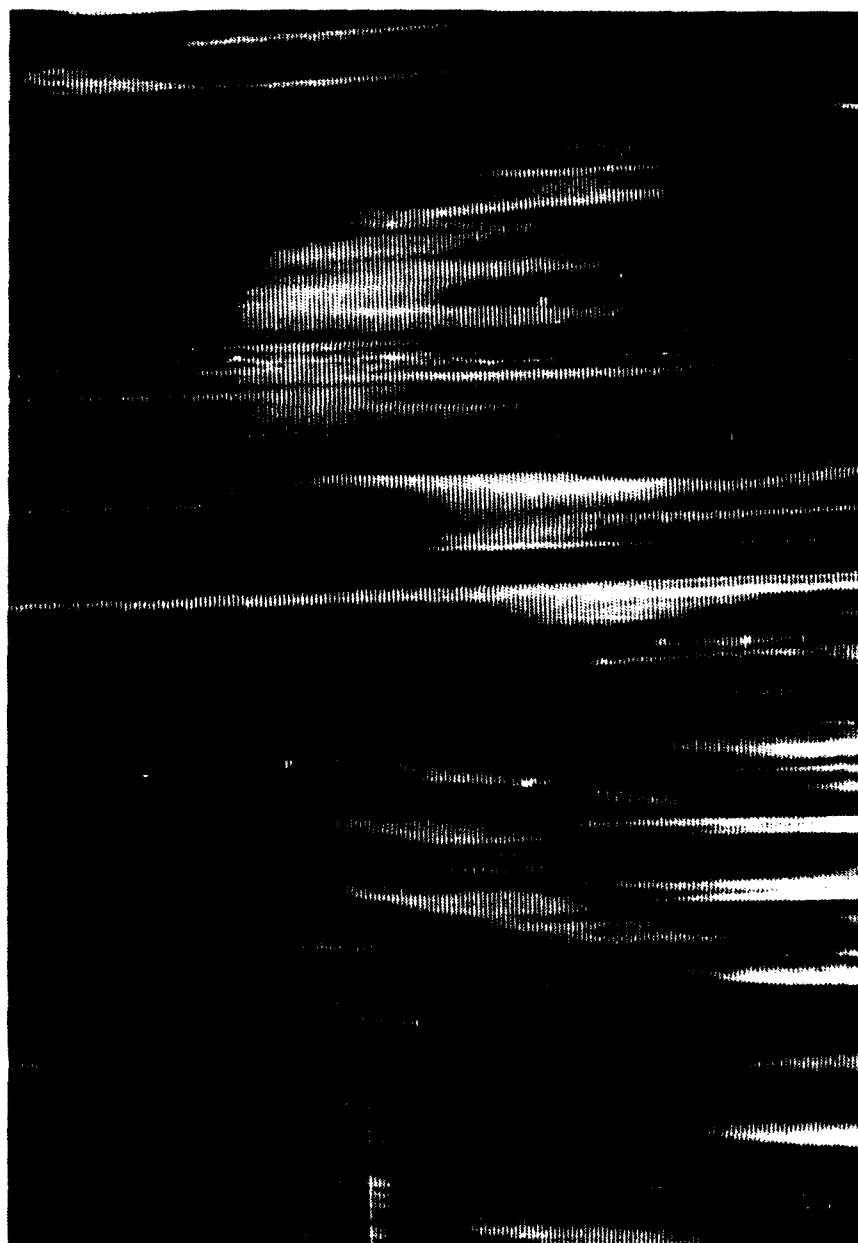


Figure 154.  $Re = 1428$

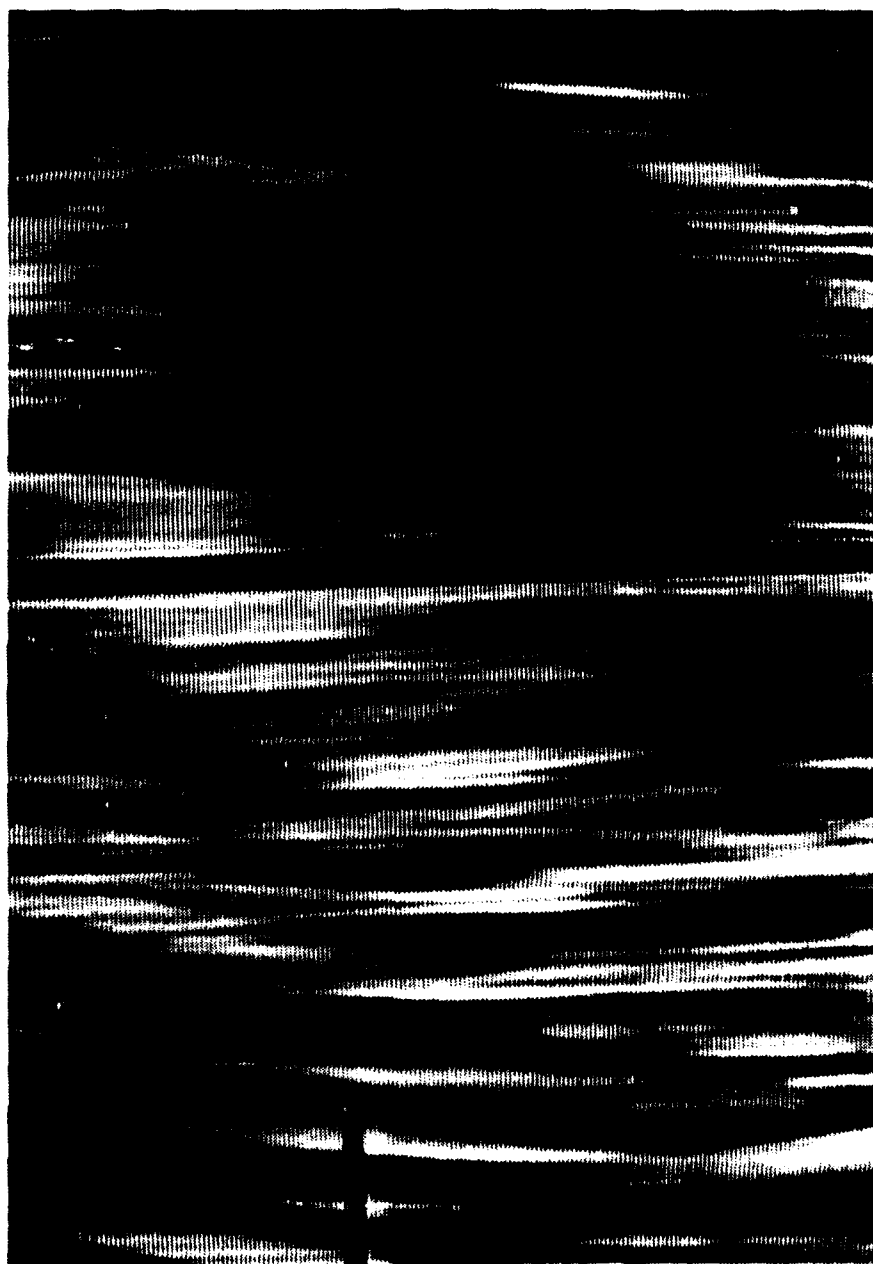


Figure 155.  $Re = 1428$



Figure 156.  $Re = 1586$

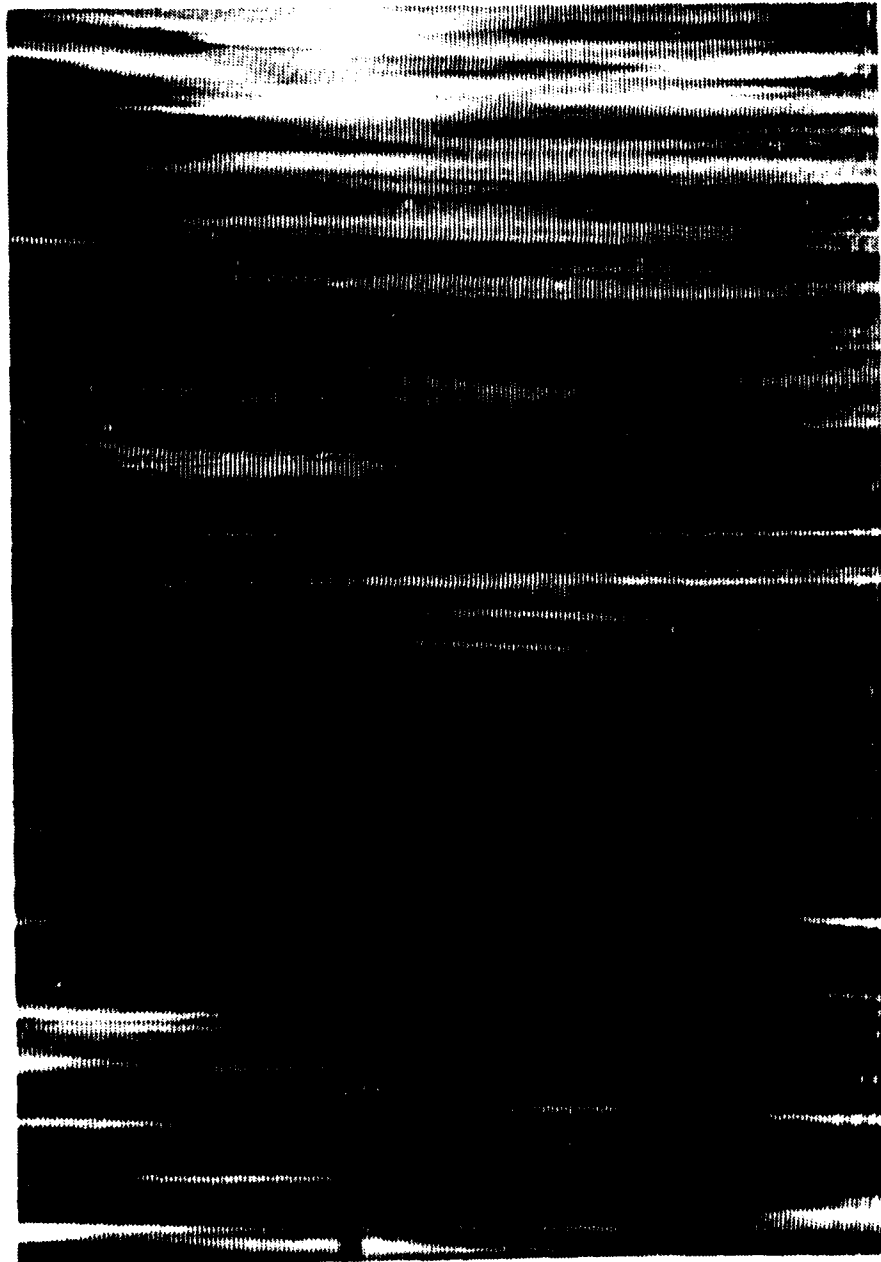


Figure 157.  $Re = 1586$

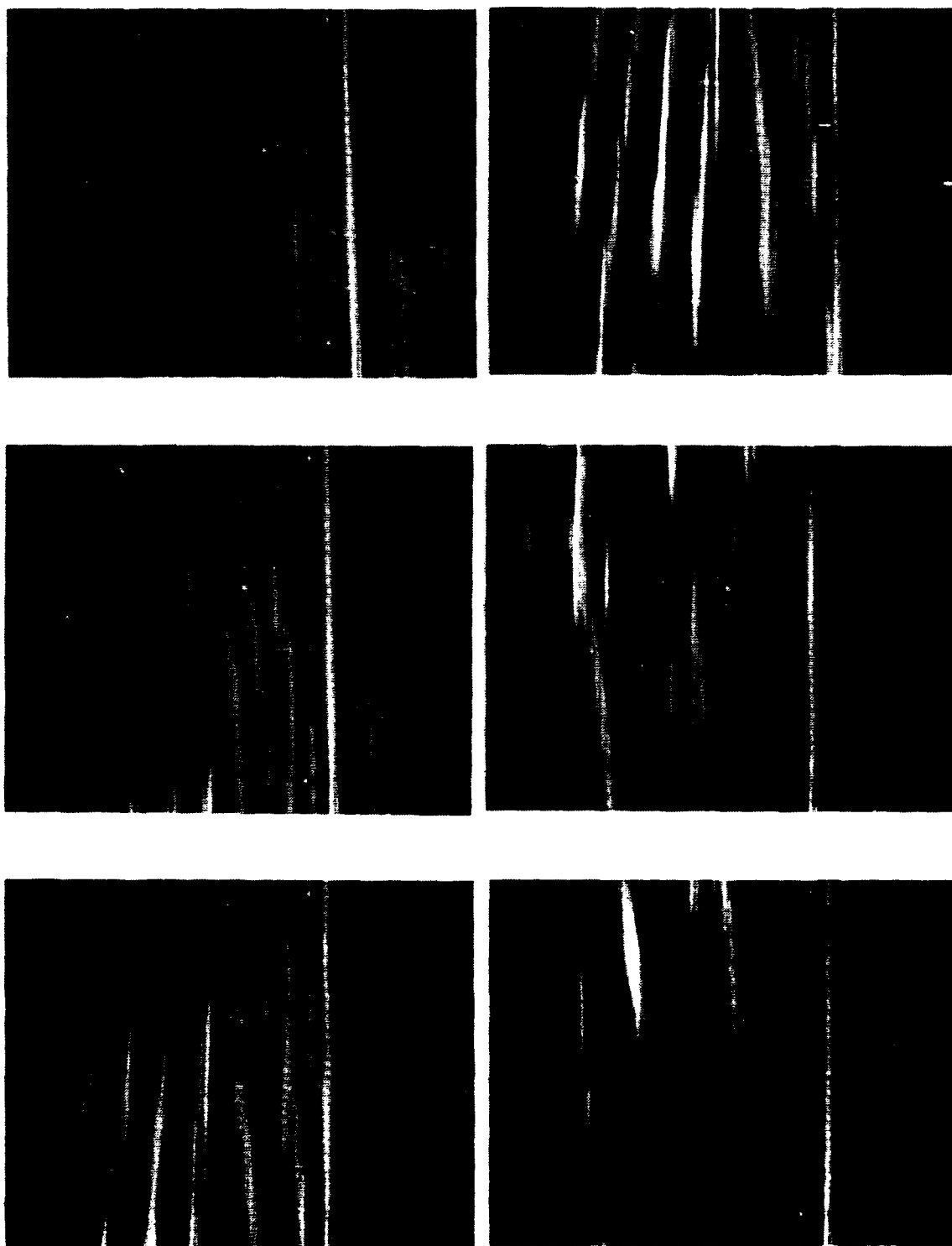


Figure 158. Time Sequence at  $Re = 1428$

## LIST OF REFERENCES

1. Thermoscience Division, Department of Mechanical Engineering, Stanford University Report TF-31, *Numerical Simulation Studies of Laminar-Turbulent Transition in the Plane Channel* by B. Singer, J. H. Ferziger, and H. Reed, May 1987.
2. Thermoscience Division, Department of Mechanical Engineering, Stanford University Report HMT-31, *Turbulent Boundary Layer on a Convex Curved Surface* by J. C. Gillis, J. P. Johnston, W. M. Kays and R. J. Moffat, 1980.
3. Ligrani, P. M., Moffat, R. J. and Kays, W. M., "Artificially Thickened Turbulent Boundary Layers for Studying Heat Transfer and Skin Friction on Rough Surfaces", *ASME Transactions - Journal of Fluids Engineering* 105, No. 2, pp. 146-153, 1983.
4. Herbert, T., "Modes of Secondary Instability in Plane Poiseuille Flow", *IUTAM Symposium on Turbulence and Chaotic Phenomena in Fluids* 1983.
5. Herbert, T., "Subharmonic Three-dimensional Disturbances in Unstable Plane Shear Flows", *AIAA Paper 83-1759* 1983.
6. Nishioka, M., Asai, M., and Iida, S., "An experimental Investigation of the Secondary Instability in Laminar-Turbulent Transition", *Laminar-Turbulent Transition* R. Eppler and H. Fasell, eds. Springer-Verlag, pp. 37-46, 1985.
7. Nishioka, M., Asai, M., "Three Dimensional Wave Disturbances in Plane Poiseuille Flow", *Laminar-Turbulent Transition* V. V. Kozlov, ed. Springer-Verlag, pp. 173-182, 1985.

8. Kozlov, V. V. and Ramazanov, M. P., "Development of Finite Amplitude Perturbations in Poiseuille Flow", *Journal of Fluid Mechanics* 147, pp. 149-157, 1984.
9. Longest, J., *Flow Visualization Studies in (1) a Curved Rectangular Channel With 40 to 1 Aspect Ratio and (2) a Straight Channel With Bulk Flow Unsteadiness*, Master's Thesis, Naval Postgraduate School, Monterey, California, June 1989.
10. Ligrani, P. M. and Subramanian, C. S., "Effects of Unsteadiness on Laminar-Turbulent Transition in Straight Channel Flow", Naval Postgraduate School Project Progress Report, Department of Mechanical Engineering, Naval Postgraduate School, Monterey, California, March 1989.
11. Schlichting, H., *Boundary Layer Theory*, McGraw-Hill, Inc, 1979.
12. Miller, J. A. and Fejer, A. A., "Transition Phenomena in Oscillating Boundary-Layer Flows", *Journal of Fluid Mechanics* vol. 18, pp. 438-448, 1964.



## INITIAL DISTRIBUTION LIST

- |  |   |
|--|---|
| 1. Defense Technical Information Center<br>Cameron Station<br>Alexandria, Virginia 22304-6145  | 2 |
| 2. Library, Code 0142<br>Naval Postgraduate School<br>Monterey, California 93943-5002  | 2 |
| 3. Professor P. M. Ligrani, Code 69Li<br>Department of Mechanical Engineering<br>Naval Postgraduate School<br>Monterey, California 93943-5000            | 6 |
| 4. Department Chairman, Code 69<br>Department of Mechanical Engineering<br>Naval Postgraduate School<br>Monterey, California 93943-5000                  | 1 |
| 5. Naval Engineering Curricular Officer, Code 34<br>Department of Mechanical Engineering<br>Naval Postgraduate School<br>Monterey, California 93943-5000 | 1 |
| 6. Professor C. S. Subramanian, Code 69Su<br>Department of Mechanical Engineering<br>Naval Postgraduate School<br>Monterey, California 93943-5000        | 2 |
| 7. LCDR Thomas M. Coumes<br>47834 McKenzie Hwy<br>Vida, Oregon 97488   | 2 |